List of Contributors

E. Alberti, *Istituto per lo Studio delle Macromolecole (ISMAC), Laboratorio di NMR, Consiglio Nazionale delle Ricerche (CNR), Via Ampère 56, 20131 Milan, Italy*

C. J. Clark, *HortResearch, Ruakura Research Center, Private Bag 3123, Hamilton, New Zealand*

R. Consonni, *Istituto per lo Studio delle Macromolecole (ISMAC), Laboratorio di NMR, Consiglio Nazionale delle Ricerche (CNR), Via Ampère 56, 20131 Milan, Italy*

Lee Griffiths, *AstraZeneca, Mereside, Alderley Park, Macclesfield, Cheshire, SK10 4TG, UK*

B. P. Hills, *Institute of Food Research, Norwich Research Park, Colney, Norwich, NR4 7UA, UK*

Jürgen Machann, *Section on Experimental Radiology, Department of Diagnostic Radiology, Eberhard-Karls-University Tübingen, 72076 Tübingen, Germany*

Irina Mader, *Section on Experimental Radiology, Department of Diagnostic Radiology, Eberhard-Karls-University Tübingen, 72076 Tübingen, Germany*

Fritz Schick, *Section on Experimental Radiology, Department of Diagnostic Radiology, Eberhard-Karls-University Tübingen, 72076 Tübingen, Germany*

Günter Steidle, *Section on Experimental Radiology, Department of Diagnostic Radiology, Eberhard-Karls-University Tübingen, 72076 Tübingen, Germany*

Claus Thamer, *Department of Endocrinology, Metabolism and Pathobiochemistry, Eberhard-Karls-University Tübingen, 72076 Tübingen, Germany*

W. S. Veeman, *Institute of Chemistry, Universität Duisburg-Essen, Duisburg, Germany*

R. Winter, *Department of Chemistry, Physical Chemistry I, University of Dortmund, Otto-Hahn Str. 6, D-44227 Dortmund, Germany*

L. Zetta, *Istituto per lo Studio delle Macromolecole (ISMAC), Laboratorio di NMR, Consiglio Nazionale delle Ricerche (CNR), Via Ampère 56, 20131 Milan, Italy*

Preface

It is my pleasure to introduce Volume 50 of Annual Reports on NMR Spectroscopy. The present volume contains first rate contributions on diverse areas of molecular science, and I am deeply indebted to the authors for their fascinating accounts and for the prompt delivery of their manuscripts.

In Vivo Proton NMR Studies in Skeletal Musculature is covered by J. Machann, G. Steidle, C. Thamer, I. Mader and F. Schick; this is followed by an account on Quality Assessment of Horticultural Products by NMR from B. P. Hills and C. J. Clark; Applications of NMR to Thermostable Proteins is reviewed by E. Alberti, R. Consonni and L. Zetta; High Pressure NMR Studies on Lyotropic Lipid Mesophases and Model Biomembrances are reviewed by R. Winter; W. S. Veeman discusses Diffusion in a Closed Sphere; finally L. Griffiths covers Automatic Analysis of NMR Spectra. It is a pleasure for me to record my gratitude to all of the authors and to the production team for this volume.

Royal Society of Chemistry
Burlington House
London
UK

G. A. WEBB
March 2003

Contents

In Vivo Proton NMR Studies in Skeletal Musculature

JÜRGEN MACHANN[1], GÜNTER STEIDLE[1], CLAUS THAMER[2], IRINA MADER[1] and FRITZ SCHICK[1]

[1]*Section on Experimental Radiology, Department of Diagnostic Radiology*
[2]*Department of Endocrinology, Metabolism and Pathobiochemistry, Eberhard-Karls-University Tübingen, 72076 Tübingen, Germany*

ANNUAL REPORTS ON NMR SPECTROSCOPY
VOLUME 50 ISSN 0066 4103
DOI 10.1016/S0066-4103(03)50001-1

This chapter reports on non-invasive characterization of human skeletal muscle by the methods of proton NMR imaging and spectroscopy. Basic knowledge about muscle structure and function is provided, followed by examples showing the appearance of musculature in contrast to surrounding tissue using established NMR imaging sequences. Special imaging techniques for musculature are presented including a spectral–spatial technique for highly selective detection of muscular lipids and magnetization transfer imaging. Patterns of proton NMR spectra of human skeletal muscle are shown to be highly dependent on the orientation of muscle fibres in relation to the static magnetic field: bulk magnetic susceptibility effects allow the separation between intramyocellular (IMCL) and extramyocellular lipids (EMCL), dipolar coupling effects cause signal splittings for creatine and the TMA complex. The differences are shown for the tibialis anterior muscle and the soleus muscle. Methods and strategies for quantification of muscular spectra are described, focusing on the separation and assessment of IMCL and EMCL. Experiments used for measuring relaxation times, magnetization transfer rates, and diffusion coefficients of water and lipids and typical results are described. Studies on lipid metabolism in human skeletal musculature are presented with the main emphasis on the role of IMCL in the pathogenesis of insulin resistance and the regulation of IMCL by exogene interventions. Examples of findings in patients with muscle diseases (e.g., muscle dystrophies, myopathies and metabolic disorders) are reported. Finally, a brief overview on muscle NMR spectroscopy at higher field strength is given, and promising applications with other nuclei such as ^{31}P and ^{13}C are discussed.

1. INTRODUCTION

All living cells can move to some degree, but this ability is highly developed in muscles, which act by fibre contraction: the fibres can shorten to two-thirds of their resting length. Muscles vary greatly in structure and function in different organs.

From a clinical point of view, muscle diseases are not as common as stroke or heart attack, but they occur in all age groups and can cause serious physical disability. Their impact is especially severe when children and young adults are affected. Some muscle diseases respond well to medical treatment, while many of the physical disabilities can be improved or prevented. There are

many different forms of muscle diseases, with different causes and outcome, and requiring different treatments. Muscle diseases can be divided into two major categories – those that are genetic, i.e., related to a gene disorder, and those that are not genetic. The genetic muscle diseases include a very wide range of diseases, the best known of which are the muscular dystrophies. Other genetic muscle diseases include congenital myopathies, storage myopathies, mitochondrial diseases and periodic paralyses. The muscle diseases which are not genetic (i.e., acquired) are also diverse. The most important among these are the inflammatory muscle diseases in which the body's own immune system inappropriately injures its muscles. Some non-genetic muscle diseases may be due to drugs or hormonal disorders.

Magnetic resonance imaging (MRI) is clinically used for diagnostic examinations in patients expected to suffer from muscle diseases. Morphological changes with very small (atrophy) or large (hypertrophy) volume of particular muscles or muscle groups can be visualized by MRI. In addition, inflammatory changes with increasing water content in the tissue are revealed by increased muscular signal intensity in T_2-weighted sequences. Fatty degeneration of musculature in some neuromuscular diseases comes along with substitution of muscular fibres by fat cells. This tissue modification is well demonstrated by bright signal in T_1-weighted and fat selective images. However, the contrast in usual proton MR images is dominated from water and lipid signals. Other metabolites have a too low concentration to significantly modify tissue contrast in images.

Musculature accounts for most of an individual's daily energy consumption. For this reason musculature plays an important role in the metabolism of the entire body. Fast acting musculature is rich in myoglobin (for oxygen transport) and creatine/creatine phosphate (for energy transport). The organ shows a distinct preference for free fatty acids (FFA), ketone bodies and lactate, but requires insulin for efficient glucose uptake and utilization. In general the routine tasks are handled by slowly contracting, economical fibres with a fat-based aerobic metabolism, and the more expensive high-speed fibres using carbohydrate fuels are only recruited when the occasion demands.

Proton NMR spectroscopy (^{1}H MRS) has shown to offer excellent possibilities for evaluation of biochemistry *in vivo*. Due to its non-invasive character it is of increasing interest not only for the study of human brain diseases, which describe the majority of clinical applications, but also for metabolic characterization of organs outside the brain, as prostate, liver, heart or skeletal muscle. Studies on skeletal muscle have been of increasing interest during the last years, since it was shown that ^{1}H MRS enables the differentiation between two muscular lipid compartments: the bulk fat components along the fasciae and muscular boundaries, which are called extramyocellular lipids (EMCL), and the metabolically highly active intramyocellular lipids (IMCL). The latter are stored in spherical droplets in the cytoplasm of muscle

cells. Mainly the IMCL compartment is of major interest under different points of view: the IMCL seems to be involved in the pathogenesis of skeletal muscle insulin resistance and type 2 diabetes mellitus, and it furthermore seems to be an important fuel during exercise and is thus of interest in the field of sports medicine.

This chapter focuses on the characterization of skeletal musculature by proton imaging and proton volume localized spectroscopy. These techniques are usually available for many clinical sites and for clinically oriented research groups. Proton examinations especially allow examinations of the lipid content and metabolism of the muscles. As mentioned above, several studies showed an important role of lipids in the pathogenesis of diabetes and obesity. In this context, a few excursions to other useful MR techniques like phosphorous spectroscopy are added in the context. The presented chapter will not comprise all important experiments on metabolism in animals using highly advanced high-field MR units providing multi-nuclear examinations, but it will provide some insight into the possibilities of adapted examination protocols working on "standard" clinical MR units.

2. STRUCTURE AND FUNCTION OF MUSCULATURE

Muscle makes up 40–50% of body mass. It is the tissue which allows one to move the limbs, which is utilized in articulating the joints of the skeleton. On closer examination all the muscles in the human body show biochemical specialization allowing them to perform their particular physiological functions: the muscles in the back and buttocks evolved for continuous heavy lifting where fuel economy is important. The eyeballs are steered by extraocular muscles when reading: they must contract quickly and precisely. The hollow viscera often require a slow steady squeeze to function properly. The heart muscle must provide continuous circulation of blood for transport of oxygen and nutritive substances. The different muscles in the body can be divided in three main types, which are described in the following.

Skeletal muscle is under conscious control. Each fibre is an enormous, multinucleate cell, formed by fusing hundreds of *myoblasts* end-to-end. They show a striated pattern, reflecting the regular arrangement of sarcomeres within each cell.

Cardiac muscle is similar to skeletal muscle, but is not under conscious control. These mono-nucleate cells are much smaller, but still show a striated pattern. The cells are in electrical contact through communicating gap junctions. These are important for the orderly spread of excitation through the heart. Spontaneous electrical depolarization of the specialized pacemaker cells together with conducting fibres activate the bulk of the ventricular muscle in the chamber walls, in each case through direct electrical contacts.

Smooth muscle is closer to non-muscle cells. No regular striations are visible and the contractions are much slower. Smooth muscle is found in the blood vessels, gut, skin, eye pupils, urinary and reproductive tracts. Smooth muscles form a very heterogeneous group of tissues, and the properties of vascular smooth muscles differ greatly from those in the airway, gut or reproductive tract.

2.1. Structure of skeletal musculature

The present work focuses on examinations in skeletal muscle, which makes up the bulk of the body's muscle and is the tissue we use for physical activity. For this reason features of this muscle type are reported in more detail in the following.

Skeletal muscle is composed of bundles of tissue, with a tendon at either end. Usually the fixed end is referred to as the tendon of origin, the end that moves, the tendon of insertion. Muscles produce force through the process of contraction. Stretching of a muscle is passive and performed by contraction of an antagonist. For this reason, at least two muscles are necessary for free movement of joints. The principle of flexion and extension of the elbow joint by two antagonistic muscles is shown in Fig. 1.

The muscle is composed of subunits called fascicles. The entire muscle and subunits with several fascicles are often surrounded by layers of connective tissue or fatty tissue. Fascicles are bundles of individual muscle fibres. Each fibre is one elongated cell that may extend for the length of the muscle. Each muscle fibre cell is segmented into distinct sectional bands. In contrast to most other tissues, cells of skeletal musculature have several nuclei. Within each muscle cell are numerous myofibrils, which also extend for the length of the muscle cell. Sarcomeres are the basic contractile subunit of myofibrils.

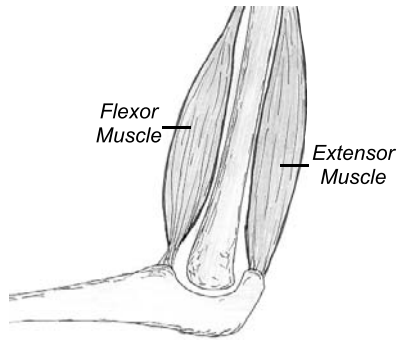

Fig. 1. The principle of articulating the joints by a pair of antagonistic muscles is shown for the elbow. On the upper end the tendons of the muscles are fixed.

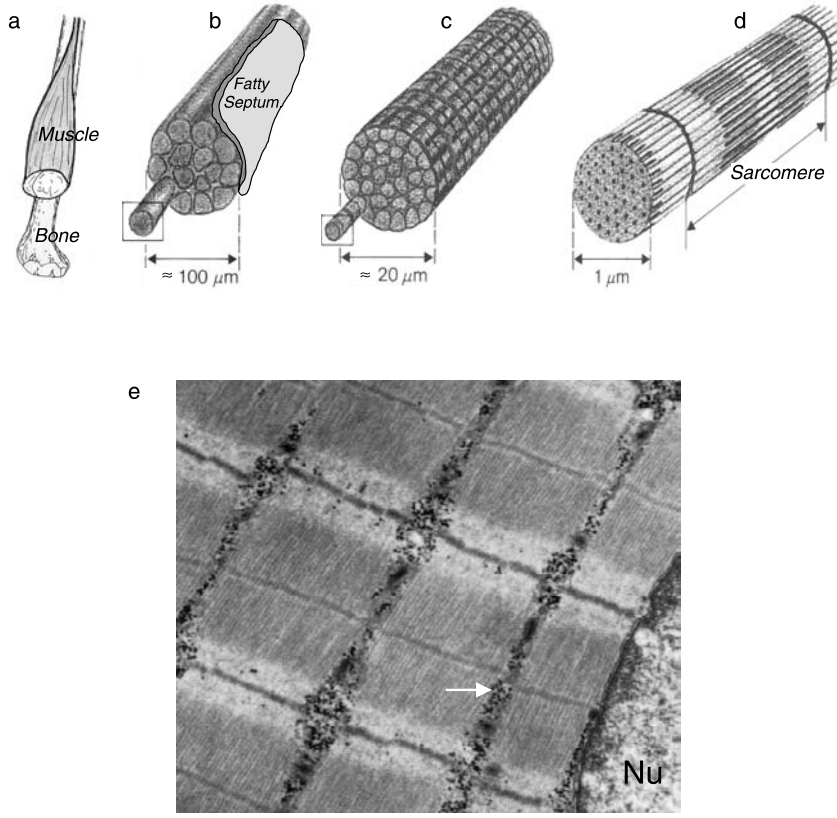

Fig. 2. Macroscopic and microscopic structure of muscle: (a) Entire muscle and its cross-section with fatty septa. (b) Fascicle with several muscle fibres (cells). A layer of fat along the fascicle is indicated. (c) Striated myofibre corresponding with one single muscle cell containing several nuclei. The lengths of a myofibre can be several tens of centimetres. (d) Myofibril inside a myocyte. It is one contractile element and contains actin and myosin and further proteins important for the muscular function. (e) Electron myograph of human skeletal muscle showing the band structure caused by the contractile myofilaments in the sarcomeres. One nucleus (Nu) and small glycogen granules (arrow, size < 0.1 μm) are indicated.

The transition from macroscopic muscles to microscopic structures is illustrated in Fig. 2.

2.2. Muscle contraction

Actin and myosin are the two principal muscle proteins in the myofibrils (Fig. 2d). They are arranged in a cylindrical structure, usually with six thin actin strands surrounding a thicker myosin fibril. The myosin fibril has

numerous small protrusions called crossbridges. The actin strand is intertwined with an even thinner, ribbon-like protein called tropomyosin, and a smaller molecule, called troponin, associates with tropomyosin in this structure. When a nerve impulse causes the muscle to contract the channels in the sarcoplasmic reticula open their gates and release calcium into the cytoplasm. At rest, the inside of the cell cytoplasm has a very low calcium concentration. After a nervous excitation calcium concentration rises, some of the calcium diffuses over to the muscle protein fibres and causes a conformational change. The Ca^{2+} ions bind to troponin and cause it to rotate slightly. This is sufficient to cause a movement of the tropomyosin, and actin now is exposed to the myosin below. The myosin crossbridge then jumps up and binds to the exposed actin. The myosin crossbridge drags along the actin fibre like a ratchet. When all the crossbridges in a sarcomere do this at the same time, the sarcomere contracts. After the nerve impulse ends, the free calcium is reabsorbed. As calcium disassociates from the troponin, ATP binds to the crossbridge to disconnect the bridge from the actin. The actin fibres change back to their previous positions and the sarcomere relaxes.

2.3. Energy metabolism and fibre types

Each activated crossbridge in the myofibrils requires ATP, and each myosin strand has dozens of crossbridges, and each muscle fibre has hundreds of myosin strands. Muscular exertion requires a lot of energy. Given the huge energy needs of muscle, and its importance to the organism's survival, the body also has a backup system. ATP in muscle exists in equilibrium with creatine. After ATP gives up a phosphate group and becomes ADP, creatine phosphate will disassociate a phosphate group and regenerate ATP. This can allow muscular work to continue even while more ATP is being created. Creatine is a short-term important reserve.

Muscle tissue accounts for most of an individual's daily energy consumption for regeneration of ATP. For this reason fuel economy is very important for minimising food requirements and for reducing unwanted heat production. In general the routine tasks are handled by slowly contracting, economical fibres with a fat-based aerobic metabolism (Type I), and the more expensive high-speed fibres using carbohydrate fuels are only recruited when the occasion demands (Type II).

Voluntary muscles contain a variety of fibre types which are specialized for particular tasks. Most muscles contain a mixture of fibre types although one type may predominate. All human skeletal muscles are composed of several different muscle fibre types. Up to seven different fibre types have been identified histochemically based on the pH stability of myofibrillar adenosine triphosphatase and on the myosin heavy chain profile.[1] Innumerable fibre type transients exist due to continuing adaptation processes. However, three main

fibre types are considered usually: Slow twitch fibres (Type I with predominantly oxidative metabolism) show about five times more triglyceride content in biopsies than fast twitch fibres (types IIa,b with predominantly glycolytic metabolism).[2] For example, the soleus muscle mainly contains Type I fibres, whereas the tibialis anterior muscle is the prototype of a glycolytic muscle.

Type I or *slow oxidative fibres* have a slow contraction speed and a low myosin ATPase activity. These cells are specialized for steady, continuous activity and are highly resistant to fatigue. They are mainly used during activities, which are moderate in intensity, up to 75% max heart rate. Their motor neurones are often active with a low firing frequency. These cells are thin (high surface to volume ratio) with a good capillary supply for efficient gas exchange. They are rich in mitochondria and myoglobin, which gives them a red colour. They are built for aerobic metabolism and prefer to use fat as a source of energy. These are the marathon runner's muscle fibres.

Type IIa or *fast oxidative-glycolytic fibres* have a fast contraction speed and a high-myosin ATPase activity. They are progressively recruited when additional effort is required, but are still very resistant to fatigue. Their motor neurones show bursts of intermittent activity. These cells are thin (high surface to volume ratio) with a good capillary supply for efficient gas exchange. They are rich in mitochondria and myoglobin, which gives them a red colour. They are built for aerobic metabolism and can use either glucose or fats as a source of energy. These are general purpose muscle fibres which give the edge in athletic performance, but they are more expensive to operate than Type I.

Type IIb or *fast glycolytic fibres* have a fast contraction speed and a high-myosin ATPase activity. They are only recruited for brief maximal efforts and are easily fatigued. Their motor neurones transmit occasional bursts of very high-frequency impulses. These are large cells with a poor surface to volume ratio and their limited capillary supply slows the delivery of oxygen and removal of waste products. They have few mitochondria and little myoglobin, resulting in a white colour. They generate ATP by the anaerobic fermentation of glucose to lactic acid. These are sprinter's muscle fibres, no use for sustained performance.

Those athletes who are genetically adapted to become very muscular – weightlifter types and body builders – are likely to have 40% Type I and 60% Type II whereas those destined to become great endurance athletes probably have 60–80% Type I and 20–40% Type II muscle fibres.

During aerobic exercise when the primary muscle fibres being utilized are Type I, FFA are used even in the presence of adequate glucose. Generally during activities of intensity between 60 and 75% max heart rate the primary muscles used are Type I. As intensity increases (to 75–85%), Type IIa come into play more and more and they utilize glucose as their source of energy – these

fibres produce most of the lactic acid. Aerobic exercise intensity between 70 and 80% max heart rate utilizes both Type I and Type IIa fibres. Aerobic exercise intensity between 80 and 85% uses almost exclusively Type IIa fibres. Exercise intensity above 85% utilizes only Type IIb fibres, which then work as anaerobic. When one runs out of glucose the only sustainable exercise is in the 60–70% range using Type I fibres.

It would take a lot of exercise to deplete the glycogen stores in muscle. Since even high-intensity aerobic exercise uses in the vicinity of 15–20 cal/min it would take at least 60 min of high intensity work to deplete glycogen stores. Endurance athletes learn to pace themselves so as to utilize both Type I (fat burning) as well as Type II (glucose burning) fibres and leave enough for the final sprint (Type IIb).

2.4. Spatial arrangement of lipids around and inside musculature

For most parts of the body a layer of subcutaneous fat (with a thickness of several millimetres to centimetres) is situated between the skin and the muscles. The muscles are arranged around the bones where the tendons insert.

Besides the subcutaneous fat layer there are two further lipid compartments inside the musculature. One of them is the so-called extramyocellular fat (EMCL) nestled in layers along the muscle fibre bundles (Fig. 2b). The thickness of those intermuscular septa containing fat is often in a range between 0.5 and 2 mm and corresponding band structures are macroscopically visible in cross-sections through skeletal musculature or in suitable MR images (e.g., T_1-weighted or fat selective techniques, as demonstrated in Section 3). The orientation of the fat layer with regard to the main axis of the extremity depends on the arrangement of the muscle fibres. Figure 3a shows a spindle-shaped (fusiform) muscle with nearly parallel fibres oriented along the axis of the muscle. Such muscles provide marked movability, but only limited force. The tibialis anterior muscle in the lower leg is an example for this type of muscle and shows fatty septa oriented along the axis of the lower leg. Reduced movability, but higher force is provided by feathered (pennate) muscles as the soleus muscle in the calf (Fig. 3b). The directions of the fibres are crossing and the orientation of the fatty septa shows a marked tilt with respect to the main axis of the extremity.

The second lipid compartment consists of microscopic nearly spherical fat droplets (smaller than 1 μm) in muscle cells. Figure 4 shows a scanning electron myograph of skeletal musculature in which the fat droplets are indicated. Those IMCL serve as a fuel for the myocytes. The lipids from blood are transported through the cytosol into the lipid droplets and are consumed mainly during long lasting moderate workload. As reported earlier Type I fibres working mainly oxidative contain clearly more IMCL than glycolytic fibres.[2]

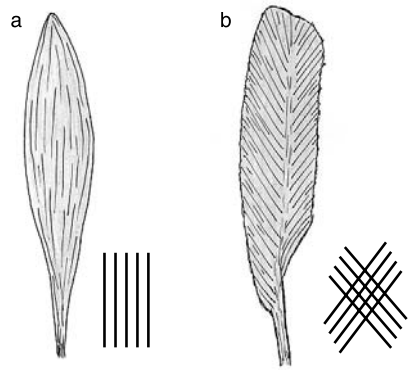

Fig. 3. Substructure of a spindle-shaped (a) and a feathered (b) skeletal muscle. The orientation of the myofibres and of the fatty septa arranged along the fibre bundles are indicated schematically.

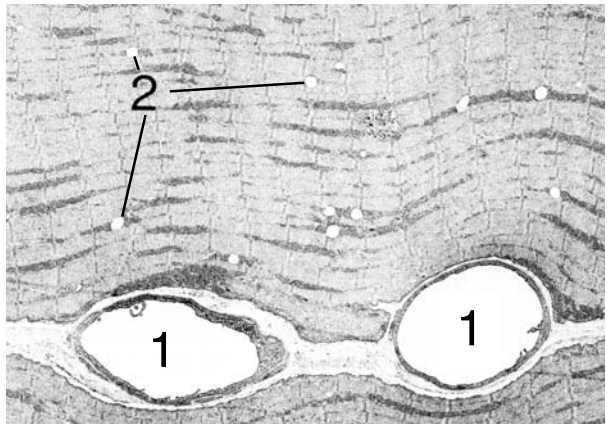

Fig. 4. Electron myograph of skeletal muscle. The band structure caused by the sarcomeres, two capillaries (1) and several small lipid droplets (2) are shown. The intramyocellular lipid droplets (size approximately 0.1–1 μm) make up the IMCL content mentioned in the context.

3. CHARACTERISTICS OF MUSCLE TISSUE IN MR IMAGING

Magnetic Resonance Imaging on whole body units provides visualization of tissue inside slices with a thickness of several millimetres. The spatial resolution in the plain is often better than one millimetre so that even relatively small structures can be well depicted. However, the spatial resolution is not sufficient to resolve the microscopic structures mentioned in Section 2. Only the cross-sections of single muscles and septa from fatty tissue or connective tissue can be visualized in MR images recorded from humans *in vivo*.

The principles of spatial encoding in MR imaging sequences are described elsewhere.[3] The contrast between different tissues is defined as the (relative) difference in their grey values in the images. The grey value of a picture element depends on the signal intensity generated by the according tissue element. There are several tissue properties, which can be used for a modification of the generated signal in proton MRI. In the following the main principles are presented for clinical and experimental characterization of musculature by MRI.

3.1. Proton density and relaxation weighted imaging

Most clinical examinations apply robust spin-echo or fast spin-echo sequences. These types of sequences provide tissue contrast changes by variation of the chosen repetition time TR (time interval between succeeding RF excitations) and echo time TE (time delay between RF excitation and signal acquisition).

Tissue contrast in sequences for standard imaging usually depends on following items:

- The proton density (= number of protons per cubic centimetre of tissue) is always contributing in a linear manner to the recorded signal intensity. Only tissues containing a sufficiently high number of protons bound to small molecules (mainly water and fatty acids, or triglycerides, respectively) can provide detectable signals in MRI and grey values in the images above the noise level.
- The longitudinal relaxation time T_1 might influence the signal contrast in the image, if the time period between successive excitations (repetition time TR) is relatively short compared with T_1 of at least one relevant tissue. In case of short TR only tissues with fast longitudinal relaxation (short T_1 values) provide high-signal intensity after the following RF excitation pulse. For T_1-weighted spin-echo imaging TR is usually chosen in a range between 400 and 700 ms for whole body MR units operating at 0.2–3.0 T.
- The transverse relaxation time T_2 has increasing influence on the tissue contrast, if the time delay between RF excitation and signal recording (echo time TE) is prolonged. Only tissues with slow transverse relaxation generate high-signal intensity for long TE. For clinical examinations TE is often chosen to be approximately 100 ms. If only free water is desired for visualization in the images (e.g., for myelography, urography or visualization of bile ducts) even longer TE up to 1.5 s are applied.

Altogether, standard spin-echo or fast spin-echo sequences can be adjusted to acquire (pure) proton density weighted images (TR > 5 s, TE < 15 ms), T_1-weighted images (TR $\approx$ 500 ms, TE < 15 ms), or T_2-weighted images (TR > 5 s, TE > 80 ms). Examples with slices containing musculature

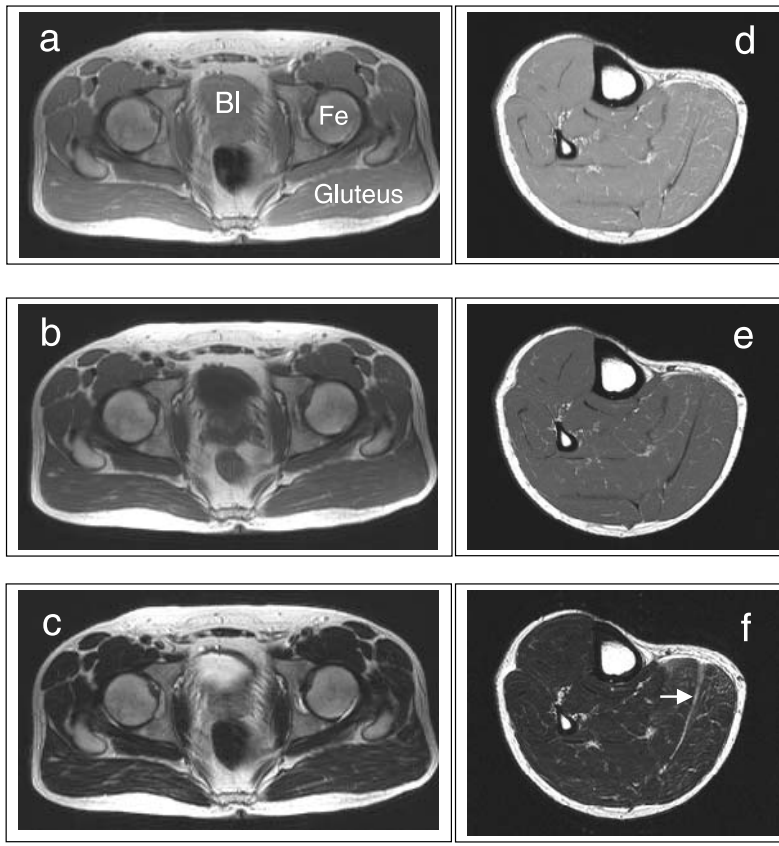

Fig. 5. Standard fast spin-echo imaging of the pelvis and the lower leg. Typical contrasts between musculature and other tissues are demonstrated. Bl = bladder, Fe = femur, Gluteus = gluteus muscle. Original recording parameters: matrix 192 × 256, slice thickness 6 mm, a–c: field of view (fov) = 380 mm, d–f: fov = 180 mm. (a) and (d): Proton density weighting: TR = 5000 ms, TE = 12 ms. (b) and (e): T_1-weighting: TR = 500 ms, TE = 12 ms. (c) and (f): T_2-weighting: TR = 5000 ms, TE = 100 ms.

are shown in Fig. 5. All images presented were recorded on a Siemens (Erlangen, Germany) whole body unit working at field strength of 1.5 T. The relevant proton density of musculature for MRI is lower than that of pure water, since the muscle proteins necessary for contraction occupy a considerable volume fraction in each cell. The protons of macromolecules do not contribute to the recorded signal in MR images due to their short $T_2 < 1$ ms.

Compared to lipids in the subcutaneous fat layer and in the bone marrow ($T_1 \approx 0.3$ s), musculature shows a clearly slower longitudinal relaxation ($T_1 \approx 1.0$ s). For this reason, musculature has lost more signal intensity than fat in T_1 weighted images, when compared with proton density weighting (Fig. 5a

vs. b and d vs. e). In contrast, free water in the bladder shows an even longer $T_1 \approx 3$ s than muscle and appears with very low signal intensity in T_1-weighted images (Fig. 5 b).

Transverse relaxation of musculature is relatively fast compared with many other tissues. Measurements in our volunteers resulted in T_2 values of approximately 40 ms, when mono-exponential fits were applied on signal intensities from images recorded with variable TE. More sophisticated approaches for relaxometry revealed a multi-exponential decay of musculature with several T_2 values.[4] Normal muscle tissue usually shows lower signal intensity than fat or free water as shown in Fig. 5c. Fatty structures inside the musculature, but also water in the intermuscular septa (Fig. 5f) appear with bright signal in T_2-weighted images.

3.2. Chemical shift selective imaging

Water and fat selective MR imaging techniques have been proven in many clinical examinations to be superior compared with standard techniques only sensitive to proton density and relaxation times. Especially MR imaging of tissues expected to consist of both, water and fat containing compartments can be improved using chemical shift selective techniques. Water selective imaging allows to determine subtle edema in bone marrow or subcutaneous fat. Areas with a high concentration of contrast medium (e.g., Gd-DTPA) leading to T_1 shortening of surrounding water molecules can be demonstrated through enhanced signal intensity when using T_1-weighted imaging. In this case, contrast is improved, if signals from fat protons having short T_1 values as well are suppressed selectively. On the other hand, fat selective imaging is an interesting tool for clinical imaging of fatty degeneration of several organs: Even small amounts of lipids in skeletal musculature or in the myocardium[5] can be assessed quantitatively.

Two principles are usually applied to clinical water or fat selective imaging: on the one hand, water and lipid signals show different longitudinal relaxation times T_1 and, on the other hand, they are recorded at slightly different Larmor frequencies due to their different chemical shifts.

Methods based on T_1 use the differences between the longitudinal relaxation times of fat protons and water protons in most tissues. The fat signal can be diminished by an inversion recovery preparation: a time delay TI of about 110–200 ms (dependent on the static magnetic field strength and on the repetition time) has to be chosen between the 180° inversion pulse and the excitation pulse. This preparation results in nulled longitudinal magnetization of fat when the excitation pulse is applied and lacking lipid signals in the final image. Lipid selective imaging with complete suppression of all water signals cannot be obtained by this method, because T_1 values of water in the tissues are different.

T_1 of water in the body ranges from 400 ms to 3 s and no single TI value leads to complete water signal suppression everywhere.

The second approach is based on chemical shift: the frequency difference between water and methylene protons in long chains of fatty acids amounts to 150 Hz per Tesla field strength. For chemical shift selective imaging of water or fat in a slice, the distribution of the static magnetic field B_0 must be improved by shimming to a field homogeneity better than 10^{-6}. Shaped RF pulses with duration of at least about 10 ms or series of short rectangular pulses allow selective excitation for fat or water selective imaging. The reported pulses work well in CHESS (CHEmical Shift Selective imaging)[6] or SENEX (SElective Non EXcitation)[7] sequences, but the frequency selective excitation does not allow additional spatial selectivity. Nevertheless, single slices can be selected using additional slice selective pulses for the generation of a spin-echo or a stimulated echo, but imaging with multi-slice operation is impossible.

3.2.1. *Technique for simultaneous slice selective and chemical shift selective excitation*

If a fast gradient system is available, it becomes possible to replace each single hard RF pulse in a frequency selective pulse train by a shaped RF pulse acting slice-selectively. Modern whole body imagers usually provide maximal gradient amplitudes of 20–50 mT/m and ramp times of 0.2–0.6 ms from zero to maximum amplitudes, which is sufficient to achieve spectral–spatial excitation. Figure 6 shows the spatial–spectral excitation in an approach which is described in detail in Ref. 8. All single RF pulses are nearly SINC-shaped and act slice-selectively in the presence of a field gradient. The refocusing of transverse magnetization in slice direction after each single RF pulse must be performed in the delay between successive pulses. Frequency selective excitation in the entire slice is obtained by the six pulses with nearly binomial amplitude ratios as in the older sequences of the SENEX type.[7] The interval between consecutive RF pulses is determined by the Larmor frequency difference of water protons and methylene (fat) protons which amounts to 215 Hz at 1.5 T. At this field strength the suitable time interval between consecutive RF pulses should be chosen to 2.32 ms to achieve a frequency difference of 215 Hz between maximum and minimum of excitation. The number of pulses and the amplitude ratios in the pulse train have to provide a relative broad frequency range without considerable excitation.[9] In the proposed spatial–spectral excitation all RF pulses were applied in the presence of slice selection gradients with constant sign and strength, because slice shifts (modulation of pulse envelopes) can be easily obtained by the usual slice shift procedure on whole-body imagers. Furthermore, gradient moment nulling for moving spin ensembles is nearly provided by the arrangement shown in Fig. 6.

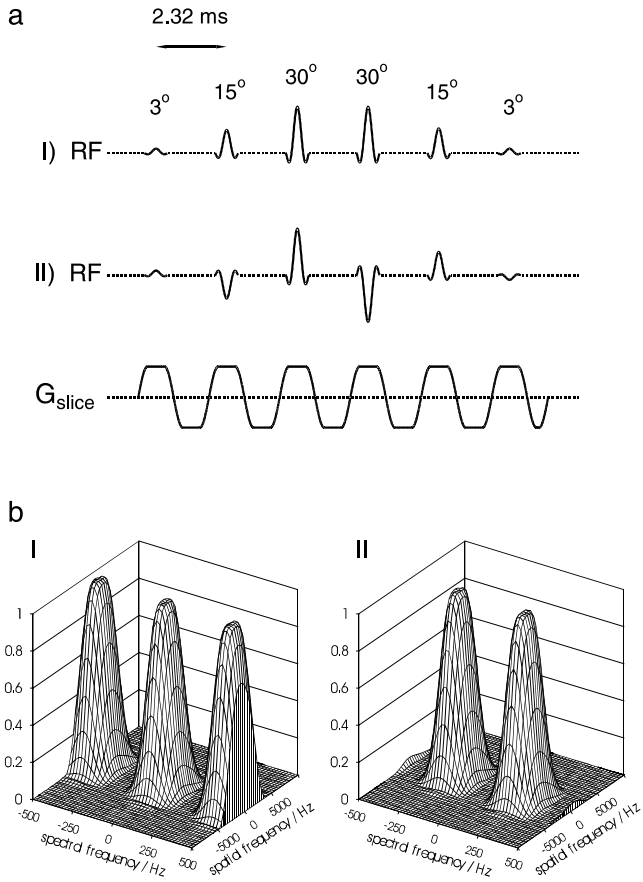

Fig. 6. Series of six RF pulses with nearly binomial amplitude ratios for spatial–spectral selective excitation and response of magnetization. (a) RF pulses and slice selection gradients: A half-period frequency shift is achieved by pulses with alternating phase of the single pulses. The gradient switching remains unchanged for excitation I and II. A slice shift can be easily obtained by usual processing of the envelopes of all single pulses (version II). (b) Excitation characteristics: The transverse magnetization after irradiation of pulse series I and II is demonstrated. The spatial frequency indicates the selected range in slice direction. If all RF pulses are irradiated with the same initial phase (I) maximum excitation is obtained at the irradiation frequency and minimum excitation for ± 215 Hz. Alternating initial phase for consecutive pulses (II) leads to minimum excitation at the irradiation frequency and maximum excitation for ± 215 Hz.

The frequency ranges for maximum and minimum excitation can be exchanged, when the phases of successive pulses are alternating (Fig. 6a, version I vs. II). Since experiments were carried out at 1.5 T, theoretical calculations were based on intervals of 2.32 ms between consecutive pulses. Transverse magnetization in Fig. 6b was calculated by a program simulating Bloch's equations.

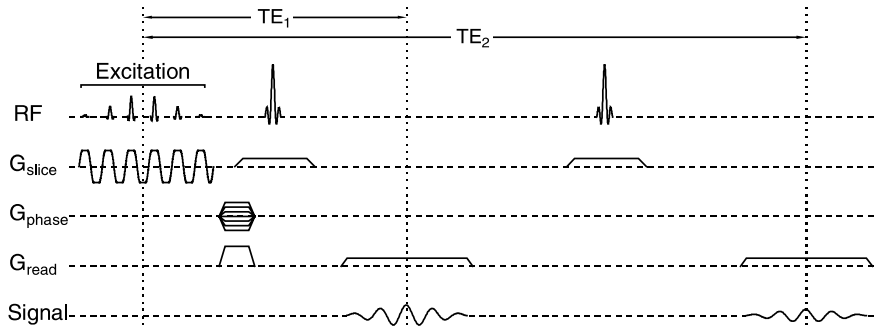

Fig. 7. Double spin-echo imaging sequence for chemical shift selective imaging. The sequence applies spectral–spatial excitation pulses as presented in Fig. 6. Refocusing is performed with standard slice selective 180° pulses. For the examples in Fig. 8 echo times were chosen to $TE_1 = 20$ ms and $TE_2 = 60$ ms.

A spin-echo multi-slice sequence with two echoes ($TE_1 = 20$ ms and $TE_2 = 60$ ms) was implemented using the described train of slice and frequency selective pulses for excitation, as shown in Fig. 7. Spin-echo refocusing provides rephasing of effects due to microscopic B_0-field inhomogeneities. Transverse water and fat selective images of the pelvis are shown in Fig. 8. Comparison of image contrast at TE = 20 ms and TE = 60 ms in the water selective images in Fig. 8a and b shows that transverse relaxation is clearly different in water containing compartments as musculature, bladder, and the cartilage of the hip. On the other hand, very similar transverse relaxation of all fatty tissues is shown in Fig. 8c and d. The same behaviour with constant values for fat but variable values for water is known from T_1 measurements. Relaxation times in muscle tissue are prolonged in cases with edema from inflammations. Even a short bout of muscular exercise leads to measurable prolongation of muscular T_2.

Proton MR examinations of musculature often focus on the lipids inside the myocytes. The role of these lipids in metabolism is reported in Section 2. Biopsies from the human vastus lateralis muscle revealed an IMCL content of 0.13–0.17% in fast glycolytic and 0.38–0.99% in slow oxidative muscle fibres.[10] Standard images recorded on whole body units provide a signal-to-noise ratio S/N > 1000 for pure fatty tissue in an acceptable measuring time of a few minutes. Due to the low fat content in musculature, the signal component of muscular fat is expected to be slightly above the noise level and the sensitivity of MR imaging to muscular fat must be optimized. To meet the requirements for high sensitivity, further sequences with gradient-echo refocusing and parameters (TR, flip angle) corresponding to the Ernst angle were combined with low receiver bandwidth. The selectivity of the spatial–spectral approach (Fig. 6) was proved by phantom measurements and was

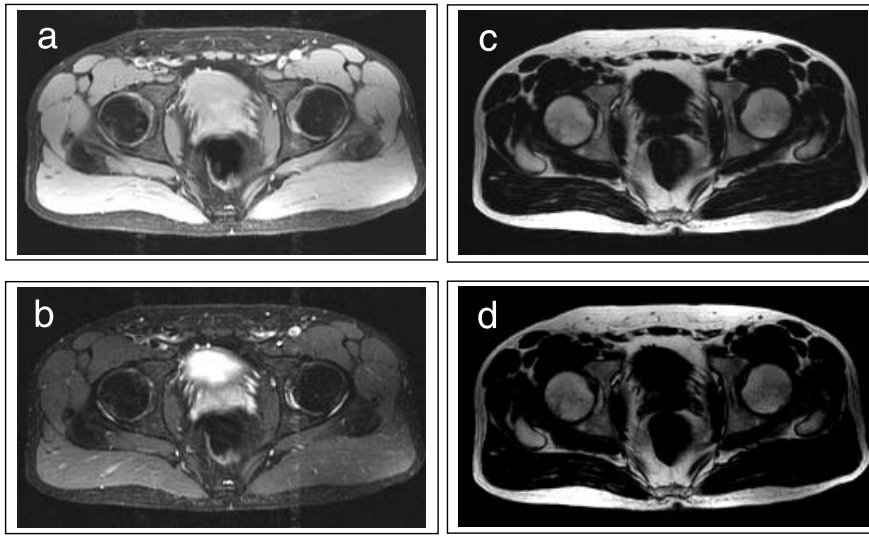

Fig. 8. Chemical shift selective imaging of the pelvis using the double-echo sequence with spectral–spatial excitation. Original parameters: matrix 192×256, slice thickness 6 mm, fov = 380 mm, TR = 5000 ms. (a) Water selective image recorded with TE = 20 ms. (b) Water selective image with TE = 60 ms shows low muscular signal intensity due to fast transverse relaxation. In contrast free water in the bladder remains bright. (c) Fat selective image using TE 20 ms. (d) Fat selective image with TE = 60 ms shows similar signal decay for all lipid containing tissues.

shown to be sufficient to detect less than 1% of IMCL in the presence of more than 50% water in musculature.[11] This optimized type of sequences was used for recording the images in Fig. 9. Figures 9a and b show highly selective water and fat images indicating tissues with high concentration of the respective component. However, the chosen slice thickness of 6 mm and 2 scans (measuring time 20 s) were not sufficient to show muscular fat properly. Using a slice thickness of 10 mm and 20 averages (measuring time 3:20 min) leads to clearly increased sensitivity to muscular fat in Fig. 9c. The homogeneous background signal is due to IMCL. Especially the tibialis anterior muscle with a high fraction of glycolytic fibres shows lower signal intensity than the flexor muscles in the calf.

Another approach to water and fat selective imaging which is also based on chemical shift effects should be mentioned here: The so-called 'Dixon' method[12] works with phase shifts in asymmetric spin-echo versus symmetric spin-echo acquisition. This method was shown to provide high-quality chemical shift selective images even in the presence of an inhomogeneous magnetic field. However, extreme high sensitivity to only one component seems to be obtained more difficult.

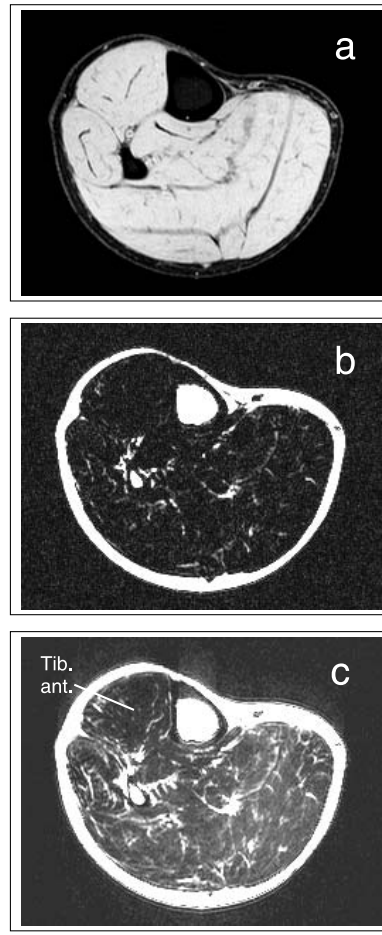

Fig. 9. Water and fat selective imaging of the lower leg using a gradient-echo sequence with spectral–spatial excitation. Original recording parameters for a and b: matrix 192×256, slice thickness 6 mm, fov = 180 mm, TR = 50 ms, TE 16 ms, flip angle (sum of all 6 RF pulses) = 48°, 2 scans. (a) Water selective image shows bright musculature and cutis. (b) Fat selective image with 2 scans and 6 mm slice thickness shows fat in the subcutaneous layer, in the bone marrow and in intermuscular septa. (c) Fat selective image recorded with 20 scans and 10 mm slice thickness reveals about 1% volume fraction of IMCL in the calf muscles as background signal slightly above the noise level. The tibialis anterior muscle contains less fat than most other muscles. Note that there are distinct interindividual differences in the distribution of muscular fat.

3.3. Magnetization transfer imaging

Magnetization transfer (MT) techniques provide additional information on the composition of tissues, which cannot be achieved by methods exclusively based on spin density, relaxation behaviour, or the chemical shift of the signals. The

mechanisms of MT are described as interactions between two pools of protons: one of the pools consists of free protons with long transverse relaxation times $T_2 > 10$ ms, whereas the other pool is represented by protons with very short $T_2 < 0.1$ ms bound to macromolecules. Selective saturation of the magnetization of the bound protons causes marked signal losses, although only the 'free proton pool' is accessible for measurements on whole body systems.[13,14] Different interactions of the 'proton pools' have been proposed resulting in MT: through-space dipole–dipole processes, the exchange by diffusion between the boundary water in the surface layer associated with macromolecules and the free water pool, and also chemical exchange are discussed to be fundamental MT processes. Signals of muscle, brain, or hyaline cartilage have been reported to be clearly influenced by MT, whereas blood, cerebrospinal or synovial fluid do not show marked signal changes due to MT. The same insensitivity to MT is reported from fatty tissue.

Sensitivity of tissue to MT can be measured by adapted imaging or spectroscopic sequences. An example of a gradient-echo imaging sequence working without or with an off-resonant MT prepulse is shown in Fig. 10. In single slice mode with short TR (about 30 ms), a Gaussian 600° MT-prepulse, irradiated 1.5 kHz off-resonant in each TR interval is used for saturation of the bound proton pool or not. The images in Fig. 11 were recorded with this sequence and reveal a marked difference in signal intensity for several types of tissue: musculature skin and cartilage are clearly influenced by MT as visible in an image, obtained by subtracting the images recorded without or with MT prepulse (Fig. 11c).

4. SIGNAL PATTERNS IN PROTON SPECTRA OF SKELETAL MUSCLE

Proton spectra of musculature in humans under *in vivo* conditions are usually recorded by volume selective techniques. Single shot approaches as Point Resolved Spectroscopy, PRESS[15] or Stimulated Echo Acquisition Mode, STEAM[16] are robust and not markedly hampered by inevitable movements of the volunteer under investigation. Both methods provide volume selection by generation of echoes which require three RF pulses. Each of these RF pulses acts slice-selectively, since a suitable band-selective RF pulse is combined with a magnetic field gradient. The slices of the three RF pulses used for echo generation define the volume, the recorded signal stems from. The principle of PRESS and STEAM sequences are shown in Fig. 12. Both sequences provide similar quality of spectra. However, STEAM allows shorter minimal echo times (TE < 10 ms), whereas PRESS obtains higher signal to noise for a given volume size and measuring time.[17]

Proton spectra of normal human skeletal muscle are dominated by the signal of water. Other metabolites contribute with clearly less than 10% to the

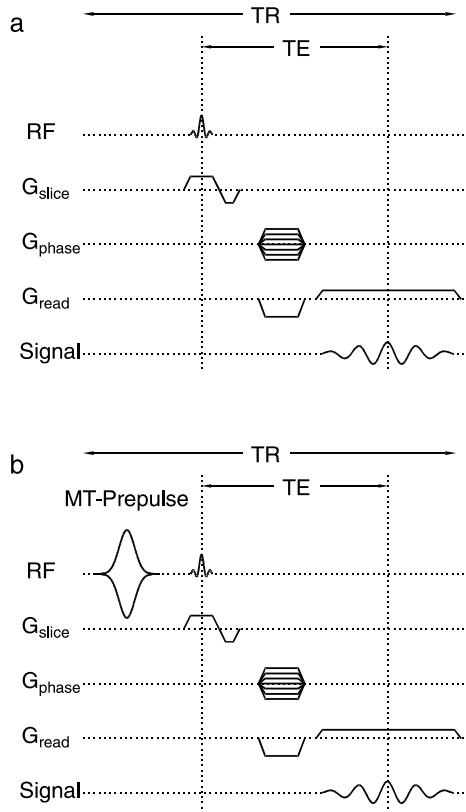

Fig. 10. Sequence for the assessment of magnetization transfer (MT) effects. Images recorded without (a) and with MT prepulses (b) have to be subtracted. In the presented example a standard gradient-echo sequence is used for MT imaging. The MT prepulse is Gaussian-shaped with a flip angle of 600° and 1.5 kHz off-resonance frequency.

measured signal intensity as shown in Fig. 13b and c. In contrast, yellow bone marrow is dominated by the signals from lipids (Fig. 13d). It is also evident that those lipid signals have the highest amplitude besides water in the muscle spectra. The recorded lipid signals stem from fatty acids in triglycerides. Figure 14 presents the structure of a triglyceride molecule and the different sorts of protons contributing to the spectrum with different chemical shifts. The spectral pattern of fat in proton spectra recorded from humans is quite stable, since chain length and type of fatty acids are only slightly variable.

In water-suppressed muscle spectra, contributions of lipids, methyl and methylene groups of creatine (Cr_3, Cr_2), trimethylammonium-containing compounds (TMA), including signals from carnitine (Ct), choline (Cho), and taurine (Tau) are well observable as demonstrated in Fig. 15. Furthermore, small signals of histidine protons of carnosine (Cs) can be sometimes identified

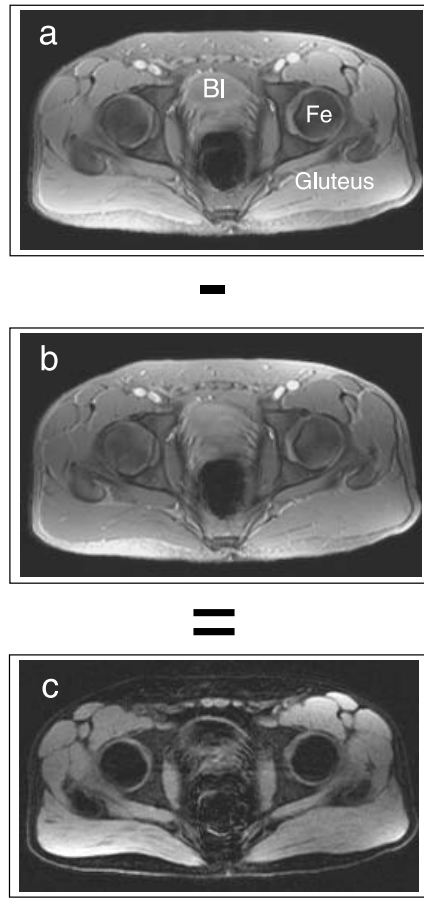

Fig. 11. Magnetization transfer (MT) imaging of the pelvis. Both images were recorded using the gradient echo sequence shown in Fig. 10. Original recording parameters for a and b: matrix 192×256, slice thickness 6 mm, fov = 380 mm, TR = 30 ms, TE 10 ms, flip angle = 15°, 15 scans for each image. (a) Gradient-echo image without application of MT-prepulses. (b) Image recorded with unchanged parameters and receiver adjustments, but with MT-prepulses switched on. (c) Image obtained by pixelwise subtraction of a and b. Musculature, cartilage and cutis show pronounced MT-effects, whereas free water in the bladder or fatty tissue are lacking sensitivity to MT-prepulses.

near 7.0 and 8.0 ppm as contributing to the ^{1}H NMR spectrum of skeletal muscle.

The first peculiarity of muscle spectra is the possibility to differentiate two lipid compartments. Furthermore, the characteristics of the lipid signals depend on the chosen particular muscle and its orientation with respect to the magnetic field. Figure 15 shows a typical spectrum of the tibialis anterior muscle (TA) in comparison with a spectrum from the fatty bone marrow of

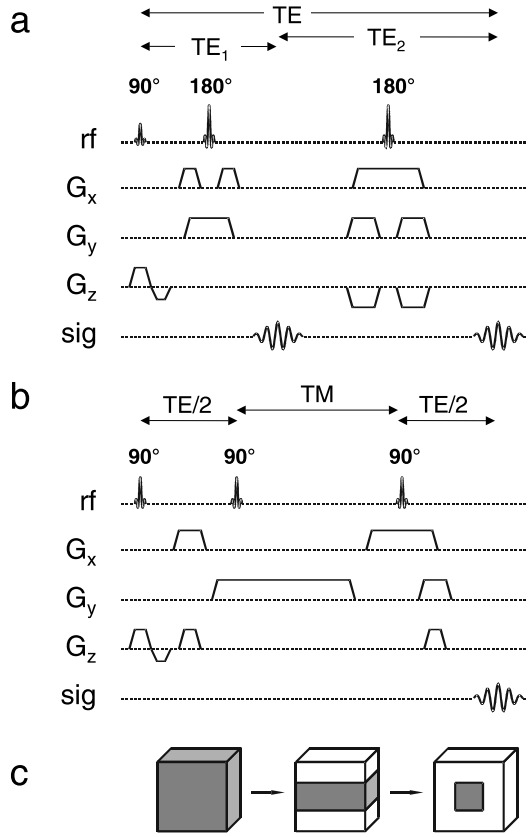

Fig. 12. Sequences for volume selective single voxel spectroscopy. Both techniques work with three slice-selective RF-pulses. (a) The Point RESolved Spectroscopy (PRESS) sequence generates a volume selective double spin-echo. The entire time delay between the initial 90° excitation and the echo is sensitive to transverse relaxation. (b) The Stimulated Echo Acquisition Mode (STEAM) sequence generates a stimulated echo. Maximal signal intensity (without relaxation effects) is only half the signal intensity of PRESS under comparable conditions, but slice profiles are often better (only 90° pulses instead of 180° pulses) and the TM interval is not susceptible to transverse relaxation. (c) The recorded echo signal is only generated in a volume corresponding to the intersection of all three slices.

tibia (BM) acquired on a 1.5 T whole body imager (Magnetom Vision, Siemens, Erlangen, Germany). Volume selective STEAM spectra were recorded using the following measurement parameters: TE = 10 ms, TM = 15 ms, TR = 2 s, 40 acq., VOI: $11 \times 11 \times 20$ mm^3 in TA and $10 \times 10 \times 20$ mm^3 in BM. Typical positions of the volume of interest (VOI) are indicated in the axial T_1-weighted image in Fig. 13a. The phenomenon of two distinct lipid resonances with a resonance frequency shift of 0.2 ppm was reported for the

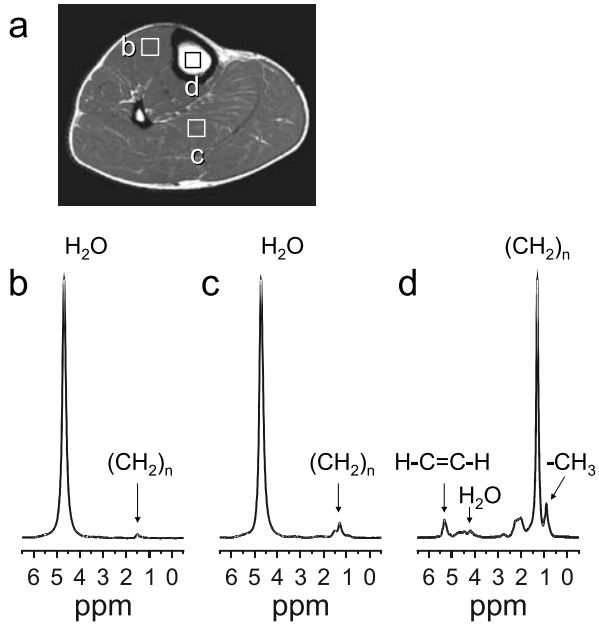

Fig. 13. Spectra from three volume elements recorded without water suppression. Measurement parameters: STEAM, TE = 10 ms, TM = 15 ms, TR = 2 s, 40 acq., VOI ($11 \times 11 \times 20$) mm^3. (a) Cross-section of the human lower leg of a volunteer. Two volume elements in musculature and one voxel inside the tibial bone marrow are indicated. (b) Spectrum recorded from the tibialis anterior (TA) muscle shows low lipid content of approximately 1% volume fraction. (c) Spectrum from the soleus (SOL) muscle indicates higher lipid content than in TA. (d) Spectrum from yellow bone marrow with dominating signal from fatty acids in triglycerides.

first time in 1993.[18] It was supposed that one of these compartments is according to the lipids within fat cells, and the other one with lower Larmor frequency stems from lipids with similar composition, but located within the cytoplasm of muscle cells. As a reason for the Larmor frequency shift, susceptibility effects within muscle cells were named. This assumption was verified and precised by the group of Boesch,[19] and the lipid compartments were attributed to EMCL at higher Larmor frequency and to IMCL at lower Larmor frequency.

The second striking feature is the splitting of the methylene and methyl signals of creatine (Cr_2 and Cr_3), and the frequency shifts of Tau, which is also dependent on the orientation of the muscle in relation to the static magnetic field. Figure 16 presents typical spectra from the tibialis anterior muscle (TA) and the soleus muscle (SOL) where the differences become obvious. The highly ordered structure of skeletal muscle described in Section 2, leads to the specific signal pattern strongly depending upon the orientation of the muscle fibres in relation to the static magnetic field B_0.

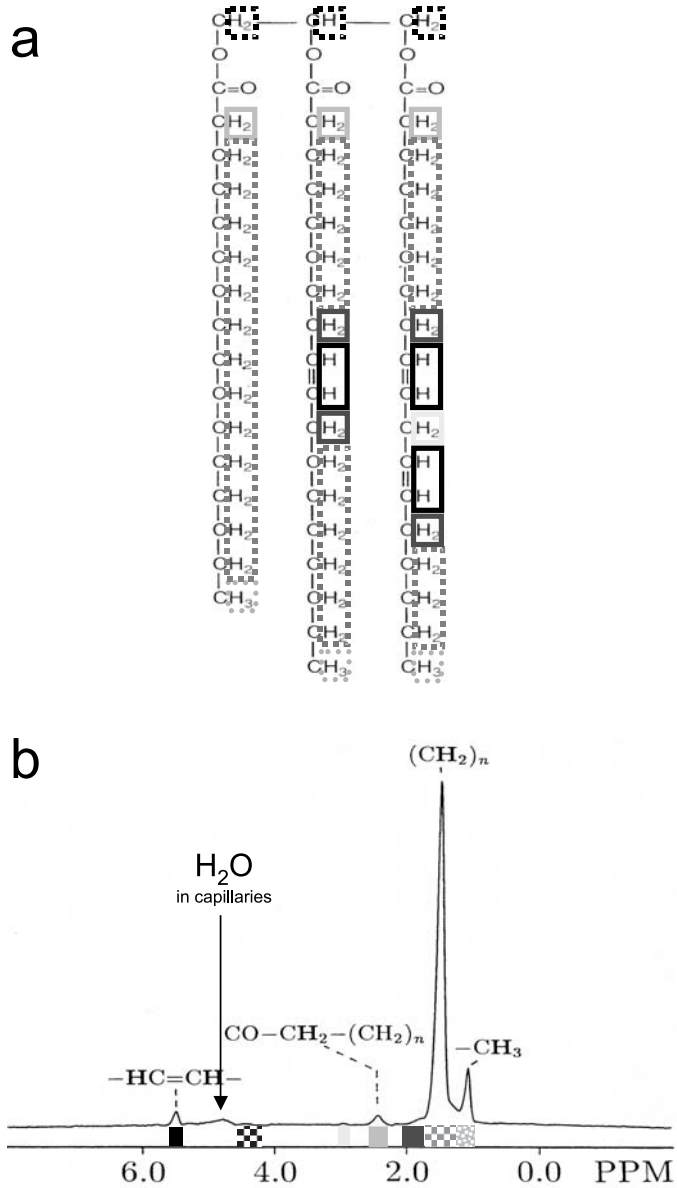

Fig. 14. Typical signals of triglycerides in a proton spectrum. (a) Structure of a triglyceride with three different fatty acids (one saturated, two unsaturated). Different positions of protons in the molecule are indicated, resulting in different chemical shifts in the spectrum. (b) Characteristic signal pattern of triglycerides (or fatty acids) in a spectrum from yellow fatty bone marrow of the tibia, containing triglycerides in the adipocytes with more than 90% volume fraction. The spectrum was recorded with TE = 50 ms by a PRESS sequence.

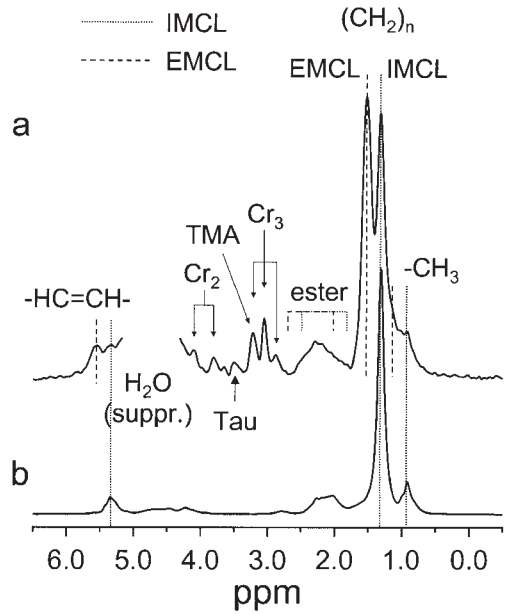

Fig. 15. Comparison of a water suppressed muscle spectrum and a spectrum from yellow bone marrow containing almost pure fat (triglycerides). Measurement parameters: STEAM sequence, TE = 10 ms, TM = 15 ms, TR = 2 s, 40 acq., VOI ($11 \times 11 \times 20$) mm^3. (a) Spectrum from TA muscle recorded after careful positioning of the VOI, avoiding inclusion of macroscopic fatty septa allows separation of extramyocellular (EMCL, broken lines) and intramyocellular lipid signals (IMCL, dotted lines) based on susceptibility differences. For this reason characteristic signals from fatty acids occur double. Signals of creatine (methyl, Cr_3, and methylene, Cr_2) show triplet and doublet structure, respectively, due to dipolar coupling effects. Further signals of TMA (including carnitine and choline compartments), Taurine (Tau), esters, unsaturated fatty acids (–HC=CH–), and residual water are indicated. (b) Spectrum from yellow fatty bone marrow of the tibia with identical measuring parameters, but different amplitude scale.

The basic physical NMR phenomena leading to changes of the appearance of these resonances in muscular proton spectra are briefly described in the following sections.

4.1. Bulk magnetic susceptibility effects

Separation of EMCL and IMCL in proton muscle spectra is possible due to the different geometrical arrangement of these lipid compartments resulting in different bulk magnetic susceptibility (BMS). EMCL are nestled in long fatty septa along the muscle fibre bundles or fasciae, and can thus be described in a simplified way as coaxial cylinders. IMCL are located in a roughly spherical

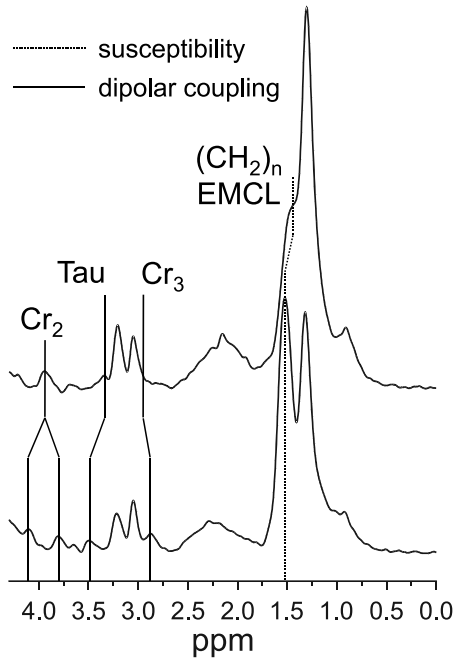

Fig. 16. Single voxel STEAM spectra of the SOL muscle (top) and the TA muscle (bottom). Different fibre orientation in those muscles results in clearly different patterns of the lines in the spectra: In SOL (feathered muscle with oblique fibres), IMCL and EMCL signals show lower frequency separation than in TA (spindle-shaped muscle) due to bulk susceptibility effects. Furthermore, in SOL the Cr_2 doublet merges into one resonance, the Cr_3 triplet is less resolved, and TAU is shifted towards TMA.

geometry as droplets within the cytoplasm of muscle cells, sometimes in close contact with mitochondria (see Fig. 4 in Section 2).

Whenever matter is placed in a magnetic field, electromagnetic interactions alter magnetic field lines, which are stretched or accumulated. The magnetic susceptibility of the bulk medium influences the individual magnetic resonance frequencies so that there is an extra frequency shift called the BMS shift.

Two contributions to the BMS shift can be distinguished theoretically:[19]

A homogenous part D and an inhomogenous part I, thus resulting in:

$$B_i(t) = (1 + D) \cdot B_o + I_i \tag{4.1}$$

where D and I are functions of the magnetic susceptibility of the substances[20] in the different compartments.

For the spherical compartment (IMCL), the BMS is determined by the diamagnetic susceptibility outside the sphere (muscular water), and can therefore be approximated by

$$D_{\mathrm{IMCL}} = \frac{\chi_{\mathrm{w}}}{3} \quad \text{and} \quad I = 0. \tag{4.2}$$

These contributions are not changed by rotation of the sample, thus leading to a constant resonance frequency independent of the orientation relative to the external magnetic field.

In contrast to this, the cylindrical symmetry of EMCL leads to

$$D_{\mathrm{EMCL}/\parallel} = \frac{\chi_{\mathrm{f}}}{3} \quad \text{and} \quad I = 0 \tag{4.3}$$

for the cylinder being parallel to B_0, and

$$D_{\mathrm{EMCL}/\perp} = \frac{\chi_{\mathrm{w}}}{2} - \frac{\chi_{\mathrm{f}}}{6} \quad \text{and} \quad I \sim \cos\frac{2\theta}{r^2} \tag{4.4}$$

for the cylinder being perpendicular to B_0. θ describes the angle between the external field and r, which is the radial distance from a nucleus to the axis of the cylinder.

Assuming standard diamagnetic susceptibilities of $\chi_{\mathrm{w}} = -9.05 \times 10^{-6}$ for water and $\chi_{\mathrm{f}} = -8.44 \times 10^{-6}$ for lipids,[19,21] these calculations predict a shift of +0.2 ppm in relation to spherical IMCL for parallel orientation of EMCL compartment (i.e., 1.5 ppm), and of −0.1 ppm for perpendicular orientation (i.e., 1.2 ppm).

In order to confirm the assignment of susceptibility effects being responsible for Larmor frequency shift between EMCL and IMCL and showing the angular dependence of the EMCL signal, experiments impressively demonstrating the phenomenon have been performed.[19] Spectra from *M. tibialis* anterior (characterized by a muscle fibre orientation parallel to the main muscle axis) were recorded at different angles relative to the static magnetic field B_0 in a range between −16° and 99°. The IMCL signal is constantly visible at 1.25 ppm independent of the bending of the leg, whereas the EMCL signal shows a clear shift when the leg was rotated in the *B*-field. In consistence with the theory the best separation between the signals is achieved when the leg is positioned parallel to the static magnetic field.

Szczepaniak performed *in vitro* measurements using Intralipid as a model for IMCL and soybean oil for EMCL,[22] confirming the theoretical assumptions and *in vivo* experiments of Boesch.

4.2. Dipolar coupling effects

Besides the susceptibility-induced Larmor frequency shift of lipid compartments further orientation-dependant resonances occur in the spectra of skeletal muscle. Direct dipole–dipole interactions between protons depend on the angle between the external field and the internuclear vector. Skeletal musculature is highly organized and spatially anisotropic resulting in visible effects in MR spectra of musculature. Two of those orientation-dependent signals were assigned to the methylene group of creatine (Cr_2) centred at 3.95 ppm and appearing as a doublet.[23] The methyl group of creatine (Cr_3) also seems to be affected by dipolar coupling and shows a triplet structure centred at 3.05 ppm.[23,24] In experiments with different angulation of the leg in relation to the B_0 field, it has been shown that the splitting is strongest when the muscle is positioned nearly parallel to B_0 and that both Cr_2 signals coincide to a single signal when the leg is rotated about 55°, corresponding with the magic angle which is determined by the relation[23]

$$\Delta f \sim \left\{1 - 3\cos^2\theta\right\} = 0 \Leftrightarrow \theta = 54.7^\circ. \tag{4.5}$$

These results suggest that the signals arise from dipole–dipole coupled protons. Kreis *et al.* confirmed this finding by measurements using one-dimensional zero- and double-quantum filtering, two-dimensional J-resolved spectroscopy, two-dimensional constant time COSY and longitudinal order separation spectroscopy.[23–25]

The dipole coupling effects in spectra from TA (spindle-shaped muscle with parallel muscle fibre orientation) and SOL (feathered muscle with oblique and crossing muscle fibre orientation – probably near the magic angle when Cr_2 signals coincide) are depicted in Fig. 16. Further dipolarly coupling effects for the signals in the TMA region have been shown in high-field muscle spectra (7 T) of mice, where signals between 3.1 and 3.5 ppm mainly result from taurine.[26] Furthermore, orientation dependent features were observed for lactate[26,27] which is only present in strongly exercised muscle, and the aromatic protons of carnosine.[28]

Altogether, all major peaks in the proton NMR spectrum of human skeletal muscle – except the water resonance and IMCL signals – are orientation-dependent, either resulting from susceptibility or from dipolar coupling effects.[29]

5. QUANTIFICATION OF SPECTRAL SIGNALS

An accurate assessment of the metabolite or lipid content in skeletal musculature plays an important role for studying physiological and pathological aspects of lipid metabolism. In principle, quantitative results

can be achieved by using *in vivo* MR spectroscopy, since the total integrated area under a resonance line in a MR spectrum is in most cases directly proportional to the concentration of the corresponding metabolite.

However, to obtain absolute concentrations of metabolites, it is necessary to analyse precisely the area under the resonance line of interest which is especially difficult for overlapping signals. In addition, a reliable calibration technique is needed to assess the correlation between the area under a resonance line and the absolute concentration of the metabolite in the tissue.

In Section 5.1 usual strategies to obtain reliable calibration by external and internal references are reported. Section 5.2 presents techniques for analysing overlapping resonance lines with symmetric and well-defined lineshapes. Section 5.3 shows a more suitable approach for differentiation of IMCL and EMCL in the complex signal patterns of lipids in muscle spectra.

5.1. Calibration using external or internal references

To obtain absolute concentrations of metabolites, calibration techniques are necessary. For this purpose an external calibration compound of known concentration can be measured to which the metabolite signals are referenced. Another possibility is the use of spectral signals from a tissue compound with known concentration serving as internal reference.

5.1.1. *External reference*

For calibration with an external reference, a sample with known concentration of the compound of interest is positioned outside the examined object, but inside the receiver coil. The desired metabolite concentration in the tissue can be calculated from the known concentration in the external reference by

$$[m] = C_{\mathrm{av}} C_{\mathrm{n}} (S_{\mathrm{m}}/S_{\mathrm{ref}})\,[\mathrm{ref}\,], \tag{5.1}$$

where S_{m} is the metabolite signal, S_{ref} the reference signal, [ref] the reference concentration, C_{n} the correction for the number of equivalent nuclei for each resonance and C_{av} the correction for the number of averages. Since many factors might influence the amplitude of the MR signal, further correction factors for the measured signals must be taken into account to obtain reliable results, e.g., differences between tissue and reference concerning relaxation times T_1 and T_2, diffusion effects and spatial positions in the receiver coil. To minimize effects of B_1 inhomogeneities, the two voxels should be chosen symmetrically inside the coil, if possible. Alternatively, if the B_1 field distribution of the particular RF coil is known, effects of B_1 inhomogeneities can be corrected for in Eq. (5.1).

5.1.2. *Internal reference*

The strategies for determination of absolute concentration of metabolites using an internal reference are similar to those of external references. Often tissue water or a metabolite which is expected to have a stable concentration in tissue is used. Total creatine and water are metabolites with relatively stable concentration in musculature, although changes in their rotational mobility may change their NMR visibility. Using water as an internal reference, Eq. (5.1) has to by modified by an additional correction factor according to

$$[m] = C_{\mathrm{av}} C_{\mathrm{n}} C_{\mathrm{wc}} (S_{\mathrm{m}}/S_{\mathrm{water}})\,[\mathrm{water}], \tag{5.2}$$

where [water] is equal to 110 mol/l and C_{wc} is a correction for the water content in the VOI. For skeletal muscle C_{wc} is about 0.78 determined by biochemical measurements. One must be aware of the fact that concentration of the internal references might vary due to physiological or pathological processes.

5.2. Quantification of overlapping symmetrical bell-shaped lines

Theoretically, it is not relevant, whether the quantification is performed in the frequency or in the time domain, since Fourier transform is a linear operator. The Fourier transform of a sinusoidal, exponentially damped signal in time domain

$$f(t) = M_0 \cdot e^{i\omega_0 t} \cdot e^{-R2 \cdot t} \tag{5.3}$$

is given by

$$F(\omega) = \frac{M_0}{R2 + i \cdot (\omega - \omega_0)} \tag{5.4}$$

and has as real part a Lorentzian lineshape

$$L(\omega) = \frac{M_0 \cdot R2}{R2^2 + (\omega - \omega_0)^2}. \tag{5.5}$$

In principle, M_0 can be determined through the first point in time domain for $t = 0$ or by integration of L. However, under experimental conditions distortions in the acquired time signal (e.g., due to eddy currents) are transferred to the frequency domain by Fourier transformation and can result in significant differences in quantification. A straightforward quantification method in the frequency domain is simply to determine the total integrated area under a resonance in a distinct frequency range of the spectrum. This method works well for spectra with well separated resonance lines and without

marked baseline fluctuations. These conditions are sometimes fulfilled in high-resolution spectra recorded *in vitro*. However, for most organs several lines are overlapping in spectra recorded *in vivo*, and the choice of lower and upper limit for integration probably leads to systematic errors.

Another problem concerning all frequency domain procedures are broad resonances caused by partly immobile molecules which might result in an overestimation of the peak areas, if the resonance lines of interest reside on the top of these broad resonances. To overcome this problem, a baseline correction processing can be performed allowing the operator to distinguish between baseline and desired signals. This corrections lead to a spectrum with improved baseline, but undesired errors can be caused by the selections of the operator. It should be mentioned that, additionally, a correct sequence timing and phasing of the MR spectrum is crucial for integration.

The Fourier transform

$$F(\omega) = \int_{t_0}^{+\infty} f(t) e^{-i\Phi_0} e^{-i\omega t} \, \mathrm{d}t \tag{5.6}$$

of a sinusoidal, exponentially damped signal with an additional phase term $e^{-i\Phi_0}$ and starting time t_0 is given by

$$F(\omega) = e^{-i(\Phi_0 + t_0(\omega - \omega_0))} \cdot \frac{M_0}{R2 + i(\omega - \omega_0)}, \tag{5.7}$$

leading to a modified Lorentzian lineshape

$$F(\omega) = M_0 \cdot \frac{\cos(\Phi_0 + t_0(\omega - \omega_0))R2 - (\omega - \omega_0)\sin(\Phi_0 + t_0(\omega - \omega_0))}{R2^2 + (\omega - \omega_0)^2} \tag{5.8}$$

showing a mixture of absorption and dispersion mode. Multiplying Eq. (5.7) by a phase factor $e^{i(\Phi_0 + t_0(\omega - \omega_0))}$ results into a pure absorption mode resonance.

The problem of overlapping lines in MR spectra which hampers the determination of metabolite concentrations can be often avoided by using fitting procedures in the time or frequency domain. The theory of fitting procedures is rather similar for both approaches. The fitted spectrum should resemble the experimental spectrum as close as possible leading to a minimization problem. Generally, the mathematical routine underlying the fitting process is a Levenberg-Marquardt algorithm for non-linear least-squares optimization.

Most methods assume an exponential decay for the resonances in the time domain giving rise to Lorentzian lineshapes in the frequency domain. This assumption is only valid for ideal experimental conditions. Under real experimental circumstances multi-exponential relaxation, imperfect shimming, susceptibility variations and residual eddy current usually lead to non-ideal

lineshapes. Therefore, other lineshapes are often applied for fitting, where the most common types are Gaussian lineshape

$$G(\omega) = \frac{M_0}{R2} \cdot e^{-((\omega-\omega_0)/R2)^2} \tag{5.9}$$

and Voigt lineshape. The latter type is a convolution between a Lorentzian and a Gaussian lineshape in the time domain. It has been shown in Ref. 30, that for ^{1}H MR spectra of muscle Voigt lineshapes gives similar or better results than Gaussian or Lorentzian lineshapes.

Processing of time domain data may cause artefacts in the frequency domain. One example for these distortions are truncations at the beginning or at the end of the FID which could lead to severe baseline artefacts which can be reduced by an appropriate filter. Undesired resonances leading to broad lines in the final spectra can be more easily eliminated in time domain by truncating the first few data points. Furthermore, the model functions in time domain are mathematically simpler to handle than the frequency domain analogues, which leads to a reduction of computation time. The advantage of the frequency domain analysis is that the quantification process can be directly interpreted visually.

The most commonly used fitting procedures in time-domain are the variable projection method (VARPRO)[31] and the linear prediction singular value decomposition (LPSVD) SVD.[32]

LPSVD is a non-iterative linear fitting procedure where all model parameters are estimated in a single step without need of any start values. This makes this method very fast and operator-independent. Disadvantages of this method are the very limited incorporation of prior knowledge and the limitation to exponentially decaying sinusoids. For this reason, LPSVD is not always appropriate for *in vivo* spectra. A more detailed description of LPSVD can be found in Ref. 33.

VARPRO is an iterative, interactive fitting procedure and will be briefly introduced here: The sampled points x_n, $n = 0, 1, 2, \ldots, N-1$, of the signal of K metabolites are described by

$$x_n = \sum_{k=1}^{K} c_k f_k(p_k, n), \tag{5.10}$$

where the linear parameters $c_k = M_{0,k} \cdot e^{i(\Phi_0+\Phi_{1,k})}$ are complex valued amplitudes considering phase distortions of zero-order and first-order by Φ_0 and $\Phi_{1,k}$, respectively. $f_k(p_k, n)$ are model functions that can be Lorentzian, Gaussian, Voigt or even non-analytic lineshapes[30] depending on non-linear parameters p_k. In matrix form, Eq. (5.10) has the compact form

$$\mathbf{x} = \mathbf{F}\mathbf{c}, \tag{5.11}$$

where $\mathbf{x} = (x_n)$ and $\mathbf{c} = (c_k)$ are column vectors and $\mathbf{F} = (f_k(p_k, n))$ is a $(n \times k)$-matrix. If $\mathbf{y}$ denotes the measured data as column vector, the sum of squared residues R of the actual data minus the model function

$$R = \|\mathbf{y} - \mathbf{x}\|^2 \tag{5.12}$$

is to be minimized by non-linear least-square fitting as a function of the variable parameters contained in $\mathbf{F}$ and $\mathbf{c}$. The special feature of VARPRO is that the minimization problem is solved in two steps. Assuming $\mathbf{F}$ to be known, the complex amplitudes determined by a linear least-squares method are given by

$$\mathbf{c}' = (\mathbf{F}^*\mathbf{F})^{-1}\mathbf{F}^*\mathbf{y}, \tag{5.13}$$

leading to a new minimization problem

$$R' = \|\mathbf{y} - \mathbf{F}(\mathbf{F}^*\mathbf{F})^{-1}\mathbf{F}^*\mathbf{y}\|^2, \tag{5.14}$$

only dependent on the non-linear parameters. The complex amplitudes can be determined by Eq. (5.13) without the need of start values for the linear parameters. The starting values for the non-linear parameters are provided by the FT spectrum of the time data points.

Prior knowledge allows to include fixed relations between some of the four parameters (amplitude, phase, frequency position, peak width) describing a symmetrical well-shaped resonance. Signal ratios, chemical shift differences, linewidth relations and zero-order phase relations can be included. The reduction of the number of unknown parameters leads to a reduced calculation time, better convergence behaviour and improved results. However, the assumptions made to include the prior knowledge must be validated for each experiment. Differences between the parameter values set by the prior knowledge and the actual parameters could lead to systematic errors.

5.3. Quantification of lipids with irregular signal patterns in muscle spectra

The recorded lipid signals in proton muscle spectra stem from IMCL and EMCL, leading to a relatively complex signal pattern in the recorded spectra due to the chemical shift distribution of the strongly coupled protons, and due to the irregular underlying magnetic field distribution (MFD) as well. IMCL are actively involved in lipid metabolism with turnover rates of several hours for substrate utilization, whereas EMCL are relatively inert to lipid metabolism and serve only as a long-term fat depot. For most studies, an accurate quantitative assessment of the IMCL is desirable. As described in Section 2, IMCL are settled in little spherical droplets with a diameter of about 0.5 μm.

IMCL signals are independent of muscle orientation relative to the magnetic field and show a regular symmetrical distribution of the experienced magnetic field. For EMCL signals the situation is more complicated: the EMCL compartments are more irregularly located in the septa between the muscle bundles and their shape is determined mainly by the tube-like structures of muscle fibre bundles. Different geometrical arrangements of EMCL relative to the magnetic field lead to orientation-dependent anisotropic susceptibility effects. For this reason, EMCL signals can show a rather inhomogeneous or even asymmetrical lineshape, especially in the SOL muscle.

The fact that the positions of lipid signals depend on the local MFD caused by BMS effects leads to a relatively small difference of the mean Larmor frequency of IMCL and EMCL, depending on the muscle fibre orientation relative to the magnetic field. For an orientation of the fibres parallel to the magnetic field the signal splitting of both lipid compartments is maximal. Possible quantification strategies for the assessment of IMCL is integration of the main peak or fitting procedures in time or frequency domain. But the superposition of the IMCL and EMCL signal component in the spectra may hinder an accurate evaluation by integration. On the other hand, fitting of a pronounced asymmetrical distribution of EMCL by symmetrical Lorentzian, Gaussian or Voigt lineshapes may lead to systematic errors.

An alternative approach for especially assessing lipid concentration is described in Ref. 34 and makes use of the description of the muscular lipid signals (L) as a convolution between the MFD of the lipid compartments and a characteristic line pattern of lipids describing only chemical shift modulations (Λ).

$$L = MFD * \Lambda. \tag{5.15}$$

The assumption of a characteristic line pattern for lipids is justified by the fact that IMCL, EMCL, and other adipose tissue in subcutaneous fat tissue or in tibial bone marrow are known to consist mainly of a very similar composition of fatty acid triglycerides. The characteristic line pattern Λ is indirectly determined by recording a reference lipid spectrum (R) out of a lipid compartment with a relatively homogenous magnetic field described by a normal distribution, i.e., a Gaussian function G. That means R can be written as

$$R = G * \Lambda. \tag{5.16}$$

The inverse Fourier transform of G again yields a Gaussian function $g(t) = e^{-(t/T_g)^2}$, the linewidth T_g of which can be numerically calculated from the known T_2 (natural linewidth) and the measured linewidth of the dominating methylene group in the lipid spectrum. Since one is only interested

in the lipid signals between 0.5 and 2.5 ppm in the recorded spectra, other signals are cut off in the frequency domain after an appropriate apodization and a baseline and phase correction. Inverse Fourier transformation of Eqs. (5.15) and (5.16) leads to

$$l = mfd \cdot \lambda \tag{5.17}$$

and

$$r = g \cdot \lambda \tag{5.18}$$

where the small letters denote the inverse Fourier transforms of the corresponding capital letters. Combination of Eqs. (5.17) and (5.18) leads to

$$mfd = g \cdot l/r. \tag{5.19}$$

Fourier transformation of mfd yields the MFD in the lipid compartments. To separate IMCL and EMCL in the MFD prior knowledge is used: In spectra from SOL and TA muscle with dominating IMCL signal, a linear correlation was shown between the linewidth of the methylene peak of IMCL and creatine. For this reason, demanding (a) a smooth but not necessarily symmetrical decay at the right side of the EMCL part and (b) the linewidths of the IMCL part kept fixed with respect to creatine, the IMCL part of MFD is fitted by a Gaussian lineshape, varying only the amplitude until the difference between the MFD and the fitted Gaussian IMCL part shows a (mostly asymmetrical) shape being as smooth as possible. Figure 17 shows the process for deconvolution of a recorded lipid signal pattern in a muscle spectrum to separate IMCL and EMCL, based on the underlying MFD. Although operator-dependent systematic errors are possible by this method, a better reproducibility in comparison to fit procedures in frequency domain of the corresponding spectra can be expected especially for the SOL muscle.

6. ASSESSMENT OF RELAXATION TIMES, MT EFFECTS AND DIFFUSION CHARACTERISTICS

Relaxation times, MT ratios, and diffusion properties allow insight into the microstructure of various tissues. Determination of these parameters is possible by recording and analysing of a series of volume selective spectra, even for metabolites with relatively low concentrations *in vivo*. For recording series of spectra usually one parameter is changeable (e.g., inversion time TI for T_1 measurements, echo time TE for T_2 measurements, MT preparation for assessment of spin transfer and chemical reaction rates, or diffusion sensitizing gradients for assessment of apparent diffusion coefficients or even diffusion

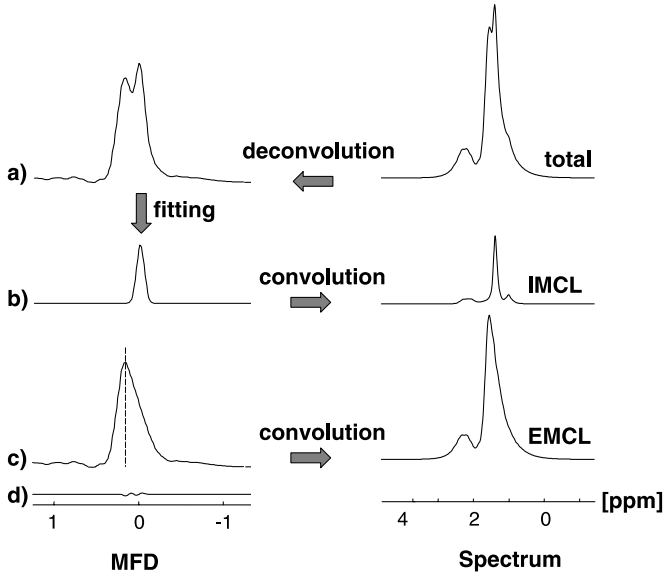

Fig. 17. Principle of separation of IMCL and EMCL signal contributions by deconvolution and analysis of the field distribution. (a) Right: cut-off spectrum out of the SOL muscle. Left: MFD of the lipids calculated by deconvolution with aid of a reference lipid spectrum out of yellow tibial bone marrow. (b) Left: fitted IMCL part of the MFD. Right: corresponding convolution with the characteristic lipid pattern Λ. (c) Left: resulting EMCL part of the MFD. Right: corresponding convolution with the characteristic lipid pattern Λ. (d) Left: residual of fitting the MFD.

tensors). For precise measurements of the effect of one variable parameter, all other measuring parameters have to remain unchanged.

For *in vivo* examinations inevitable movements of the volunteer often lead to voxel deplacements and inaccurate results, especially for components with inhomogeneous spatial distribution, as layers of EMCL in human musculature. In most examinations single spectra of a series are recorded consecutively, varying the relevant measuring parameter after recording of the complete spectrum with many acquisitions. A sampling strategy with interleaved acquisition of multiple spectra (i.e., the variable parameter is changed cyclically after each acquisition in the sequence) seems advantageous,[35] because in this case movements influence all spectra in a similar manner. This strategy (called INTACTSPEC) can be applied for arbitrary numbers of spectra and for all types of single voxel spectroscopy sequences. INTACTSPEC has demonstrated clearly smaller variation coefficients for assessed signal intensities of methylene signals of EMCL in multiple spectra compared to the common approach. Most examples of series of spectra reported in the following were recorded using this approach.

6.1. Relaxation times

Both, longitudinal and transverse relaxation of protons in tissue depend on the microstructure and on the chemical composition of several microscopic compartments. Relaxation properties are not necessarily constant for the different compartments inside the cells (cytosol and cavities in cell organella) and in the extracellular space (interstitium and vessels). However, water exchange processes between the compartments are often fast enough to generate one effective relaxation time, which can be assessed by mono-exponential fitting of the relaxation dependent data.

Mainly the water resonance can often be used as an indicator for inflammations or tumours, because effective relaxation times tend to be prolonged in tissue with increasing interstitial or intracellular water content. As reported in Section 3.2, lipids (mainly consisting of triglycerides) reveal more stable relaxation characteristics in all tissues and no significant alterations have been reported so far.

Spectroscopic relaxometry performed in human muscles of the lower leg is described in the following sections.

6.1.1. *Longitudinal relaxation*

Longitudinal relaxation times T_1 of spectral signals can be evaluated using the inversion recovery method. The series of spectra shown in Fig. 18 was recorded by a PRESS single voxel spectroscopy sequence. After a 180° rectangular inversion pulse different inversion times TI between 50 and 1820 ms were applied before excitation. Unchanged intervals between signal recording and the inversion pulse of the next scan were chosen (TR = 3 s+TI) in order to rule out effects of incomplete relaxation. T_1 times of the signals were determined from a series of 15 spectra with an echo time TE = 140 ms by mono-exponential fitting. Table 1 lists the resulting T_1 times. Relaxation times T_1 of methylene resonances of IMCL and EMCL were almost identical with those determined from other localizations with pure fatty content as tibial bone marrow ($T_1 = 270$ ms) or subcutaneous fat ($T_1 = 260$ ms).[18]

6.1.2. *Transverse relaxation*

Relaxation times T_2 were measured in TA and SOL of 20 volunteers by a series of 5 spectra with increasing echo times, TE = 10, 20, 50, 100 and 170 ms. Thirty-two acquisitions from a VOI of $(11 \times 11 \times 20)$ mm^3 were averaged for each single spectrum. TR was set to 2 s leading to a measurement time of about 5 min for a complete series of spectra. Figure 19 depicts spectra series from TA (a) and SOL (b) of a 32-year-old male volunteer. T_2 values resulting from mono-exponential fits are given in Table 2. In TA relaxation times T_2 of 77 ± 12 ms for EMCL and 88 ± 11 ms for IMCL were not significantly different. The signal decay of TMA and Cr_3 indicates a non-exponential decrease for longer echo times. Reliable values for T_2 cannot be derived for

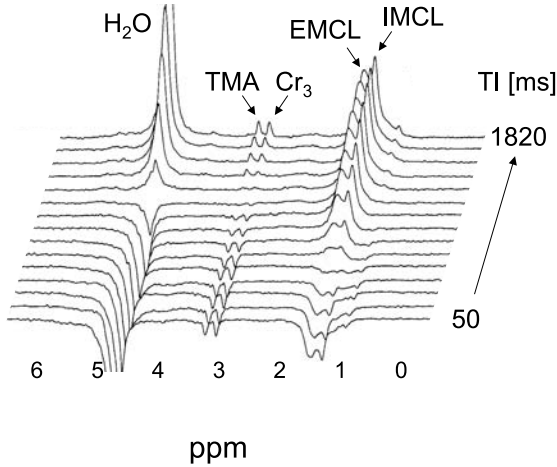

Fig. 18. Stacked plot of a series of 15 spectra (inversion recovery) with different TI for determination of T_1 in SOL. Measurement parameters: PRESS, TI = 50–1820 ms, TE = 140 ms, TR = 3s + TI, VOI (2 cm)^3, 32 acq.

Table 1. Longitudinal relaxation times T_1 of metabolites in skeletal muscle

	$(CH_2)_n$		Cr_3	TMA	H_2O
	EMCL	IMCL			
T_1 [ms]	270	280	1100	1100	1180

these species, because the signal intensities were more than 3 standard deviations of the mean apart from the fitted mono-exponential curve, probably due to dipolar coupling effects[23,24] leading to a modulation of the transversal decay characteristics.[36,37] For this reason, determination of T_2 times is aggravated for these resonances. In SOL (Fig. 19b), relaxation behaviour of methylene components in EMCL ($T_2 = 77 \pm 4$ ms) and IMCL ($T_2 = 78 \pm 5$ ms) is similar to that of TA with a slightly lower T_2 for the methylene component of IMCL. Szczepaniak *et al.* described T_2 times of 71 ± 5 ms for EMCL and 86 ± 4 ms for IMCL in SOL using a PRESS sequence, which is slightly different from our results.[38] However, the T_2 times of the methylene lipid resonances are comparable with those obtained from tibial bone marrow ($T_2 = 84$ ms)[35] and subcutaneous fat,[18] leading to the assumption, that the composition of the fatty acids in all these locations is very similar. In contrast to the findings in TA, in SOL signals of TMA and Cr_3 show a nearly mono-exponential decrease. A fitting procedure resulted in T_2 times of 156 ± 39 ms for TMA and 119 ± 35 ms for Cr_3. There is no apparent residual dipolar splitting in SOL due to a muscle fibre orientation near the magic angle in relation to the magnetic field as mentioned in Section 4. It has been shown that two creatine pools

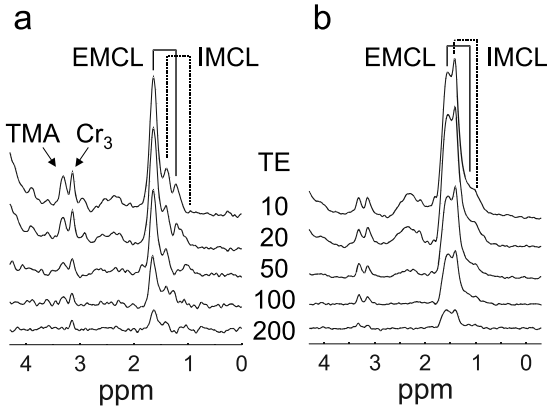

Fig. 19. Series of five spectra with different TE for assessment of T_2 in TA (a) and SOL (b). Measurement parameters: STEAM, TE = 10, 20, 50, 100, 200 ms, TM = 15 ms, TR = 2 s, VOI ($11 \times 11 \times 20$) mm^3, 32 acq.

Table 2. Transverse relaxation times T_2 of metabolites in skeletal muscle

	$(CH_2)_n$		Cr_3	TMA
	EMCL	IMCL		
T_2 (TA) [ms]	77 ± 12	88 ± 11	–	–
T_2 (SOL) [ms]	77 ± 4	78 ± 5	119 ± 35	156 ± 39

contribute to the recorded signals: One pool does not show dipolar coupling effects and slow transverse relaxation. Signals from the other pool with dipolar line shifts are influenced by rapid dipolar dephasing which must be considered for detailed analysis.[36,37]

6.2. Magnetization transfer spectroscopy

A short introduction in the application of MT techniques has been given in Section 3.3. Mechanisms of MT are described by interactions between two separated pools of protons, one of them consisting of free protons with long transverse relaxation time (pool A, $T_2 > 10$ ms) and the other of protons bound to macromolecules with an inherent short transverse relaxation time (pool B, $T_2 < 10$ μs). By selective saturation of the magnetization of the protons in pool B it is possible to reduce signal intensity of pool A and therefore to draw conclusions about the amount of protons present in pool B.

Different interactions for exchange of magnetization between the proton pools were proposed, which are through-space dipole–dipole processes,[39,40]

exchange by diffusion between the boundary water in the surface layer associated with macromolecules and free water,[41] and chemical exchange.[42] Selective saturation of the immobile magnetization pool can be obtained by two techniques.

6.2.1. *The 'off-resonance MT' method*

Irradiation of long narrowband RF-pulses with frequency offsets between 1 and 20 kHz relative to the resonance frequency of the free protons selectively influences transitions which correspond to the slopes of the broad resonance lines from the 'bound pool' of spins. Therefore, only the spins of protons with restricted motion are saturated, whereas the free protons remain unaffected (e.g., see Refs. 13 and 43).

6.2.2. *The 'pulsed MT' method*

Irradiation of a sequence of very short resonant RF-pulses with a sum of pulse angles of 0° for on-resonant spins. Spin ensembles with long T_2 show nearly full longitudinal magnetization M_z after the pulse sequence. Spin ensembles with short T_2 get severe transverse magnetization loss between and during the pulses and therefore M_z is clearly reduced after application of the pulse sequence (e.g., Ref. 44).

MR imaging provides determination of the MT-effect only for the water signal, whereas MR spectroscopy can enable determination of MT of metabolites. A detailed review on MT measurements by MR spectroscopy is given in Ref. 45.

In order to assess the MT effect in different skeletal muscle groups, several experiments have been performed on whole body units as described in the next section exemplarily.

6.2.2.1. Magnetization transfer in different muscle groups

Muscular magnetization transfer rates (MTR) were examined in TA and SOL of 20 volunteers. Three spectra were recorded using off-resonant Gaussian MT prepulses with variable flip angles of 0°, 400°, and 800°. The irradiation frequency was 1.5 kHz off-resonant in relation to the Larmor frequency of water resonance. All other parameters (sequence timing, transmitter and receiver adjustments) remained unchanged. To enable a sufficient interaction between the bound and free proton pools, prepulses were irradiated 10 times, each pulse with a duration of 7.68 ms and a time delay of 40 ms between successive pulses.[46] Further measurement parameters were TR = 2 s and TE = 10 ms (without water suppression), 10 acq., measuring time 1.07 min. In an additional experiment, MTR of Cr_3 (MTR_{cr}) was investigated using a 2.56 ms Gaussian prepulse for water suppression. To obtain a sufficient signal to noise ratio, 40 acquisitions were acquired for each spectrum (measurement time 4.07 min). Further measurement parameters remained unchanged.

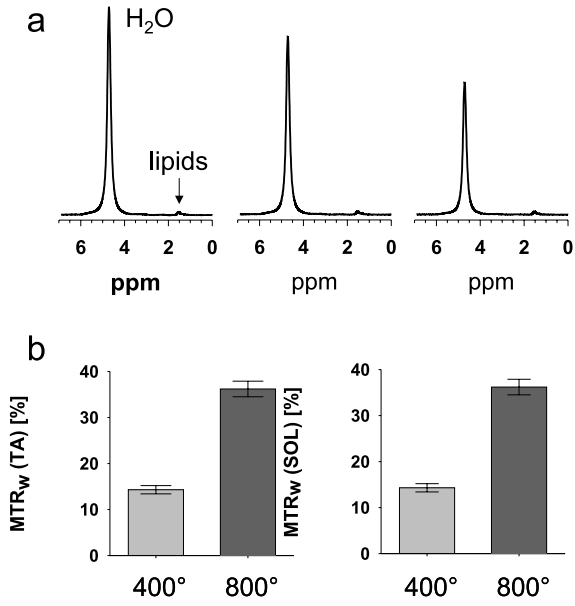

Fig. 20. (a) Magnetization transfer effect on water signal in TA using prepulse series with 0°, 400° and 800° amplitude (from left to right) as described in the text. (b) Magnetization transfer ratios of water (MTR_w) for TA (left) and SOL (right).

Spectral series for determination of MTR_w in TA is shown in Fig. 20a, indicating a strong signal decrease caused by MT preparation, dependent on the MT-prepulse amplitude. However, no significant differences in MTR_w were found between the two muscle types examined (see Fig. 20b).

In contrast to the water resonance, Cr_3 did not show a considerable MT effect in the water suppressed spectra resulting in MTR_{cr} lower than 1%. Significant MT effects on the creatine/phosphocreatine signal in skeletal muscle have exclusively been described in rats.[47–49]

6.3. Diffusion weighted spectroscopy

Diffusion is defined as the random translational motion of molecules or ions that is driven by internal thermal energy – the so-called Brownian motion. The mean movement of a water molecule due to diffusion amounts to several tenth of micrometres during 100 ms. Magnetic resonance is capable of monitoring the diffusion processes of molecules and therefore reveals information about microscopic tissue compartments and structural anisotropy. Especially in stroke patients diffusion sensitive imaging has been reported to be a powerful tool for an improved characterization of ischemic tissue.[50,51]

In addition, spectroscopic techniques have been applied for assessment of diffusion properties (e.g., Refs. 52–56). Changes in the diffusion of water molecules and further metabolites reveal pathological alterations of tissue compartments not visualized by other modalities. Information about cellular tissue architecture under normal and pathological conditions can be provided.

In diffusion-weighted NMR experiments, preparation of magnetization is obtained by a pair of dephasing/rephasing field gradients, leading to diffusion-related signal losses.[57] Sensitivity to diffusion can be established by variation of the *b*-value:

$$b = (\gamma \cdot A \cdot \delta)^2 \left(\Delta - \frac{1}{3}\,\delta \right), \tag{6.1}$$

where $\gamma = 2.675 \times 10^8$ rad/Ts represents the gyromagnetic ratio of protons, A is the amplitude of the diffusion sensitizing gradients, δ their duration, and Δ the time interval between them.

Using a single voxel STEAM technique for volume selection, diffusion sensitizing gradients are applied between the first and the second and after the third 90° pulse as shown in Fig. 21. The STEAM approach allows assessment of diffusion with high sensitivity even in cases with relatively short transverse relaxation times (e.g., muscle, $T_2 \approx 50$ ms). The reason is that the time interval Δ can be prolonged by increasing the TM interval which is only sensitive to longitudinal relaxation.

6.3.1. *Anisotropic diffusion*

Since musculature shows a structure with oriented contractile proteins, cells and fibres (see Section 2) diffusion is not expected to be isotropic.[58] Assessment

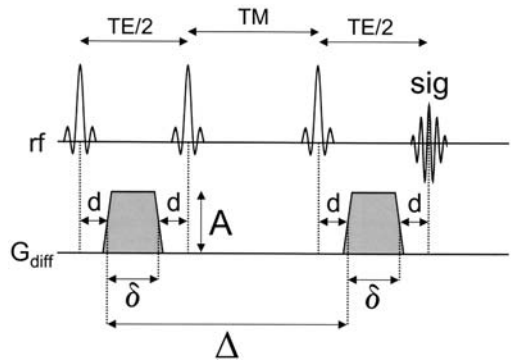

Fig. 21. Timing scheme of a STEAM sequence for diffusion measurements with a pair of diffusion weighting dephasing/rephasing gradients. Parameters δ, A, and Δ determine the diffusion weighting (*b*-value).

of anisotropic diffusion in the calf muscles was performed in 20 volunteers recording 9 spectra within one INTACTSPEC cycle. The first spectrum in the series was recorded without diffusion weighting ($b = 0$ s/mm^2), the following spectra (Nos. 2 to 5) with increasing b-values of 250, 500, 1000 and 2000 s/mm^2 and diffusion sensitizing gradients oriented parallel to the muscle axis ($G_\parallel$). Further spectra in the series (Nos. 6 to 9) were recorded with the mentioned b-values, but diffusion gradients applied perpendicular to the muscle axis ($G_\perp$). Duration of diffusion gradients was $\delta = 32$ ms with amplitudes A of 0.00, 6.01, 8.50, 12.02 and 17.00 mT/m, respectively. Linear gradient ramps of 500 μs were used. Parameter Δ was chosen to 105 ms resulting in TE = 80 ms and TM = 65 ms. These values were optimized considering $T_1 = 1500$ ms and $T_2 = 50$ ms for muscular water.[18] Ten acquisitions were recorded for each spectrum with TR = 2 s. The total measuring time for the spectral series was 3.19 min. As signal phase shifts occur due to linear bulk motion, resulting in an additional signal dispersion and in an overestimation of the diffusion coefficient after averaging of several acquisitions,[17] a zero order phase correction was applied on each acquisition before signal averaging, as proposed by Posse *et al.*[52] Diffusion coefficients $D_\parallel$ and $D_\perp$ were calculated using a mono-exponential fitting procedure according to the equation $S = S_0\, e^{(-Db)}$.

Series of diffusion weighted spectra recorded from TA (a) and SOL (b) are presented in Fig. 22. As muscle fibres are oriented nearly parallel to the main muscle axis in TA, diffusion of muscular water molecules is less hindered along the muscle fibre direction, resulting in a higher diffusion coefficient $D_\parallel$ (at least 1.6-fold in all volunteers) compared to $D_\perp$. In contrast, spectra from SOL show less differences between parallel and perpendicular orientation of diffusion sensitizing gradients, resulting in very similar diffusion coefficients $D_\parallel$ and $D_\perp$. Four out of 20 volunteers showed even a lower diffusion coefficient $D_\parallel$ compared to $D_\perp$ in this muscle. The range of individual diffusion coefficients is broader in SOL, as indicated by the higher standard deviations. The reason for the diffusion behaviour of SOL is that this muscle is of the feathered type (see Fig. 3) with oblique fibre orientation and fibre crossings. The diffusion coefficients from 20 volunteers (mean values and standard deviations of individual data) are shown in Fig. 22c. de Graaf showed diffusion anisotropy in rat muscle using ^{31}P NMR spectroscopy,[53] and for creatine in a ^{1}H-study, applying a new single shot diffusion trace technique.[54] With the gradient systems obtainable on modern MR units, examinations of diffusion properties of the water resonance can also be performed using NMR imaging techniques, as recently proposed.[50,59] Even 'fibre tracking' techniques seem applicable after pixelwise determination of the diffusion tensor in musculature. Those techniques promise to be clinically useful for characterizing and monitoring the progression of musculoskeletal diseases.

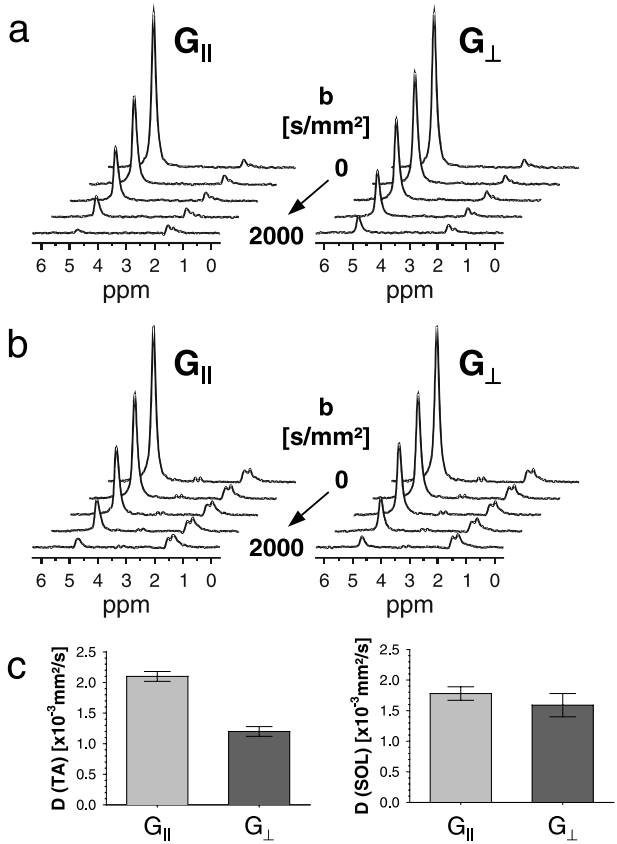

Fig. 22. Diffusion weighted spectral series recorded from TA (a) and SOL (b). Diffusion sensitizing gradients with *b*-values of 0, 250, 500, 1000 and 2000 s/mm^2 are applied parallel ($G_{\parallel}$) and perpendicular ($G_{\perp}$) to the muscle axis. In contrast to SOL, TA shows clearly anisotropic signal losses. Mean diffusion coefficients of 20 subjects are given in (c).

6.3.2. *Diffusion of lipids*

Fatty acids are clearly larger in size and show markedly slower diffusion velocity than the small water (or creatine) molecules which have been examined so far by diffusion weighted NMR spectroscopy. However, assessment of diffusion properties of lipids could be a key step for further experimental studies of skeletal muscle lipid metabolism. Diffusion properties of FFA and triglycerides are likely different due to differences in molecular weight. In addition, effects of temperature, chemical surroundings, and the mobility of small lipid droplets in the cytosol may also lead to measurable differences in the diffusion characteristics.

In the literature, only one study reported on diffusion effects in lipid signals in humans *in vivo*[60] showing only a slight reduction in lipid signal probably due to insufficient diffusion weighting ($b_{max} = 6000$ s/mm^2). In order to achieve high *b*-values, long diffusion preparation times are needed due to the limited gradient strength on whole body MR systems. This results in severe relaxation dependent signal losses and therefore requires optimized diffusion preparation.[61]

The maximum signal yield of a STEAM-sequence – neglecting diffusion – is determined by the relaxation losses:

$$S_{max}\,(\mathrm{STE}) = \frac{1}{2} \cdot S_0 \cdot e^{-((2\delta+4d)/T_2)} \cdot e^{-(TM/T_1)}. \tag{6.2}$$

The sensitivity of the diffusion weighting of the sequence is given by the *b*-value defined by Eq. (6.1). To obtain maximum signal yield for a given *b*-value, relaxation losses have to be minimized.

Using Eqs. (6.1) and (6.2) and neglecting the duration of the time elements *d* ($d \ll \delta$) representing the gradient ramp times, maximum signal yield can be obtained by choosing δ and TM according to

$$\frac{TM}{\delta} = \frac{T_1}{T_2} - 1. \tag{6.3}$$

Hence, the optimum ratio TM/δ in STEAM sequences is given by the relaxation times of the substance leading to TM/$\delta = 2.2$ for lipids when relaxation times of the dominating methylene signal of human lipids are considered ($T_1 = 270$ ms and $T_2 = 85$ ms).

Relaxation-optimized INTACTSPEC sequence trains for diffusion measurements with high *b*-values up to 80,000 s/mm^2 were implemented for *in vivo* applications on human lipids (bone marrow and skeletal muscle) and for examination of aliphatic organic compounds (butanol [C_4H_9OH], decanol [$C_{10}H_{21}OH$], oleic acid [$C_{17}H_{33}COOH$]) to study the effect of increasing chain length on diffusion properties. Following sequences were applied: S_1: TE = 80 ms, TM = 65 ms, $\delta = 32$ ms, $b = 0$, 250, 500, 1000, 2000 s/mm^2, S_2: TE = 154 ms, TM = 149 ms, $\delta = 69$ ms, $b = 0$, 2500, 5000, 10,000, 20,000 s/mm^2, S_3: TE = 250 ms, TM = 261 ms, $\delta = 117$ ms, $b = 0$, 12,500, 25,000, 50,000, 80,000 s/mm^2.

Repetition time TR was set to 2 s, voxel sizes were $10 \times 10 \times 10$ mm^3 (*in vitro*) and $15 \times 15 \times 30$ mm^3 (*in vivo*). Derived ADC values are given in Table 3.

Butanol with a molecular weight (MW) of 74 u and a chain length of 4 shows strong signal decrease even at low *b*-values (S_1), resulting in an ADC of $(37.8 \pm 1.9) \times 10^{-5}$ mm^2/s. Oleic acid (MW = 282 u, chain length 18) revealed the lowest ADC of the organic compounds with $(3.2 \pm 0.1) \times 10^{-5}$ mm^2/s as

Table 3. ADC values of organic compounds and of lipids in humans

	Butanol	Decanol	Oleic acid	Bone marrow	EMCL	IMCL
Chain length	4	10	18	18–20	18–20	18–20
ADC [$\times 10^{-5}$ mm^2/s]	37.8 ± 0.4	7.9 ± 0.1	3.3 ± 0.1	1.1 ± 0.1	1.8 ± 0.2	3.6 ± 0.8

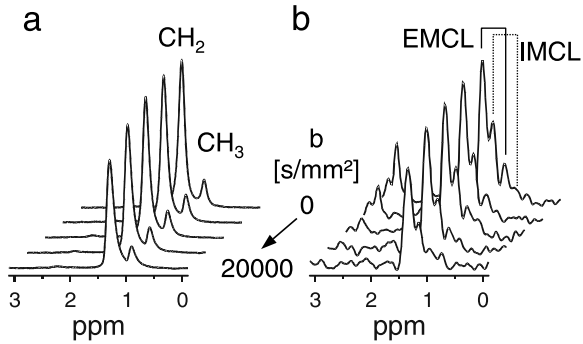

Fig. 23. Diffusion weighted spectral series of tibial bone marrow (a) and TA (b) of a 27-year-old healthy female subject for determination of ADC in lipids. Spectra were recorded using sequence S_2 with TE = 154 ms, TM = 149 ms, $\delta = 69$ ms, $b = 0$, 2500, 5000, 10,000 and 20,000 s/mm^2. Similar diffusion characteristics are visible for marrow fat and EMCL, whereas IMCL shows more pronounced diffusion related signal loss.

determined from S_3. Figure 23 shows two series of diffusion weighted spectra, recorded from tibial bone marrow (a), and tibialis anterior muscle (b). Examinations resulted in $(1.1 \pm 0.1) \times 10^{-5}$ mm^2/s in bone marrow using S_3, ADC's of muscular lipids were calculated to $1.8 \pm 0.2 \times 10^{-5}$ mm^2/s for EMCL and $3.6 \pm 0.8 \times 10^{-5}$ mm^2/s for IMCL. Examinations in muscle were performed using S_2, as due to their low concentration of about 1%[11] longer TE intervals would lead to intolerable T_2-related signal attenuation. However, a signal reduction of 52% (EMCL) and 41% (IMCL) was achieved, allowing reliable determination of ADC's.

These preliminary results indicate that it is possible to assess diffusion coefficients of human lipids, especially in musculature. However, it has to be mentioned that incoherent voxel motion influences the *in vivo* results to an unknown degree due to high motion sensitivity. Limitations in SNR and timing will be overcome with higher field strength and more powerful gradient systems as currently available on whole body MR systems. Assessment of diffusion properties of muscular lipid might then contribute to a better understanding of composition and metabolism of the lipid compartments under physiological and pathological conditions.

7. STUDIES ON LIPID METABOLISM IN SKELETAL MUSCULATURE

An increasing number of studies on lipid metabolism in human skeletal muscle using localized MR proton spectroscopy have been performed since the first description of the phenomenon that proton NMR spectroscopy allows the differentiation of two distinct lipid compartments[18] and the experimental confirmation that one of these compartments is attributed to the IMCL pool.[19,38,62–64] The non-invasiveness and the high sensitivity even to low lipid concentrations under physiological conditions denote the uniqueness of this modality and allow examinations of large numbers of healthy volunteers and follow-up metabolic intervention studies.

Twenty years ago increased amounts of muscular lipids were reported to be present during the pathogenesis of metabolic disorders.[65,66] It is now widely accepted that increased IMCL levels often occur in subjects with skeletal muscle insulin resistance and beginning type 2 diabetes mellitus. Stein *et al.*[67,68] were the first group who did describe this correlation in humans. Negative correlations between IMCL content in different muscle groups and insulin sensitivity in lean healthy volunteers have been reported by several working groups.[69–72] However, little was known about the regulation of the IMCL, bringing up the question whether it is possible to increase or decrease IMCL by exogene influences.

The observation of possibly increased IMCL levels in highly trained athletes led to a second focus of research in the field of sports medicine. Besides carbohydrates, lipids are the major fuel of skeletal muscle during work and rest. A variety of questions have to be answered. It was examined, whether exercise of various intensities alters IMCL levels, whether those changes depend on the duration of exercise, and finally, how IMCL are replenished during post-exercise recovery.

The following sections summarize several studies concerning the inter-relationship between IMCL and insulin resistance and the regulation of IMCL, and it reviews the experiences of different working groups in the field.

7.1. Experimental

All studies in our group were performed on a 1.5 T whole body imager (Magnetom Vision, Siemens, Erlangen, Germany). The circularly polarized extremity coil of the manufacturer was used as combined transmitter/receiver coil. Subjects were in supine position with the most extended part of the right lower leg in the centre of the coil. For follow-up measurements, accurate repositioning was guaranteed by marking the exact localization of the leg inside the coil. Reproducibility of the voxels could also be controlled by the individual unambiguous macroscopic fatty septa in the recorded

T_1-weighted images. For spectroscopic volume selection and signal acquisition a single voxel STEAM technique was used[16] applying 2.56 ms Hanning-filtered sinc pulses and 4 mT/m slice selection gradients. Homogeneity of the magnetic field was optimized by volume selective shimming prior to the spectroscopic examinations. Further measurement parameters for all examinations: TE = 10 ms, TM = 15 ms, TR = 2 s, VOI ($11 \times 11 \times 20$) mm^3, water suppression by selective Gaussian prepulse, 40 acquisitions, measurement time 1:23 min. Post-processing included 4 k zero-filling, multiplication by a Gaussian filter function (FWHH = 150 ms), Fourier transformation, and zero and first-order phase correction. Spectral intensities were referenced to the methyl signal of Cr at 3.05 ppm serving as internal reference. Examinations were performed in the tibialis anterior (TA) and in the soleus muscle (SOL) – two muscles with different muscle fibre composition, metabolism and innervation,[73,74] as described in Section 2.

7.2. Intra- and interindividual variabilities in IMCL content

Reliable assessment of IMCL content in different muscle groups requires the knowledge about the regional distribution of IMCL content inside the single muscle groups and about the reproducibility of the spectroscopic measurements. For this reason, series of measurements were performed in four male volunteers applying voxel shifts in TA and SOL in all spatial directions for determination of intramuscular variability of IMCL/Cr and EMCL/Cr ratios. All measurements were repeated three times after new positioning of the volunteer in the scanner. Variation of the IMCL/Cr ratio within the muscles was between 5 and 11% in TA, and between 4 and 12% in SOL. Hwang *et al.*[75] described mean intra-subject coefficients of variance of 13.0% (TA) and 18.6% (SOL) applying a spectroscopic imaging technique at 4.7 T with high-spatial resolution of the voxels (0.25 ml). These variations can be attributed to intrinsic differences in the fibre type composition[76] or methodological variability. The lower variability in our measurements might be due to the greater voxel dimensions. In contrast to IMCL/Cr ratios, EMCL/Cr data showed markedly stronger variation in TA (between 12 and 45%) despite choosing voxel positions without visible contamination of macroscopic fatty septa in the images. In SOL fatty septa are distributed more homogeneously, and EMCL/Cr ratios showed minor variations (between 8 and 17%).[77] EMCL signals in the recorded spectra depend strongly on the position of the voxel and physiological information seems to be limited.[78]

Reproducibility measurements were performed in three sessions for which identical voxel positions were intended. Sessions 1 and 2 were done on the same day but with repositioning of the volunteer after a short break with the volunteer leaving the imager. Session 3 was performed one week later. Volunteers were instructed to maintain their dietary and sporting habits during

this time. Variations of IMCL/Cr were between 2 and 12% in TA and between 2 and 15% in SOL. EMCL/Cr again showed greater variations in TA (up to 40%) compared to SOL (about 10%).

The results correspond well with observations of other groups[19,79] who showed a residual coefficient of variance in IMCL content of about 6% in TA[19] and SOL.[79] Altogether, reproducibility of IMCL is comparable to that achievable for other MR visible metabolites (e.g., in brain) and sufficient for determination of metabolic correlations. It should be mentioned that in contrast to many other metabolites detectable by NMR *in vivo* inter-individual variations of the IMCL content is markedly higher (up to 20-fold).

7.3. The role of IMCL in the pathogenesis of insulin resistance and type 2 diabetes

A brief overview about the fundamental principles of the pathogenesis of skeletal muscle insulin resistance and its contribution to the development of type 2 diabetes mellitus is given in the following. Priority is given to the role of lipid metabolism, which is the main field of the reported spectroscopic studies. Furthermore, the technique of euglycemic hyperinsulinemic glucose clamp is described allowing determination of the individual insulin sensitivity of musculature. The role of IMCL in insulin resistance of the skeletal muscle is discussed.

7.3.1. *Lipid metabolism and skeletal muscle insulin resistance*

The prevalence of Type 2 Diabetes (T2D) is increasing world-wide and considered one of the main threats to human health in the 21st century.[80] In 2010, 221 million patients are expected to be diabetic (compared to 151 million in the year 2000). The increase in diabetes prevalence is considered to be secondary to changes in human lifestyle accompanied by physical inactivity and unlimited food supply.[80] Skeletal muscle insulin resistance, defined as the reduced response of skeletal muscle to a given dose of insulin, is a common finding in patients with type 2 diabetes mellitus and can be found before the onset and predict the development of the disease.[81] Several factors determine skeletal muscle insulin sensitivity and among others alterations in fatty acid metabolism have been proposed.[82]

In addition to glycogen, lipids represent a form of energy stored within the muscle cell and the existence of metabolically relevant trigylceride stores has long been established.[83] In 1962, Randle *et al*. proposed a metabolic principle known as the Randle-Cycle.[84] According to this principle an increase of fatty acid concentrations inside the skeletal muscle cell results in increased fatty acid oxidation in favour of glucose oxidation. The reduction in glucose oxidation is responsible for the reduced glucose uptake upon stimulation with insulin (insulin resistance). Consequently, the quantification of muscle triglyceride

stores is of interest in metabolic studies. Healthy human muscle oxidizes both, preferentially glucose in the post-prandial 'insulin stimulated' and fatty acids in the fasting state. More recently, the inability of skeletal muscle to shift fuel oxidation from fatty acids to glucose upon insulin stimulation has been identified as a characteristic feature of insulin resistance.[85]

7.3.2. *Hyperinsulinemic euglycemic clamp*

The hyperinsulinemic euglycemic clamp represents the gold standard to assess insulin sensitivity *in vivo*. First, an antecubital vein is cannulated for infusion of insulin and glucose. A dorsal hand vein of the contra lateral arm is cannulated and placed under a heating device to permit sampling of arterialized blood. By means of a insulin bolus and a primed insulin infusion (1 mU of insulin per kg body weight and minute) plasma insulin levels are raised to high physiological levels ($\sim$400 pM) for 2 h. Blood is drawn every 5 min for determination of blood glucose and a glucose infusion is adjusted appropriately to maintain the fasting glucose level. The glucose infusion rate (GIR) necessary to maintain euglycemia in the second hour of the clamp procedure (in μmol/kg/min) is used to express the sensitivity of peripheral organs to insulin. The less glucose needs to be infused the more 'insulin resistant' is the subject.

Clamp examinations were performed in most of the studies in order to correlate the NMR data with the individual GIR.

7.3.3. *Relation between IMCL content and insulin sensitivity*

To gain further insight into the mechanisms involved in defective insulin-stimulated glucose uptake in skeletal muscle of insulin-resistant subjects, the possible role of IMCL in the pathogenesis of skeletal muscle insulin resistance and type 2 diabetes mellitus was explored by comparing insulin sensitivity (GIR) and IMCL content of insulin-resistant and insulin-sensitive offsprings of patients with type 2 diabetes. Twenty-six healthy subjects were included in the first study, 13 of them classified as insulin-sensitive and further 13 as insulin-resistant. Metabolic and anthropometric data are given in Table 4.

In order to minimize the effects of other confounding parameters contributing to insulin resistance subjects were matched for body mass index, body fat, physical fitness, and waist-to-hip (circumference) ratio. The groups studied were selected from a well characterized population and underwent metabolic as well as NMR spectroscopic examinations of TA and SOL. NMR examinations and hyperinsulinemic euglycemic clamp were performed in the early morning after overnight fasting. This fixed time frame was chosen in order to rule out short term changes of IMCL content or insulin sensitivity.

IMCL-content of both muscle groups showed a negative correlation with insulin sensitivity, i.e., the higher the IMCL-content, the lower the GIR.[70]

Table 4. Characteristics of the study population

	Insulin-sensitive	Insulin resistant	
Sex (M/F)	7/6	7/6	
Age (years)	31.8 ± 2.4	29.4 ± 1.5	n.s.
BMI (kg/m^2)	22.9 ± 0.6	23.4 ± 0.35	n.s.
VO_{2max} (ml/kg)	35.3 ± 2.7	33.5 ± 2.4	n.s.
Percent body fat	19.1 ± 2.0	22.1 ± 1.5	n.s.
Waist-hip-ratio	0.83 ± 0.02	0.80 ± 0.02	n.s.
$IMCL_{TA}$ (a.u.)	2.08 ± 0.28	3.26 ± 0.36	$p < 0.05$
$IMCL_{SOL}$ (a.u.)	6.40 ± 0.59	11.80 ± 1.60	$p < 0.01$

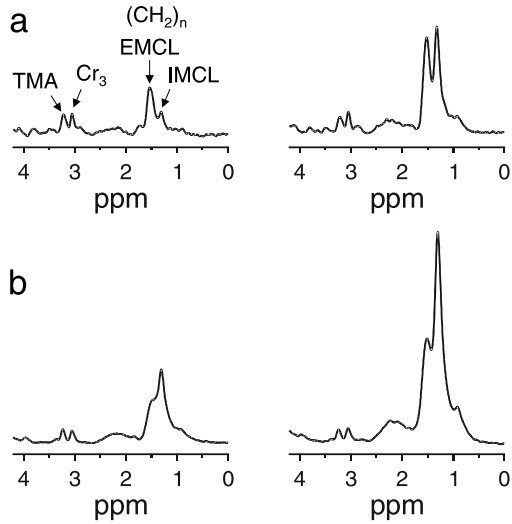

Fig. 24. Spectra of TA (a) and SOL (b) of a 34-year-old male insulin sensitive volunteer (left row) with low IMCL content, and a 32-year-old male insulin resistant volunteer (right row) with markedly higher IMCL in both muscle groups.

Figure 24 depicts exemplary spectra of TA (a) and SOL (b) of a 34-year-old male insulin sensitive subject with very low IMCL (left row), and a 32-year-old male insulin resistant subject with high IMCL content (right row).

Several other studies also showed an association between IMCL accumulation and insulin resistance, however, there are also contradictory reports: Krššák *et al.*[69] studied a group of 23 normal weight non-diabetic adults without family history of diabetes and found a significant negative correlation between IMCL of soleus muscle and insulin sensitivity, but no relation between IMCL and BMI, age, and fasting plasma concentrations of triglycerides.

Perseghin *et al.* examined the differences between IMCL content in matched groups of offsprings and normal volunteers without family history[71] and found

a significant higher IMCL in SOL in the offspring group. Following the multivariate analyses, IMCL of SOL is the most useful variable in predicting insulin sensitivity.

According to the median IMCL content in vastus lateralis, Virkamäki *et al.*[72] subdivided a cohort of 20 healthy men without family history in two groups with high IMCL (10 subjects) and low IMCL (10 subjects) comparable with respect to age, BMI and maximal oxygen consumption (VO_{2max}) and found a significantly lower whole body insulin-stimulated glucose uptake in the groups with high IMCL. This association was independent of body weight and physical fitness. In contrast, the study of Forouhi[86] led to the statement that the relationship between IMCL and insulin sensitivity is disappearing after adjusting for obesity.

As a conclusion of these preliminary results of comparative studies using small cohorts of more or less matched subjects, a potential role of IMCL in the pathogenesis of skeletal muscle insulin resistance has been stated. However, it has to be taken into consideration that physical fitness as well as confounding parameters for obesity and probably genetic predispositions might also influence the individual IMCL content and insulin sensitivity.

7.4. Regulation of IMCL by exogene interventions

7.4.1. *Effect of intravenous lipid infusion*

Aim of this study was to find out whether an increase of circulating FFA and prolonged experimental hyperinsulinemia might lead to an elevation of IMCL. The experimental protocol (which is given in more detail in Refs. 87 and 88) comprised three different study groups: [1] combination of lipid infusion and hyperinsulinemia (L+HI, 12 male volunteers), [2] hyperinsulinemia alone (HI, 6 male volunteers), and [3] lipid infusion without concomitant insulin infusion (L, 3 male volunteers).

In the study groups with HI (protocols [1] and [2]), a 6 h hyperinsulinemic euglycemic glucose clamp was performed. Constant hyperinsulinemia was achieved by a continuous intravenous insulin infusion of 1.0 mU/kg per minute. Blood was drawn every 20 min for determination of serum insulin and plasma FFA. Blood glucose was measured using a bedside glucose analyser, and a glucose infusion was adjusted appropriately to maintain the fasting glucose level. The glucose infusion rate, necessary to maintain euglycemia, was used as a measure of insulin sensitivity.

Plasma non-esterified fatty acids (NEFA) were elevated by infusion of a lipid emulsion and heparin with a constant rate of 1.5 ml/min (lipid emulsion, protocols [1] and [3]) and 0.4 IU/kg per minute (heparin). In protocol [2] a solution of 0.9% saline was infused as a control for the lipid emulsion.

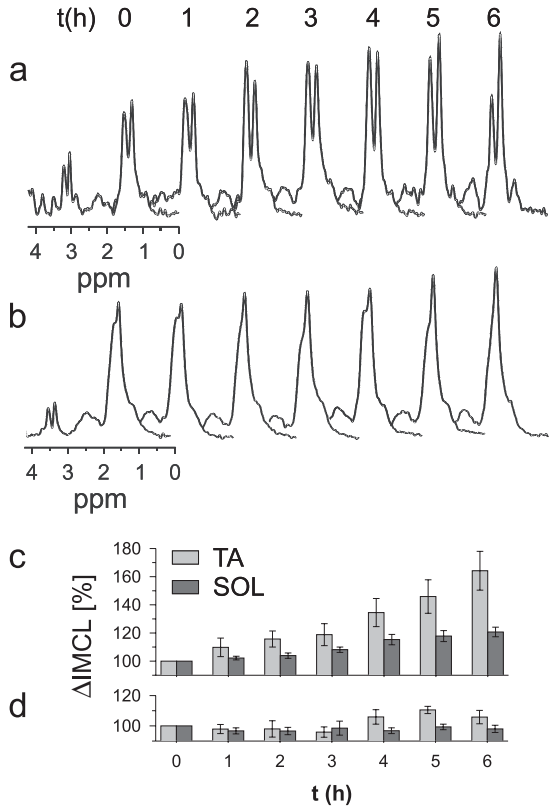

Fig. 25. Series of spectra of TA (a) and SOL (b) acquired during intravenous lipid infusion under hyperinsulinemia in a 25-year-old male volunteer. Time courses of ΔIMCL of all volunteers (mean ± SEM) are given in (c) for HI+F, and (d) for HI alone.

NMR spectroscopy of TA and SOL was repeated every 60 min parallel to the metabolic examinations, with the volunteers resting in the magnet for the entire time of 6 h.

Protocol [1] resulted in a marked steady increase of IMCL levels. In TA, a significant increase compared to the baseline value was to be noted after 2 h ($\Delta IMCL_{TA} = +15.7 \pm 5.8\%$, $p < 0.05$) and in SOL after 4 h ($\Delta IMCL_{SOL} = +12.3 \pm 3.5\%$, $p < 0.05$). After 6 h IMCL were increased by $64.2 \pm 13.8\%$ in TA and $20.7 \pm 3.4\%$ in SOL. Figure 25 depicts typical series of spectra from one subject recorded from TA (a) and SOL (b) in the course of protocol [1], demonstrating the significant increase in IMCL content. Time courses of the mean IMCL content in TA and SOL of all volunteers are shown in Fig. 25c. In the same time period insulin sensitivity of the volunteers worsened by approximately 40%, with the GIR declining from 48.9 ± 2.8 μmol/kg/min to 30.0 ± 3.9 μmol/kg/min.

The control experiment (protocol [2]) did not reveal such significant changes in the IMCL content. After 6 h only increases of $+8.8 \pm 4.4\%$ in TA and $+1.5 \pm 1.6\%$ in SOL were measured (both n.s., see Fig. 25d). Insulin sensitivity improved with GIR increasing from 42.2 ± 7.8 μmol/kg/min to 76.1 ± 5.0 μmol/kg/min.

Increase of IMCL content was also clearly less pronounced under lipid infusion without hyperinsulinemic conditions (protocol [3]). This protocol was carried out in a very similar way by Krššák *et al.*,[89] who reported that elevation of FFA without hyperinsulinemia does not alter IMCL content. In contrast to those findings are the results of Boden *et al.*,[90] who observed a massive increase of IMCL under similar conditions as in protocol [3], but only a low increase after protocol [1]. The reasons for these discrepancies are still debated.

However, the experiments showed for the first time that rapid changes in IMCL levels are possible by a short-term intervention, and that the IMCL compartment shows high metabolic activity, at least under distinct circumstances.

7.4.2. *Effect of short term fat rich diet*

The lipid infusion protocol represents an experimental situation with supraphysiologically high NEFA blood levels. In the following study it was examined, whether an extrapolation of the results to physiological situations is possible. For this purpose, the effects of short term dietary interventions on IMCL levels and insulin sensitivity were studied.[88] Twelve healthy, lean male subjects with intermediate insulin sensitivity (BMI 23.2 ± 0.6 kg/m^2, GIR $= 46.1 \pm 2.8$ μmol/kg/min received a high caloric (HC) and a normal caloric (NC) diet. The diets had a duration of 3 days and were characterized as follows:

(1) HC: high caloric, high in fat (approximately 60% of energy intake, predominantly saturated fat) and low in carbohydrate (30–35%) and protein (10–15%). Total energy intake: 2667–2943 kcal/day.
(2) NC: normal caloric, low in saturated fat (18–23%) and high in carbohydrate (62–64% of energy intake) with 16–18% protein and fibre. Total energy intake: 1901–2125 kcal/day.

The diets consisted of commonly available food items. No alcohol was permitted during the study period. Two days before the metabolic investigations the subjects were on a prescribed standardized well balanced diet. The time delay between both dietary interventions was 4 weeks.

Before and after the dietary interventions, IMCL was measured in TA and SOL, and insulin sensitivity was assessed by a euglycemic hyperinsulinemic glucose clamp.

After HC diet the IMCL content increased in the TA by $48.0 \pm 16.9\%$ ($p < 0.005$). In SOL the IMCL level was increased by 14%, but this increase

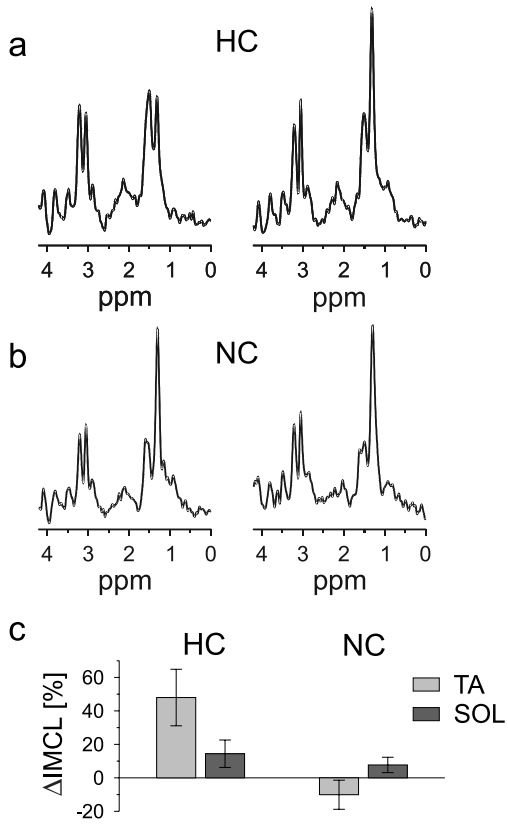

Fig. 26. Spectra recorded from TA of a 32-year-old male volunteer before (left row) and after (right row) short term diets. (a) After high caloric diet (HC) there is a marked increase in IMCL, whereas IMCL content is nearly unchanged after normal caloric diet (NC) as shown in (b). (c) Relative changes of IMCL from baseline after the dietary intervention in the two muscle groups (12 subjects; data are given as mean ± SD).

failed statistical significance (14.4 ± 8.2%, n.s.). The spectra in Fig. 26a were recorded from one volunteer before and after HC diet, supporting the presented results. In all volunteers with HC diet insulin sensitivity decreased significantly to GIR = 38.3 ± 3.3 μmol/kg/min ($p < 0.033$).

NC diet resulted in nearly unchanged IMCL contents in TA and SOL ($\Delta IMCL_{TA}$: −10.1 ± 8.7%, n.s.; $\Delta IMCL_{SOL}$: +7.7 ± 4.6%, n.s.) as shown for one subject in Fig. 26b. GIR was not significantly altered during NC diet as well, mean values raised slightly from 41.7 ± 2.8 μmol/kg/min to 42.8 ± 3.3 μmol/kg/min (n.s.).

The mean changes in the IMCL content caused by the two different dietary interventions are shown in Fig. 26c.

7.4.3. *Effect of fasting*

Not only different types of nutrition, but also longer periods of fasting are known to influence metabolism. For this reason, the effect of fasting on IMCL levels in human skeletal muscle was examined. Early consumption of muscular glycogen and low glucose and insulin levels lead to a markedly reduced supply with carbohydrates during longer fasting periods. Thus, adipose tissue triglycerides are the body's major source of fuel during periods of food deprivation. Increased mobilization of adipose tissue triglycerides is an important adaptive response to fasting, leading to high levels of fatty acids and triglycerides in blood. Free fatty acids derived from adipose tissue lipolysis become a major source of oxidizable metabolic fuel for heart, liver and skeletal muscle. Since both, supply and consumption of fatty acids, are increased in musculature during fasting, it has been unclear what happens with the amount of IMCL under these circumstances. The aim was to find out whether several days of fasting conditions with increased amount of FFAs in the blood, increased consumption of lipids in musculature, and hypoinsulinemia, influence IMCL levels.[91]

Three female and one male volunteer, aged 31–45 years, with normal oral glucose tolerance participated in a voluntary 5-day fasting period. During the fasting period three out of the four volunteers abstained completely from any caloric nutrition. Only water and electrolytes were substituted. One female subject drank a glass of apple juice (containing fructose) on the second day of the fasting period.

The first MRS examination was performed in the early morning before the participants started their voluntary fasting. Further MR examinations followed after the first (24 h), third (72 h) and fifth (120 h) day of fasting. Blood samples for measurements of plasma FFAs, glucose, and insulin concentrations were taken parallel to each MRS examination.

Figure 27a and b show series of spectra recorded from the 45-year-old female volunteer during the course of the fasting cure. Both series of spectra, from TA (a) and from SOL (b), depict a remarkable increase of the IMCL signal intensity with a nearly unchanged EMCL content.

The IMCL content after 120 h showed a very pronounced mean elevation in the subjects in both muscles to a level of more than 430% compared to the baseline values in TA ($IMCL_{TA} = 430 \pm 213.9\%$, range: 264–722%) and to a level of about 150% in SOL ($IMCL_{SOL} = 152.2 \pm 26.1\%$, range: 130–177%).

In a more detailed analysis $IMCL_{TA}$ showed a relative increase of more than 30% already after the first day of fasting ($IMCL_{TA} = 131.0 \pm 46.8\%$, range: 85–195%), and rose to more than 300% on the third day ($IMCL_{TA} = 310 \pm 165.4\%$, range: 128–522%) with the lowest increase of only 28% for the female volunteer who had drunk fructose containing juice

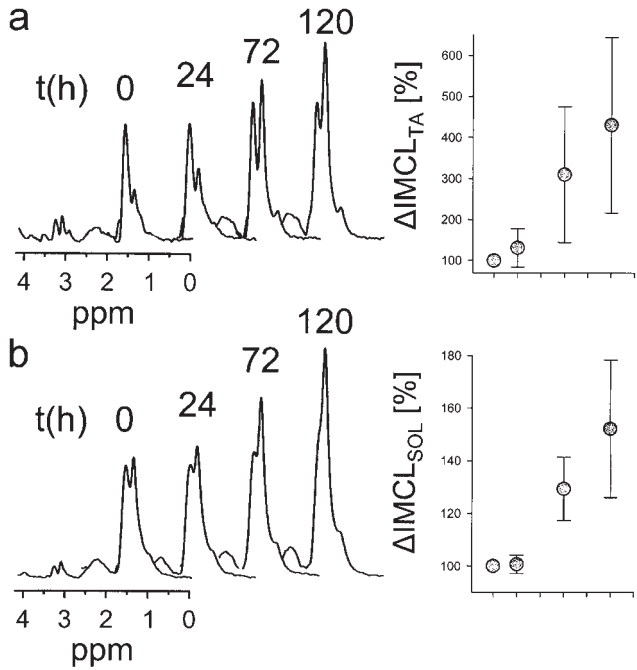

Fig. 27. Increasing IMCL content in TA (a) and SOL (b) during a fasting period. Spectra were recorded of a 45-year-old female subject before, after 24 h, 72 h, and 120 h of fasting. Means and SD of all four volunteers are given on the right side.

on the second day of the fasting period. $IMCL_{SOL}$ revealed a slightly different time course, with generally lower percentage changes and a delayed increase, as already observed in the lipid infusion and the dietary studies. $IMCL_{SOL}$ did not show any significant difference after 24 h of fasting ($IMCL_{SOL} = 100.7 \pm 3.5\%$, range: 98–105%), but after the third day a significant increase of more than 29% ($IMCL_{SOL} = 129.4 \pm 12.0\%$, range: 120–145%) was observed.

During the fasting period FFAs increased from a physiological level of 580.2 ± 269.1 μg/dl to more than 1500 μg/dl (1531.5 ± 640.7 μg/dl) after the fifth day. Simultaneously, plasma insulin decreased by 45% in the mean from 4.4 ± 2.3 μU/ml to a level of 2.4 ± 1.6 μU/ml and plasma glucose declined by 33% in the mean from 90.7 ± 0.9 mg/dl to 60.5 ± 5.3 mg/dl in the four subjects.

The results revealed that fasting in humans, going along with elevated circulating FFA together with low insulin and glucose plasma levels, induces an extreme and continuing formation of IMCL in human skeletal musculature, providing further insight in the complex and not fully understood regulation of muscular lipid metabolism.

7.5. IMCL in sports medicine

Besides the cited studies concerning elevation of IMCL by nutrition-related exogene interventions there is great interest in understanding the regulation of IMCL during exercise. It is known that fat and carbohydrates are the major fuels of skeletal muscle during work and rest. With increasing duration of submaximal exercise, fuel utilization shifts from carbohydrates to lipids.[92–94] With increasing intensity of exercise, fat oxidation increases further until exercise intensities of about 65% of maximum aerobic capability ($=100\%$ VO_{2max}), after which a decline in the rate of fat oxidation is observed. The changes in fat oxidation as a function of the exercise intensity have recently been described by Achten *et al.*[95] During low- and moderate-intensity exercise, lipolysis in adipose tissue is increased, providing an important source of FA for the muscle. At high intensities, the delivery of FA from adipose tissue to the muscle and the use of FA by the muscle are reduced. There is clear evidence that the availability of FA is important for fat oxidation.

Evaluation of dynamic changes in IMCL during prolonged exercise have been performed by muscle biopsies showing a significant depletion of intramuscular lipid stores during exercise and furthermore an increase in these stores during the recovery phase (e.g., Refs. 96 and 97). However, the classic biopsy method does not distinguish intra- from extracellular fat, and repeated biopsy is problematic because of its invasiveness.

With the non-invasive tool of muscular proton MR spectroscopy it is possible to study lipid oxidation, especially oxidation of IMCL, during exercise much more comfortably and precisely. Boesch *et al.*[19] revealed a decrease of IMCL in one subject performing a mountain bike ride over 3 h at about 70% of VO_{2max}, for the first time suggesting that IMCL are metabolized during this form of exercise.

The effects of aerobic exercise of different workloads and durations on IMCL were examined in several studies.[98] Twelve well-trained male Caucasian subjects participated in these studies. All volunteers were in good health and none was taking any medication. BMI and VO_{2max} were comparable in all volunteers.

7.5.1. *Exercise protocols*

Six subjects were told to run at a moderate speed (corresponding to a workload of 60–70% of the individual VO_{2max}) for about 100 min without competition (NCR). Three subjects took part in a competitive marathon run (M, 42 km) corresponding to 60–70% of the individual VO_{2max}. The remaining three subjects participated in a competitive half marathon run (HM, 21 km; corresponding to 80–90% of the individual VO_{2max}).

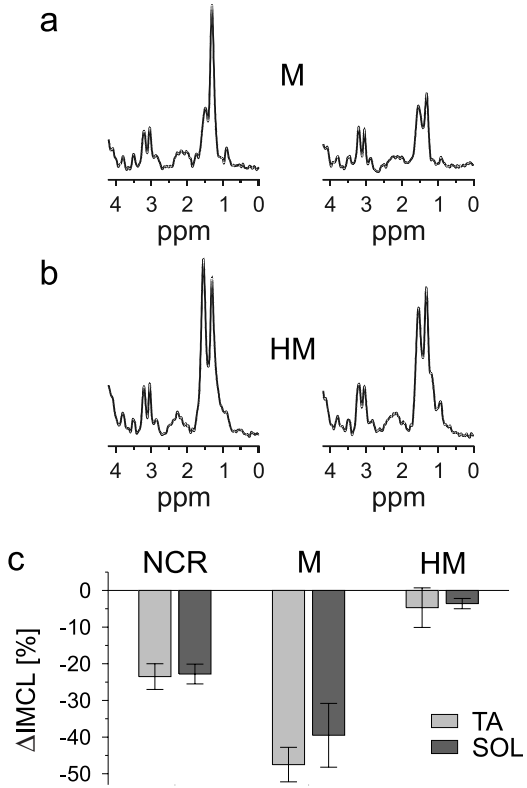

Fig. 28. (a) Spectra from TA of a 33-year-old male subject before (left) and after (right) a marathon run (M) with submaximal intensity indicate a massive reduction in IMCL. (b) IMCL is nearly unchanged after a high-intensity half-marathon run (HM) in a 42-year-old male subject. (c) Relative changes in IMCL after non-competitive run (NCR, 6 volunteers), marathon run (M, 3 volunteers), and half-marathon run (HM, 3 volunteers). Data are given as means ± SEM.

7.5.2. *Results*

During NCR a clear reduction of IMCL in both muscles was observed (about 20%, spectra not shown), which was even more prominent after M (about 50–60%, Fig. 28a). In contrast to this, IMCL were nearly unchanged after HM (Fig. 28b). The mean reduction of IMCL in all subjects is given in Fig. 28c. The studies show that decline of IMCL levels depends on exercise intensity, as a marked decrease in IMCL after exercise of similar duration is only observable at lower aerobic workloads (NCR vs. HM). IMCL reduction also depends on exercise duration, as shown by the greater decline after the marathon run (M = 225 min) compared to the non-competitive exercise bout (NCR = 106 min).

There are several reports on reduced IMCL levels during exercise (e.g., Refs. 19, 79, 99–103) and some of these studies additionally concentrate on the determination of replenishment of IMCL after exercise. It was reported that most IMCL are replenished after endurance running within approximately 3–5 days. Based on the results it was suggested that diets containing moderate amounts of fat should be consumed and, consequently, that diets too low in fat are probably not ideal for endurance athletes.

8. CHARACTERIZATION OF MUSCLE DISEASES

Diseases of muscle are usually classified as muscular dystrophies, inflammatory or congenital myopathies, metabolic disorders affecting the muscle, and neurological diseases affecting the innervation of the muscle (so-called motor neuron diseases). In the past, the energy metabolism of some muscular diseases has been investigated by ^{31}P spectroscopy, but only few experiences with ^{1}H spectroscopy exist in this field. Animal models have been used to investigate the effects of gene defects on muscular spectra. In the following, some exemplary clinical experiences shall be given.

8.1. Muscular dystrophies

Duchenne and Becker muscular dystrophies are hereditary myopathies. Both forms are x-linked recessively inherited, and characterized by a progressive muscular wasting and weakness. Duchenne muscular dystrophy is one of the most common and the most severe. Generally, it leads to death before the third decade of life. Becker muscular dystrophy is less common, and more benign. In both forms a protein, the so-called dystrophin, is deficient. It is thought, that the deficient dystrophin leads to an instability of the muscular membranes and loss of muscle tissue.[104] Necrotic and hypercontracted fibres appear, and thus the normal muscular pattern in ^{1}H spectroscopy is lost: instead of the muscular tissue adipose tissue is found. An MR image and two proton spectra recorded from musculature in a 13-year-old boy with Duchenne's dystrophy are presented in Fig. 29. The muscular tissue of the lower leg is thinned, and the lipid containing septa are very prominent. A marked muscular atrophy is visible on the transversal image of the calf. In ^{1}H spectroscopy, EMCL are clearly dominating the pattern.

8.2. Inflammatory myopathy – Eosinophilia Myalgia syndrome

The eosinophilia myalgia syndrome (EMS) is a complex systemic syndrome with inflammatory and autoimmune components that affects the skin, fascia,

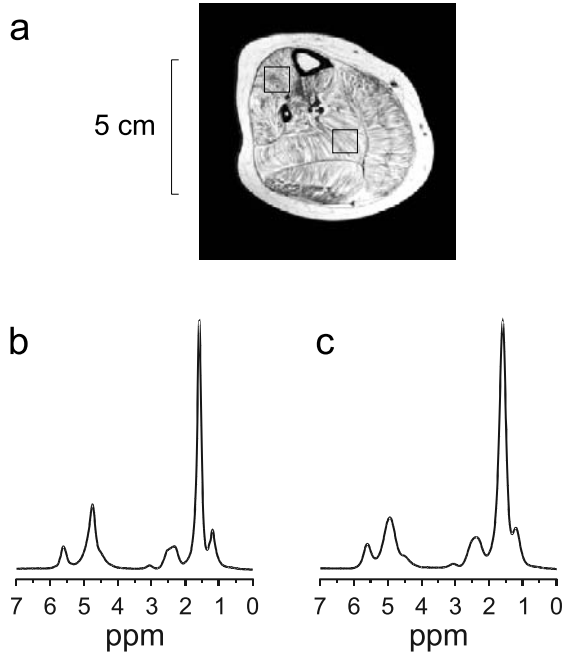

Fig. 29. Thirteen-year-old boy with Duchenne Dystrophy. (a) The fat selective image shows a fatty degeneration of all muscles in a cross-section of the lower limb. The fat tissue is orientated in the direction of the muscle fibres, and is present between the fibres and in the septa. (b, c) The spectra from both volume elements indicated in (a) reveal signals from EMCL. Muscle specific metabolites (TMA and creatine) are clearly reduced and not visible in the proton spectra due to the reduction of muscle tissue in favour of adipose tissue.

muscle, nerve, blood vessels, lung and heart. The varied symptoms include severe muscle pain and abnormally high numbers of eosinophil cells (more than 2000/mm^3). It was supposed[105] that contaminations from a special manufacturing process of L-tryptophan (probably originating from a genetically engineered bacterial strain) are responsible for the multi-system disease as the disease has presented itself only in people taking this amino acid as medication.

In a study with 3 EMS patients[106] the relative signal intensities in proton spectra recorded at an echo time of 50 ms with a repetition time of 2 s were quantitatively compared with healthy controls. It was evident that the muscle specific signals from TMA and Cr are relatively low in EMS patients (TMA: 0.20–0.43% in the patients and 0.47–0.68% in the controls; creatine: 0.32–0.60% in the patients and 0.48–0.77% in the controls) probably indicating changes of concentrations and altered chemical surroundings of TMA and Cr in the myoplasm of the diseased cells. The overall lipid signal was found to be

similar or slightly increased. The signal from unsaturated fatty acids was slightly elevated in the EMS patients compared with the healthy volunteers which might result from alterations of lipid metabolism in involved muscles. Marked atrophy of the calf musculature was shown in two EMS patients. In addition thickening of the skin and high water content of the cutis could be shown by water selective imaging.

8.3. Congenital myopathies

Congenital muscle disorders are inherited diseases presenting in early life or infancy with generalized hypotonia, which means that the muscular tonus is reduced. Often, the other so-called dysmorphic features such as an elongated face, and deformities of the vertebral columns, hip and foot can additionally be found. The rare desmin storage myopathies belong to this group, where inclusion bodies or deposits with desmin were found in ultrastructural investigations of the muscle cell. Desmin is a part of the cytoskeleton and is discussed to be involved to the linkage of the so-called sarcomeres, which are the contractile elements of the muscular fibres.[107] In desmin storage myopathies, there is a surplus desmin deposits (only detectable in electron microscopy), and a so-called atrophy (volume reduction of the muscle). Muscular atrophy is visible on the transversal images of the calf, as shown in Fig. 30a. In ^{1}H spectroscopy, EMCL are dominating the pattern (Fig. 30b).

8.4. Metabolic disorders affecting the muscle

There is a large variety of metabolic disorders affecting the muscle, all being relatively rare in incidence. One disease from this group is the glutaric aciduria Type II, where the oxidative reactions within several tissues are hindered. The patients suffer from a progressive proximal myopathy, and sometimes symptoms of the central nervous system.[108] Herein presented is one case with glutaric aciduria Type I presenting predominantly with central symptoms, but only mild muscular symptoms.[109] In ^{1}H spectroscopy, interestingly a reduction of the carnitine-containing tri-methyl-amine (TMA) peak was visible as indicated in Fig. 31.

Another disease with metabolic effects on musculature is acquired generalized lipodystrophy (AGL). It is characterized by generalized disappearance of fat (subcutaneous fat and probably other adipose tissue) occurring during childhood and adolescence. The onset of the disease is gradual over months to years. Up to now, a total of about 100 cases have been reported. In contrast to patients with congenital generalized lipodystrophy (CGL), AGL-patients show normal body fat at birth. AGL could be due to panniculitis (inflammation in the fat) or autoimmune diseases. However, in

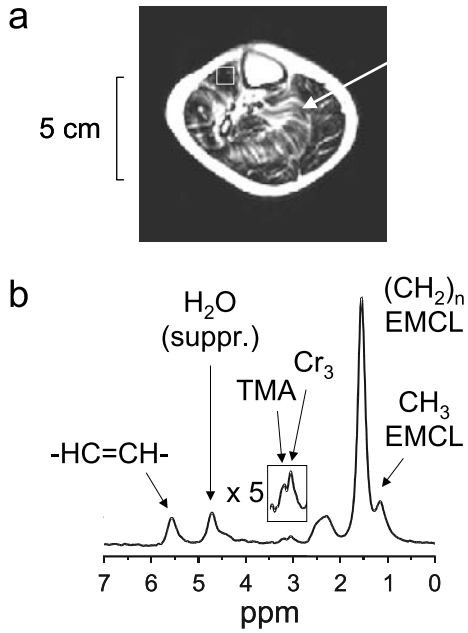

Fig. 30. Thirteen-year-old boy with desmin storage myopathy. (a) The T_1 weighted image shows an atrophy of the tibialis anterior muscle (with the volume element indicated) and a fatty degeneration of the soleus muscle (arrow). (b) The spectrum from the tibialis anterior muscle shows prominent EMCL. TMA is reduced as indicated in the area of the 5-fold magnification.

several cases no causative factor could be identified. In some cases chronic infection was described prior to the disease suggesting an immunologic disturbance.[110,111] Eventually generalized and near complete loss of fat may occur in some patients resulting in muscular appearance and prominent superficial veins (veins under the skin). There is loss of fat from the palms and soles also.

The precise mechanism involved in loss of body fat in this disorder however remains speculative but it is likely that autoimmune mechanisms (body defense mechanisms acting against body fat) are involved. Interestingly, in AGL severe insulin resistant diabetes mellitus is a typical clinical feature.[110–112] Insulin resistance is frequently associated with an increased body weight and fat mass. Therefore, AGL is an interesting and unique 'knockout model' of subcutaneous adipose tissue combined with insulin resistant diabetes mellitus.

We examined a 30-year-old male AGL-patient (BMI 15.4 kg/m^2, severe insulin resistance) to assess and compare findings of derived metabolic data and NMR examinations.[113] A reduction of subcutaneous adipose tissue was

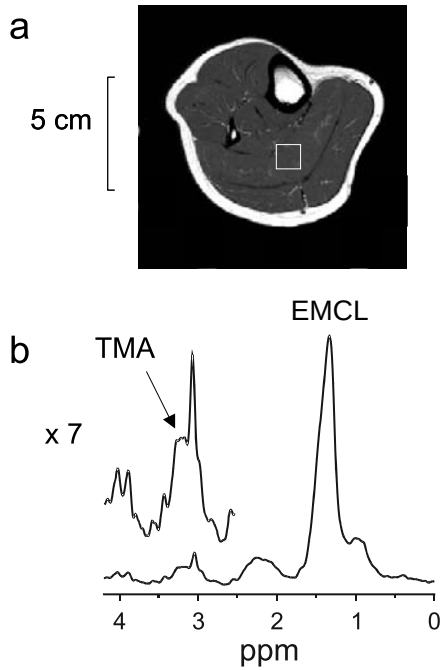

Fig. 31. Twenty-year-old woman with glutaric aciduria type I. (a) The T_1 weighted image shows normal findings for the cross-section of the lower limb. The volume element for spectroscopy was chosen in the soleus muscle. (b) The 7-fold magnification depicts a reduction of TMA. Although no fatty degeneration is visible on the image, the spectrum is dominated by EMCL.

clinically obvious, but body impedance measurement revealed a body fat content of more than 15%.

Figure 32 shows a transverse T_1-weighted image of the AGL patient (Fig. 32a) and the corresponding fat selective image (Fig. 32b), demonstrating the missing subcutaneous fat as well as fatty septa between the muscle fibre bundles.

In comparison to an insulin resistant subject without AGL (spectrum in Fig. 32c) the spectrum from the SOL of the AGL patient (Fig. 32d) shows a single signal peak at 1.3 ppm representing the methylene signal of IMCL whereas the methylene signal peak of EMCL at 1.5 ppm is almost completely missing.

The group of Stein reported on spectroscopic examinations on patients suffering from CGL. These patients also showed a single methylene peak of IMCL due to the lack of adipose tissue (i.e., EMCL in the musculature).[38,114] Spectra obtained from patients with AGL or CGL confirm the earlier statements concerning the possibility of distinguishing IMCL and EMCL by ^{1}H NMR spectroscopy.

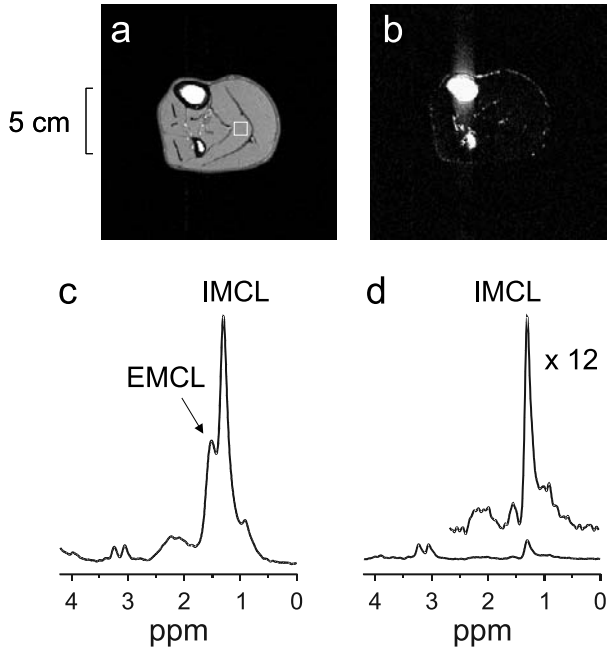

Fig. 32. The 30-year-old male patient with acquired generalized lipodystrophy (AGL) shows lacking lipids in the subcutaneous layer and in the musculature in a T_1-weighted spin-echo image (a) and in a fat selective image (b). Only marrow fat in the tibia and fibula of the patient seems to be not affected by the disease. Comparison between a spectrum from a insulin resistant subject without AGL (c) and the spectrum from the AGL patient (d) reveals that the AGL patient has nearly lacking EMCL and markedly reduced IMCL content.

8.5. Motor neuron diseases

The most frequent disease of the motor neuron diseases is the amyotrophic lateral sclerosis (ALS) or so-called Lou Gehrig's disease. It is a progressive disorder with degeneration of the motor neurons of the cerebral motor cortex, brainstem, and the spinal cord. It is an illness of the late adult life with a slight male preponderance. In dependence of a predominant impairment of upper or lower motor neurons, different clinical features are present. In the case of an involvement of the lower motor neuron, signs of denervations will be visible.[115] But muscle biopsy is seldom necessary for the diagnosis, because the diagnosis is often clinically apparent and diagnosed by electrophysiology.

Another motor neuron disease, which is rare and x-linked inheritance, shows certain similarities with ALS but has a much more benign course. It is so-called Kennedy's disease or x-linked spino-bulbar muscular atrophy (X-SBMA). It is caused by a mutation of the androgen receptor gene. A progressive spinal,

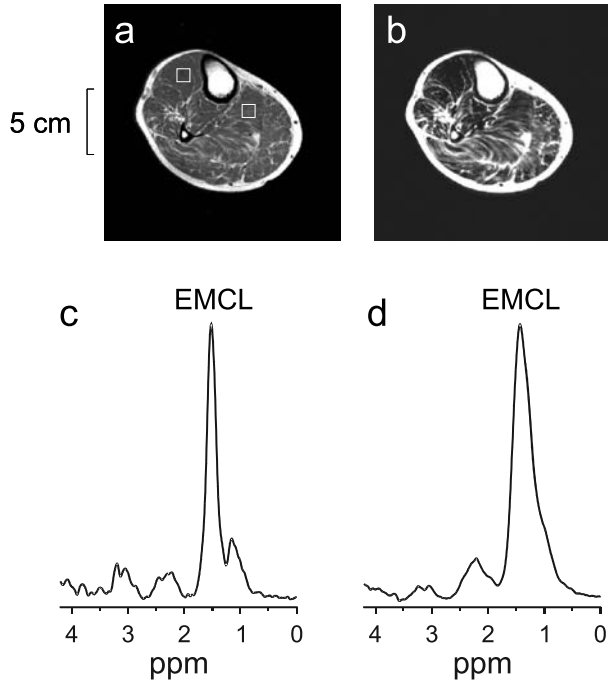

Fig. 33. Thirty-six-year-old man with Kennedy's Syndrome. (a, b) The T_1 weighted and the fat selective images show an atrophy and a fatty degeneration of the muscles of the lower leg with a relative sparing of the tibialis anterior muscle. (c) The spectrum from the tibialis anterior muscle shows prominent EMCL, although no obvious fatty degeneration is visible on the images. (d) The spectrum from the soleus muscle is merely dominated by EMCL.

bulbar and muscular atrophy, a gynecomastia and a reduced fertility are clinically predominant. A diabetes mellitus can occur. The diagnosis can clinically be established, and verified by gene analysis. In ^{1}H spectroscopy the spectra are dominated by extracellular lipids, because a muscular atrophy occurs, from which the tibialis anterior muscle is relatively preserved. An example is presented in Fig. 33.

9. MUSCLE SPECTROSCOPY AT HIGHER FIELD STRENGTH

Most applications of muscular NMR spectroscopy have been performed at a magnetic field strength of 1.5 T, as commonly available on clinical whole body imagers. Recent technical development has led to whole body imagers with a magnetic field strength of 3.0 T. Higher field strength provides improved spectral resolution as the dispersion increases linearly with frequency, and higher signal gain. For this reason spectra can be recorded with higher signal to

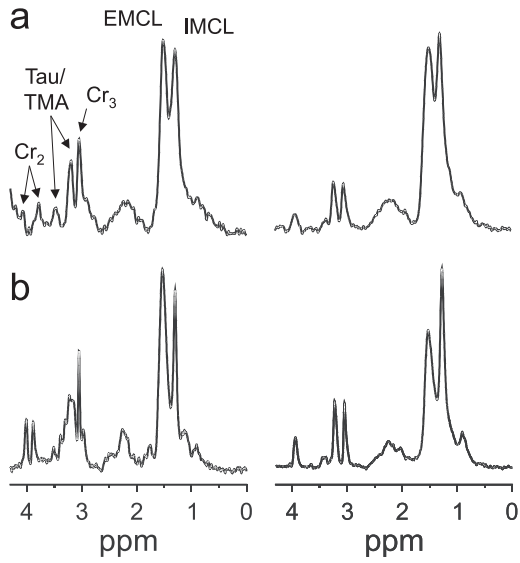

Fig. 34. Comparison between spectra of skeletal muscle recorded from TA (left row) and SOL (right row) at 1.5 T (a) and 3.0 T (b). IMCL and EMCL as well as Cr_3 and TMA are better separated in both muscles at 3.0 T. TMA signal shows line splitting in TA which are not shown in SOL spectra.

noise ratio, or alternatively, from smaller volumes within the same measuring time. On the other hand, there are increasing susceptibility effects. In muscle spectra especially the linewidth of the EMCL signal is affected by susceptibility-induced MFD as mentioned in Sections 4 and 5.

In order to compare the patterns of muscular spectra at different magnetic field strenghts, 5 male subjects have been examined at 1.5 T (Magnetom Vision, Siemens, Germany) and at 3.0 T (Magnetom Trio, Siemens/Bruker, Germany).

Spectra were recorded from the same VOI with identical measurement parameters: STEAM, TE = 10 ms, TR = 15 ms, TR = 2 s, 32 acq., VOI $(11 \times 11 \times 20)$ mm^3.

At 3.0 T additional spectra were recorded using smaller voxel sizes of $(9 \times 9 \times 18)$ mm^3, 48 acq., $(7 \times 7 \times 14)$ mm^3, 64 acq., and $(5 \times 5 \times 10)$ mm^3, 80 acq.

Figure 34 shows spectra of TA and SOL from a 24-year-old male volunteer recorded at 1.5 T (a) and 3.0 T (b). Besides the clearly improved SNR, which is elevated by a factor of 1.7 to 1.8 at 3.0 T, distinct differences can be observed for the two magnetic field strengths: In both muscles, IMCL and EMCL are clearly better separated at 3.0 T as the methylene resonance of IMCL shows smaller natural linewidths (in ppm). However, EMCL signals remain with a broad lineshape in TA as well as in SOL, since the lineshape is dominated by susceptibility induced static field inhomogeneities. Cr_3 and TMA signals are

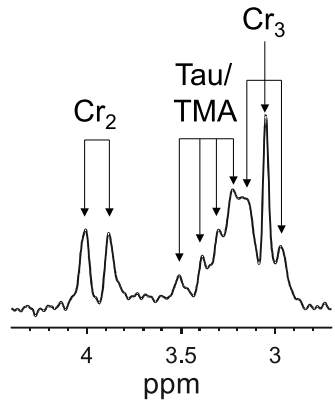

Fig. 35. Part of the spectrum recorded at 3.0 T from TA (shown in Fig. 33b) demonstrating the line splitting caused by dipolar coupling. Triplet structure of Cr_3 is resolved, Tau/TMA lead to 4 signal components. The frequency difference between the two Cr_2 signals centred at 3.95 ppm is smaller compared to 1.5 T, but these signals are of higher amplitude than in Cr_3.

better resolved at 3.0 T in SOL, whereas in TA the TMA/Tau resonances are split in four signals at 3.0 T. As this splitting does not occur in SOL it is probably attributed to dipolar coupling effects, as already mentioned in Section 4 and described from examinations of mouse gastrocnemius muscle on a 7 T NMR spectrometer.[26] Additionally, Cr_2 signals show minor spectral separation and markedly higher relative amplitudes at 3.0 T compared to 1.5 T in TA. The relevant chemical shift region of the spectrum is shown in Fig. 35.

Spectra recorded from smaller VOI (down to 0.25 ml) with careful positioning in regions without fatty septa provide a clearly decreasing EMCL signal contamination, resulting in improved visibility of IMCL in SOL at 3.0 T (see Fig. 36). Separate depiction of IMCL improves quantification of this lipid compartment, as inaccuracies due to the inhomogenous lineshape and resulting contaminations of EMCL can be avoided.

In conclusion, muscular spectroscopy profits of the higher field strength. Clearly narrower IMCL resonances and nearly unchanged susceptibility based broad EMCL signals occur at higher field strength. Dipolar coupling effects especially observed in TA (with parallel muscle fibre orientation to B_0) have to be further studied in detail.

10. MUSCLE SPECTROSCOPY USING OTHER NUCLEI THAN PROTONS

The presented chapter focuses on proton NMR of skeletal musculature in humans. It should be mentioned in this context that especially examinations

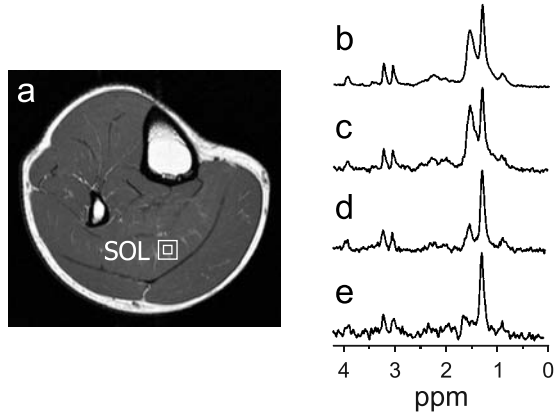

Fig. 36. Spectra recorded from SOL with decreasing voxel size as indicated in the T_1-weighted image (a). (b) $(11 \times 11 \times 20)$ mm^3, 32 acq. (c) $(9 \times 9 \times 18)$ mm^3, 48 acq. (c) $(7 \times 7 \times 14)$ mm^3, 64 acq. (e) $(5 \times 5 \times 10)$ mm^3, 80 acq. Examinations using smaller volumes provide an assessment of IMCL. Disturbing EMCL contaminations can be excluded from the voxel in this example.

with ^{31}P and ^{13}C can contribute to further insight in muscle metabolism. Examination volumes have to be chosen clearly larger for those nuclei than in proton spectroscopy due to the lower spin density in biological tissue and due to the lower MR sensitivity of the nuclei with lower magnetogyric ratio.

Phosphorus spectroscopy has been frequently employed for *in vivo* studies of musculature, since information about metabolites playing a key role in tissue energy consumption can be obtained in measuring times of a few minutes.[116–118] Signals from phosphocreatine (PCr), adenosine triphosphate (ATP), and inorganic phosphate (Pi) occur in the spectra with relatively high SNR. In addition, signals from NADH, phosphomonoesters and phosphodiesters occur in well-resolved spectra employing longer acquisition times. Further biologically relevant parameters as pH can be derived from the chemical shift of the inorganic phosphate. Functional tests can be performed by ^{31}P spectroscopy during exercise.[119] Figure 37 shows an example of a series of phosphorous spectra recorded during exercise of the human calf and the following recovery. Concentrations of PCr and Pi show dramatic changes caused by the increased energy consumption of the musculature during the workload. Muscle diseases were described which lead to changes in phosphorus spectra,[120] but all of the described diseases are rare and most clinical scanners are not equipped with phosphorus spectroscopy. On the other hand, the described results from proton spectroscopy lead to new questions, for example about the oxidative capacity in insulin resistant and well trained subjects, which possibly could be answered by future studies involving ^{31}P examinations.

Several studies on human musculature have been performed using ^{13}C spectroscopy.[71,121–123] Many metabolically relevant compounds (e.g., glucose,

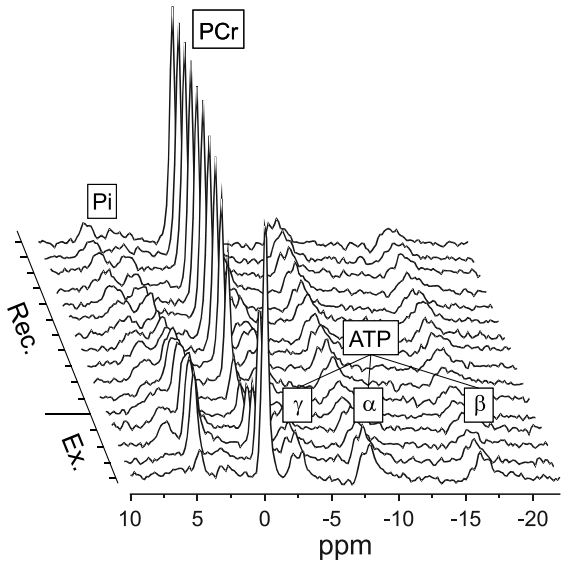

Fig. 37. Stacked plot of ^{31}P spectra recorded from the lower leg of a 35-year-old male volunteer. Spectra were recorded each 15 s during exhaustive exercise inside the imager (spectra 1 to 5) and in the recovery phase after exercise (spectra 6 to 16). Four acquisitions were recorded for each FID with TR = 3 s.

glycogen, fatty acids) contain carbon. Since the chemical shift range of the signals is approximately 200 ppm, high dispersion and selectivity is provided. Unfortunately, sensitivity of ^{13}C NMR *in vivo* is relatively low due to the low natural abundance of ^{13}C of only 1%. On the other hand, application of ^{13}C labelled substrates allows to follow metabolic processes, as for example storage of glycogen in musculature after administration of glucose.[124] It has been shown that clearly improved localized ^{13}C studies are feasible *in vivo* using high-field systems.[125] Carbon studies in humans can be expected for the future to elucidate relevant metabolic processes in the pathogenesis of wide spread diseases such as obesity, diabetes and arteriosclerosis.

ACKNOWLEDGEMENTS

Several studies reported in this review were supported by grants from the DFG (JA 1005/1-1), the Federal Ministry of Education and Research (Fö. 01KS9602), the Interdisciplinary Centre of Clinical Research Tübingen (IZKF) and by grants from the university clinic of Tübingen (fortüne). Klaus Brechtel and Beate Wietek from the Department of Diagnostic Radiology (Head: Professor C.D. Claussen) and the Section on Experimental Radiology were actively involved in the examinations and are gratefully

acknowledged. We also want to thank our clinical collaborators from the Department of Internal Medicine (Head: Professor H.-U. Häring), especially Stephan Jacob, Michael Stumvoll, Andreas Fritsche, Oliver Bachmann, Dominik Dahl, and Michael Haap for organization of many interesting studies. Andreas Niess from the Department of Sports Medicine is acknowledged for his help and collaboration in studies with athletes.

We wish to thank Dr. Hansjörg Graf for carefully reading the manuscript, and Karin Werz and Holger Putzhammer for their help with its preparation. Members of Siemens Medical Systems supported the installation of new sequence techniques, which allowed to record many of the examples presented in the review.

REFERENCES

1. R. S. Staron, *Can. J. Appl. Physiol.*, 1997, **22**, 307–327.
2. H. Lithell, J. Orlander, R. Schele, B. Sjodin and J. Karlsson, *Acta Physiol. Scand.*, 1979, **107**, 257–261.
3. E. M. Haake, R. T. Brown, M. R. Thompson and R. Venkatesan, *Magnetic Resonance Imaging, Physical Principles and Sequence Design*, John Wiley, New York, 1999.
4. G. Saab, T. Thompson and G. D. Marsh, *Magn. Reson. Med.*, 1999, **42**, 150–157.
5. F. Schick, S. Miller, U. Hahn, T. Nägele, J. Forster, U. Helber, P. E. Huppert and C. D. Claussen, *Invest. Radiol.*, 2000, **35**, 311–318.
6. A. Haase, J. Frahm, W. Hänicke and D. Matthaei, *Phys. Med. Biol.*, 1985, **30**, 341–344.
7. M. Braun, W.-I. Jung, O. Lutz and R. Oeschey, *Z. Naturforsch.*, 1988, **43a**, 291–296.
8. F. Schick, J. Forster, J. Machann, P. E. Huppert and C. D. Claussen, *Magn. Reson. Med.*, 1997, **38**, 269–274.
9. F. Schick, *MAGMA*, 1993, **1**, 158–168.
10. F. P. Prince, R. S. Hikida, F. C. Hageman, R. S. Staron and W. A. Allen, *J. Neurol. Sci.*, 1981, **49**, 165–179.
11. F. Schick, J. Machann, K. Brechtel, A. Strempfer, B. Klumpp, D. T. Stein and S. Jacob, *Magn. Reson. Med.*, 2002, **47**, 720–727.
12. W. T. Dixon, *Radiology*, 1984, **153**, 189–194.
13. R. S. Balaban and T. L. Ceckler, *Magn. Reson. Q.*, 1992, **8**, 116–137.
14. R. M. Henkelman, G. J. Stanisz and S. J. Graham, *NMR Biomed.*, 2001, **14**, 57–64.
15. P. A. Bottomley, *Ann. N.Y. Acad. Sci.*, 1987, **508**, 333–339.
16. J. Frahm, K. D. Merboldt and W. Hänicke, *J. Magn. Reson.*, 1987, **72**, 502–508.
17. C. T. W. Moonen, M. von Kienlin and P. C. M. van Zijl, *NMR Biomed.*, 1989, **2**, 201–208.
18. F. Schick, B. Eismann, W. I. Jung, H. Bongers, M. Bunse and O. Lutz, *Magn. Reson. Med.*, 1993, **29**, 158–167.
19. C. Boesch, J. Slotboom, H. Hoppeler and R. Kreis, *Magn. Reson. Med.*, 1997, **37**, 484–493.
20. D. R. Lide, *Handbook of Chemistry and Physics*, 74th edn, CRC Press, Boca Raton, FL, 1993.
21. R. J. Havel, L. E. Carlson, L. G. Ekelund and A. J. Holmgren, *Appl. Physiol.*, 1964, **19**, 613–618.
22. L. S. Szczepaniak, R. L. Dobbins, D. T. Stein and J. D. McGarry, *Magn. Reson. Med.*, 2002, **47**, 607–610.
23. R. Kreis and C. Boesch, *J. Magn. Reson.*, 1994, **104**, 189–192.
24. R. Kreis and C. Boesch, *J. Magn. Reson. B*, 1996, **113**, 103–118.

25. R. Kreis, M. Koster, M. Kamber, H. Hoppeler and C. Boesch, *Magn. Reson. Med.*, 1997, **37**, 159–163.
26. H. J. in't Zandt, D. W. Klomp, F. Oerlemans, B. Wieringa, C. W. Hilbers and A. Heerschap, *Magn. Reson. Med.*, 2000, **43**, 517–524.
27. I. Asllani, E. Shankland, T. Pratum and M. Kushmerick, *J. Magn. Reson.*, 1999, **139**, 213–224.
28. R. Kreis and C. Boesch, *Proc. Intl. Soc. Magn. Reson. Med.*, 2000, **8**, 31.
29. C. Boesch and R. Kreis, *NMR Biomed.*, 2001, **14**, 140–148.
30. J. Slotboom, C. Boesch and R. Kreis, *Magn. Reson. Med.*, 1998, **39**, 899–911.
31. J. W. van der Veen, R. de Beer, P. R. Luyten and D. van Ormondt, *Magn. Reson. Med.*, 1988, **6**, 92–98.
32. R. de Beer and D. van Ormondt, P. Diehl, E. Fluck, H. Gunther, R. Kosfeld, and J. Seelig, eds., *NMR Basic Principles and Progress*, Vol. 26, Springer-Verlag, Berlin, 1992, 201–248.
33. R. A. de Graaf, *In Vivo NMR Spectroscopy*, John Wiley, Chichester, 1998, 372–406.
34. G. Steidle, J. Machann, C. D. Claussen and F. Schick, *J. Magn. Reson.*, 2002, **154**, 228–235.
35. J. Machann, F. Schick, S. Jacob and C. D. Claussen, *Magn. Reson. Imaging*, 2000, **18**, 189–197.
36. C. C. Hanstock, R. B. Thompson, M. E. Trump, D. Gheorghiu, P. W. Hochachka and P. S. Allen, *Magn. Reson. Med.*, 1999, **42**, 421–424.
37. M. E. Trump, C. C. Hanstock, P. S. Allen, D. Gheorghiu and P. W. Hochachka, *Am. J. Physiol. Regul. Integr. Comp. Physiol.*, 2001, **280**, R889–R896.
38. L. S. Szczepaniak, E. E. Babcock, F. Schick, R. L. Dobbins, A. Garg, D. K. Burns, J. D. McGarry and D. T. Stein, *Am. J. Physiol.*, 1999, **276**, E977–E989.
39. T. L. Ceckler and R. S. Balaban, *J. Magn. Reson.*, 1991, **93**, 572–588.
40. S. H. Koenig, R. D. Brown and R. Ugolini, *Magn. Reson. Med.*, 1993, **29**, 311–316.
41. H. T. Edzes and E. T. Samulski, *J. Magn. Reson.*, 1978, **31**, 207–229.
42. S. Forsen and R. A. Hoffman, *J. Chem. Phys.*, 1963, **39**, 2892–2895.
43. J. Eng, T. L. Ceckler and R. S. Balaban, *Magn. Reson. Med.*, 1991, **17**, 304–314.
44. S. D. Wolff and R. S. Balaban, *Magn. Reson. Med.*, 1989, **10**, 135–144.
45. D. Leibfritz and W. Dreher, *NMR Biomed.*, 2001, **14**, 65–76.
46. F. Schick, *J. Comput. Assist. Tomogr.*, 1996, **20**, 73–79.
47. M. J. Kruiskamp, R. A. de Graaf, G. van Vliet and K. Nicolay, *Magn. Reson. Med.*, 1999, **42**, 665–672.
48. M. J. Kruiskamp, G. van Vliet and K. Nicolay, *Magn. Reson. Med.*, 2000, **43**, 657–664.
49. M. J. Kruiskamp and K. Nicolay, *J. Magn. Reson.*, 2001, **149**, 8–12.
50. J. M. Bonny and J. P. Renou, *Magn. Reson. Imaging*, 2002, **20**, 395–400.
51. B. M. Damon, Z. Ding, A. W. Anderson, A. S. Freyer and J. C. Gore, *Magn. Reson. Med.*, 2002, **48**, 97–104.
52. S. Posse, C. A. Cuenod and D. Le Bihan, *Radiology*, 1993, **18**, 719–725.
53. R. A. de Graaf, A. van Kranenburg and K. Nicolay, *Biophys. J.*, 2000, **78**, 1657–1664.
54. R. A. de Graaf, K. P. Braun and K. Nicolay, *Magn. Reson. Med.*, 2001, **45**, 741–748.
55. K. Nicolay, A. van der Toorn and R. M. Dijkhuizen, *NMR Biomed.*, 1995, **8**, 365–374.
56. K. Nicolay, K. P. Braun, R. A. Graaf, R. M. Dijkhuizen and M. J. Kruiskamp, *NMR Biomed.*, 2001, **14**, 94–111.
57. D. Le Bihan, *Magn. Reson. Q.*, 1991, **7**, 1–30.
58. S. T. Kinsey, B. R. Locke, B. Penke and T. S. Moerland, *NMR Biomed.*, 1999, **12**, 1–7.
59. U. Sinha and L. Yao, *J. Magn. Reson. Imaging*, 2002, **15**, 87–95.
60. R. V. Mulkern, H. Gudbjartsson, C. F. Westin, H. P. Zengingonul, W. Gardner, C. R. G. Guttmann, R. L. Robertson, W. Kyriakos, R. Schwarz, D. Holtzman, F. A. Jolesz, S. E. Maier, *NMR Biomed.*, 1992, **12**, 51–62.
61. F. Schick, *MAGMA*, 1998, **6**, 53–61.
62. D. T. Stein, L. Szczepaniak, F. Schick, R. Dobbins, E. E. Babcock, C. R. Malloy and J. D. McGarry, *Proc. Int. Soc. Magn. Reson. Med.*, 1997, **5**, 1333.
63. C. Boesch, J. Decombaz, J. Slotboom and R. Kreis, *Proc. Nutr. Soc.*, 1999, **58**, 841–850.

64. H. Howald, C. Boesch, R. Kreis, S. Matter, R. Billeter, B. Essen-Gustavsson and H. Hoppeler, *J. Appl. Physiol.*, 2002, **92**, 2264–2272.
65. J. B. Shumate, M. H. Brooke, J. E. Carroll and R. M. Choksi, *Arch. Neurol.*, 1982, **39**, 561–564.
66. A. J. Shah, V. Sahgal, A. P. Quintanilla, V. Subramani, H. Singh and R. Hughes, *Clin. Neuropathol.*, 1983, **2**, 83–89.
67. D. T. Stein, L. S. Szczepaniak, R. Dobbins, C. R. Malloy and J. D. McGarry, *Diabetes*, 1997, **46**(Suppl. 1), 23A.
68. D. T. Stein, L. S. Szczepaniak, R. L. Dobbins, P. Snell and J. D. McGarry, *Proc. Int. Soc. Magn. Reson. Med.*, 1998, **6**, 388.
69. M. Krššák, K. F. Petersen, A. Dresner, L. DiPietro, S. M. Vogel, D. L. Rothman, G. I. Shulman and M. Roden, *Diabetologia*, 1999, **42**, 113–116.
70. S. Jacob, J. Machann, K. Rett, K. Brechtel, A. Volk, W. Renn, E. Maerker, S. Matthei, F. Schick, C. D. Claussen, H. U. Häring, *Diabetes*, 1999, **48**, 1113–1119.
71. G. Perseghin, P. Scifo, F. De Cobelli, E. Pagliato, A. Battezzati, C. Arcelloni, A. Vanzulli, G. Testolin, G. Pozza, A. Del Maschio, L. Luzi, *Diabetes*, 1999, **48**, 1600–1606.
72. A. Virkamäki, E. Korsheninnikova, A. Seppala-Lindroos, S. Vehkavaara, T. Goto, J. Halavaara, A. M. Hakkinen and H. Yki-Järvinen, *Diabetes*, 2001, **50**, 2337–2343.
73. V. R. Edgerton, J. L. Smith and D. R. Simpson, *Histochem. J.*, 1975, **7**, 259–266.
74. W. Scott, J. Stevens and S. A. Binder-Macleod, *Phys. Ther.*, 2001, **81**, 1810–1816.
75. J. H. Hwang, J. W. Pan, S. Heydari, H. P. Hetherington and D. T. Stein, *J. Appl. Physiol.*, 2001, **90**, 1267–1274.
76. K. B. Henriksson-Larsen, J. Lexell and M. Sjostrom, *Histochem. J.*, 1983, **15**, 167–178.
77. K. Brechtel, J. Machann, S. Jacob, A. Strempfer, F. Schick, H. U. Häring and C. D. Claussen, *Fortschr. Röntgenstr.*, 1999, **171**, 113–120.
78. C. Boesch and R. Kreis, *Ann. N.Y. Acad. Sci.*, 2000, **904**, 25–31.
79. D. E. Larson-Meyer, B. R. Newcomer and G. R. Hunter, *Am. J. Physiol. Endocrinol. Metab.*, 2002, **282**, E95–E106.
80. P. Zimmet, K. G. Alberti and J. Shaw, *Nature*, 2001, **414**, 782–787.
81. J. H. Warram, B. C. Martin, A. S. Krolewski, J. S. Soeldner and C. R. Kahn, *Ann. Intern. Med.*, 1990, **113**, 909–915.
82. G. I. Shulman, *J. Clin. Invest.*, 2000, **106**, 171–176.
83. G. R. Dagenais, R. G. Tancredi and K. L. Zierler, *J. Clin. Invest.*, 1976, **58**, 421–431.
84. P. J. Randle, P. B. Garland, C. N. Hales and E. A. Newsholme, *Lancet*, 1963, **281**, 784–789.
85. D. E. Kelley and L. J. Mandarino, *Diabetes*, 2000, **49**, 677–683.
86. N. G. Forouhi, G. Jenkinson, E. L. Thomas, S. Mullick, S. Mierisova, U. Bhonsle, P. M. McKeigue and J. D. Bell, *Diabetologia*, 1999, **42**, 932–935.
87. K. Brechtel, D. B. Dahl, J. Machann, O. P. Bachmann, I. Wenzel, T. Maier, C. D. Claussen, H. U. Häring, S. Jacob, F. Schick, *Magn. Reson. Med.*, 2001, **45**, 179–183.
88. O. P. Bachmann, D. B. Dahl, K. Brechtel, J. Machann, M. Haap, T. Maier, M. Loviscach, M. Stumvoll, C. D. Claussen, F. Schick, H. U. Häring, S. Jacob, *Diabetes*, 2001, **50**, 2579–2584.
89. M. Krššák, M. Krebs, H. Stingl, V. Mlynarik, S. Gruber, E. Moser and M. Roden, *Proc. Intl. Soc. Magn. Reson. Med.*, 2000, **8**, 1883.
90. G. Boden, B. Lebed, M. Schatz, C. Homko and S. Lemieux, *Diabetes*, 2001, **50**, 1612–1617.
91. B. Wietek, C. Thamer, J. Machann, M. Haap, C. D. Claussen, H. Häring and F. Schick, *MAGMA*, 2002, **15**(Suppl. 1), 271–272.
92. K. Scheele, W. Herzog, G. Ritthaler and H. Weicker, *Eur. J. Appl. Physiol.*, 1979, **41**, 101–108.
93. M. Callow, A.and Morton and M. Guppy, *Eur. J. Appl. Physiol.*, 1986, **55**, 654–661.
94. B. F. Hurley, P. M. Nemeth, W. H., III, Hagberg, J. M. Martin, G. P. Dalsky and J. O. Holloszy, *J. Appl. Physiol.*, 1986, **60**, 562–567.
95. J. Achten, M. Gleeson and A. E. Jeukendrup, *Med. Sci. Sports Exercise*, 2002, **34**, 92–97.
96. R. S. Staron, R. S. Hikida, T. F. Murray, F. C. Hagerman and M. T. Hagerman, *J. Neurol. Sci.*, 1989, **94**, 29–40.

97. F. Brouns and G. J. van der Vusse, *Br. J. Nutr*., 1998, **79**, 117–128.
98. K. Brechtel, A. M. Niess, J. Machann, K. Rett, F. Schick, C. D. Claussen, H. H. Dickhuth, H. U. Häring and S. Jacob, *Horm. Metab. Res*., 2001, **33**, 63–66.
99. J. Rico-Sanz, J. V. Hajnal, E. L. Thomas, S. Mierisova, M. Ala-Korpela and J. D. Bell, *J. Physiol*., 1998, **510**, 615–622.
100. M. Kršsák, K. F. Petersen, R. Bergeron, T. Price, D. Laurent, D. L. Rothman, M. Roden and G. I. Shulman, *J. Clin. Endocrinol. Metab*., 2000, **85**, 748–754.
101. J. Decombaz, M. Fleith and H. Hoppeler *Eur. J. Nutr*., 2000, **39**, 244–247.
102. J. Rico-Sanz, M. Moosavi, E. L. Thomas, J. McCarthy, G. A. Coutts, N. Saeed and J. D. Bell, *Lipids*, 2000, **35**, 1313–1318.
103. J. Decombaz, B. Schmitt and M. Ith *Am. J. Physiol. Regul. Integr. Comp. Physiol*., 2001, **281**, R760–R769.
104. A. G. Engel, M. Yamamoto and K. H. Fischbeck, A. G. Engel and C. Franzini-Armstrong, eds., *Myology*, 2nd edn, McGraw-Hill, New York, 1994, 1130–1187.
105. P. A. Hertzman, W. L. Blevins, J. Mayer, B. Greenfield, M. Ting and G. J. Gleich, *New. Engl. J. Med*., 1990, **322**, 869–873.
106. F. Schick, S. H. Duda, H. Dürk, M. Bunse, O.and Lutz and C. D. Claussen, *Magn. Reson. Imaging*, 1994, **12**, 513–522.
107. M. Fardeau and F. M. S. Tomé, A. G. Engel and C. Franzini-Armstrong, eds., *Myology*, 2nd edn, McGraw-Hill, New York, 1994, 1522–1532.
108. S. Di Donato, A. G. Engel and C. Franzini-Armstrong, eds., *Myology*, 2nd edn, McGraw-Hill, New York, 1994, 1587–1609.
109. O. Bahr, I. Mader, J. Zschocke, J. Dichgans and J. B. Schulz, *Neurology*, 2002, **59**, 1802–1804.
110. M. Seip and O. Trygstad, *Acta Paediatr. Suppl*., 1996, **413**, 2–28.
111. O. Sovik, H. Vestergaard, O. Trygstad and O. Pedersen, *Acta Paediatr. Suppl*., 1996, **413**, 29–38.
112. A. Huebler, K. Abendroth, T. Keiner, W. Stoecker, E. Kauf, G. Hein and G. Stein, *Exp. Clin. Endocrinol. Diabetes*, 1998, **106**, 79–84.
113. K. Brechtel, S. Jacob, J. Machann, B. Hauer, M. Nielsen, H. P. Meissner, S. Matthaei, H. U. Häring, C. D. Claussen, F. Schick, *J. Magn. Reson. Imaging*, 2000, **12**, 306–310.
114. D. T. Stein, L. Szczepaniak, A. Garg, C. R. Malloy and J. D. McGarry, *Diabetes*, 1997c, **46**(Suppl. 1), A929.
115. A. J. Windebank and D. W. Mulder, A. G. Engel and C. Franzini-Armstrong, eds., *Myology*, 2nd edn, McGraw-Hill, New York, 1994, 1854–1869.
116. R. B. Moon and J. H. Richards, *J. Biol. Chem*., 1973, **248**, 7276–7278.
117. D. I. Hoult, S. J. B. Busby, D. G. Gadian, G. K. Radda, R. E. Richards and P. J. Seeley, *Nat. Lond*., 1974, **252**, 285–287.
118. W. I. Jung, S. Widmaier, U. Seeger, M. Bunse, A. Staubert, L. Sieverding, K. Straubinger, F. van-Erckelens, F. Schick, G. Dietze, O. Lutz, *J. Magn. Reson. B*, 1996, **110**, 39–46.
119. P. A. Mole, R. L. Coulson, J. R. Caton, B. G. Nichols and T. J. Barstow, *J. Appl. Physiol*., 1985, **59**, 101–104.
120. J. P. Mattei, G. Kozak-Ribbens, M. Roussel, Y. Le-Fur, P. J. Cozzone and D. Bendahan, *Biochem. Biophys. Acta*, 2002, **1554**, 129–136.
121. M. J. Avison, D. L. Rothman, E. Nadel and R. G. Shulman, *Proc. Natl. Acad. Sci. USA*, 1988, **85**, 1634–1636.
122. P. A. Bottomley, C. J. Hardy, P. B. Roemer and O. M. Mueller, *Magn. Reson. Med*., 1989, **12**, 348–363.
123. P. Bachert, M. E. Bellemann, G. Layer, T. Koch, W. Semmler and W. J. Lorenz, *NMR Biomed*., 1992, **5**, 161–170.
124. R. G. Shulman and D. L. Rothman, *Annu. Rev. Physiol*., 2001, **63**, 15–48.
125. W. Chen, G. Adriany, X. H. Zhu, R. Gruetter and K. Ugurbil, *Magn. Reson. Med*., 1998, **40**, 180–184.

Quality Assessment of Horticultural Products by NMR

B. P. HILLS[1] and C. J. CLARK[2]

[1]*Institute of Food Research, Norwich Research Park, Colney, Norwich NR4 7UA, UK*
[2]*HortResearch, Ruakura Research Centre, Private Bag 3123, Hamilton, New Zealand*

ANNUAL REPORTS ON NMR SPECTROSCOPY
VOLUME 50 ISSN 0066 4103
DOI 10.1016/S0066-4103(03)50002-3

The potential for developing NMR as an on-line sensor of the internal quality of fruits and vegetables is discussed. The literature on the NMR of horticultural products is first surveyed for potentially useful correlations between NMR characteristics and internal quality factors in commercially important harvested products. This is followed by discussions on the cellular origins of these correlations and of the technical problems to be overcome in the development of a commercial on-line NMR sensor.

1. INTRODUCTION

NMR spectroscopy and imaging have been applied widely to most parts of plant systems and the literature has been reviewed.[1–4] Although a majority of these publications are purely academic in nature and focus on issues such as plant development and physiology, a significant number also highlight correlations between NMR parameters and internal quality factors that could have commercial importance in the fruit and vegetable sectors of the food industry. The size and importance of this market should not be underestimated. In the United States alone, the fruit and vegetable industry generates over $6 billion in income annually and there is a constant demand for new sensors of fruit and vegetable quality. For this reason a number of research groups are seeking to exploit NMR-quality correlations on a commercial basis by developing low-cost NMR sensors for sorting fruit and vegetables on industrial conveyor belts. This review aims to assist this endeavour by gathering together these potentially useful NMR-quality correlations from the much larger literature on the NMR of horticultural products. This is followed by a brief summary of some of the challenges involved in developing low-cost, on-line NMR sensors for exploiting these NMR-quality correlations.

The motive for developing commercial NMR sensors of horticultural products hardly needs to be laboured. Consumers expect their fruit and vegetables to be of consistent high quality, at optimum ripeness, juiciness and texture and, of course, free from bruises, disease, infestation and other internal quality defects. Unfortunately for the fruit or vegetable grower, many of these quality factors are outside their control. Factors such as the weather, harvesting conditions and natural biological diversity mean that the quality of

fruits and vegetables is variable. Off-season fruit coming out of long-term cold storage show particularly high degrees of quality variation because of the progressive development of bruises, fungal infections, chill damage, and over-ripeness. For this reason most fruits and vegetables need to be examined and sorted before transportation, sale or processing. Of course the quality criteria used to sort and grade horticultural products depends on the nature of the sample. Consider the situation with apples. Before sale as fresh packs, apples are sorted on conveyors according to their size, shape, and colour as well as their degree of ripeness, as judged by their hardness. Shape, size and colour sorting can be done with fully-automated optical sensors arrayed across the moving conveyor belt. The degree of hardness can also be determined fully automatically by tapping each apple with fast bellows-type sensors[5] after the apples have been singulated (placed in single-file conveyor lines). However, attempts to determine internal quality defects such as bruises, watercore, worm damage, mealiness, and degree of ripeness, as defined by acidity and soluble solids content (the Brix value), on-line with automated sensors have met with only marginal success. In principle on-line Near Infra-Red (NIR) sensors can determine the Brix and acidity factors but they suffer from poor reliability, the need for frequent recalibration and expensive technology.[6] Mealiness, which results from a breakdown of cellular adhesion in the parenchyma tissue, is an internal quality defect that is prevalent in several apple varieties, but no on-line sensor has yet been developed to detect it reliably. The lack of suitable sensors for internal quality has meant that many sorting and packing facilities employ small armies of people to try to grade out as many bruised and damaged apples as possible as they move at speed down the conveyor lines. This is a wearisome and repetitive task, made difficult by the noisy environment. Not surprisingly, staff turnover is high. The cost and inefficiency of such manual sorting is an additional economic motive for researching novel types of internal quality sensor, and being non-invasive and sensitive to internal quality attributes, NMR sensors are prime candidates. What has been said for apple sorting also applies to many other horticultural products and the aim of this review is to survey the NMR horticultural literature for other potentially useful correlations.

With a few exceptions to be discussed, all the NMR-quality investigations listed in this review have been undertaken with commercially-available NMR equipment on stationary samples, and generally, the time taken to collect the data was not an important consideration. Nevertheless, choice of the fastest possible pulse sequences, the degree of image resolution required to identify a particular disorder, and the impact of motion on image quality and relaxation processes will be important considerations when introducing NMR for samples moving on conveyors. For this reason we briefly review some of the technical hurdles to be faced in the development of on-line NMR sensors of internal quality. Although continuous motion of the samples through the spectrometer on conveyors at speeds of 1 or 2 m/s greatly

complicates NMR acquisition protocols, motion *per se*, is not expected to significantly alter the relationship between intrinsic tissue parameters, such as relaxation and diffusion rates, and quality factors such as brix, acidity, or tissue damage. A more serious limitation is the magnetic field strength used in some of the cited literature. It is very unlikely that expensive high-field (1–7 T) superconducting magnets will ever be used in a packhouse environment as the basis of a sensor to sort fruits and vegetables, yet many of the measurements reported here have been made with superconducting magnets. It remains to be researched whether the correlations established at high-field also pertain to low-fields, where chemical shift and magnetic susceptibility differences are smaller and signal/noise may be problematic. In this context the paucity of NMR field cycling relaxation studies of horticultural products is particularly noticeable. The field-dependence of the longitudinal relaxation time, T_1, is of both fundamental and commercial interest. From the fundamental science perspective the spectral densities measured by NMR field cycling offer unique insight into the dynamic state of water and biopolymers in plant tissue; while from the commercial viewpoint, choosing the optimum field strength for maximum image contrast and quality assessment is vital.

Of course, the motive for working at high-fields, (>0.5 T), is that the associated high signal/noise permits high-resolution microimaging of various plant tissues. The same high-field strength enables chemical shifts to be resolved either in non-spatially-resolved high resolution spectra or in spatially-resolved chemical shift images which reveal the distribution of metabolites, lipids and carbohydrates present at concentrations much lower than that of the more mobile water molecules which are, of course, the principal proton-containing species stimulated by the NMR process. These high-resolution morphological and histochemical studies extend the range of products examined by MRI, but do not address quality issues pertinent to commercially-relevant quality factors. They have therefore, for the most part, been excluded from consideration in this review. In a similar manner, the numerous references where NMR is used to follow the effects of processing operations such as freezing and drying on horticultural products will, for the most part, be excluded unless they are relevant for potential exploitation in an on-line situation. The interested reader will find useful background material on these other aspects in the book of one of the authors,[7] as well as those of McCarthy[8] and Ruan.[9]

2. NMR QUALITY ASSURANCE OF HARVESTED FRUIT

Since the seminal papers in the late 1980s announcing the ability of MRI to detect quality disorders in fruits and vegetables[10,11] the range of disorders investigated has extended remarkably. The literature to the end of 1999 relating

Table 1. Summary of references to NMR studies of quality factors in the major types of fruit and vegetables

Product	Maturity	Bruises/voids	Tissue breakdown	Heat and Chill injury		Infections
				Heat	Chill	
Fruit						
Apple	13, 14, 15	11, 14, 15, 23, 24	10, 14,15, 25, 26, 27, 28, 29, 30, 31, 32, 33,34	–	–	–
Avocado	35, 36, 37	–	–	–	–	–
Banana	40	–	–	–	–	–
Cherimoya	79	–	–	–	–	–
Durian	49, 50, 51	–	49	–	–	–
Kiwifruit	52	–	–	–	53, 54	–
Mandarin	56	–	–	–	–	57
Mango	51, 58, 59, 60	–	–	61, 62	–	–
Mangosteen	49	–	49	–	–	–
Melon	63, 64	63, 64, 65	66	–	–	–
Nectarine	36	–	67	–	–	68
Orange	36	–	11	–	–	–
Papaya	69	–	–	69	–	–
Peach	–	–	67	–	–	–
Pear	51	11	70, 71	–	–	–
Persimmon	–	–	–	–	72, 73	–
Pineapple	64	–	11	–	–	–
Sapota	78	–	–	–	–	–
Tangerine	82	82	82	–	–	–
Berries						
Blueberry	46	–	–	–	46	–
Grape	44, 45, 77	–	–	–	–	–
Strawberry	42, 43	42, 43	–	–	–	42, 43
Small, stone fruit (*drupes*)						Pit detection
Cherry	77	–	–	–	–	74
Olive	–	–	–	–	–	75
Plum/prune	76	–	–	–	–	–
Vegetables						
Potato	89	92	92			85, 86, 87
Squash					93, 94, 95	64
Tomato	11, 59, 96, 97, 98					

to internal defects and storage disorders has been summarized by Clark *et al.*[1] and Koizumi *et al.*[12] The types of produce imaged and the quality disorders investigated are summarised in Tables 1–3. Each product listed in Table 1 will be discussed in Section 2.1.

Table 2. NMR methodology used to study quality attributes or disorders in fruit

Product	Attribute/Disorder	Field strength (Tesla)	Methodology	Ref.
Apple	Bruising	2	se imaging	11
	Bruising	2	se, ge imaging	23
	Bruising	4.7	se imaging	24
	Internal browning	1.5	se imaging	25
	Internal browning	0.6	T_1, T_2, PD (se mapping)	26
	Internal browning	0.13	T_2-CPMG	27
	Mealiness	4.7	T_2 (se mapping)	32,33
	Mealiness	2.3	T_2	34
	Superficial scald	4.7	se imaging	31
	Watercore	1.5	se imaging	28
	Watercore	0.5	se imaging	29
	Watercore	0.5	se imaging	10
	Watercore	0.13	T_2-CPMG and PFGSE	14
	Ripeness (Brix)	0.13	T_2-CPMG and D_w	14,15
Avocado	Dry matter	2	se imaging; MRS-T_1, IR; T_2-se. Use of surface coils	35
	Dry matter	2	FID, fruit moving over surface coil at 0–250 mm/s	37
	Dry matter	0.13	FID T_2-CPMG	36
Banana	Ripening		T_2-CPMG, D_w	40
Cherimoya	Maturity	4.7	T_1-IR, T_2-se imaging	79
Durian	Maturity-rots	0.5	se imaging	49
	Maturity (?)	2	FID spectrum from surface coil, at speeds up to 300 mm/s.	51
Kiwifruit	Sugar content	Earth's field	FID T_1 and T_2	117
	Maturity	2	T_1, T_2 (se mapping)	52
Mandarin	Maturity	4.7	T_1, T_2, PD (se mapping)	56
Mango	Heating injury	4.5	se imaging	61
	Insect infestation	4.5	se imaging	1
	Maturity	4.5	T_2 (se mapping)	62
	Maturity (?)	2	FID spectrum with surface coil, speeds up to 300 mm/s	51
Mangosteen	Maturity-rots	0.5	se imaging	49

(*Continued*)

Table 2. Continued.

Product	Attribute/Disorder	Field strength (Tesla)	Methodology	Ref.
Melon	Internal necrosis	2.0	se and ge imaging	64
	Sugar content (water suppression)	4.7	single pulse and IRFT	13
Nectarine	Woolly breakdown	0.5	se, ge imaging	67
	Fungal infection	4.7	T_1, T_2, PD (se mapping)	68
Orange	Dehydration	2	se imaging	11
	Sugar content	0.13	FID, T_2-CPMG	36
Papaya	Heating injury	1.5	se T_1-, T_2-, PD-weighted imaging	69
Peach	Bruising	2	se imaging	11
	Bruising	2	se imaging	64
	Mealiness	4.7	T_2 (se mapping)	32
Pear	Bruising	2	se imaging	11
	Core breakdown	0.5	se imaging	70
	Core breakdown	4.7	T_1-weighted se imaging	71
	Firmness (?)	2	FID spectrum with surface coil, speeds up to 300 mm/s	51
Pineapple	Maturity	2	se imaging	11
	Ripening	2	T_2 se mapping	64
Tangerine	Quality disorders	0.5	se imaging	82
Watermelon	Void detection	0.5	1-D projection profiles on static samples	65
	Sugar content	0.5	T_1 and T_2 volume-selected	63
	Void detection	0.5	se imaging at speeds up to 350 mm/s	63
Berries				
Blueberry	Freezing effects	7.1	T_1-Null imaging	46
Grape	Sugar content	0.2	FID T_2-CPMG	77
Strawberry	Fungal infection	4.7	IR se imaging; T_1-, PD-weighted imaging	42
Small, stone fruits (drupes)				
Cherry	Quality evaluation (pits)	2	1-D se imaging projections	74
Cherry	Sugar content	0.2	FID T_2-CPMG	77,115
Olive	Quality evaluation (pits)	2	1-D se imaging projections at speeds up to 250 mm/s	75
Plum (prunes)	Sugar content	2	FID spectrum with surface coil	76

Abbreviations: D_w, self-diffusion coefficient; ge, gradient-echo; IR, inversion recovery; IRFT, inversion recovery fourier transform; MRS, magnetic resonance spectroscopy; PD, proton density; PFGSE, pulsed field gradient spin echo; se, spin-echo.

Table 3. NMR methodology used to study quality attributes or disorders in vegetables

Product	Attribute/Disorder	NMR field strength (Tesla)	Methodology	Ref.
Courgette/ Zucchini	Chill injury	4.7	T_1 and T_2 weighted se imaging	93
Cucumber	Pathogen invasion	2	se imaging	64
	Chilling injury	0.6	T_1 se mapping	95
Onion	Bruising	2	se imaging	11
Potato	Disease	7	se, ge imaging	85–87
	Sensory texture	0.5	T_2	90
	Dry matter	7	T_1-IR, T_2-CPMG	89
	Hollow heart, brown core	4.7	se imaging, 1-D se imaging projections	92
Tomato	Maturity	2	se imaging	11
	Maturity	6.3	se imaging	97
	Maturity	6.3	T_1 (se mapping)	98
	Maturity	2	Se imaging	96
	Firmness	0.2; 0.6	MRI–se, ge; MRS–T_1 IR, T_2	59

Abbreviations: ge, gradient-echo; IR, inversion recovery; PD, proton density; se, spin-echo.

2.1. Apple

Sorting and grading apple varieties according to recognized quality criteria is of considerable commercial importance. In the UK alone, 102,200 tons of eating apples were grown in 2000–2001, worth an estimated £36 million, as well as 97,200 tons of cooking apples, worth £23 million. Nevertheless, apple quality has become a political issue recently with an article in the Times newspaper debating whether supermarkets have become too selective and fussy over the quality of apples on their shelves. Apparently, thousands of tons of apples grown in the UK are being dumped because they do not meet supermarket quality criteria and this has been compensated by the import of 599,000 tons of apples and pears worth £300 million into the UK in 2000. In the USA apple production was worth $1.1 billion in 1995, which emphasizes the size and importance of the market. Currently, internal defects are determined by random destructive sampling of apples from batches. High percentage defects result in the whole batch either being discarded or used for processing at a value less than a quarter of that for fresh, healthy produce. The need for on-line sorting of internal defects such as bruising, mealiness, browning and watercore is therefore paramount. We therefore begin with an NMR analysis of the degree of apple ripeness and then proceed to internal defects.

2.1.1. *Apple maturity*

Cho and co-workers[13] reported that the amplitude of the sugar proton peak following water suppression with a T_1 null sequence correlated well with the

sugar content in apples (as well as banana and muskmelon). This exploited the observation that the T_1 of exchangeable water protons was at least twice as long as that of the non-exchanging sugar protons, so a simple inversion recovery sequence with a delay time chosen to null the water signal, leaves a substantial positive sugar proton signal. The original experiments were undertaken at 4.3 T (200 MHz) so it remains to be investigated whether the signal/noise ratio of the sugar protons at much lower fields is sufficient to permit direct sugar concentration measurements and hence soluble solids content.

Keener and co-workers[14] have investigated the relationship between low-field (0.13 T; 5.4 MHz) apparent water proton diffusion coefficients (D_w), CPMG T_2s with a pulse spacing of 2 ms, and degree of ripeness (soluble solids content) as measured by refractometry. Measurements were not spatially resolved but undertaken on pieces of dissected apple tissue from three varieties ('Golden Delicious', 'Red Delicious' and 'Granny Smith'). Two studies were undertaken, the first in 1997,[15] then again in 1999.[14] Unfortunately only four apple samples were examined from each of the three varieties, and of these two were healthy and two bruised. The statistical significance of the results is therefore questionable. Nevertheless, the following trends were reported:

(a) In healthy 'Golden Delicious' and 'Granny Smith' apples the T_2 decreased with increasing soluble solid content (^{o}Brix) in healthy apples.
(b) The water diffusivity decreased with increasing soluble solid content in all samples, both bruised and healthy. This is no doubt a result of the increasing viscosity of more concentrated sugar solutions.
(c) Internal defects caused by bruising, watercore and internal browning resulted in a decrease in T_2 in all varieties at this low field strength. It remains to be seen whether T_1 also shows useful correlations with soluble solids and internal defects.

Although the decrease in T_2 with increasing sugar concentration might be expected because the same trend is observed in simple sugar solutions, the situation in apple tissue is rather more complicated. Ripening is associated with the hydrolysis of starch granules which causes an increase in sugar concentration. However starch granules themselves behave as relaxation sinks because they comprise semicrystalline amylopectin and an amylose matrix and there is fast exchange of water and starch hydroxyl protons. Their progressive hydrolysis during ripening reduces the number and size of the granules and this should result in an increase in relaxation time. However the effect is counteracted by the increasing sugar concentration but it should be remembered that the relaxation rate of a dissolved sugar solution depends sensitively on frequency and CPMG pulsing rate. In fact their relaxation behaviour can, in principle, be quantitatively predicted by the proton exchange model.[16] Whether ripening and the overall conversion of starch into sugar

increases or decreases the CPMG transverse relaxation rate of the tissue therefore depends on the spectrometer field strength and pulsing rate. There is clearly a need to explore this dependence in greater detail over a range of spectrometer frequencies.

It is worth bearing in mind that the transverse water proton relaxation behaviour of healthy apple tissue is actually multiple exponential. Standard exponential deconvolution packages such as CONTIN, or Non-Negative Least Squares (NNLS) approaches are able to fit a continuous distribution of exponentials to FID or CPMG decay curves, where the output is just a spectrum of transverse relaxation times.[17,18] The difficulty lies in interpreting these relaxation time spectra with physically meaningful models. This topic is discussed in more detail in Hills.[19] Up to three peaks have been reported in the distribution of water proton transverse relaxation times in parenchyma apple tissue measured with the CPMG sequence with a short 90–180° pulse spacing at 2.3 T (100 MHz).[20] These peaks have been assigned to vacuolar water and water associated with cytoplasm and cell wall. The effect of freezing and drying on this relaxation time spectrum have been modelled with a Numerical Cell Model with moderate success.[20] Such subcellular relaxation time investigations are extremely useful for understanding the cellular origins of image contrast in both healthy and defective tissue, and we shall return to this point in a later section.

2.1.2. *Apple bruises*

Image contrast between bruised and healthy tissue of 'Red Delicious' apples, peach, 'Twentieth Century' pear and white onion was first reported in 1989 by Chen and co-workers[11] who acquired spin-echo images in a 2 T (46 MHz) superconducting magnet Fig. 1. The bruises appeared as regions of higher intensity in the image, except for dehydrated, old bruises in apples where the lower water density resulted in a darker contrast. Not long after this seminal paper, the origin of image contrast in cellular tissue was investigated by Hills and related to the chemical and diffusive exchange of water protons in the subcellular compartments of the tissue.[21] This work culminated in the numerical cell model of water proton relaxation in cellular tissue.[20–22] The particular case of bruised apple tissue was investigated by McCarthy and co-workers.[23] Using a combination of spin-echo and gradient reversed echo imaging in a high-field magnet at 1.4 T, they showed that the redistribution of intracellular and extracellular water arising from cell and membrane damage in the bruised region actually results in a decrease in the mean transverse relaxation rate, T_2, as measured by the CPMG sequence. This established that the enhanced image intensity at high-fields could not be a result of intrinsic T_2 changes. Instead the enhanced brightness was attributed to a reduction in the signal attenuation arising from water diffusing through internal magnetic field gradients created by the magnetic susceptibility difference between air in extracellular spaces and cellular fluid. This is an important observation because

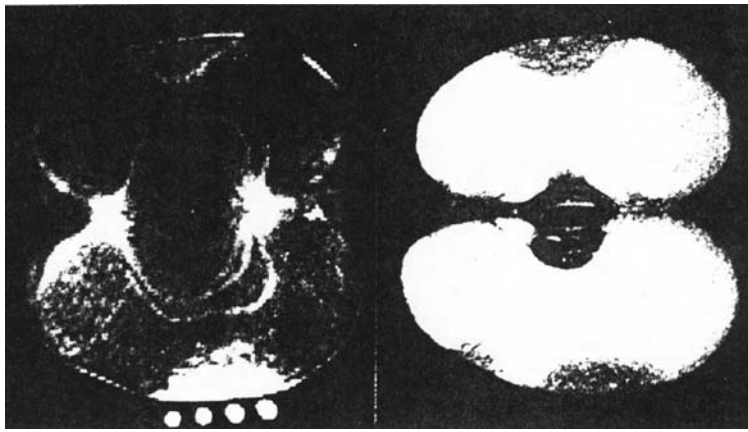

Fig. 1. (Left) MR image of bruises (white area on top and bottom) in 'Red Delicious' apples. (Right) The corresponding optical micrograph. Reprinted with permission from Chen *et al.*[11]

the effect of internal gradients on the effective relaxation rate is expected to vary as the square of the applied field as well as on the pulse spacing. Reducing the field strength to say 0.14 T (a proton frequency of ca. 6 MHz) would be expected to reduce the effect of the internal gradients on the relaxation rate by at least two orders of magnitude, so that bruises in a low-field imaging system could actually appear with lower rather than higher intensity. This prediction remains to be investigated but highlights the importance of repeating the NMR-internal quality correlations over a range of frequencies, especially the low-field range. The measurements of CPMG-T_2 of bruised and healthy tissues by Keener and co-workers[14,15] at 5.4 MHz confirmed that T_2 measured with a pulse spacing of 2 ms was less in bruised tissue than in healthy apples but whether susceptibility effects will control the contrast in spin-echo images at these low fields remains to be explored. It should also be noted that the observed changes in apple may not be representative of bruising in other types of fruit. Apple is unusual in having a high percentage of intercellular gas space (ca. 20%). This should be compared with fruit such as kiwifruit, which has only 2% gas space, so susceptibility effects may not always be the dominant effect. The extent of the gas spaces in apple tissue can even be seen in the optical micrograph in Fig. 3.

The importance of the image processing step in automated sensing of quality factors was emphasized in an important paper by Zion and co-workers.[24] While the human eye and brain are adept at image processing and can readily distinguish a bruised region from, for example, the vascular system in a three dimensional image of an apple, it is necessary to develop fast image processing algorithms to do this job in an automated on-line context. With images of bruised apples acquired at high-field, it is necessary to distinguish high intensity

Table 4. NMR characteristics of normal, and light and dark brown tissue in 'Fuji' apples subjected to different storage conditions[26]

Tissue	T_1 (ms)	T_2 (ms)	Proton density (arbitrary units)
Storage: 9 days at 20 °C and 18% CO_2			
Normal	1337 ± 64.3	54 ± 4.7	1361 ± 93.2
Light brown	1082 ± 112.5	37 ± 7.3	1117 ± 31.9
Dark brown	1139 ± 95.7	230 ± 21.9	1057 ± 36.2
Storage: 91 days at 0 °C and 3% CO_2			
Normal	1661 ± 55.6	57 ± 3.9	1723 ± 72.5
Light brown	1295 ± 93.3	40 ± 5.5	1184 ± 163.0
Dark brown	981 ± 71.6	271 ± 28.3	1117 ± 79.2

voxels in the bruised region from those of the vascular system of the tissue. This was achieved using a simple threshold technique combined with considerations of apple geometry.

2.1.3. *Internal browning disorders in apples*

Internal browning disorder manifests itself as brown patches throughout the cortex and core. The disorder is induced by high CO_2 concentrations, especially during storage in modified atmospheres, but can also appear in unpicked fruit on the tree. As its name implies, the brown patches are not visible from the outside but give contrast in MRI spin-echo images at high-field. The first qualitative images of this disorder were reported in 1999 and were acquired at 1.5 T using a standard multislice Hahn spin-echo imaging sequence with an echo time of 40 ms and a repetition time of 1 s. The brown patches showed up as regions of high intensity, though the reasons for this were not investigated.[25] Subsequent quantitative spin-echo image mapping by Gonzalez and co-workers[26] at a lower field of 0.6 T distinguished light and dark brown regions and succeeded in measuring their associated NMR parameters (Table 4). The light brown regions had a lower signal intensity than normal tissue because of a reduced proton density and a shorter T_2. Dark brown regions had higher intensity than normal tissue because of a longer T_2. In contrast, by placing whole fruit in a 0.13 T permanent magnet, Jung *et al.*[27] demonstrated that the average T_2-CPMG values of apples with internal browning gradually *decreased* with increasing severity of internal browning. Unfortunately the role of magnetic susceptibility differences was not investigated in any of these studies nor the physiological basis for the differences, so much research remains to be done in understanding this disorder.

2.1.4. *Watercore in apples*

In normal apple tissue the intercellular spaces are ordinarily filled with air. However, in watercore-affected tissue, the air is replaced by water (or more

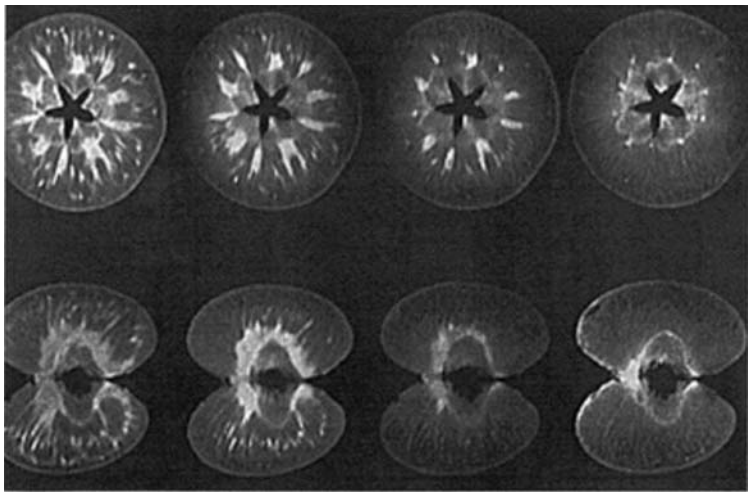

Fig. 2. MR images of 'Fuji' apples with watercore symptoms. Images from left to right depict the progressive disappearance of watercore during storage. From Clark and Bieleski.[30]

precisely, a sorbitol solution) giving the cut tissue a translucent watery appearance. Watercore is associated with elevated water content and decreased reducing sugars. The disorder mostly occurs late in the growing season in over-mature unpicked fruit and cannot be visibly detected in the intact fruit. The higher water proton density in the affected tissue gives a higher image intensity, allowing watercore to be readily identified, even at a moderate field of 0.5 T.[10] Keener and co-workers[14,15] later reported that watercore resulted in a decrease in T_2 at the low field of 0.13 T, which should result in a decreased image intensity. The fact that the affected tissue gives a higher intensity signal therefore supports the idea that the increase in water proton density dominates the image contrast at low fields. Clark and co-workers have undertaken MRI studies of watercore amelioration in 'Braeburn' apples at 1.5 T.[28] They used image analysis to monitor the time course of watercourse dissipation but made no attempt to quantify the relationship between watercore and NMR relaxation or diffusion behaviour. Such relationships will need to be reinvestigated at low field strengths if the potential of on-line MRI sensors for watercore detection is to become a reality. Loss of watercore in 'Fuji' apples has also been studied by NMR (Fig. 2).[29,30]

2.1.5. *Superficial scald in apples*

This is a visible storage disorder in apples arising from the loss of water from a region associated with hypodermal cells located 200–600 μm below the skin surface. The lower water content gives a loss of signal intensity in MRI images of the affected region.[31] The fact that the disorder is a visible surface defect in

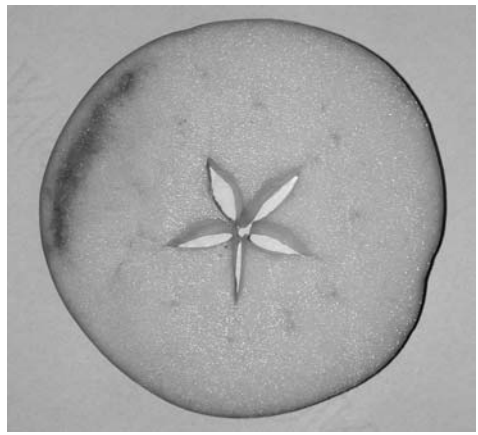

Fig. 3. Optical micrograph showing Gorgate Syndrome in apples. Courtesy of Dr. Mary Parker, IFR, Norwich, UK.

the peel means that on-line MRI scald detection is merely an added bonus not the main rationale for using NMR. However, a related disorder has been recognized in some apple varieties. It is a browning at the calyx underneath a healthy layer of tissue just under the skin. It has been called Gorgate Syndrome after its discovery in 1992 in apples from an orchard in the Gorgate Estate in Kent. Apparently it is a widespread disorder of economic significance, but has not been investigated by NMR as yet. Figure 3 shows an optical micrograph of the disorder.

2.1.6. *Mealiness in apples*

Mealiness in apples results from a breakdown in adhesion between cells so that chewing the apple tissue results in cell separation rather than cell rupture. Eating a mealy apple is therefore associated with the unpleasant sensory perception of a lack of juiciness, loss of crispness and hardness. A number of studies have succeeded in correlating the degree of mealiness with destructive reference tests such as the Magness-Taylor firmness and confined compression juiciness, but clearly there is a need for non-destructive, on-line detection of mealiness in apples.

The first significant correlations between NMR measurements and mealiness were reported by Barreiro and co-workers[32,33] who found that the histogram of T_2 values (i.e., the number of pixels having a particular T_2) for mealy apples was skewed to shorter relaxation times with a significant tail located in the maximum T_2 range (Fig. 4). In contrast, non-mealy apples had normal, non-skewed T_2 histograms. While this observation is interesting, it is, unfortunately, of little practical relevance for on-line detection of mealiness because the measurements were undertaken using a high-field imaging system operating at 4.65 T, and required acquisition of 20 spin-echoes for each image

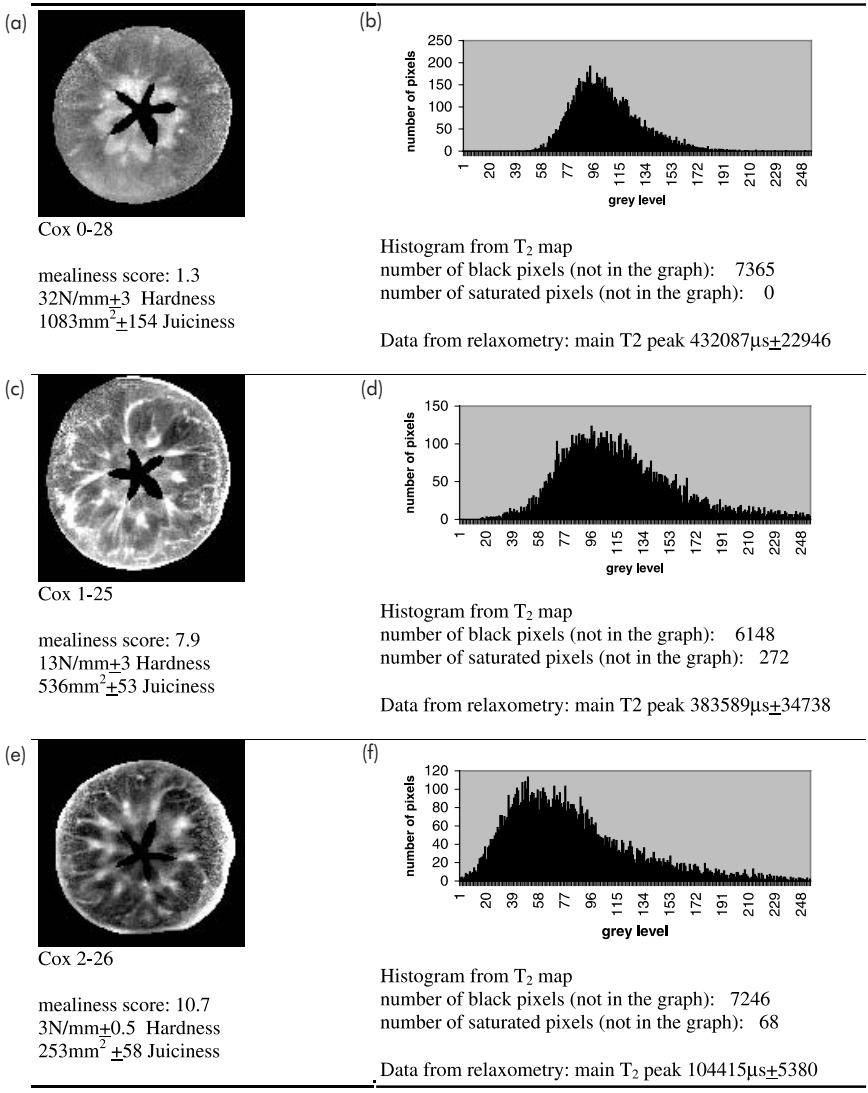

Fig. 4. (a) Image of 'Cox's' apple labelled 0–28 with a mealiness score of 1.3; (b) histogram from the T_2 map of the apple in (a); (c) image of 'Cox's' apple labelled 1–25 with a mealiness score of 7.9; (d) histogram from the T_2 map of the apple in (c); (e) image of 'Cox's' apple labelled 2–26 with a mealiness score of 10.7; (f) histogram from the T_2 map of the apple in (e). From Ref. 34.

to extract a T_2 map and histogram. More recently, increasing mealiness has been shown to cause a systematic reduction in the non-spatially resolved CPMG-T_2 values undertaken at the slightly lower field of 2.32 T.[34] The relaxation times were then correlated with mealiness using multivariate PLS

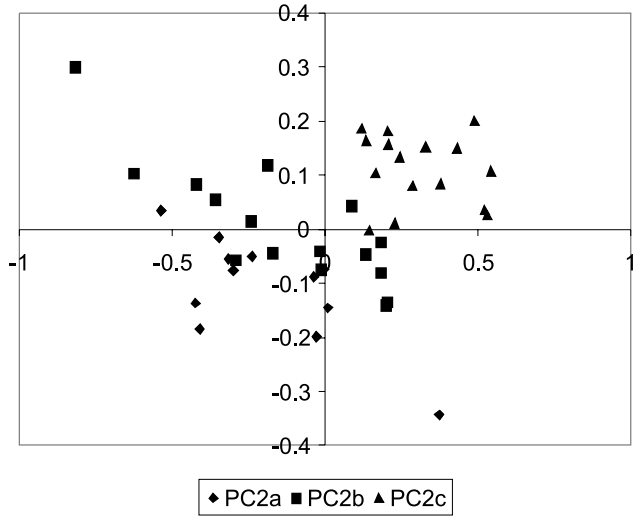

Fig. 5. Discriminant PLS analysis of NMR time domain CPMG data acquired at 100 MHz versus mealiness in 'Cox's' apples having three degrees of mealiness and labelled (Coxa, Coxb and Coxc), acquired in the data for Ref. 34.

analysis (Fig. 5). It can be seen that this succeeds in discriminating among apples with three levels of mealiness (as measured by sensory and hardness tests). This is a promising result but it remains to be investigated whether useful correlations will also be found at the much lower fields relevant to on-line NMR sensors.

2.2. Avocado

2.2.1. *Avocado maturity*

Unfortunately there are no visible external changes in avocado to indicate its maturity but it has been shown that increasing oil content and decreasing water content correlate closely with sensory measures of maturity and that the oil content correlates well with the increasing dry weight during maturation. The relationship between NMR parameters and oil content and/or dry weight in avocado has been investigated by MR techniques.[35,36] Working at a high-field of 2 T (85 MHz) Chen and co-workers showed that the T_1 and T_2 of water decreased linearly with increasing dry weight with correlation coefficients, R^2, of 0.58 and 0.51, respectively. T_1 for water in avocado during maturation typically varies from 1.0 to 0.4 s. No change in the relaxation times of the oil component were found. Of course, the ratio of the oil–water peak heights in the single pulse spectrum correlated well with the dry weight giving an R^2 of 0.92.

Unfortunately, the chemical shift difference between the oil and water peaks, ca. 3.5 ppm, sets a lower limit on the field strength and an upper limit on the sensor field inhomogeneity which can be tolerated in low cost on-line sensors. The relaxation time correlations may therefore eventually prove to be the most useful. In later work[37] at the same field strength but with a surface coil and with avocados moving on a conveyor it was shown that the linear correlation between the oil–water peak ratio and percentage of dry matter was robust at least up to speeds of 0.3 m/s. Unfortunately, typical industrial conveyor speeds can be about 1 or 2 m/s so, while suggestive, industrially-useful correlations have still to be established. It is also noteworthy that, because the surface coil samples only a small part of the fruit, the avocados were always positioned with the stem end facing the direction of travel. Whether such good correlations would be maintained with randomly oriented fruit on an industrial conveyor remains to be seen. More recent chemical shift imaging work from the same group has shown that there is strong spatial variation in the oil–water ratio throughout the avocado.[38] The oil–water ratio is lower near the skin and increases towards the seed. It is also large along the middle ring of flesh near the seed. Whether the oil and water signals can be separated by T_1 null methods remains to be investigated but would alleviate the requirements for high-field homogeneity.

2.2.2. *Fungal infections in avocado*

Post-harvest rots of avocado caused by fungal infection are an important but unsolved problem in quality control. Even with optimized post-harvest storage regimes about 20% of 'Hass' avocado were found to be infected by post-harvest rots in New Zealand.[39] It is therefore surprising that no NMR/MRI investigations appear to have been reported on this quality factor.

2.3. Banana

The changes in CPMG-T_2 and apparent water self-diffusion coefficients, D_w, during the ripening of banana have been investigated Raffo and co-workers.[40] Following the methodology of earlier work on apple[20] and potato tissue[41] the CPMG echo decays for banana were deconvoluted into three components corresponding to cellular, cytoplasmic and vacuolar water. It was then found that the cytoplasmic and vacuolar water T_2s showed significant increases from 90 to 190 and 320 to 610 ms, respectively over 7 days storage. The changes were explained as the progressive enzymic hydrolysis of starch granules during ripening. Measurements were undertaken on a Bruker minispec operating at 0.47 T (20 MHz), which suggests that similar correlations should be useful in on-line situations. There do not appear to be other reports of the effects of physiological disorders or bruising on NMR characteristics for bananas.

2.4. Berries

It is debatable whether on-line NMR sensor technology is appropriate for on-line sorting of small fruit such as strawberries and grapes. There is no doubt that NMR microscopy has provided invaluable insight into the development and physiology of such fruit, but these are unlikely to be examined one-by-one in single file through a sensor magnet. It is conceivable that whole bunches or pallets of the fruit could be imaged in stationary mode on conveyors, but whether this would ever be commercially viable remains to be investigated. We therefore include this category of fruit with the reservation that the off-line studies may never be exploited commercially in an on-line sense.

A number of groups have studied strawberry physiology with high-field microimaging. Using a 4.7 T (200 MHz) instrument, Maas and Line[42] have imaged bruised strawberries as well as those infected with *Botrytis cinerea, Colletotrichum acutatum* and *Phytophthora cactorum*. A more detailed study has been reported by Goodman and co-workers.[43] Like bruised apple tissue, the redistribution of water accompanying bruising resulted in brighter intensity in spin-echo images of bruised regions compared to healthy tissue. Infection also caused contrast changes, with water proton densities usually greater, and T_2s longer, in lesions. The mean T_2 of unripe, green strawberries (ca. 16–20 ms) is also significantly shorter than that of ripe red strawberry (ca. 21–100 ms). The relative magnitudes of T_1 between vascular and parenchyma tissue also changed with ripening. The distribution of sugar in grapes and blueberries during ripening and freeze-thawing has also been imaged at high-field.[44–46] Goodman and co-workers using spin-echo and gradient-echo microimaging have also studied the time course of *Botrytis* infection in raspberry and blackcurrant.[47,48]

2.5. Durian

2.5.1. *Durian maturity*

Durian is one of the most commercially important fresh fruits in S.E. Asia, yet sorting immature from mature fruit by external measures is very difficult, so it is a prime candidate for non-invasive methods. Yantarasri and co-workers[49,50] have sought correlations between soluble solids and sensory estimates of maturity with X-ray CT and NIRS measurements with moderate success but more recently they observed that MRI spin-echo image contrast at 0.5 T varied with the degree of maturity. Unfortunately no attempt was made to quantify relaxation time changes or separate oil–water peaks. However it was suggested that the contrast differences indicated significantly lower oil content in unripe durian compared to the ripe and overripe fruit.

The feasibility of on-line quality detection of durians, as well as mango and pear, was investigated by Kim and co-workers at UC Davis.[51] They used a surface coil and a superconducting 2 T horizontal bore magnet with a conveyor system to carry the fruit through the magnet at controlled speeds. Three spectral peaks were observed for durian, corresponding to water, oil and sugar and it was shown that increased speeds up to 0.3 m/s caused only a slight decrease in peak magnitude. This is a useful result, but it is debatable whether a 2 T magnet system is commercially viable and whether useful results would still be obtained at higher speeds up to 1 or 2 m/s.

2.5.2. *Durian watercore*

Watercore in durian is usually associated with a bitter taste and unacceptable fruit quality so the ability of MRI to detect this condition is significant. The watercore disorder shows up as a bright region of increased free water near the central core of the fruit;[49] not a dissimilar observation to that of Wang and co-workers[10] with watercore in apples.

2.6. Kiwifruit

2.6.1. *Kiwifruit maturity*

A quantitative imaging study on kiwifruit fruit focused on the changes in relaxation time and diffusion maps in kiwifruit as they ripened.[52] Measurements were made at 2 T (86 MHz) and T_1, T_2 (spin-echo) and T_2^* (gradient-echo) maps were reported over a 30-day ripening period. It was shown that all relaxation times show significant *increases* during ripening, especially in the flesh and locule regions. The increase in relaxation times during ripening appears to contradict the observed increase in free and total sugars in the tissue, which increased between 100 and 300% and would have been expected to *decrease* the relaxation times. Here again, the most probable explanation is the progressive hydrolysis of the large amount of starch granules in the unripe tissue, though this hypothesis remains to be tested.

2.6.2. *Frost damage and rots in kiwifruit*

Kiwifruit typically requires 25 weeks from anthesis to reach a level of physiological maturity such that it can be removed from the vine and still continue to ripen.[52] This long maturation period increases the likelihood that both immature and mature fruit are damaged by autumn frosts. Unless the damage is very severe, most frost damaged fruit shows no external visible symptoms, yet the frost damaged fruit subsequently develop abnormal and undesirable quality characteristics during storage. It is therefore important to be able to detect the frost damage as early as possible. The first qualitative MR images of New Zealand kiwifruit were reported in 1993 and established that

premature softening, frost damage and rot (*Botrytis*) lead to significant image contrast in spin-echo images.[53] Subsequently a more detailed MRI investigation of freezing effects has been reported by Kerr and co-workers,[54] using a wide bore, high-field, 7.1 T (303 MHz) imager. Picked fruit was frozen in a gas stream at $-40\,^{\circ}C$ and subsequently thawed and compared with fresh fruit. A treatment resulted in a reduction in the average T_2 from 312 ms in fresh kiwifruit to 208 ms in frozen-thawed fruit. The apparent water diffusion coefficient as measured by the PGSE sequence also increased after freeze-thawing, no doubt because of the breakdown in cell membrane and cell wall diffusion barriers. The reasons for the changes in relaxation behaviour are potentially more difficult to explain. Freeze-thawing a uniform gel creates a highly heterogeneous structure because the ice crystals melt into microscopic pools of water surrounded by more concentrated gel. In general this changes the single exponential transverse relaxation of a uniform gel into multiple exponential relaxation whose T_2 distribution depends on the size distribution of the ice crystals, which, in turn, depends on the rate of freezing and the nature of the matrix.[55] It would therefore be of interest to undertake a combined microscopic and multiple exponential CPMG analysis of the frozen-thawed tissue to investigate in more detail the microscopic origin of the apparent relaxation time reduction. The fact that there is a significant change does, however, bode well for the eventual on-line detection of frost damage in kiwifruit.

2.7. Mandarin

2.7.1. *Maturity*

Clark and co-workers[56] have reported quantitative MRI studies at 4.7 T (200 MHz) of satsuma mandarins as they matured during a 15-week period commencing 10 weeks after anthesis. T_1, T_2 and proton density maps were reported, but, curiously, showed no spatial gradients in the more mature fruit during the period of cell enlargement (10–25 weeks after anthesis). Changes in the relaxation times with maturation were found but showed no obvious correlation with independent measurements of pH, Brix, and sugar concentrations in expressed juice. It was surmised that the relaxation changes were being dominated by microstructural factors related to cell structure rather than the chemical composition of the cell fluids.

2.7.2. *Detection of seeds*

Spanish mandarins, mostly clementines, are seedless but cross pollination with new late hybrids such as ‘Fortune’ or ‘Nova’ has led to an increase in the number of seeds in the clementines and this loss of quality is adversely affecting exports. To try to identify the best pulse sequence for detecting the seeds, a

comparative study using spin-echo, half-spin-echo and gradient-echo sequences with varying acquisition parameters was undertaken by Blasco and co-workers[57] using a permanent magnet MRI system operating at 0.2 T. Thirteen 'Fortuna' mandarins (assumed to contain seeds) were imaged and compared with 13 'Reina' mandarins (assumed seedless). The images involved taking only three 5-mm slices with a gap of 2 mm across the centre of the fruit where the seeds are located. The mandarins were typically 5–7 cm in cross section. The results showed that the spin-echo sequence with short echo times and repetition times of 18 and 50 ms, respectively, gave the best seed–pulp contrast. Destructive testing confirmed that all seeds in these mandarins were detected by this protocol. Unfortunately the acquisition time of 7 s for a FOV of 160×160 pixels is too slow for detection of such fruit in a commercial grading situation. Nevertheless the results show the feasibility of future on-line applications.

2.8. Mango

2.8.1. *Maturity*

Apart from a recent 400 MHz high resolution study of mango juice during ripening[58] there does not appear to have been any systematic low-resolution or relaxation time NMR study of mango maturity. Kim *et al.*[59,60] recorded the FID-spectrum of a ripe mango at various conveyor speeds up to 0.3 m/s in a 2 T (85.5 MHz) system. At this relatively high-field it was still possible to distinguish separate sugar and water proton peaks with a 1 ppm separation but the broadening of the main water peak at higher conveyor speeds caused it to overlap with the sugar peak. The simple FID-spectrum is not therefore a viable candidate for on-line maturity measurement of mango. However, no attempt was made to use T_1-null methods to suppress the water peak and there do not appear to have been any systematic reports of correlations between NMR relaxation times and mango maturity. This is surprising because mango is the most significant commercial tropical fruit crop after banana but trade is being limited by significant post-harvest wastage due to the highly perishable nature of the fruit.

2.8.2. *Heat treatment injury*

To facilitate international export, mangos are usually disinfested from insect larvae by either chemical or heat treatment.[1,61] Unfortunately, heat treatments severe enough to kill the larvae can also damage the skin and pulp (mesocarp). Pulp symptoms include impaired starch degradation and development of internal cavities, which are manifest in MRI. Spin-echo image contrast showed[62] the initiation of heat injury around vascular traces in the mesocarp possibly because they form a network for rapid heat transfer and/or retain heat

longer than surrounding cells. Heat-damaged mesocarp tissue was revealed as a contrast darkening because transverse relaxation times are shortened, though the reasons for this are unknown. Heat treatment also resulted in eventual formation of air-filled cavities and islands of starchy mesocarp. Although there was no attempt to calculate spin-density or relaxation time maps and quantify the changes, the results show the potential for on-line detection of such heat damage.

2.9. Melon

2.9.1. *Melon maturity*

The legal minimum soluble solids content for harvesting melons is an average of 10%, based on the results of analysis of a specified number of fruit. Typical average values range between 11 and 14%. Perhaps the sweetest melon variety is 'Melody No. 2' which has an average soluble solids content of 15–16%. It should, however be noted that these are average values and although the sugar content in ripe melons is nearly constant throughout the central region extending radially from the centre to about a quarter of the diameter, it falls off rapidly at larger radial distances.[63] Typical soluble solids contents are 15% in the central region dropping to 6% near the skin. Saito and co-workers[63] used the relationship between water proton T_2 and sugar concentration to determine soluble solids content. The fast proton exchange between water and sugar-OH protons means that the relaxation rates are linearly proportional to sugar concentration. In fact the data was plotted as a linear relationship between soluble sugar content and decreasing water proton T_1 (and T_2) values, expressed as the linear regression

$$\text{Soluble solids content (\%)} = A - BT_1 - CT_2.$$

Clearly the coefficients A, B and C will depend on instrument factors such as the field strength, pulse spacing, and temperature as well as sample variety. It should, however, be noted that in pure sugar solutions the theoretical relationship is a linear increase in the relaxation *rate* with increasing sugar concentration and not between the relaxation times themselves. The fact that in many plant tissues, such as apples, and kiwifruit, the relaxation time *increases* with increasing sugar content suggests that it is actually the removal of starch granules by hydrolysis during ripening that is dominating the relaxation behaviour and not the sugar component. No attempt was made to use the T_1 null method to suppress the water signal and measure sugar concentrations directly.

Hall and co-workers[64] have imaged overripe melons suffering from internal necrosis with both spin-echo and gradient-echo sequences at 2 T (86 MHz).

The spin-echo images showed no obvious differences between ripe and overripe samples, but the gradient-echo images of the over-ripe melons showed decreased intensity. It was surmised that the increased air spaces in the overripe tissue intensified the internal magnetic susceptibility gradients, whose dephasing effects can be refocused by a spin-echo but not by a gradient-echo.

2.9.2. *Void detection in melons*

One-dimensional projection imaging has been successfully used to determine the presence of voids inside watermelons.[63,65] A simple spin-echo imaging sequence was used with a 0.5 T (21.5 MHz) superconducting horizontal bore magnet system on watermelons moving at speeds up to 0.35 m/s. Imaging times were 900 ms per sample which was considered to be commercially viable. Projections in two orthogonal directions were necessary to identify voids, which tended to be elongated in shape. A simple projection threshold algorithm was then used to categorize void size. Although this establishes the feasibility of MRI void detection it remains to be seen whether similar success is achieved with more rapidly moving samples because the degree of sample polarization then becomes limiting. The commercial viability of the imaging system may also be limited because the study used an expensive wide-bore self-shielded imager.

2.9.3. *Internal tissue breakdown in melons*

Internal tissue breakdown in melons such as Galia and Cantaloupe occurs around the seedbed and eventually results in collapse of the seed bed into a mixture of liquid, seeds and tissue pieces. Unfortunately this disorder does not affect the skin or hardness of the outer layers so cannot be detected by visual inspection. Preliminary reports from the Volcani Center in Israel[66] have shown that the tissue breakdown results in a small increase in T_2 from, typically, 35 to 45 ms and a corresponding increase in signal intensity in spin-echo projection images acquired with a 4.7 T (200 MHz) imaging magnet. There is therefore a reasonable possibility of being able to detect this disorder by on-line projection MRI.

2.10. Nectarine and peach

Cold storage of nectarines and peaches can lead to a condition known as woolly breakdown. It is believed to be caused by membrane damage at low temperature allowing intracellular solutes and ions to leak through the membrane into the intercellular spaces where they interact with high molecular weight pectins to form pectin gels. Cell adhesion is reduced, giving the fruit a 'dry-mouth' texture, not unrelated to mealiness in apples. The reduced cell adhesion also increases the number and size of intercellular air spaces. The condition can be detected non-invasively with MRI as the increased air gaps in

affected regions leads to a lower water proton density and hence lower image intensity.[67] Quantitative MRI investigations on the development of Brown Rot (*Monilinia fructicola*) in 'Fantasia' nectarine show striking contrast differences between sound and infected tissues.[68] Diseased tissue is characterized by markedly longer T_2 spin-echo times and elevated proton spin density concentrations compared to that associated with uninfected tissue; a situation closely similar to that described for *Botrytis* infection in strawberry.[43] The two types of tissue are sufficiently different to suggest they could be useful as the basis of an on-line grading technique for this crop.

There do not appear to be any reports of NMR correlations with maturity in nectarine or peach.

2.11. Papaya

Imported papayas are subjected to quarantine vapour heat treatment at 47.2 °C for 30 min for disinfection of fruit fly eggs and larvae. Unfortunately this treatment can also cause heat damage, which motivated a quantitative MRI study of the damage by Suzuki and co-workers[69] Proton density, T_1 and T_2 maps of unripe and ripe papaya, a wrapped heat-treated fruit and a thermally injured fruit were compared. Somewhat surprisingly, the unripe and ripe papaya samples had almost equal proton densities, equal and uniform T_1s and T_2s. However heat damage caused irregularities to appear in each map. Black areas appeared in the proton density maps, corresponding to low proton density regions. Similarly, T_1 maps showed regions of long and short T_1, the short areas corresponding to lower polygalacturonase enzyme activity, which is responsible for the softening of the ripening tissue. Regions of longer T_2 appeared to correspond to crumbled parts of overripe tissue.

2.12. Pear

The behaviour of bruises in pears appears to mirror that in apples. Chen and co-workers[11] showed that bruises in a 'Twentieth Century' pear and a 'Red Delicious' apple appeared as bright regions in spin-echo images acquired in a 2 T field. An MRI study of core breakdown in pears was first reported by Wang and Wang in 1989 using a 0.5 T (20 MHz) whole body scanner.[70] Core breakdown in pears, like that in apples, is a disorder caused by elevated CO_2 and decreased oxygen levels during storage. It results in a brown discolouration of the internal tissue and the eventual formation of cavities from the browned regions. The increased tissue water content associated with core breakdown resulted in brighter contrast in spin-echo images. These brighter regions were interspersed with darker regions where cavaties had formed. More recent investigations by Lammertyn *et al.*[71] used MRI to follow the time-course of the

disorder and noted two patterns of browning, a radial and localized pattern. Neither pattern grew with storage time but only increased in contrast to healthy tissue. It was also found that cavities grew at the expense of brown tissue. The contours of brown tissue were parallel to the fruit boundaries, suggesting a relation between the disorder symptoms and gas diffusion from the environment.

2.12.1. *Botrytis Gray Mold and superficial scald in pears*

Botrytis infection of pears is a significant postharvest problem and results in stem-end rot and the rot of punctures and wounds resulting from picking and handling. Despite its importance there do not yet appear to have been any NMR studies on this infection. Similarly, little or no NMR work has been reported for superficial scald and pithy brown core in pears, which are major physiological disorders developed during post-harvest storage. This is a significant problem because, according to USDA regulations, not more than 10% of pears in any lot should suffer from such defects.

2.13. Persimmon

The development of chilling injury in 'Fuyu' persimmon was investigated with MRI by Clark and co-workers.[72,73] This is an important problem because southern hemisphere countries are expanding their orchards as a response to opportunities to supply out-of-season persimmons to northern hemisphere consumers. But this requires long-term storage for sea freighting at chilling temperatures. Two storage treatments were therefore compared. The first involved hermetically sealing the persimmons in small polythene bags under a modified atmosphere; the other involved holding the fruit in perforated bags that allowed gas exchange but reduced water loss. Both batches were then stored at 7 °C for 4 weeks and then returned to room temperature. MRI revealed that fruit stored in the hermetically sealed bags had shorter relaxation times than those in the perforated bag and suggests that a more detailed investigation of the causes is warranted.

2.14. Pineapple

T_2 maps of unripe and ripe pineapple at 2 T have been reported by Hall and co-workers.[64] The mean T_2 increased from 45 ± 12 ms in unripe pineapple, to 81 ± 30 ms in ripe pineapple. This was thought to be due to an increase in sugar concentration and to a breakdown in cellular matrix during ripening. An increase in sugar concentration would, by itself, decrease the relaxation times, so whether starch granule hydrolysis and/or cellular structural changes account for the increase remains to be investigated.

2.15. Small stone fruits (Drupes)

Pitting fruit such as cherries, plums and olives is an important industrial process, usually performed in automation by holding the fruit and pushing the pit (or stone) out of the fruit with a mechanical plunger. It is, of course, important that any samples still containing pits are detected with the highest efficiency possible. The feasibility of using one-dimensional spin-echo image projections to detect pits has been explored by Zion and co-workers.[74,75] The first report[74] focused on cherries positioned in the grove of a stationary belt. A saggital slice was taken through the cherries, followed by transverse projections through the slice. Of course, the echo-time had to be less than the T_2 for the pit, for this to be detected as an additional central peak in the projection. Unfortunately, this simple concept is complicated by additional peaks in the projection arising from noise, shape distortions and missing flesh. This difficulty was circumvented using a more sophisticated classification based on simulations of projection line shapes. A criterion for deciding between the pitted or un-pitted states was based on calculating the intensity ratio of the middle peak(s) to the outer peak(s). This succeeded in correctly distinguishing 88% of cherries with pits, which, though high, is still not good enough for commercial exploitation. Moreover, it relied on the use of an expensive superconducting magnet equipped with slice selection capabilities. The 88% detection rate was also based on static samples placed inside the magnet. Motion of the cherries through the magnet would be expected to degrade the quality of the projections further by introducing additional dephasing caused by movement through field inhomogeneities. This pioneering study therefore highlighted some of the practical difficulties in implementing an on-line detection method. These will be analysed in greater detail in a subsequent section.

A subsequent study by the same research group focused on pits in olives.[75] This time the olives travelled at various speeds through a 2 T horizontal bore magnet. Segregating 300 pitted and non-pitted olives gave classification errors of 4.3, 4.7, 2.3 and 4% at belt speeds of 0, 5, 15 and 25 cm/s, respectively.

NMR measurements of the soluble solids of fresh prunes at 2 T have also been reported.[76] Prune juice is a high value product so the on-line, non-destructive determination of soluble sugars in prunes is commercially significant. Attempts to resolve the sugar and water proton peaks in a FID spectrum with a birdcage coil in a 2 T magnet were unsuccessful due to significant field inhomogeneity. However success was achieved with a 20 mm diameter surface coil, and a good correlation ($r = 0.91$) between the ratio of the sugar and water peak amplitudes and refractometer Brix was achieved with stationary samples, which were simply placed on the coil without retuning or matching. Whether a similar good correlation could be achieved with the birdcage coil and the T_1-null water suppression sequence was not investigated. It is interesting to note that in an earlier study, Cho *et al.*[77] had noted a linear

correlation between the decrease in water proton T_2 measured at low field (0.23 T, 10 MHz) and soluble solids for intact 'Red Flame' seedless grapes as well as for 'Bing' sweet cherries.

2.16. Other fruit

Qualitative MRI contrast changes associated with degree of maturity and the rotten pulp condition of mangosteen have been successfully observed by Yantarasri and co-workers[49] but no quantitative measurements of relaxation or diffusion rates were undertaken. Chaughule and co-workers[78] have recently reported MRI studies of developing sapota fruit. This is a sweet-tasting fruit especially popular in India where it is mostly consumed domestically. T_1 was observed to initially decrease during the first 5 months of growth and then increase during the final ripening stage. The changes in water proton T_2 and T_1 during the ripening of cherimoya (custard apple) fruit have been reported by Munoz-Barrio and Merodio.[79] The relaxation times were extracted from region-of-interest (ROI) measurements in MRI images acquired at 4.7 T (200 MHz). The T_2 of the whole fruit increased strongly (by 90%) in the first 2 days and correlated well with the decrease in firmness ($R^2 = 0.92$). T_1 for the outer pulp also increased progressively from 349 to 465 ms during the ripening period and correlated strongly with skin rupture force ($R^2 = 0.95$). Other tropical crops containing quality disorders producing image contrast include coconut and egg plant.[80]

Citrus are a major and important category of fruit, whose individual members are each subject to their own particular storage and physiological disorders. A transverse image slice of lemon (Nature cover December 22/29) accompanying the article by Hinshaw[81] was amongst the first images published to highlight the power and potential of MRI. Since then, remarkably few imaging studies have employed citrus fruits. Exceptions, apart from mandarin above, include the imaging of dry juice sacs in Washington Navel orange,[11] and the detection of quality disorders such as granulation, dry juice sacs, loose peel and sunburn at 0.5 T (21 MHz) in tangerines harvested in northern Thailand.[82]

3. NMR QUALITY ASSURANCE OF VEGETABLES

3.1. Potato

Most NMR studies of potato have focused on understanding the effects of processes such as boiling, frying, freezing and drying.[41,83,84] Exceptions are the NMR microimaging of healthy and diseased potato tubers reported by Goodman and co-workers,[85–87] and relaxometry responses in healthy tubers

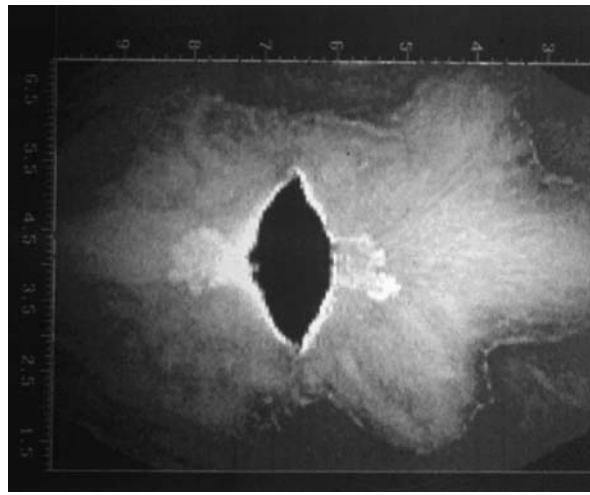

Fig. 6. Spin-echo Image of diseased potato showing hollow heart (dark area) surrounded by brown tissue (bright area). Printed with permission, from Ref. 92.

following induced wounding damage.[88] Most recently a number of papers[89–91] have appeared where NMR relaxometry on raw potato has been used to predict the sensory texture after boiling. It is surprising therefore, despite the importance of potato and its processed products and the fact that it is prone to internal defects that affect both processing and consumer acceptance, that there are so few published studies where NMR/MRI has been used to detect internal quality defects in tubers. Such internal defects include Brown core and hollow heart. Using multi-slice spin-echo imaging, Wang *et al.*[92] have demonstrated that both brown core and hollow heart can be detected by MR techniques (Fig. 6). Brown core, a physiological disorder of potato characterized by medula tissues in the centre of the tuber turning from light- to dark-brown in colour, is recognizable by the presence of high intensity signal in scans with long echo times. Electron microscopy shows that this condition is associated with loss of membrane structures, cytoplasm, and organelles and a thickening of cell walls that results in the affected tissue having a longer T_2 relaxation time. Cells in the pith area of the tuber may eventually split apart to form star or lens-shaped hollow cavities near the centre of the tuber, which is the so-called 'hollow-heart' condition. The absence of water means in the hollow heart is distinguishable by the absence of signal in images or one-dimensional profiles.

Another quality defect which is adversely affecting the marketing of potato products has been termed the hardening syndrome. Here, internal lumps form inside the potato during cooking. While a number of biochemical and physiological investigations are underway to try and understand the origins of

this syndrome it remains to be seen whether NMR studies on the raw potato can identify regions likely to form internal lumps.

3.2. Squash

Squash such as courgette (zucchini) and cucumber is a chill-sensitive commodity. Exposure to chilling temperatures causes loss of membrane integrity and water redistribution from the cell to the intercellular space. Visible injury symptoms such as surface pitting and dark watery patches eventually develop. Early detection of chill injury is important in order to ascertain the necessity and correct timing of treatments such as heat shock, that can reverse the condition. However, delaying treatment to the point where visible symptoms appear is too late for reversal.

Chilling injury in courgette/zucchini has been studied by MRI.[93,94] After just 3 days of storage T_1 decreased from an average of 1.41 s for non-chilled courgette held at 12.5 °C to 0.99 s for chilled courgette held at 2.5 °C. The T_1 was derived from cortical tissue just beneath the epidermis. In contrast, the corresponding T_2 changes for the whole image increased from 31 to 46 ms for the non-chilled and chilled samples respectively. Because visible chill injury symptoms only appeared after 6 days storage, the possibility of using NMR for rapid assessment of chill injury looks quite promising.

More recently Naruke and co-workers[95] have studied chilling injury in cucumber with very similar results. Cucumbers were stored either at 15 °C or at 2 °C for 9 days. Visible pitting appeared after 5 days storage in the chilled samples, but T_1 measured at 0.58 T (25 MHz) showed an abrupt increase after just 3 days storage.

3.3. Tomato ripeness

Tomato ripeness can be defined on the basis of external colour as, 1 = mature green (MG), 2 = breaker, 3 = turning, 4 = pink, 5 = light red, 6 = red-ripe.[96–98] Four additional substages of the first mature-green (MG) stage have been identified on the basis of the internal colour and tissue consistency. These substages are MG1, characterized by firm green locular tissue and soft seeds that cut easily; MG2, characterized by soft green locule tissue and hard seeds that do not cut when the tissue is sliced with a sharp knife; MG3, characterized by some gel in the locule, but no internal red colour; and MG4, where locular tissue is predominantly gel-like with some red appearance. Perhaps the most important stage from an MRI perspective, is the liquification of the locular tissue during stages MG1 to MG4 since this heralds the onset of the later ripening stages. If this change could be detected rapidly and non-destructively it would greatly reduce the variability in the ripeness of tomatoes marketed for

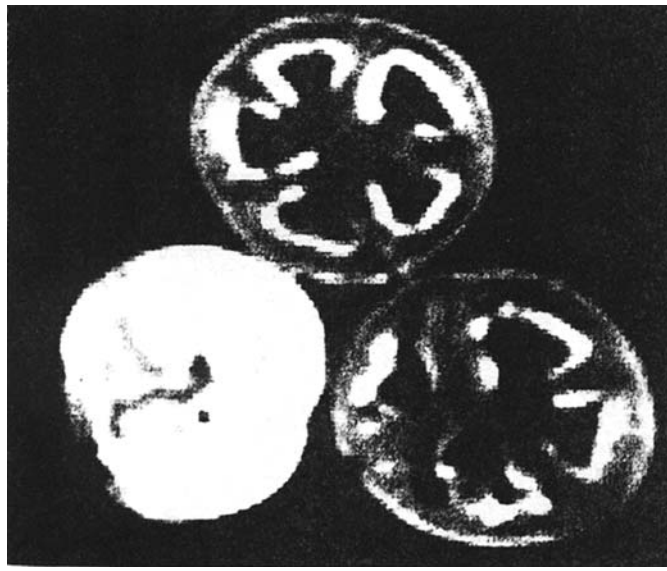

Fig. 7. Images of a red-ripe tomato (lower left) and two green tomatoes. Taken from Ref. 11.

international export. Such tomatoes are picked at the MG stage and transported in boxes gassed with ethylene. But on arrival the tomatoes display the whole range of ripeness up to 6 (red-ripe) and require a second costly (and damaging) hand-sorting stage. If the tomatoes, when picked, could be classified on the MG1 to MG4 scale, then ripening would be more uniform thereby eliminating the subsequent sorting stage. This was the motive for an early MRI study by Saltveit[96] which showed that as locular tissue ripened from stage MG1 to MG3, its water content increased. This was seen as an increased intensity in the spin density map recorded in the absence of significant relaxation attenuation (Fig. 7). Later stages of ripening were associated with an increasing graininess in the pericarp tissue as small air pockets developed in the tissue. Whether these observations can be developed into an on-line NMR sensor for tomato grading remains to be investigated.

4. NMR QUALITY ASSURANCE OF BULBS

Although fruit and vegetable quality has been the main thrust of this review it should not be forgotten that the quality of flower bulbs are also of major importance, especially in countries such as the Netherlands where export markets in tulips are commercially significant. Bud abortion is a disorder of tulips associated with a dehydrated flower after planting, while induction often takes place during storage. In an attempt to use MRI as a possible detector of

tulip bulbs likely to show this disorder, van Kilsdonk and co-workers[99] undertook spin-echo images of tulip bulbs on a 4.7 T instrument over a course of 35 weeks storage under conditions conducive to bud abortion. It was found that the mean proton density, T_1 and T_2 for the scale, shoot and stamens all showed progressive decrease during the storage period. This was interpreted as a progressive loss of internal quality, such that the bulb eventually became too weak for the fast root and shoot elongation required during the planting phase, resulting in bud abortion. There is therefore the possibility of using low field NMR to monitor bulb viability and water status during storage.

5. THE CELLULAR ORIGINS OF RELAXATION AND DIFFUSION CONTRAST

5.1. Relaxation processes

The cellular origins of relaxation contrast in plant tissue have been alluded to several times in the previous section. Understanding the molecular and microstructural origin of water proton transverse and longitudinal relaxation times in plant tissue is essential if NMR acquisition sequences and field strengths are to be optimized for monitoring degrees of maturity and for detecting defects in plant tissue. In an attempt to rationalize relaxation time differences the early literature relied heavily on the very loose concept of free and bound water in cellular tissue; but it is now acknowledged by most researchers that such language is misleading and of little predictive value. In fact there is no such thing as bound water, unless one is prepared to call water hydrogen bonding biopolymers with the longest exchange lifetimes of the order of microseconds bound. In a series of papers[21,22,100] Hills and co-workers showed that in most plant tissue, in the absence of paramagnetic ions, there are three dominant relaxation pathways for water proton relaxation, viz.

(a) Fast proton exchange on a (sub-) millisecond timescale between water and exchangeable protons on cell metabolites, especially sugars and biopolymers, including the cell wall biopolymers and starch granules.
(b) Dephasing of transverse magnetization by the diffusion of water molecules through internal field gradients created by magnetic susceptibility discontinuities in the tissue, especially across the interface of intercellular air gaps. This effect is especially important at high-field strengths when gradients are largest.
(c) Diffusion of water between the various subcellular (vacuolar, cytoplasmic) and extracellular water compartments which averages the magnetization to an extent that depends on cell morphology and membrane permeability.

These various processes have several important implications for plant tissue relaxometry. First, the fact that plant cells are compartmentalized means that, in general, the transverse and longitudinal relaxation will be multiple exponential when measured with the CPMG sequence and enough data points to give well characterized decay to the baseline. Such multiple exponential relaxation is observed with apple,[20,21,101] onion,[21] courgette,[21] carrot[22] and potato.[41] Many of the values of T_2 and T_1 reported in the previous section are therefore only average values obtained by fitting a limited number of data points with a single exponential function. Secondly, if transverse relaxation occurs by the proton exchange and internal field gradient mechanism then, generally, the observed CPMG transverse relaxation behaviour depends on the field strength and the CPMG pulse spacing. This is also observed to be the case with apple, potato, carrot and onion. The situation can be modelled theoretically by combining the proton exchange model[16] with a simplified spherical cell model[20,101] of a plant cell. This has proved useful in fitting the changing relaxation data during the drying and freezing of apple,[20] carrot[22] and potato[41] parenchyma tissue.

It would be interesting to explore whether the same numerical cell model can explain the changes in relaxation behaviour observed as plant tissue ripens. The role of starch granule hydrolysis during ripening is of particular interest. As mentioned earlier, starch granules act as relaxation sinks for water protons in a field- and pulse spacing-independent way and this effect has been investigated in a number of recent papers.[102,103] As starch granules are hydrolysed into sugars during ripening the decrease in the size and number of starch granule relaxation sinks would be expected to lead to an increase in water proton relaxation times. However, the effect is counteracted by the increasing concentration of sugars, whose transverse relaxation behaviour has been successfully modelled with the proton exchange model.

Given the likelihood that on-line NMR sensors will be based on low rather than high-field strengths it is surprising that so little field cycling relaxometry has been reported for plant tissue. The dependence of the longitudinal relaxation time on field strength gives a direct handle on the spectral densities describing molecular mobility in the tissue, data that could provide a useful test of the numerical cell model. It would be especially useful to see how the spectral densities change during tissue breakdown for conditions such as mealiness and chilling injury.

Although correlations between relaxation and quality naturally focus on simple T_2 and T_1 measurements it should not be forgotten that these are not the only types of relaxation that can be studied. Relaxation in the rotating frame, characterized by $T_{1\rho}$, is another potentially valuable handle on tissue quality and this, in general, depends on the strength of the spin-locking field and the spin-locking angle.

Possible correlations between cross-polarization rates and quality factors are an additional aspect that appears to have been overlooked, yet image contrast

based on cross relaxation is an important diagnostic tool in clinical imaging and therefore, potentially, in plant imaging. In this context cross relaxation refers to the transfer of longitudinal proton magnetization between water and more rigid biopolymers in the plant tissue matrix. These rates can be measured by sequences such as those of Goldman and Shen.[104]

5.2. Water diffusivity

In contrast to water proton relaxation, there have been very few attempts to correlate water diffusivity in cellular tissue as measured with PGSE sequences to plant quality factors. An exception is the early work of Keener and co-workers[14] who found a useful correlation between the apparent water diffusion coefficient and apple maturity as measured by the refractometer Brix value. The paucity of work on water diffusivity is surprising because the restriction of water diffusion by cell membrane and cell wall barriers is a useful and sensitive probe of changes in cell morphology. The potential of PGSE studies of cellular tissue was illustrated by Hills and Snaar in their studies of fresh parenchyma apple tissue.[101] In a PGSE, Stejskal-Tanner experiment (Fig. 8), the echo amplitude, $S(q, \Delta, \tau)$ is a function of both the echo time, 2τ, the diffusion time, Δ, defined as the time between gradient pulses, and the wavevector, q, defined as the area of the gradient pulse, $\gamma G\delta/2\pi$.

In the limit of zero gradient, the sequence reduces to the Hahn echo, and it is conventional to expand the echo amplitude as a multiple exponential function of τ, and define, the usual transverse relaxation times, T_i,

$$S(2\tau) = \sum_i P_i \exp(-2\tau/T_i). \tag{1}$$

As already discussed, modelling this multiple exponential decay function with the numerical cell model gives valuable information about cell morphology and membrane permeability. Similar information is available

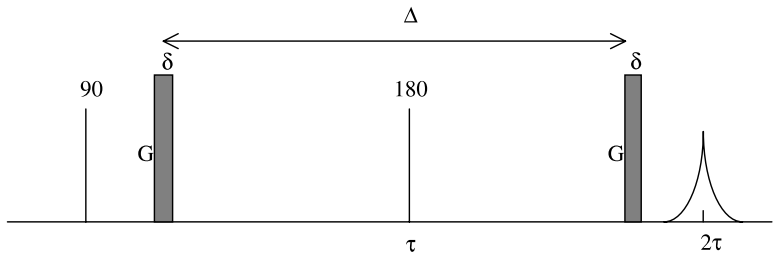

Fig. 8. The Stejskal-Tanner pulsed gradient spin-echo sequence.

from the CPMG sequence, but in multicompartment, cellular tissue, the τ-dependence of the Hahn-echo will not, in general, be the same as the echo decay envelope of the CPMG sequence. However, in the PGSE experiment the diffusion time is an additional variable. For variation of Δ at fixed τ we can write

$$S(q, \Delta, \tau) = \sum_i p_i\,(q, \tau)\,\exp(-\Delta/a_i(q, \tau)), \tag{2}$$

where the $a_i(q, \tau)$ is the generalized diffusion times and p_i are the associated fractional populations. Both these coefficients depend on the wavevector, q. In principle these additional coefficients can be analysed and related to quality factors in an analogous manner to the relaxation times discussed in the previous section, though no one has yet attempted to do this. It is also possible to vary τ and Δ together by setting $\Delta = 2\tau - \varepsilon$, where ε is a constant time delay much less than Δ. In this case relaxation and diffusion become explicitly coupled together and multiple exponential analysis yields

$$S(q, \tau) = \sum_i P_i\,(q)\,\exp(-2\tau/T_i(q)). \tag{3}$$

The $T_i(q)$ behave as wavevector-dependent relaxation times and the form of the wavevector dependence can provide a useful check on the consistency of models. Table 5 shows a comparison of the experimental coefficients for fresh apple tissue with those calculated with the numerical cell model. The agreement is quite reasonable and supports the general theoretical framework. It would be interesting to apply this approach to mealy apple and to other types of fruit and vegetable.

Diffusive attenuation is not merely of academic interest because it will probably be an inherent cause of echo attenuation in on-line NMR sensors whenever the sample moves through gradients and inhomogeneities in the main sensor field. It is therefore important to understand their potential effect and possible use in assessing quality of horticultural products.

Quite clearly there remains a great deal of basic NMR and modelling work to be done before we can claim to understand the relaxation and diffusion behaviour of horticultural products. In particular there is a need for more

Table 5. Comparison of theoretical and experimental p_i and a_i in Eq. (2) for apple parenchyma tissue (Taken from Ref. 101)

i	a_i (experimental)	a_i (theory)	p_i (experimental)	p_i (theory)
1	0.292	0.302	0.78	0.80
2	0.032	0.044	0.13	0.10
3	0.007	0.017	0.09	0.10

systematic relaxation and diffusion studies combined with modelling over a range of field strengths and pulse spacings. A model of these changes would be invaluable for predicting optimum field strengths and acquisition parameters for on-line detection of degrees of maturity. This raises the question of the design and operation of potential on-line NMR sensors, to which we now turn.

6. ON-LINE NMR SENSOR DESIGN

6.1. Background

The potential for MR sensors to interrogate on-line/in-line processes in the Food Processing industry is reiterated on an almost annual basis.[8,9,51,105–110] Nevertheless there are a number of significant technical hurdles to be overcome[7,111] which explains why it is difficult to identify one working on-line MR system that monitors even a simple process such as moisture content which is in widespread industrial use. On-line MR sensors have been described by Pearson *et al.*,[112] Nicholls and De Los Santos[113] and Pearson and Job[114] that are suitable for the determination of moisture content in flowing grains, oxides and coal. However, the Pearson design (US Patent 5530350) was ultimately rejected as being too unreliable. Chen and co-workers[11,35,37] described the design of a permanent magnet system for on-line applications but this has not been exploited commercially. The reasons for this failure to develop commercial NMR sensors are worth reviewing, as they need to be overcome if the NMR-quality correlations reviewed in the previous section are ever to be exploited.

6.2. Sample polarization

The first bottleneck can be labelled sample polarization. If a sample is travelling on a conveyor belt at a speed, v, the sample will have moved a distance $v5T_1$ in a magnetic field before it is fully polarized, and for typical conveyor velocities of 2 m/s and a representative T_1 of about a second the sample has travelled 10 m down the magnet before we even start the NMR acquisition! Obviously we can shorten this distance by working with suboptimum polarizations which compromise the signal/noise, but even then, the polarization time will limit the number of acquisitions that are possible. A prepolarising unit is one obvious possibility but stopping each sample in the sensor for the polarization and acquisition is not a commercially viable possibility!

6.3. Magnet considerations

The high cost of commercial NMR spectrometers is another factor hindering their development as on-line sensors. Most modern systems are based around expensive superconducting magnets because they provide high-field strengths and do not require a power source. However, the high cost of these magnets means this technology is inappropriate for most factory situations. Permanent magnet systems are more robust and cheaper but the difficulties in shimming permanent magnet systems over the large volumes needed when a sample is moving at speed through the magnet are prohibitive.[115] Permanent magnets are also sensitive to temperature and may not perform effectively in environments where temperatures fluctuate. For example, a 1 °C change in magnet temperature can alter field-strength by 0.10%, sufficient to seriously attenuate the signal.[116] Eustace and Jordan,[117] using an earth's field instrument, reported an effect of temperature when using relaxation measurements to determine soluble solids – a 1 °C change resulted in a 1% unit change in reduction in sugar content in the range 0–20%. Conversely, if the system temperature is adequately controlled, we need to consider the implications when fruit taken directly from cold storage for grading are passed over a NMR sensor. This leaves only resistive solenoid magnets, which were first used in the early pioneering days of NMR. The problems associated with resistive magnets are well known. The high currents needed for creating substantial magnetic field strengths deposit large amounts of heat in the coils, which necessitates expensive water-cooling. Special steps are also needed to avoid current fluctuations and temperature variations in the magnet.

The issue of field strength has already been referred to. Obviously high-fields are desirable for good signal/noise and high spatial resolution. However, higher fields also mean greater expense. Hence there is a need for research into the efficacy of low-field NMR quality correlations, where low-field could mean as low as 0.05 T (2.15 MHz) generated in an electromagnet. Such field strengths were used in the very first whole body imagers because of fears about adverse clinical effects of higher fields. Whether they would be adequate for on-line applications remains to be explored.

6.4. Field inhomogeneity

Perhaps the most serious hurdle to be overcome in the development of on-line NMR sensors is the requirement for a magnetic field of sufficiently high spatial homogeneity for meaningful NMR. Most NMR researchers using sophisticated laboratory spectrometers take it for granted that, after shimming, there is field homogeneity to a few ppm over the sample volume. But when the sample is moving and multiple acquisitions are required, we are faced with the problem of shimming quite large volumes. This is technically possible and is done in

whole body imagers, but the design of magnet and shim coils that permits this high degree of field homogeneity is an expensive and technically demanding exercise. This hurdle has to be faced by anyone aspiring to design a commercially viable on-line NMR sensor. It is therefore worth analysing in some detail the effects of field inhomogeneity on the NMR of a discrete sample, such as an apple, moving at constant velocity through the field.

As a first step let us expand the inhomogeneous magnetic field at a point, r, as a Taylor series:

$$\mathbf{B}(r + \Delta r) = \mathbf{B}_0(r) + \mathbf{G}_{\text{eff}}(r)\Delta r + \cdots \tag{4}$$

This shows that the field inhomogeneity can, to first order, be represented as an effective local gradient, $\mathbf{G}_{\text{eff}}(\text{r})$, whose direction and magnitude will vary with position, r. Let us therefore analyse the effect of these local gradients on the FID of a rigid sample, such as an apple, moving at constant velocity, $\mathbf{v}$, through the sensor field. For the time being effects of spin relaxation, spin diffusion, and spin couplings are ignored. Consider spins in the volume element dV at position vector $\mathbf{r}(0)$ at time 0. After a time t, this element will have moved to $\mathbf{r}(t) = \mathbf{r}(0) + \mathbf{v}t$, where $\mathbf{v}$ is the linear velocity. For notational convenience we drop the subscript effective in the field gradient, $\mathbf{G}_{\text{eff}}$. The precession frequency at $\mathbf{r}(t)$ will then be

$$\omega(\mathbf{r}(t), t) = 2\pi f(\mathbf{r}(t), t) = \gamma B_0 + \gamma \mathbf{G} \cdot \mathbf{r}(t) = \gamma B_0 + \gamma \mathbf{G} \cdot \mathbf{r}(0) + \gamma \mathbf{G} \cdot \mathbf{v}t. \tag{5}$$

As the spins initially at $\mathbf{r}(0)$ are carried along in the field gradient, they will accumulate a net phase angle given by

$$\varphi(\mathbf{r}(t), t) = \int_0^t \mathrm{d}t' 2\pi f(r(t'), t') = \gamma B_0 t + \gamma \mathbf{G} \cdot \mathbf{r}(0)t + \gamma \mathbf{G} \cdot \mathbf{v}t^2/2. \tag{6}$$

The spin density $\rho(\mathbf{r}(t), t)$ of spins at $\mathbf{r}(t)$ at time t is clearly equal to $\rho(\mathbf{r}(0), 0)$ if we ignore diffusion and bulk motion of the sample other than the linear translation, $\mathbf{v}$. The contribution $\mathrm{d}S(\mathbf{r}(t), t)$ to the total signal $S(t)$ from spins at $\mathbf{r}(t)$ is therefore given by

$$\begin{aligned} \mathrm{d}S(\mathbf{r}(t), t) &= A \cdot \rho(\mathbf{r}(t), t) \cdot \exp[\mathrm{i}\varphi(\mathbf{r}(t), t)] \\ &= A \cdot \rho(\mathbf{r}(0), t) \cdot \exp[\mathrm{i}\gamma B_0 t + \mathrm{i}\gamma \mathbf{G} \cdot \mathbf{r}(0)t + \mathrm{i}\gamma \mathbf{G} \cdot \mathbf{v}t^2/2]. \end{aligned} \tag{7}$$

The phase factor $\exp(\mathrm{i}\gamma B_0 t)$ is eliminated by setting the RF coil on-resonance so, neglecting the constant of proportionality, A, and writing $\mathbf{r}(0)$ simply as r, and $\rho(\mathbf{r}(0), t)$ simply as $\rho(\mathbf{r})$ this becomes

$$\mathrm{d}S(\mathbf{r}(t), t) = \rho(\mathbf{r}) \cdot \exp[\mathrm{i}\gamma \mathbf{G}(\mathbf{r}) \cdot \mathbf{r}t + \mathrm{i}\gamma \mathbf{G}(\mathbf{r}) \cdot \mathbf{v}t^2/2]. \tag{8}$$

The total signal $S(t)$ is obtained by integrating over the whole sample volume

$$S(t) = \int \mathrm{d}V \rho(\mathbf{r}) \cdot \exp[\mathrm{i}\gamma \mathbf{G}(\mathbf{r}) \cdot \mathbf{r}t + \mathrm{i}\gamma \mathbf{G}(\mathbf{r}) \cdot \mathbf{v}t^2/2]. \quad (9)$$

The first term in this expression is just the conventional imaging algorithm for stationary samples. The complications associated with moving samples arise from the second term. Not only is there additional dephasing from the term, $\gamma \mathbf{G}_{\mathrm{eff}}(\mathbf{r}) \cdot \mathbf{v}t^2/2$, where $\mathbf{G}_{\mathrm{eff}}(\mathbf{r})$ differs from point to point in the magnet, there is an even more serious problem arising from the sample motion because the dephasing cannot necessarily be refocused as a meaningful spin-echo. This is because each moving spin will experience different local effective field gradients before and after a refocusing 180° pulse, so that it will no longer be returned to its initial phase at the expected echo time 2τ. Even if a spin-echo can be observed from a moving sample in an inhomogeneous field it will not necessarily contain any useful information about the nature of the sample, such as its transverse relaxation time, T_2, but only information about the local magnetic field inhomogeneities the spins have experienced in their journey during the echo time! The magnitude of this effect increases dramatically with increasing sample velocity and it is noteworthy that in all of the references concerned with moving samples, the conveyor speeds were much less than the 1–2 m/s speeds usually encountered in industrial situations.

6.5. Probe design

Rapid dephasing of moving samples by field inhomogeneities also means that we require RF coils with short ring-down times if we are to have any hope of picking up NMR signals. Because the ring-down time is $2Q/\omega_0$, this means we must design RF probes with low Q factors. Low Q factors are also needed to avoid over-sensitive probe tuning whereby the tuning varies from one sample to the next, which is potentially disastrous in an on-line situation. Consequently, there is a compromise to be made between high signal/noise, requiring a high Q factor, and short probe ringdown times and low tuning sensitivity which requires a low Q factor. Birdcage coils enable a large volume of the sample to be interrogated. While suitable for imaging they were not as effective for acquiring frequency-domain data in on-line testing of fruits.[76] Surface coils reduce the complexity and cost of the sensor and are better adapted to operating in inhomogeneous magnetic fields. Conversely, they limit the amount of information acquired (non-penetrating) and neglect to address within-fruit variability issues. Receiver coils must also be adequately shielded from external electromagnetic noise.

6.6. Compatibility with commercial graders

The conveyor systems employed in the on-line studies by the UC Davis team,[37] and Saito *et al.*[63] were manufactured from non-ferrous, non-magnetic materials. This is not the case on existing commercial fruit grading equipment. Therefore, some consideration needs to be given to how a NMR sensor can be married to existing technology. It may be that techniques based on the new open-magnet architecture are able to accommodate inhomogeneities in the magnet field better.[118] Presently, however, it would seem that a NMR sensor will not be a simple 'clip-on' attachment to existing grading equipment, but rather one requiring invasive surgery.

6.7. Cost considerations

These various considerations illustrate some of the major scientific and technical problems to be overcome if conventional laboratory NMR is to be adapted as a sensor of produce quality in on-line situations. Of course, all of the technical problems can be overcome at a price. Indeed, apart from the price tag, there is nothing preventing a whole body clinical imager being used in a pack house to monitor, for example, apple mealiness on a conveyor. However, even with a whole body scanner one would be restricted by sample speeds. An apple moving at 2 m/s through the imager would not be fully polarized by the time it reached the central homogeneous part of the magnet and a very fast imaging sequence such as EPI or FLASH would be needed to acquire a 3D image before the sample departed. Unfortunately such rapid acquisition sequences require expensive and very carefully adjusted gradient controllers and coils. Indeed, just one standard gradient power amplifier costs about £10,000 and three would be needed for three-dimensional imaging, which illustrates the need for developing new generations of low cost hardware for on-line applications. Few fruit or vegetable packhouses would be prepared to pay the prices of conventional NMR hardware for marginal improvements in sorting efficiency! All this points to the need for novel approaches to on-line NMR if commercially viable NMR sensors are to become commonplace on the factory floor. We therefore explore the potential of two less conventional NMR systems, beginning with the NMR MOUSE.

6.8. The NMR-MOUSE

The Mobile Universal Surface Explorer (MOUSE) is described as a new-generation, hand-held instrument with exciting potential for use on-line.[118–120] MOUSE devices are based on the principles of 'inside-out' NMR where open magnet designs are used for measurements within the field. Essentially the unit

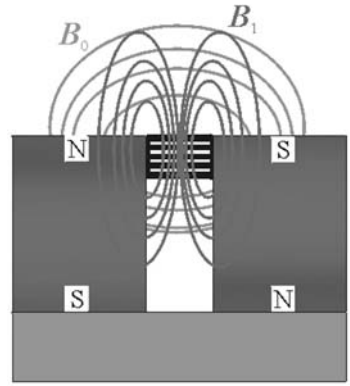

Fig. 9. Schematic of the NMR-MOUSE. Samples are placed on top of the surface coil located between the two permanent magnets.

consists of two permanent magnets side by side, separated by a surface coil (Fig. 9). Sample-size restrictions are thus reduced and samples are probed by relaxation time measurements. By employing magnetic field gradients it is claimed that spatially-resolved characteristics of materials can be obtained with inhomogeneous magnetic fields without the need for superconducting magnets. In principle, any of the current echo-based excitation schemes employed in conventional NMR can be used with inhomogeneous fields. A disadvantage is that the sampling region is quite close to the surface, which limits the technique to those quality factors that are distributed with near spatial-uniformity throughout the fruit, such as mealiness. Bruises would also not necessarily be detected unless the fruit were rotated over an array of the sensors. Instruments weigh around 5 kg and have field strengths of around 0.5 T.

6.9. SQUIDS

SQUIDS (or **S**uperconductive **Qu**antum **I**nterference **D**evices) are superconducting devices that directly transform changes in sample magnetization induced by spin transitions into voltages. They therefore act essentially as linear magnetic flux to voltage converters and replace the conventional tuned RF coil for detecting NMR signals. They can detect both changes in longitudinal and transverse magnetization so are more flexible than conventional RF coils that detect only transverse magnetization. Because SQUIDS detect changing magnetization their sensitivity does not depend on resonance frequency so they can operate at ultralow frequencies less than 200 kHz. This has the outstanding advantage that highly inhomogeneous magnetic fields do not cause large frequency differences and therefore loss of resolution. In other words, for a given field inhomogeneity the width of the NMR line scales linearly with the

Fig. 10. ^{1}H image of mineral oil phantom at 2 mT using a SQUID spectrometer (from website – http://waugh.cchem.berkeley.edu/noframes/research/).

measurement field and so peak height and signal/noise are enhanced as the measurement field is reduced. For the same reason SQUIDS do not need to be tuned. To detect an NMR signal the sample still needs to be polarized and the small polarization at very low-fields is a potential problem in lost signal/noise that can be overcome with some form of rapid prepolarization. The sample also needs to be excited with RF radiation, but this can be done in a small static magnetic field of less than 10 mT with conventional RF coils. This means that the SQUID is usually spatially separated from the sample environment to avoid direct RF irradiation. Recently an MR image of a small tube of water has been obtained[121] at field-strengths only a small fraction of that of the Earth's field using a SQUID sensor (Fig. 10).

The SQUID obviously has several potential advantages for on-line applications. It can operate at very low inhomogeneous magnetic fields, avoiding the need for large expensive shimmed magnets. It also does not require tuning and has very low power requirements. However there are also severe technical limitations to be overcome before it can be used in on-line commercial operations. The whole SQUID needs to be immersed in liquid helium and a conventional RF coil is still needed to excite the NMR resonance. It remains to be seen whether such devices will find future on-line application in horticulture.

7. CONCLUDING REMARKS

Although we have shown that many diverse quality factors in fruit and vegetables can be detected with NMR it is also clear that a great deal of

fundamental NMR remains to be done. Apple is one of the most intensively studied fruit, yet we find no reports on field cycling relaxometry, no attempts to measure cross relaxation rates or $T_{1\rho}$ and no systematic investigation of water diffusivity in relation to physiological defects such as mealiness. Little work has been done to correlate PGSE measurements of the restriction of water diffusivity to quality factors. The gaps in Table 1 also emphasize the extent of the more applied work that remains to be done before NMR sensors can be applied to all these diverse types of fruit and vegetables. The limited nature of the work reviewed to date, is, to some extent, understandable given the huge diversity of physiological conditions in fruit and vegetables and the large number of potential NMR/MRI pulse sequences that can be used. One obvious advantage with the large number of pulse sequences is that it increases the chances that at least one type of NMR measurement will be sensitive to the quality factor of concern. At the same time the sheer diversity of quality issues and pulse sequences means that the task of identifying the best sequences and acquisition conditions for each quality factor can be very time-consuming. This becomes even more of a problem when it is remembered that all the relaxation characteristics are, in general, field- and frequency-dependent and, potentially, multiple exponential. For example, a single T_2 value has little real meaning unless one also specifies the pulse sequence (Hahn echo, CPMG, gradient-echo), the refocusing pulsing rate, the spectrometer frequency and number of decay points and exponential analysis technique. Likewise, the longitudinal relaxation time, T_1, for water protons in cellular tissue depends, in general, on field strength (or, equivalently, spectrometer frequency) and this frequency dependence can be measured directly in field cycling relaxometry, though there are no reported studies of this frequency dependence as a probe of quality factors in fruit or vegetables. It is also surprising that there have been no reports of spin-locked relaxation times, $T_{1\rho}$, of plant tissue of differing quality. In like manner there is a dearth of PGSE measurements in plant tissue of varying quality. Bearing in mind that fruit or vegetables may require sorting and grading as they emerge from cold storage, there is also a need to report relaxation times and diffusion rates as a function of temperature between at least 0 °C and room temperature if useful NMR-quality correlations are to be identified.

The task of identifying the optimum pulse sequence for each quality factor might, perhaps, be simplified using chemometric techniques. At least two research groups are active in the multivariate analysis of time-domain NMR data. One group, lead by Douglas Rutledge at the INA (Paris), is exploring the possibility of concatenating the raw data from a number of different pulse sequences and using multivariate methods to find out which combination of NMR sequences is most sensitive to any given quality factor.[122] Another group, lead by Soren Engelsen is exploring use of multivariate methods such as PLS in complex NMR time domain data.[123]

Very few of the references in Tables 1–3 attempt any quantitative modelling of their NMR data in terms of cell microstructure or composition. Such models would be extremely useful in choosing the optimum acquisition pulse sequences and for rationalising differences between sample batches, varieties and the effects of harvesting times and storage conditions. The Numerical Cell Model referred to earlier is a first step in this direction but more realistic cell morphologies could be tackled with finite element and Monte Carlo numerical methods.

As mentioned in the introduction, many of the reports cited in this review have been based on measurements made with superconducting magnets at relatively high spectrometer fields. Unless there is a major breakthrough such as high temperature supercon magnets, these high-field magnets are unlikely to be used on industrial conveyor belts. There is therefore a need to repeat many of the measurements at much lower fields (< 0.5 T) appropriate to permanent and resistive magnet technology.

ACKNOWLEDGEMENTS

B. P. Hills gratefully acknowledges the financial support of the BBSRC during the preparation of this work.

REFERENCES

1. C. J. Clark, P. D. Hockings, D. C. Joyce and R. A. Mazucco, *Postharv. Biol. Technol.*, 1997, **11**, 1.
2. J. A. Chudek and G. Hunter, *Prog. NMR Spectros.*, 1997, **31**, 43.
3. M. Faust, P. C. Wang and J. Maas, *Hort. Rev.*, 1997, **20**, 225.
4. N. Ishida, M. Koizumi and H. Kano, *Ann. Bot.*, 2000, **86**, 259.
5. J. Briggs, *Eurofruit Magazine*, 2002, August, 42.
6. T. Fearn, *J. NIR Spectros.*, 2001, **9**, 229.
7. B. P. Hills, *Magnetic Resonance Imaging in Food Science*, Wiley, New York, 1998, 152.
8. M. J. McCarthy, *Magnetic Resonance Imaging in Foods*, Chapman and Hall, New York, 1994.
9. R. R. Ruan and P. L. Chen, *Water in Foods and Biological Materials: A Nuclear Magnetic Resonance Approach*, Technomic Publishing, Basel, 1998.
10. S. Y. Wang, P. C. Wang and M. Faust, *Scientia Hortic.*, 1998, **35**, 227.
11. P. Chen, M. J. McCarthy and R. Kauten, *Trans. ASAE*, 1989, **32**, 1747.
12. M. Koizumi, N. Ishida and H. Kano, *Curr. Topics Plant Biol.*, 2000, **2**, 1.
13. S. I. Cho, V. Bellon, T. M. Eads, R. L. Stroshine and G. W. Krutz, *J. Food Sci.*, 1991, **56**, 1091.
14. K. M. Keener, R. L. Stroshine and J. A. Nyenhuis, *J. Amer. Soc. Hort. Sci.*, 1999, **124**, 289.
15. K. M. Keener, R. L. Stroshine and J. A. Nyenhuis, *Trans. ASAE*, 1997, **40**, 1633.
16. B. P. Hills, *Molec. Phys.*, 1992, **76**, 489.
17. R. M. Kroeker and R. M. Henkelman, *J. Magn. Reson.*, 1986, **69**, 218.
18. K. P. Whittall and A. L. MacKay, *J. Magn. Reson. Imaging*, 1989, **84**, 134.
19. B. P. Hills, *Magnetic Resonance Imaging in Food Science*, Wiley, New York, 1998, 205.
20. B. P. Hills and B. Remigereau, *Int. J. Food Sci. Technol.*, 1997, **32**, 51.

21. B. P. Hills and S. L. Duce, *Magn. Reson. Imaging*, 1990, **8**, 321.
22. B. P. Hills and K. P. Nott, *Appl. Magn. Reson.*, 1999, **17**, 521.
23. M. J. McCarthy, B. Zion, P. Chen, S. Ablett, A. H. Darke and P. J. Lillford, *J. Sci. Food Agric.*, 1995, **67**, 13.
24. B. Zion, P. Chen and M. J. McCarthy, *Comput. Elect. Agric.*, 1995, **13**, 289.
25. C. J. Clark and D. M. Burmeister, *HortScience*, 1999, **34**, 915.
26. J. J. Gonzalez, R. C. Valle, S. Bobroff, W. V. Viasi, E. J. Mitcham and M. J. McCarthy, *Postharv. Biol. Technol.*, 2001, **22**, 179.
27. K. H. Jung, R. Stroshine, P. Cornillon and P. M. Hirst, *ASAE Conference Paper No. 98-6020*, Orlando, FL, 1998.
28. C. J. Clark and C. A. Richardson, *N. Z. J. Crop Hort. Sci.*, 1999, **27**, 47.
29. C. J. Clark, J. S. MacFall and R. L. Bieleski, *Scientia Hortic.*, 1998, **73**, 13.
30. C. J. Clark and R. L. Bieleski, *Proceeding of the Sensors for Nondestructive Testing Conference*, Orlando, FL, p. 211, 1997.
31. J. B. Golding, V. Sarafis, S. Crozier and S. E. Rose, *HortScience*, 1997, **32**, 112.
32. P. Barreiro, C. Ortiz, M. Ruiz-Altisent, J. Ruiz-Cabello, M. E. Fernandez-Valle, I. Recasens and M. Asensio, *Magn. Reson. Imaging*, 2000, **18**, 1175.
33. P. Barreiro, J. Ruiz-Cabello, M. E. Fernandez-Valle, C. Ortiz and M. Ruiz-Altisent, *Magn. Reson. Imaging*, 1999, **17**, 275.
34. P. Barreiro, A. Moya, E. Correa, M. Ruis-Altisent, M. Fernandez-Valle, A. Peirs, K. M. Wright and B. P. Hills, *App. Magn. Reson.*, 2002, **22**, 387.
35. P. Chen, M. J. McCarthy, R. Kauten, Y. Sarig and S. Han, *J. Agric. Engng Res.*, 1993, **55**, 177.
36. R. L. Stroshine, W. K. Wai and G. W. Krutz, *ASAE Conference Paper No. 93-6535*, Chicago, IL, 1993.
37. P. Chen, M. J. McCarthy, S. M. Kim and B. Zion, *Trans. ASAE*, 1996, **39**, 2205.
38. S. Pathaveerat, M. J. McCarthy and P. Chen, *Abstracts of the Potsdam Symposium on Fruit Quality*, ATB, Potsdam, 2001.
39. G. Hopkirk, A. White, D. J. Beever and S. K. Forbes, *N. Z. J. Crop Hort. Sci.*, 1994, **22**, 305.
40. A. Raffo, R. Gianferri, R. Barbieri and E. Brosio, *Food Chem.*, in press.
41. B. P. Hills and G. Le Floch, *Food Chem.*, 1994, **51**, 331.
42. J. L. Maas and M. J. Line, *Acta Hortic.*, 1995, **398**, 241.
43. B. A. Goodman, B. Williamson, E. J. Simpson, J. A. Chudek, G. Hunter and D. A. M. Prior, *Magn. Reson. Imaging*, 1996, **14**, 187.
44. B. A. Goodman, B. Williamson and J. A. Chudek, *Magn. Reson. Imaging*, 1993, **11**, 1039.
45. J. M. Pope, D. Jonas and R. R. Walker, *Protoplasma*, 1993, **173**, 177.
46. G. R. Gamble, *J. Food Sci.*, 1994, **59**, 571.
47. B. A. Goodman, B. Williamson and J. A. Chudek, *Protoplasma*, 1992, **166**, 107.
48. B. Williamson, B. A. Goodman, J. A. Chudek and D. J. Johnston, *Recent Advances in Botrytis Research-Proceedings of the 10th International Botrytis Symposium*, K. Verhoeff, N. E. Malathrakis and B. Williamson, eds., Heraklion, Greece, 1992, 140.
49. T. Yantarasri, J. Sornsrivichai and P. Chen, *Acta Hortic.*, 1998, **464**, 97.
50. T. Yantasari, K. Kalayanamitra, S. Saranwong and J. Somsrivichai, *Proceedings of the ACIAR Conference*, G. I. Johnson, L. van To, D. D. Nguyen, and M. C. Webb, eds., 2000.
51. S. M. Kim, M. J. McCarthy and P. Chen, *European Agricultural Engineering Conference Paper 98-F-017*, Oslo, 1998.
52. C. J. Clark, L. N. Drummond and J. S. MacFall, *J. Sci. Food Agric.*, 1998, **78**, 349.
53. C. Clark, *N. Z. Kiwifruit*, 1993, February, 10.
54. W. L. Kerr, C. J. Clark, M. J. McCarthy and J. S. de Ropp, *Scientia Hortic.*, 1997, **69**, 169.
55. J. Godward, P. Gunning and B. P. Hills, *App. Magn. Reson.*, 1999, **17**, 537.
56. C. J. Clark, A. C. Richardson and K. B. Marsh, *HortScience*, 1999, **34**, 1071.
57. J. Blasco, E. Molto and M. C. Alamar, *Abstracts of the 6th International Conference on Applications of NMR in Food Science*, Paris, 2002.

58. A. M. Gil, I. F. Duarte, I. Delgadillo, I. J. Colquhoun, F. Casuscelli, E. Humpfer and M. Spraul, *J. Agric. Food Chem.*, 2000, **48**, 1524.
59. S. M. Kim, M. J. McCarthy and P. Chen, *ASAE Conference Paper No. 94-6519*, Atlanta, GA, 1994.
60. S. M. Kim, P. Chen, M. J. McCarthy and B. Zion, *J. Agric. Engng. Res.*, 1999, **74**, 293.
61. D. C. Joyce, P. D. Hockings, R. A. Mazucco, A. J. Shorter and I. M. Brereton, *Postharv. Biol. Technol.*, 1993, **3**, 305.
62. D. C. Joyce, P. D. Hockings, R. A. Mazucco and A. J. Shorter, *Functional Plant Biol.*, 2002, **29**, 873.
63. K. Saito, T. Miki, S. Hayashi, M. Shimada, D. Ikegaya, N. Kimura and K. Takabatake, *Abstracts of Magnetic Resonance/Spectroscopy in Food Science, International Workshop*, Harima, Japan, 1997.
64. L. D. Hall, S. D. Evans and K. P. Nott, *Magn. Reson. Imaging*, 1998, **16**, 485.
65. K. Saito, T. Miki, S. Hayashi, H. Kajikawa, M. Shimada, Y Kawate, T. Nishizawa, D. Ikegaya, N. Kimura, K. Takabatake, N. Sugiura, M. Suzuki, *Cryogenics*, 1996, **36**, 1027.
66. B. Zion, 1994, personal communication.
67. L. Sonego, R. Ben-Arie, J. Raynal and J. C. Pech, *Postharv. Biol. Technol.*, 1995, **5**, 187.
68. C. J. Clark, *HortScience*, under review.
69. K. Suzuki, T. Tajima, S. Takano, T. Asano and T. Hasegawa, *J. Food Sci.*, 1994, **59**, 855.
70. C. Y. Wang and P. C. Wang, *HortScience*, 1989, **24**, 106.
71. J. Lammertyn, T. Dresselaers, P. van Hecke, P. Jancsok, M. Wevers and B. M. Nicolai, *Postharv. Biol. Technol.*, 2003, **29**, 19.
72. C. J. Clark and S. K. Forbes, *N. Z. J. Crop Hort. Sci.*, 1994, **22**, 209.
73. C. J. Clark and J. S. MacFall, *Postharv. Biol. Technol.*, 1996, **9**, 97.
74. B. Zion, M. J. McCarthy and P. Chen, *Lebensm. Wiss. Technol.*, 1994, **27**, 457.
75. B. Zion, S. M. Kim, M. J. McCarthy and P. Chen, *J. Sci. Food Agric.*, 1997, **75**, 496.
76. B. Zion, P. Chen and M. J. McCarthy, *J. Sci. Food Agric.*, 1995, **67**, 423.
77. S. I. Cho, R. L. Stroshine, I. C. Baianu and G. W. Krutz, *Trans. ASAE*, 1993, **36**, 1217.
78. R. S. Chaughule, N. Ishida, S. Naito and H. Kano, *Abstracts of the 6th International Conference on Applications of NMR in Food Science*, Paris, 2002.
79. M. T. Munoz-Barrio and C. Merodio, *Acta Hortic.*, 1997, **463**, 385.
80. N. R. Jagannathan, R. Jayasundar, V. Govindaraju and P. Raghunathan, *Ind. Acad. Sci. (Chem. Sci.)*, 1994, **106**, 1595.
81. W. S. Hinshaw, P. A. Bottomley and G. N. Holland, *Nature*, 1977, **270**, 722.
82. T. Yantarasri and J. Sornsrivichai, *Acta Hortic.*, 1998, **464**, 494.
83. C. A. Kantt, A. G. Webb and J. B. Litchfield, *J. Food Sci.*, 1997, **62**, 1001.
84. R. Ruan, S. J. Schmidt, A. R. Schmidt and J. B. Litchfield, *J. Food Process Engng.*, 1991, **14**, 297.
85. A. J. Snijder, S. M. Glidewell and B. A. Goodman, *Abstracts of the 3rd International. Conference of Magnetic Resonance Microscopy*, Würzburg, Germany, 1995.
86. B. A. Goodman and S. M. Glidewell, *Phyton: Ann. Rei Bot.*, 1995, **37**, 81.
87. A. J. Snijder, R. L. Wastie, S. M. Glidewell and B. A. Goodman, *Biochem. Soc. Trans.*, 1996, **24**, 442.
88. R. S. Chaughule, G. N. Iyer and N. C. Shah, H. E. Flores, J. P. Lynch and D. Eissenstat, eds., *Radical Biology: Advances and Perspectives on the Function of Plant Roots*, American Society of Plant Physiologists, Rockville, MD, 1997, 480.
89. A. K. Thybo, H. J. Andersen, A. H. Karlsson, S. Donstrup and H. Stodkilde-Jorgensen, *Lebensm. Wiss. Technol.*, 2003, **36**, 315.
90. A. K. Thybo, I. E. Bechmann, M. Martens and S. B. Engelsen, *Lebensm. Wiss. Technol.*, 2000, **33**, 103.
91. L. G. Thygesen, A. K. Thybo and S. B. Engelsen, *Food Sci. Technol.*, 2001, **34**, 469.

92. P. C. Wang, H. F. Song and Z. J. Yan, *Proceedings of the 35th Experimental NMR Conference (ENC)*, Pacific Grove, CA, 1994.
93. C. Y. Wang and P. C. Wang, *Environ. Exp. Bot.*, 1992, **32**, 213.
94. S. L. Duce, T. A. Carpenter and L. D. Hall, *J. Food Engng.*, 1992, **16**, 165.
95. T. Naruke, S. Oshita, J. H. Walton, S. Kuroki, Y. Deo and Y. Kawagoe, *Abstracts of the Postharvest Unlimited Conference*, Leuven, Belgium, 2002.
96. M. E. Saltveit, *Postharv. Biol. Technol.*, 1991, **1**, 153.
97. N. Ishida, T. Kobayashi, M. Koizumi and H. Kano, *Agric. Biol. Chem.*, 1989, **53**, 2363.
98. N. Ishida, M. Koizumi and H. Kano, *Scientia Hortic.*, 1994, **57**, 335.
99. M. van Kilsdonk, R. van Sluis, H. Franssen, C. Kolloffel and K.Nicolay, *Abstracts of the Postharvest Unlimited Conference*, Leuven, Belgium, 2002.
100. S. L. Duce, T. A. Carpenter, L. D. Hall and B. P. Hills, *Magn. Reson. Imaging*, 1992, **10**, 289.
101. B. P. Hills and J. E. M. Snaar, *Molec. Phys.*, 1992, **76**, 979.
102. H.-R. Tang and B. P. Hills, *Carbohydr. Polym.*, 2000, **43**, 375.
103. H.-R. Tang and B. P. Hills, *Carbohydr. Polym.*, 2001, **46**, 7.
104. M. Goldman and L. Shen, *Phys. Rev.*, 1966, **144**, 321.
105. G. W. Schrader, J. B. Litchfield and S. J. Schmidt, *Food Technol.*, 1992, **46**, 77.
106. B. P. Hills, *Trends Food Sci. Technol.*, 1995, **6**, 111.
107. S. J. Schmidt, P. S. Belton, B. P. Hills and G. A. Webb, eds., *Advances in Magnetic Resonance in Food Science*, Royal Society of Chemistry, Cambridge, 1999, 79.
108. S. J. Schmidt, X. Sun and J. B. Litchfield, *Crit. Rev. Food Sci. Nutr.*, 1996, **36**, 357.
109. J. A. Abbott, R. Lu, B. L. Upchurch and R. L. Stroshine, *Hort. Rev.*, 1997, **20**, 1.
110. C. Tellier and F. Mariette, *Ann. Rpts. NMR Spectros.*, 1995, **31**, 105.
111. P. J. McDonald, *Food Processing: Recent Developments*, A. G. Gaonkar, ed., Elsevier Science, Amsterdam, 1995, 23.
112. R. M. Pearson, L. R. Ream, C. Job and J. Adams, *Cereal Foods World*, 1987, **32**, 822.
113. C. I. Nicholls and A. de Los Santos, *Drying Technol.*, 1991, **9**, 849.
114. R. M. Pearson and C. Job, *Proceedings of the 2nd Food Process Automation Conference*, Lexington, KY, 1992.
115. N. Ishida, H. Ogawa, M. Koizumi and H. Kano, *J. Magn. Reson. Anal.*, 1996, **2**, 168.
116. R. L. Stroshine, W. K. Wai, K. M. Keener and G. W. Krutz, *ASAE Conference Paper No. 94-6539*, Atlanta, GA, 1994.
117. C. A. Eustace and R. B. Jordan, *Trans. ASAE*, 1995, **38**, 1563.
118. B. Blümich, P. Blümler, G. Eidmann, A. Guthausen, R. Haken, U. Schmitz, K. Saito and G. Zimmer, *Magn. Reson. Imaging*, 1998, **16**, 479.
119. H. Kühn, M. Klein, A. Wiesmath, D. E. Demco, B. Blümich, J. Kelm and P. W. Gold, *Magn. Reson. Imaging*, 2001, **19**, 479.
120. P. J. Prado, *Magn. Reson. Imaging*, 2001, **19**, 505.
121. R. McDermott, A. H. Trabesinger, M. Mück, E. L. Hahn, A. Pines and J. Clarke, *Science*, 2002, **295**, 2247.
122. D. N. Rutledge, A. S. Barros, M. C. Vacier, S. Baumberger and C. Lapierre, P. S. Belton, B. P. Hills and G. A. Webb, eds., *Advances in Magnetic Resonance in Food Science*, Royal Society of Chemistry, Cambridge, 1999, 201.
123. I. E. Bechmann, H. T. Pedersen, L. Norgaard and S. B. Engelsen, *Advances in Magnetic Resonance in Food Science*, P. S. Belton, B. P. Hills and G. A. Webb, eds., Royal Society of Chemistry, Cambridge, 1999, 217.

Applications of NMR to Thermostable Proteins

E. ALBERTI, R. CONSONNI and L. ZETTA

Istituto per lo Studio delle Macromolecole (ISMAC), Laboratorio di NMR, Consiglio Nazionale delle Ricerche (CNR), Via Ampère 56, 20131 Milan, Italy

Thermostable proteins have always been of significant interest in several scientific areas. In the last decade, the developments in the field of molecular and structural biology have offered important insights into the determinants of protein thermostability. Following an introductory section on thermostable proteins, extremophilic organisms and the determinants of protein thermostability, this chapter covers applications of NMR to the study of thermoresistant proteins. Particular attention has been paid to papers dealing with structural comparisons between proteins from thermophilic micro-organisms and their corresponding mesophilic counterparts, the structure–function relationships of proteins from thermophilic sources and the factors involved in protein thermostability. The data reported, highlight the accepted assumption that there is not a single determinant of protein thermostability, rather an optimal occurrence of several factors.

ANNUAL REPORTS ON NMR SPECTROSCOPY
VOLUME 50 ISSN 0066 4103
DOI 10.1016/S0066-4103(03)50003-5

1. INTRODUCTION

Thermally stable proteins have always been of significant interest and a growing consideration has been developed in the last decade since the genome map of extremophilic micro-organisms (in particular, archaea) has become available and several structures of thermostable proteins have been solved by high-resolution techniques such as X-ray crystallography and NMR spectroscopy. This chapter will emphasize particularly on NMR studies of proteins from thermophilic organisms as most of the current research is focused on these proteins. However, examples of thermostable proteins from other sources are also considered. In this case, the authors have chosen to consider only those proteins whose melting temperature (T_m) is higher than 60 °C. First, the thermostable proteins and extremophilic micro-organisms are described followed by a general review of studies on possible determinants of protein thermostability which mainly include biochemical, thermodynamical and crystallographic investigations of large proteins. In Section 5, the attention is focused on those thermostable proteins which for their size and physico-chemical properties are suitable for NMR characterization. These studies include mainly structure determinations using $^{13}C/^{15}N$ double enriched proteins in combination with homonuclear and heteronuclear multidimensional NMR techniques. In addition, the NMR spectroscopy of nuclei such as ^{113}Cd or ^{199}Hg, the use of dipolar couplings and paramagnetic probes, such as nitroxides, or the $^{1}H/^{15}N$ relaxation processes to get information on protein flexibility are also studied. In order to keep the number of references to a manageable size, we have limited our selection to papers published mainly in the last decade and in which NMR plays a major role as an experimental method.

2. THERMOSTABLE PROTEINS

Most proteins suffer irreversible denaturation at temperatures exceeding the optimum body temperature by only a few degrees (e.g., at 40–50 °C for proteins from mammalian sources). On the contrary, thermally stable proteins maintain their activities and are stable at high temperatures. Clearly, they are of great interest for several reasons: they can be used to improve the efficiency of many industrial processes and provide insight into the general mechanisms of protein folding and stabilization. Identifying and understanding the factors contributing to their stability has been a long-standing problem. A proper understanding of the molecular basis of thermal stability in proteins could have important consequences for their application in a range of industrial processes and in designing efficient enzymes that can work at high temperatures.

In particular, thermostable enzymes (thermozymes), which are optimally active between 60 and 125 °C, have attracted increasing attention in the recent

years due to their biotechnological potential. They have been used in molecular biology (e.g., Taq polymerase), in addition to the detergent (e.g., protease) and starch processing industries (e.g., α-amylase, glucose isomerase), and are suitable for numerous additional applications that require high stability such as organic synthesis (e.g., lipases, proteases, oxidoreductase), diagnostic, waste treatment, pulp and paper manufacture, and animal feed.[1] Industrial applications of thermostable enzymes offer the benefits of increased reaction rates, higher substrate solubility, decreased media viscosity, longer enzyme shelf life at normal storage temperatures (e.g., protein pharmaceuticals) and lowered risk of microbial contamination when reactions are carried out at high temperatures. Several reviews have dealt with thermozymes and their properties[2–7] and an increase in interest has been shown on the design of enzymes or proteins with increased stability to temperature whilst retaining catalytic efficiency.[8–15] This will be of great importance in many areas of biotechnology and will offer insights into protein structure–function relationships.

3. EXTREMOPHILIC ORGANISMS

Life on Earth exhibits an enormous adaptive capacity. Extremophiles are micro-organisms that are found in environments at extreme temperature (from −2 to 15 °C and from 60 to 110 °C), ionic strength (2–5 M NaCl), pH (< 4, > 9) or pressure (from 200 to 2000 bar). Their discovery and characterization have led to major improvements in understanding the environmental conditions that limit life and in the current description of the early stages of cellular evolution. The majority of extremophiles are members of archaea[16] (i.e., *Sulfolobus*, *Pyrococcus*, *Methanococcus*, *Thermococcus*), one of the three phylogenetic domains of life, although extremophilic members of the bacterial domain are also known (i.e., *Thermotoga*, *Hydrogenobacter*, *Aquifex*). Extremophiles thrive under high temperatures and non-physiological pHs in submarine hydrothermal areas and in continental sulfataras, low temperatures in Antarctica, high salt concentration in the Dead Sea and in the Great Salt Lake, and high pressure in deep sea vents. According to their optimal growth temperature (T_{opt}), micro-organisms can be roughly classified into four groups: psychrophilic ($T_{opt} = 0$–20 °C), mesophilic ($T_{opt} = 20$–50 °C), thermophilic ($T_{opt} = 50$–80 °C) and hyperthermophilic ($T_{opt} = 80$–120 °C). Up to the present, the highest growth temperature observed is 113 °C for *Pyrolobus fumarii*.[17] Current theory and circumstantial evidence suggests that hyperthermophiles were the first life-forms to have arisen on Earth[18] and that they have evolved so that they can not only tolerate extreme conditions, but also require them for their survival. The interest shown by the scientific community to hyperthermophiles is demonstrated by the number of extensive reviews[19–21] and publications on

the subject and by the major place occupied by hyperthermophiles in the worldwide genome-sequencing projects (i.e., http://www.tigr.org, http://www.ncgr.org).[7] Proteins from these organisms can serve as model systems for use by biologists, chemists and physicists interested in understanding protein evolution, molecular mechanisms for protein stability and the upper temperature limit for enzyme function.

4. FACTORS DETERMINING PROTEIN THERMOSTABILITY

Proteins, independent of their mesophilic or extremophilic origin, consist exclusively of the 20 canonical natural amino acids. It is therefore interesting to understand the reasons how some proteins are stabilized so as to resist exceptional temperatures.[22,23]

The first high resolution crystal structure of thermolysin was published more than 25 years ago[24] when Perutz and Raidt[25] also commented on the stereochemical basis of thermostability of ferredoxins and hemoglobin A2. Since these pioneering efforts, several investigators have focused on the problem of the molecular basis of protein thermostability. During recent years, the origin of protein stability at high temperatures has been dramatically expanded due to the development of sophisticated methods in the field of both molecular and structural biology, which allow rapid gene isolation and sequencing, the effective production of the necessary amount of protein for structural investigations and the design of site-specific mutants. One approach to understanding the molecular basis of protein thermostability involves site-directed mutagenesis in conjunction with structure determination by X-ray crystallography or NMR spectroscopy, comparing the sequences and structures of homologous proteins from thermophilic and mesophilic organisms, e.g., hyperthermophilic and mesophilic archaeal histones, cold-shock proteins from *Thermotoga maritima* and *Bacillus subtilis*, ribonuclease H from *Thermus thermophilus* and *Escherichia coli*. It has been shown that proteins from thermophilic organisms are 48–85% similar to those of their mesophilic counterparts, that their three-dimensional structures are superimposable and they share the same catalytic mechanisms. Several factors have been shown to have an effect on thermostability protein, such as greater hydrophobicity, better packing, amino acid substitution. A list of the most relevant factors which have been attributed to the greater stability of thermophilic proteins is reported in Table 1 with relevant references. These studies have been carried out mainly comparing the crystal structures of thermophilic–mesophilic proteins characterized by a high degree of sequence identity that are available from the Protein Data Bank (PDB).

Despite these numerous studies, it is still a matter of debate as to which structural factors are the main determinants of the increased stability in thermostable proteins. There are substantial differences between the

Table 1. List of the most relevant factors attributed to the greater stability of thermostable proteins

Factor affecting thermostability	Reference
Increased number of salt bridges	26–36
Increased electrostatic interactions	37–39
Increased number of hydrogen bonds	40–43
Greater hydrophobicity	44–47
Occurrence or absence of certain amino acids	48–52
Better packing, smaller and less numerous cavities	53–55

conclusions reached with different proteins and there appears to be no universal rule for the structural basis of thermostability.[2,56–64] Rather, the basis of thermostability appears to be a more optimal occurrence of several determinants.

5. NMR OF THERMOSTABLE PROTEINS

5.1. Electron transfer proteins

Electron transfer proteins, or reduction enzymes, participate in the mainstream of electron transport from organic substrates to O_2. They include iron–sulphur proteins (Fe–S proteins), cytochromes and thioredoxins. Fe–S proteins are a group of proteins containing iron atoms, either Fe^{2+} or Fe^{3+}, bound tetrahedrally by sulphur atoms and include rubredoxins (Rds) and ferredoxins (Fds). NMR studies of Rds and Fds have been reviewed by Sticht and Rösch[65] and Goodfellow and Macedo.[66] Unknown structures of ferredoxins were described and factors that influence geometry, stability, redox potential, electronic properties and electron-transfer reactivity of iron–sulphur clusters have been presented and discussed.[65] An introductory theory of the electron–nucleus interaction and how it affects NMR parameters, such as chemical shift and relaxation times, has been presented and the problems in determining the structure of paramagnetic proteins have been reported and discussed.[66] One of the major problem encountered in the structure determination of Fe–S proteins was the inclusion of the metal centre in the structural calculations. This problem was approached[67,68] and solved[69] by Bertini *et al*. implementing the pseudocontact shift constraints as a module of the DYANA[70] program and defining an additional 'special' amino acid in which the metal-sulphur bond length and angles were defined using the distance constraints for metal, sulphur and carbon atoms taken from metalloproteins whose structure was already solved by X-ray analysis.

5.1.1. *Rubredoxins*

Rubredoxins are 53–54 residue globular proteins containing a single four cysteine-iron centre (Fig. 1a). There has been a plethora of studies focusing on the metal site structure and the mechanisms of hyperthermostability comparing mesophilic and thermophilic rubredoxins by NMR, circular dichroism, X-ray, high-level calculations, and voltammetry.[71–76] However, the origin of the greater stability of thermophilic Rds has not been found yet.

The first NMR structural data on a thermostable Rd was obtained on the Rd from the hyperthermophilic *Pyrococcus furiosus*, *Pf*Rd, (T_m close to 200 °C) in which the paramagnetic iron was substituted with Zn.[77] This substitution allowed one to overcome the paramagnetic line broadening occurring in both the Fe(III) and Fe(II) *Pf*Rd forms and enabled detailed NMR assignments. Signal intensities and chemical shifts of the observable cross peaks in the two-dimensional spectra of Zn*Pf*Rd matched relevant cross peaks in the spectrum of Fe(II) *Pf*Rd, providing good evidence that the global fold of the two proteins was the same. Also, by replacing the metal centre with other NMR active nuclei like ^{113}Cd or ^{199}Hg, no extensive structural perturbations occurred.[78] Metal substitutions have also been conducted on the homologous Rd from the mesophilic *Clostridium pasteurianum*, *Cp*Rd (amino acid sequence homology with *Pf*Rd of 78%, $T_m = 82$ °C)[79] and in a series of its mutants.[80,81] The single Fe(II) of the reduced form was found to be quantitatively displaced by either Cd^{2+} or Zn^{2+} when a modest molar excess of the substituting metal salt was anaerobically incubated with the reduced Rd under mild conditions. ^{1}H and ^{113}Cd NMR experiments showed that the cadmium-substituted Rd prepared by the non-denaturing substitution method retained the pseudo-tetrahedral $M(SCys)_4$ co-ordination geometry and secondary structural elements characteristic of the native Rd, and that 'unzipping' of the β-sheet did not occur during metal substitution.[79]

Interestingly, the overall structural features of Zn*Pf*Rds were found to be very similar to those of Rds from mesophilic organisms, consisting of three antiparallel β strands joined by two loops, each containing two cysteines bound to a metal ion.[78,82–85] Comparison of the amino acid sequences of *Pf*Rd with those of mesophilic Rd indicated only a few features that could be of significance to the enhanced thermostabilty of *Pf*Rd namely, (i) absence of a charged or amide group at position 2 (Ala), (ii) a charged residue at position 7 (Lys), (iii) a hydroxyl group (Ser) at position 25 and (iv) a glutamyl rather than aspartyl group at position 32.[77]

From the analysis of the secondary structure of *Pf*Rd and *Cp*Rd, it was proposed that potentially stabilizing electrostatic interactions involving the charged groups of residues Ala1, Glu14 and Glu52 were responsible for the higher stability of *Pf*Rd. The same electrostatic interactions are not present in Rd from mesophilic organisms and the authors supposed that they might prevent the β-sheet from 'unzipping' at high temperatures.[67] Comparison of

the *Pf*Rd and *Cp*Rd structures showed a more uniform distribution of negative charge density in *Pf*Rd, despite the similar number of ion pairs. A comparison of the amide exchange behaviour of *Pf*Rd with that of *Cp*Rd has been presented by Hernández and Le Master[86] and differences in the rates and in the activation energies of exchange are interpreted in terms of structural distribution and collective modes of exchange.

A large number of Rd mutants have been studied in order to find the structural determinants of thermostability. Contributions of the β-sheet conformation to thermostability were investigated examining Zn*Cp*Rd and one mutant in which the residues near the N-terminus, namely Met1, Lys2 and Pro15 were mutated to (−), Ala and Glu, respectively,[87] which are the residues supposed to contribute to the thermostability of *Pf*Rd.[77] The secondary structure of the wild-type and the mutated Zn*Cp*Rds was essentially the same. The mutation did not increase the thermostability of Zn*Cp*Fd significantly, suggesting that the thermostabilization mechanism of *Pf*Rd is not determined by hydrogen bonds or electrostatic interactions involving the

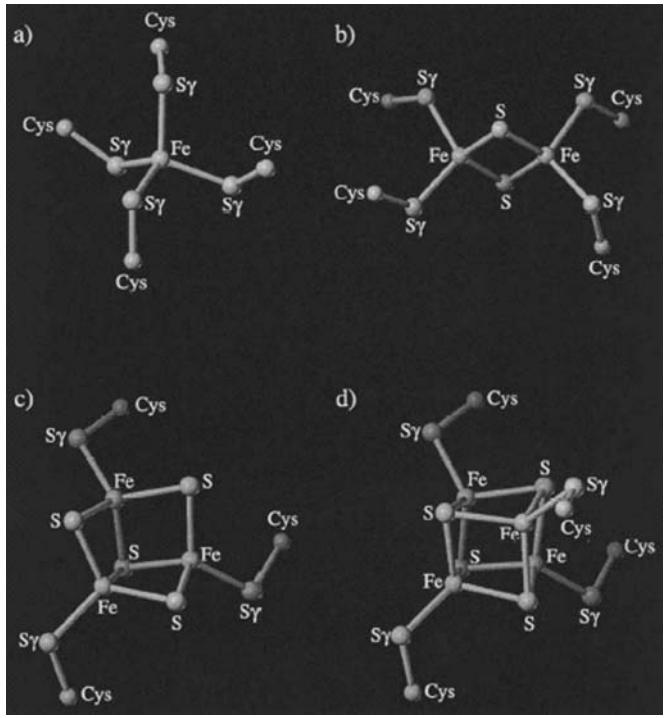

Fig. 1. Schematic representation of the four basic types of iron–sulphur clusters. The rubredoxin-type and the [2Fe–2S], [3Fe–4S] and [4Fe–4S] clusters are shown in (a) to (d), respectively. Reprint from *Prog. Biophys. Mol. Biol.*, Vol. 70, H. Sticht and P. Rösch, 'The structure of iron–sulfur proteins', pp. 95–136, Copyright 1998, with permission from Elsevier Science.

N-terminal strand of the β-sheet. The hyperthermophilic *Pf*Rd was compared with the mesophilic counterpart *Dv*Rd from *Desulfovibrio vulgaris* and some mutants in which the four iron-binding cysteines had been suitably substituted in order to eliminate the iron centre.[88,89] NMR and CD spectroscopies, together with computational modelling showed that the apo *Pf*Rd was stabilized by a salt bridge between the N-terminus and Glu14[88] and reversibly unfolded with $T_m = 82\,^{\circ}C$.[89] The structures of *Pf*Rd and *Cp*Rd mutants have also been investigated using dipolar couplings.[90] A *Pf*Rd mutant with the hydrophobic core mutated to match that of *Cp*Rd showed no change in thermostability in the metal-free state. In contrast, a metal-free chimera with residues 1–15 of *Cp*Rd and the remaining 38 residues of *Pf*Rd were severely destabilized and unfolded at 25 °C. Hence, the hydrophobic core did not seem to be the key determinant of thermostability. Rather, a possible contributor to the thermostability was found to be the hydrogen bond network centred on the first 15 residues or the interaction of these 15 residues with other parts of the protein. Indeed, a unique network of hydrogen bonds and salt bridges centred on the side chain of Glu14 was found in *Pf*Rd. In *Cp*Rd this residue is a proline, an amino acid incapable of supporting a hydrogen-bonding network.

The mesophilic Zn*Dg*Rd from *Desulfovibrio gigas* has been studied in the presence of diglycerol phosphate (DPG), a solute identified in hyperthermophilic organisms in which it accumulates in response to salt stress.[91] A structural stabilizing effect of the solute on the protein (free energy change of 1.2 kJ/mol) has been found by determining selected amide proton exchange rates. Amide protons surrounding the metal centre were found to be pointing inward and relatively shielded from the solvent. According to the authors, stabilization by DPG did not involve changes in the protein structure and derived from concerted movements around the metal centre and in the β-sheet.

5.1.2. *Ferredoxins*

Ferredoxins (Fds) are widespread in the three domains of life and an abundance of sequence data and structural information are available for Fds isolated from several sources. In particular, the bacterial type Fds are small electron-transfer proteins that posses cubane *x*Fe–*y*S clusters attached to the protein matrix by Fe ligation of Cys via a conserved consensus ligating sequence. The archaeal type ferredoxins are water-soluble electron acceptors for the acyl-coenzyme A forming 2-oxoacid/ferredoxin oxidoreductase, a key enzyme involved in the central archaeal metabolic pathways. Fds have been distinguished according to the number of iron and inorganic sulphur atoms, 2Fe–2S, 4Fe–4S/3Fe–4S (Fig. 1b–d) and Zn-containing Fds.

5.1.2.1. Ferredoxins containing 2Fe–2S clusters

Ferredoxins of the 2Fe–2S type play a role in the photosynthetic electron transport as an essential electron acceptor of photosystem I. The solution

structure of *Se*Fd from the thermophilic *Synechococcus elongatus* (97 amino acids, $T_m = 76\,^{\circ}C$) was independently determined by NMR by two different groups.[92,93] The overall structure was found to be very similar to the crystal structures of Fds from mesophiles and consisted of a four-stranded parallel/antiparallel β-sheet, a short double-stranded antiparallel β-sheet and three short helices. Baumann *et al*. found that *Se*Fd contains a salt bridge inside a 17 residue hydrophobic core, absent in mesophilic Fds and which was suggested to be related to thermostabilty.[92] The *Se*Fd solution structure found by Hatanaka *et al*. included an extension of the hydrophobic core, a unique hydrophobic patch on the surface of the large β-sheet and two charged networks not observed by Baumann *et al*.[93] The authors suggested that some of these features could contribute to thermostabilty. In contrast to the finding of Baumann *et al*., they found that the salt bridge between Lys51 and Glu56 was exposed to the solvent similar to the corresponding residues in the mesophilic Fd structures.

5.1.2.2. Ferredoxins containing 4Fe–4S or 3Fe–4S clusters

This type of Fds are small (6–10 kDa) electron-transfer proteins that possess one or two cubane 4Fe and/or 3Fe clusters.[94–97] Several Fds belonging to this class have been purified from mesophilic and thermophilic organisms and structurally characterized by X-ray crystallography or NMR spectroscopy allowing important information to be collected about cluster formation, electronic properties, protein stability, molecular–electronic structure and structure–function relationship. NMR has made important contributions in understanding the molecular–electronic structure of cubane 4Fe and/or 3Fe clusters[98–101] and to the elucidation of the solution structure[102–109] as a complement to the X-ray crystallography. The highly conserved fold consists of two antiparallel, double-stranded β-sheet, two helices and five turns. Recently, an NMR study of hyperthermostable ferredoxins has been reported, in which the most relevant papers on the topic have been reviewed.[110]

The *Pf*Fd from the hyperthermophilic archaeon *Pyrococcus furiosus* (66 amino acids, $T_m = 114\,^{\circ}C$) is one of the most extensively studied Fds.[111–121] Unique among the other hyperthermostable Fds, it possesses an aspartic acid as one of its cluster ligands in the native 4Fe–4S state, which significantly affects the electron exchange rate[117] and allows facile interconversion between 4Fe–4S and 3Fe–4S forms.[111] Structural characterization of *Pf*Fd by crystallography has not been successful. Co-crystallization of the protein with its redox partner oxidoreductase revealed a well-resolved Fd cluster in contact with the enzyme, while the remainder of Fd was lost due to disorder.[122] Thus, solution ^{1}H NMR studies have been carried out to elucidate both the cluster electronic properties[98,99,123,124] and the solution molecular structure of *Pf*Fd.[102,114,120,125] All forms of wild-type and cluster-ligand *Pf*Fd mutants with an intact disulphide exhibited a dynamic equilibrium heterogeneity that has been proposed to originate from population of alternate *R* or *S* C_β–S–S–C_β

orientations of the disulphide bond.[120,121,126,127] This heterogeneity was suggested to be related to the structural disorder observed in the crystal structure. A solution molecular model for the conformationally heterogeneous aspartate-ligated protein has been constructed on the basis of reported NMR constraints using distance geometry and simulated annealing protocols. Additional stabilizing interactions, due to a longer helix near the C-terminus and a larger β-sheet, have been found relative to the hyperthermophilic Fds from *Thermotoga maritima* (*Tm*Fd) and *Thermococcus litoralis* (*Tl*Fd). According to the authors, the structural modification observed for *Pf*Fd does not increase the protein thermostability but places 'stress' on the disulphide bond increasing its potential reducibility.[121]

*Tm*Fd (60 amino acids, $T_m = 125\,^{\circ}C$) is a monomer containing a single 4Fe–4S cluster and displaying a high degree of sequence homology with other ferredoxins from archaea, such as *Tl*Fd (75%) and *Pf*Fd (48%). The NMR structure[128] was elucidated before the X-ray structure determination[129] and compared with that of the hyperthermophilic *Pf*Fd, and those of *Dg*Fd and *Da*Fd from the mesophilic *Desulfovibrio gigas* and *D. africanus*.[130] The NMR data was not sufficient to explain protein thermostability and indicated that, in ferredoxins, thermostabilty was not necessarily correlated with the content of stable elements of regular secondary structure.

*Tl*Fd (59 amino acids, stable up to 90 °C) contains a single cluster that can exist in both 3Fe–4S and 4Fe–4S forms. The molecular and electronic structures were solved by NMR[131,132] whereas the X-ray structure is still unknown. Compared to other mesophilic and thermophilic Fds, *Tl*Fd showed several structural adjustments such as the addition of a third strand of β-sheet, a likely Lys2-Glu38 salt bridge from this β-sheet and the N-terminus and a more hydrophobic and compact interaction between the large β-sheet and the long helix. According to the authors, each of these modifications contributes to the extraordinary protein thermostability.

*Bs*Fd from the thermophilic *Bacillus schlegelii* (77 amino acid residues, stable up to at least 90 °C) contains 4Fe–4S and 3Fe–4S clusters. The electronic properties of the clusters have been investigated,[133] the NMR structure has been solved[134] and compared with the crystal structure of the homologous *Av*Fd from the mesophilic *Azotobacter vinelandii*.[135] The number of salt bridges per residue was found to be doubled in *Bs*Fd with respect to *Av*Fd. Besides, strong hydrophobic interactions among side chains belonging to the first β-sheet and the C-terminal helix were observed in *Bs*Fd but not in *Av*Fd. These features have therefore been considered to contribute to the thermal stability of *Bs*Fd. This quite rigid Fd has been the object of a model-free analysis aimed at the characterization of the backbone mobility in a wide range of temperatures (276–330 K).[136] ^{15}N spin–lattice and spin–spin relaxation times together with ^{1}H–^{15}N Nuclear Overhauser Effect were measured and compared with those of the mesophilic 4Fe–4S high-potential iron proteins (HPIP) from *Chromatium vinosum*. Results indicated that the

rigidity (of the order of subnanoseconds) of the thermostable protein was not related to its thermostabilty.

The solution structure of Asp13Cys,[137] a thermostable mutant of *Bs*Fd, has been solved by ^{1}H-NMR and compared to that of the wild-type (WT) protein.[138] The overall folding of the WT protein was maintained in the mutant, except for the immediate vicinity of the new cysteine. The geometry of the new cluster was a typical 4Fe–4S cubane, as monitored by the ^{1}H hyperfine shifts of the co-ordinated cysteines. Conformational heterogeneity, which was partly abolished by heat treatment, was observed and ascribed to a kinetic phenomenon.

5.1.2.3. Ferredoxins containing zinc

Ferredoxins from thermoacidophilic archaea such as *Thermoplasma acidophilum* and *Sulfolobus* sp. contain, in addition to one 3Fe–4S (cluster I) and one 4Fe–4S (cluster II) cluster, one zinc centre tetrahedrally co-ordinated to three histidines in the N-terminal region and to one aspartate in the ferredoxin core domain.[139] These Fds contain an unusually long N-terminal extension region of unknown function, which was not detected in other bacterial type Fds. Upon oxidative degradation of Fd from *Sulfolobus* sp. strain 7 ($T_{opt} = 80\,^{\circ}C$)[140] cluster II is selectively converted into a cubane 3Fe–4S, generating a stable intermediate containing two 3Fe–4S clusters and a zinc centre, without leading to a significant structural rearrangement of the protein. The determinants of thermostability for this class of proteins have not yet been investigated.

5.1.3. *Cytochromes*

Cytochromes are electron-transfer proteins having one or several haem groups. Cytochrome *c* binds to the protein by one or, more commonly two, thioether bonds involving sulphydryl groups of cysteine residues. The fifth haem iron ligand is always provided by a histidine residue. Cytochrome *c* has been proved to be a useful model system for studying the relationship between protein structure and thermostability due to the availability of its three-dimensional structure from a wide variety of organisms, both mesophiles and thermophiles.

Cytochrome *c*-552 (*Htc*-552) from the thermophilic hydrogen oxidizing bacterium *Hydrogenobacter thermophilus* is an 80 amino acid protein with a haem covalently attached to the polypeptide chain, which shows 56% sequence identity to an 82 amino acid monohaem cytochrome *c*-551 (*Pac*-551) from mesophilic *Pseudomonas aeruginosas*. The main folding of these proteins is almost the same although *Htc*-552 is more stable to heat than *Pac*-551 as expected from the different optimal growth temperatures of *H. thermophilus* and *P. aeruginosas* (70 °C and 37 °C, respectively). Both X-ray crystallography and high-resolution NMR spectroscopy have been used to determine the structures of the mesophilic[141,142] and thermophilic[143,144] cytochromes.

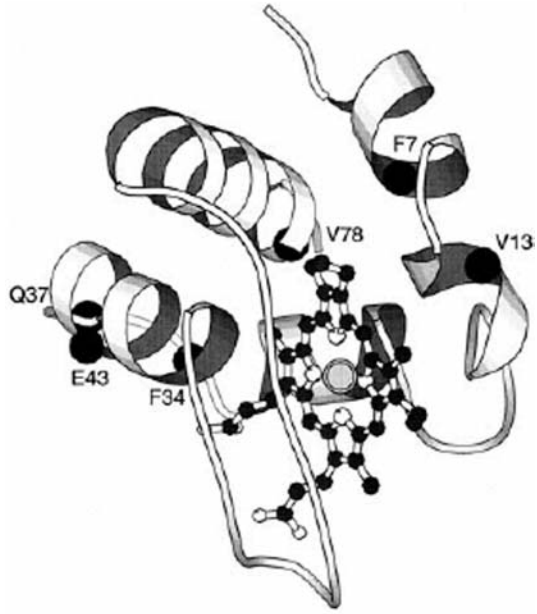

Fig. 2. Schematic view of mutation points in cytochrome *Pac*-551. The position of α carbon atoms of the mutated residues are shown by closed circles. Haem iron is indicated as double lined circle. The atomic co-ordinated for *Pac*-551 were taken from Protein Data Bank (code 451C). Reprinted with permission from *J. Biol. Chem*., Vol. 274, J. Hasegawa, H. Shimahara, M. Mizutani, S. Uchiyama, H. Arai, M. Ishii, Y. Kobayashi, S. J. Ferguson, Y. Sambongi and Y. Igarashi, 1999, p. 37,533.

The high thermostability in the thermophilic counterpart was due to amino acid residues located in three distal regions of the protein as shown in Fig. 2.[145] The introduction of five selected mutations in those regions of *Pac*-551 caused the protein to attain a similar thermostability to that of the thermophilic protein probably due to a tighter side chain packing and increased total accessible surface area.[146]

Htc-552 when expressed in *E. coli* undergoes spontaneous cytoplasmatic maturation (covalent haem attachment), in contrast to the usual periplasmatic maturation route for bacteria. NMR spectroscopy together with other techniques were employed to characterize *Htc*-552 expressed in the cytoplasm and periplasm of *E. coli*. It was shown that the cytoplasmatic product exhibits lower thermostability ($T_m = 85\,^{\circ}C$ compared to the periplasmatic $T_m = 90\,^{\circ}C$) because of structural anomalies in the region of the N-terminal helix, due to the retention of the N-terminal methionine and not to haem attachment errors.[147]

The solution structures of the reduced and oxidized forms of a biologically fully active 10.5 kDa fragment of the *Paracoccus denitrificans* cytochrome *c-552* enriched with ^{13}C and ^{15}N isotopes were obtained. No significant

redox-induced differences have been observed with regard to either the structural fold or backbone dynamics within the ps/ns timescale. Nevertheless, the oxidized protein was much less stable compared to the reduced form, displaying a considerably lower transition temperature (34 °C compared to 77 °C) and a much faster exchange of backbone amide protons.[148]

The solution structure of the 87-residue cytochrome c_6 from the thermophilic cyanobacterium *Synechococcus elongatus* (optimal temperature for photosynthetic activity = 57 °C) was determined by multidimensional NMR spectroscopy and molecular dynamics calculations and exhibited the overall topology of class I *c* cytochromes with four α-helices and a small antiparallel β-sheet near Met58, one of the axial haem ligands.[149]

5.1.4. *Thioredoxins*

Thioredoxins (Trx) are small disulphide-containing redox proteins, typically with a molecular weight of 10–12 kDa and an acidic pI. Thioredoxin is a remarkable stable protein showing particularly high denaturation temperature ($T_m = 88$ °C for *E. coli*; $T_m = 91$ °C for human; $T_m = 76$ °C for human–*E. coli* hybrid; $T_m = 103$ °C for *Bacillus acidocaldarius*).[150] The three-dimensional structures of thioredoxins from different origins have been determined either by X-ray crystallography or NMR spectroscopy, showing a common fold including a central core of five β-strands surrounded by four α-helices.[151–156] The solution structure of a thioredoxin from *B. acidocaldarius* ($T_{opt} = 60$ °C) has been studied by NMR and compared with that of *E. coli* determined by X-ray analysis. It was found that the higher thermostability of the former is due to cumulative effects, the main factor being an increased number of ionic interactions cross-linking different secondary structural elements.[157] Multidimensional heteronuclear NMR spectroscopy was also employed to characterize thioredoxin homologues found in the hyperthermophilic archaeon *Methanococcus jannaschii* (*Mj*0307; $T_{opt} = 80$ °C)[158,159] and the thermophilic archaebacterium *Methanobacterium thermoautotrophicum* (*Mt*H895; $T_{opt} = 65$ °C).[160]

5.2. Nucleic-acid related proteins

5.2.1. *DNA- and RNA-binding proteins*

Small basic DNA-binding proteins are believed to be involved in the packing and unpacking, maintenance and control of the genomic DNA. Some of these proteins are related to histones whereas others are believed to have more specialized functions, such as to bend the DNA at specific sites.

The protein high homologous (HU) binds non-specifically to both single- and double-stranded DNA as well as to RNA. The HU protein from *Bacillus stearothermophilus* (*Bst*HU) ($T_{opt} = 55$–60 °C) consists of two identical

monomers of 90 amino acids and its solution structure has been determined by NMR.[161,162] The region of residues 55–74 forms an antiparallel β-hairpin arm which is involved in the DNA-binding as confirmed by photochemically induced nuclear polarization (photo-CIDNP) measurements,[163] dynamic studies[164,165] and calculation of its dipole moment.[166] Site-directed mutagenesis was employed to evaluate the contribution of amino acid residues on the thermostability of *Bst*HU and it was found that certain residues (Gly15, Ala27, Glu34, Lys 38, Val42) were essential for its thermostability.[167–169]

Sac7 is a group of 7 kDa DNA-binding proteins from the archaeon *Sulfolobus acidocaldarius* ($T_{opt} = 70–80\,^{\circ}C$), individually referred to as Sac7a to Sac7e in order of increasing basicity.[170] The function of Sac7d, the most abundant form of the Sac7 proteins, *in vivo* is unknown. The protein binds DNA to form nucleoprotein complexes and probably plays a role in DNA packing and duplex stabilization in archaeabacteria at high temperatures. Sac7 proteins are in fact remarkably thermostable with an unfolding midpoint temperature at pH 7 near 100 °C. The solution structure of Sac7d was determined by NMR[171] and it was suggested that monomethylation of Lys5 and Lys7 could be associated with enhanced thermostability, whereas Trp24 could be implicated in DNA-binding.[170,171] Recently, molecular dynamic simulation studies have given more emphasis to the role of a network of salt bridges as a stabilizing force for the hyperthermophilic Sac7d at elevated temperatures.[172]

Sso7d is a 7 kDa DNA-binding protein isolated from the archaeon *Sulfolobus solfataricus* ($T_{opt} = 87\,^{\circ}C$) possibly involved in protection of the genetic material from thermal denaturation. The solution structure of natural and recombinant Sso7d has been determined.[173,174] ^{15}N- and ^{13}C-labelled Sso7d was employed to carry out NMR studies of protein–DNA complexes, in order to characterize the DNA-binding surface of Sso7d and to propose a model for the complex architecture.[175,176] A protein from *Sulfolobus solfataricus*, which was later recognized to be identical to Sso7d, has been suggested to act also as a ribonuclease and will be discussed in Section 5.4.1. Recently, an NMR study has indicated that an extensive network of salt bridges is important in conferring thermostability to Sso7d protein.[177]

Transcription factor IIB (TFIIB) is an essential component of the transcription complex and facilitates the recruitment of RNA polymerase (RNAP) through a zinc-binding motif near the N-terminus. *Pf*TFIIB from the hyperthermophilic *Pyrococcus furiosus* ($T_{opt} = 100\,^{\circ}C$) possesses high thermal stability and its N-terminal 1–49 fragment has been structurally characterized by NMR.[178] The global fold was found to be very similar to that of the C-terminal zinc-ribbon domain of the human transcription elongation factor, *h*TFIIS, previously determined by NMR,[179] although the triple-stranded β-sheet of the archaeal protein is shorter than that of *h*TF. The determinants of thermostability were not investigated. In a following work, the human N-terminal fragment 2–59 TFIIB was independently studied by NMR and

compared with the homologous proteins from archaea and eukarya, including *Pf*TFIIB.[180] The authors suggested that the zinc-ribbon structure might increase the stability of the β-sheet.

Protein SRP19 is an essential RNA-binding component of the signal recognition particle in archaea and eukarya. The solution structure of the 104 residues SRP19 from the hyperthermophilic *Archaeoglobus fulgidus* ($T_{opt} = 83\,^{\circ}C$) was determined by NMR indicating a secondary structure topology of the $\beta\alpha\beta\beta\alpha$ type.[181,182]

Aminoacyl-tRNA synthetases are key enzymes in protein biosynthesis. For a correct translation of the genetic code, the enzyme must recognize different molecules such as amino acids and the corresponding tRNA. The crystal structure of the homodimeric tyrosyl-tRNA synthetase from *Bacillus stearothermophilus* ($T_{opt} = 55$–$60\,^{\circ}C$) revealed the presence of three domains.[183] The C-terminal domain (residues 320–419) interacts with the anticodon arm of tRNA and is essential for binding and charging tRNA. The structure of the C-terminal domain has been determined by NMR spectroscopy and has been shown to consist of a five-stranded β-sheet packed against two α helices on one side and one α helix on the other side.[184,185] A large part of the domain has been found to be structurally similar to other families of RNA-binding proteins.

5.2.2. *Histones*

Archaeal histones are small, basic DNA-binding proteins that wrap DNA into nucleosome-like structures increasing the melting temperature of DNA molecules *in vitro* of $\sim 20\,^{\circ}C$. Despite the terminology, archaeal histones bear no sequence or structural resemblance to bacterial 'histone-like' proteins such as HU. They range in length from 66 to 69 residues and they have been purified and characterized from mesophilic, thermophilic and hyperthermophilic micro-organisms,[186] thus becoming good models for studying the factors conferring stability to proteins at extreme temperatures. In particular, the best characterized histones are those from the hyperthermophilic *Methanothermus fervidus* (*Mf*H) which grows optimally at $83\,^{\circ}C$. *Mf*H preparations contain two polypeptides, *Mf*HA and *Mf*HB, which may form homodimers and heterodimers. The solution structure of the recombinant $(MfHB)_2$ has been determined using homonuclear-correlated, ^{15}N-double resonance and ^{15}N, ^{13}C triple resonance NMR experiments.[187] It was found that the monomer consisted of three α-helices and two short segments of β-strand similar to the canonical 'histone fold', as confirmed later by crystallographic studies.[188] In the same work, two hydrophobic 'proline Ncaps', four inter-helical hydrogen bonds and short N- and C-terminal disordered tails were predicted to impart thermal stability to the protein. The comparison of the NMR structure of *Mf*HB with that of the homologous protein from the mesophile *Methanobacterium formicicum* (*MFo*HB) has suggested that the lower stability of the latter resulted from unfavourable

surface-located ionic interactions and a larger, more solvent-accessible cavity within the hydrophobic core.[189]

5.2.3. *Ribosomal proteins*

Ribosomes are essential for protein synthesis in all living cells and they consist of two subunits, each composed of RNA molecules and proteins. The large subunit includes two RNA molecules and 34 proteins (called L1–L34) whereas the small subunit includes one RNA molecule and 21 proteins (called S1–S21). Molecular mechanisms of translation cannot be understood without a detailed knowledge of the structure of ribosomal components. Thus, structural studies have been focusing on ribosomal proteins, many of which are from thermophilic organisms such as *Bacillus stearothermophilus* ($T_{opt} = 55$–$60\,^{\circ}C$) and *Thermus thermophilus* ($T_{opt} = 75\,^{\circ}C$). Multidimensional homonuclear and heteronuclear NMR spectroscopy has been employed to solve the secondary and tertiary structures of several ribosome proteins and to recognize their RNA-binding sites. The most relevant works on ribosomal proteins from thermophilic organisms are listed in Table 2.

The structure of the ribosomal protein L9 from *B. stearothermophilus* is shown in Fig. 3. The folding kinetics and thermodynamics of its C-terminal domain have been studied as a function of pH by NMR and CD spectroscopies. The ionization state of the two histidines (His106 and His134) was found to be essential for the global stability and the folding rate of the protein.[208]

The ribosome recycling factor (RRF) is a 21 kDa protein which is involved in the termination step of protein biosynthesis and catalyses the breakdown of the post termination complex into ribosome, tRNA and mRNA. The solution structure of RRF from the hyperthermophilic bacterium *Aquifex aeolicus* ($T_{opt} = 85\,^{\circ}C$) was determined by heteronuclear multidimensional NMR spectroscopy,[209] whereas the backbone NMR assignment was recently carried out for RRF from *Themotoga maritima*[210] and *Thermus thermophilus*.[211]

Table 2. NMR studies of thermostable ribosomal proteins

Protein	Origin	Reference
L9	*Bacillus stearothermophilus*	190–192
L11	*B. stearothermophilus*	193–195
L11	*Thermus thermophilus*	196
L18	*T. thermophilus*	197,198
L36	*T. thermophilus*	199
S4	*B. stearothermophilus*	200–202
S15	*T. thermophilus*	203
S16	*T. thermophilus*	204
S17	*B. stearothermophilus*	205
S19	*T. thermophilus*	206,207

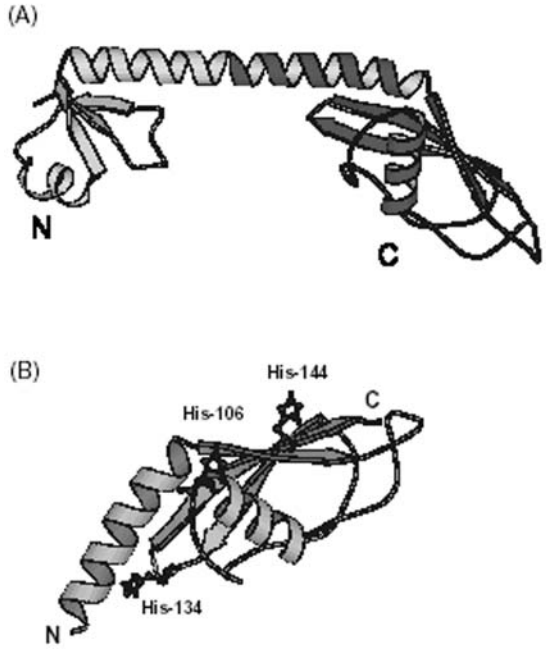

Fig. 3. (A) Ribbon diagram of ribosomal L9 protein from *B. stearothermophilus*. The N- and C-terminal domains are labelled. The C-terminal construct consisting of residues 58–149 is shaded. (B) Ribbon diagram of the C-terminal domain showing the location of the three histidine residues. Reprinted from *J. Mol. Biol.*, Vol. 318, S. Sato and D. P. Raleigh, 'pH-dependent stability and folding kinetics of a protein with an unusual alpha-beta topology: The C-terminal domain of the ribosomal protein L9', pp. 571–582, Copyright 2002, with permission from Elsevier Science.

The small protein B (SmpB) is an essential component of the tmRNA-SmpB system used by prokaryotes for releasing stalled ribosome from damaged messanger RNAs and targeting incompletely synthesized protein fragments for degradation. The solution structure of SmpB from the thermophilic *A. aeolicus* was solved by NMR.[212]

5.3. Thermally induced proteins

Some proteins, generally with limited molecular weight, are expressed at high levels as a response to thermal shocks.

Cold-shock proteins (Csps) are transiently expressed at a higher level in bacteria as a response to an abrupt decrease from normal physiological temperature. Their exact biological function is still unknown, but translational regulation, possibly via RNA chaperoning, has been discussed.[213,214] Csps from mesophiles and thermophiles differ widely in their stability, but show

close structural similarity, becoming an ideal system to study differences in a single protein family derived from mesophilic, thermophilic and hyperthermophilic organisms. NMR and X-ray studies have been carried out for *Ec*CspA from *E.coli*[215–218] ($T_{opt} = 37\,^{\circ}C$), *Bs*CspB from *Bacillus subtilis*[219,220] ($T_{opt} = 37\,^{\circ}C$), *Bc*CspB from the thermophilic *Bacillus caldolyticus*[221] ($T_{opt} = 72\,^{\circ}C$) and the *Tm*Csp from the hyperthermophilic *Thermotoga maritima*[222] ($T_{opt} = 90\,^{\circ}C$). The latter is the only Csp from a hyperthermophilic organism whose structure has been studied by NMR so far. The 66 residue *Tm*Csp has been found to be a globular protein, forming a closed β barrel consisting of five β-strands, the first four, showing a Greek-key fold (Fig. 4).[222] It has been suggested that the higher stability of *Tm*Csp with respect to its mesophilic and moderately thermophilic counterparts was due to a peripheral ion cluster around the side chain of Arg2 (Asp20–Arg2–Glu47–Lys63) (Fig. 4C) and to a hydrophobic stacking of side chains at the surface area.[46,222,223]

^{19}F NMR was used to monitor the folding kinetics of *Tm*Csp labelled with 5-fluorotryptophan.[224] It was found that the increased thermostability of *Tm*Csp ($T_m = 87\,^{\circ}C$) compared to *Bs*CspB ($T_m = 52\,^{\circ}C$) was due to lower unfolding rate constants over a wide temperature range. This suggested that entropic factors play an important role in the thermostabilization of *Tm*Csp.

Heat-shock proteins (Hsps) are proteins expressed virtually in all organisms as a response of exposure to a stress, such as elevated temperature (fever), protein degradation, mechanical or chemical stress. As chaperone proteins they are concerned with the intracellular folding and refolding, assembly and translocation of damaged proteins.

The eye lens α-crystallins have been suggested to stabilize other proteins under conditions of stress (i.e., heating, oxidation, denaturant), thus preventing their precipitation.[225] Several NMR studies have been carried out on α-crystallin and recently reviewed by Carter.[226] Despite its relatively large size (average mass of around 800 kDa), α-crystallin gives rise to well-resolved NMR spectra arising from the C-terminal extension which is particularly flexible. This extension has been found to be common to other Hsps and is thought to be important for chaperone activity. An NMR and fluorescence study on mutants of α-crystallin has shown that insertion of a hydrophobic tryptophan residue in the C-terminal extension led to a marked reduction in thermostability and chaperone activity.[227]

A combination of crystallographic and NMR methods was used to obtain the high-resolution structure of the domain of a Hsp from the thermophilic *T. thermophilus* ($T_m > 100\,^{\circ}C$) and to compare it to the homologous domain of Hsp from *E. coli* ($T_m = 65\,^{\circ}C$). It was found that the structure of the domain of the *T. thermophilus* Hsp contained additional salt bridges which could be responsible for the higher thermostability.[228]

Although not directly related to protein thermostability, several NMR studies have been also carried out on other Hsps such as mouse Hsp25,[229,230] *E. coli* Hsp40[231–237] and mammalian Hsp70.[238–240]

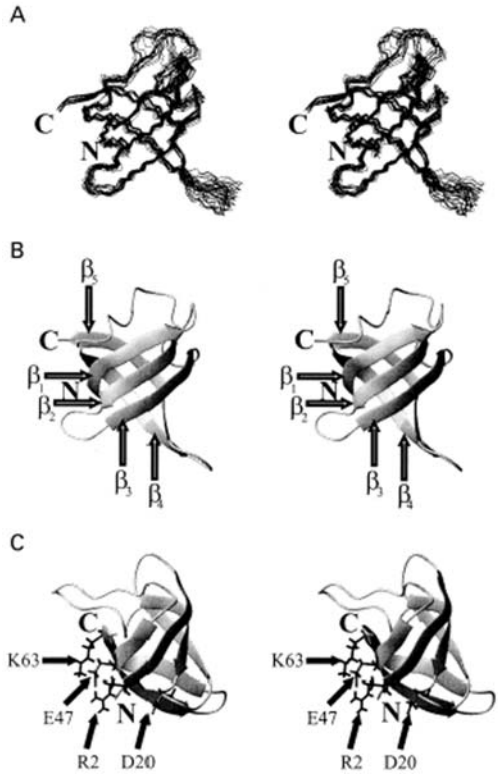

Fig. 4. Stereoviews of *Tm*Csp. (A) Stereoview of a superposition of the backbone atoms of the 21 accepted structures of *Tm*Csp. (B) Stereoview of a representative ribbon diagram of *Tm*Csp. The secondary-structure elements are indicated. (C) Stereoview of the solution NMR structure of *Tm*Csp (rotated ribbon diagram). Location of a possible peripheral ion cluster. Reprinted from *Eur. J. Biochem.*, Vol. 268, W. Kremer, B. Schuler, S. Harrieder, M. Geyer, W. Gronwald, C. Welker, R. Jaenicke and H. R. Kalbitzer, 'Solution NMR structure of the cold-shock protein from the hyperthermophilic bacterium *Thermotoga maritima*', pp. 2527–2539, Copyright 2001, with permission from Blackwell Science.

5.4. Enzymes

5.4.1. *Ribonucleases*

In recent years, several papers appeared in the literature concerning NMR and X-ray studies of thermostable ribonucleases. Among archaebacteria, several histone-like proteins from *Sulfolobus* strains have been identified and grouped into molecular mass classes. From the 7 kDa class, Sac7e from *S. acidocaldarius* and Sso7d from *S. solfataricus*, possessing DNA binding activity in combination with non-specific RNase activity, were identified.[241,242]

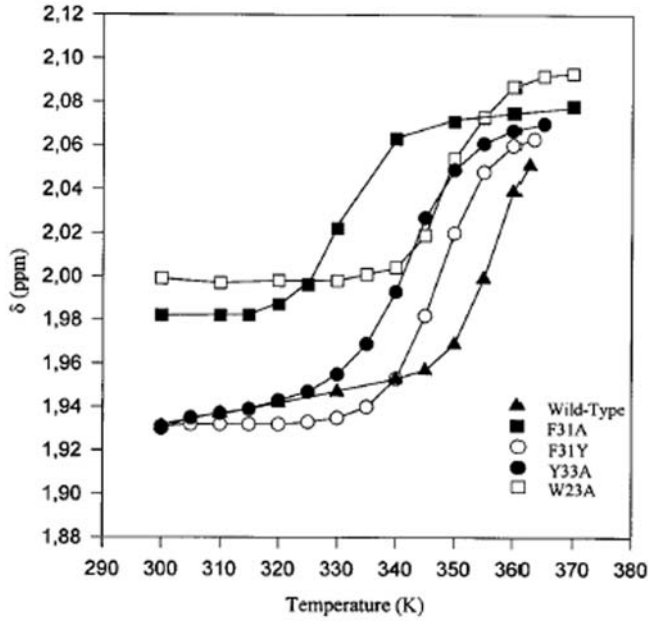

Fig. 5. NMR thermal denaturation profiles of the Sso7d wild type and its Phe31Ala, Phe31Tyr, Tyr23Ala and Trp33Ala mutants determined by monitoring changes in ^{1}H chemical shifts of the methyl resonances of Met57. Reprinted with permission from *Biochemistry*, Vol. 38, R. Consonni, L. Santomo, P. Fusi, P. Tortora and L. Zetta, 1999, p. 12,709. Copyright (1999) American Chemical Society.

The stability determinants of recombinant Sso7d and its mutants have been investigated by means of NMR (thermostability, $T_m > 88\,^{\circ}C$) and FTIR (piezostability, $P_m > 14$ Kbar) spectroscopies.[243] In addition to a very compact hydrophobic core and an aromatic cluster of three-membered-pairs of aromatic rings displaying a fishbone geometry, an extensive network of salt bridges has been found on the surface of the protein which could confer high stability to the protein.[177] Single point mutations of Phe31, which is involved in the aromatic cluster of the protein core, induced destabilization of the protein as shown in Fig. 5 by the NMR thermal denaturation profiles.[174] In particular, the mutant Phe31Ala was dramatically destabilized, with a loss of thermostability and piezostability of at least 27 °C and 10 kBar, respectively. The solution structure of this mutant was determined by NMR.[174] The most remarkable feature found in the structure was the change in orientation of the aromatic ring of residues belonging to the aromatic core which prevented the formation of a cavity in the hydrophobic core. The same mutation produced additional changes, notably a strong distortion in the β-sheet, the loss of several H-bonds, increased flexibility of some backbone stretches and some local strains.

Ribonuclease H is a small, single domain protein that cleaves RNA from RNA–DNA hybrids. RNase H from *E. coli* ($T_m = 66\,^{\circ}C$) has been structurally studied by ^{15}N NMR spectroscopy.[244] Hydrogen exchange NMR experiments have been used to examine the structural distribution of stability in RNase H from *T. thermophilus* ($T_m = 86\,^{\circ}C$) and to compare its stability with that of the homologous RNase H from the mesophilic *E. coli*.[245] The general distribution of stability was found to be similar in the two proteins at the optimal growth temperature of their host organisms. This feature indicated that the structural distribution of stability is an intrinsic property of the protein fold and that almost every region of the molecule contributed equally.

5.4.2. *RNA polymerases*

RNA polymerases (RNAPs) are multisubunit enzymes which play a fundamental role in the gene expression of every organism. The eukaryotic RNAPs are complex enzymes containing between 12 and 18 different subunits, called RPBs, whereas bacteria and archaea RNAPs are single enzymes containing 4 and 12 subunits, respectively. NMR investigations on thermostable RNAPs are quite recent and deal with single RPB subunit or RPB fragments. Particular attention has been devoted to the structural characterization of RPB subunits containing zinc ions, which are required for the RNAP function.

The C-terminal Zn-binding domain (residues 58–110 in the intact protein) of RBP9 from the hyperthermophilic archaeon *Thermococcus celer* was investigated by multidimensional NMR spectroscopy and compared with the homologous motif present in the two transcription factors of the human TFIIB and yeast TFIIS proteins.[246] The structure was found to be stable at least up to $80\,^{\circ}C$ and consisted of a zinc-ribbon with an apical tetrahedral Zn-binding site ($CX_2CX_{24}CX_2C$), a central β-sheet and a disordered loop. Structural differences were observed from the comparison, although no structural basis of thermal stability was determined. Despite the lack of a globular hydrophobic core, the two surfaces of the β-sheet contain well-ordered aromatic rings engaged in serial edge-to-face interactions. It has been speculated that the aromatic-rich surface contributes to the RBP9 thermodynamic stability and provides a nucleic acid binding site in the archaeal and eukaryotic transcriptional machinery.[247]

The subunit RPB10 (55–80 amino acid residues) is required for cell growth and displays a high level of conservation across archaea and eukarya. However, little is known about the role of this subunit in transcription. An NMR structure determination of the double enriched ^{13}C, ^{15}N recombinant *Mt*RPB10 from *M. thermoautotrophicum* ($T_m = 85\,^{\circ}C$) revealed a topology consisting of three α-helices stabilized by a zinc ion.[248] The metal ion is bound within an atypical CX_2CX_nCC metal binding motif, which was termed a zinc-bundle. Inspection of the surface features of this subunit demonstrated that *Mt*RPB10 had a distinctly dipolar charge distribution together with a

neutral region, which has been suggested to possibly serve as a protein-binding interface.

The RPB5 subunit seems to play a fundamental role in transcription, both in archaea and in eukaryotes. The solution structure of the *Mj*RPB5 subunit (79 amino acid residues) from the hyperthermophilic archaeon *Methanococcus jannaschii* ($T_{opt} = 85\,^{\circ}C$) revealed a novel fold consisting of a four-stranded mixed β-sheet flanked on one side by three short helices.[249] In a different study, the solution structure of *Mt*RPB5 (77 amino acid residues, $T_m = 85\,^{\circ}C$) from the archaeon *M. thermoautotrophicum* was elucidated and found to consist of a four-stranded β-sheet flanked on each side by two short helices, resulting in an overall mushroom shape that did not appear to have any homologues in the structural database.[250] While the secondary structure and the β-sheet topology of the two RPB5 subunits were similar, the tertiary structure differed significantly. The presence of surface ion pairs, conserved in other thermophilic archaeal, but not in eukaryal or viral RPB5s, has been suggested to contribute to the high thermal stability of the *Mt*RPB5 subunit.

The C-terminal domain (85 amino acid residues, not completely denatured at 90 °C) of the so-called α subunit of the RNAP from the extremely thermophilic eubacterium *T. thermophilus* (*Tt*) has been expressed uniformly $^{15}N/^{13}C$-labelled and structurally characterized by the NMR spectroscopy.[251] The tertiary structure of the domain, comprising a helical turn and four helices, was found to be almost identical to that of the corresponding domain from the mesophilic *E. coli*, despite 32% sequence homology. The interaction of the *Tt* domain with a variety of DNAs at 37 °C and 50 °C was investigated by chemical shift perturbation of the NMR signals and the DNA binding site was localized.[251]

5.4.3. *Multi enzyme complexes*

Cellulolytic micro-organisms produce enzymatic systems capable of degrading cellulose. These systems comprise multiple types of cellulases known to act synergistically to degrade cellulose. Some micro-organisms produce enzymes containing a carbohydrate-binding module (CBM) and a catalytic module within a single polypeptide chain. CBM binds to the plant cell wall bringing these enzymes into prolonged and intimate proximity with their target substrates, thus increasing the efficiency of catalysis. On the contrary, the cellulose systems of other micro-organisms are characterized by large multi-component protein assemblies named 'cellulosomes' in which the enzymes are incorporated into a multisubunit complex.

Several NMR studies have been carried out in order to reveal the three-dimensional structure of CBMs and to understand the mechanism by which CBMs from thermophilic organisms bind to their polysaccharide ligands (CBM22,[252,253] CBM4,[254] and CBM4-2[255–257]). It has been found that CBMs are composed mainly of β-strand and contain a planar hydrophobic platform comprising aromatic residues that bind to the surface of the polysaccharide.

Within the cellulosome complex, type I dockerin domain is responsible for incorporating its associated glycosyl hydrolase in the bacterial cellulosome via interaction with a reception domain, the cohesin domain. The three-dimensional solution structure of the 69-residue dockerin domain from the thermophilic *Clostridium thermocellum* ($T_{opt} = 55–65\,^{\circ}C$) was solved by NMR and was found to consist of two Ca^{2+}-binding loop-helix motifs connected by a linker.[258,259] Each Ca^{2+}-binding subdomain is stabilized by a cluster of buried hydrophobic sidechains. Recently, the NMR sequence-specific resonance assignment of type II cohesin module from *C. thermocellum* has been published.[260]

The pyruvate dehydrogenase multienzyme complex catalyses the oxidative decarboxylation of pyruvate, producing carbon dioxide and acetyl-CoA. The peripheral subunit-binding domain from the dihydrolipoamide acetyltransferase component (E2) of the pyruvate dehydrogenase multienzyme complex from the thermophilic *Bacillus stearothermophilus* ($T_{opt} = 55–60\,^{\circ}C$) is stably folded, despite its short sequence of only 43 amino acid residues. Its three-dimensional structure has been determined by means of a multi-cooling dynamical simulated annealing protocol using restraints derived from the ^{1}H NMR spectroscopy.[261] A 41 residue peptide derived from this domain, psbd41, undergoes a co-operative thermal unfolding transition with a T_m of $54\,^{\circ}C$. A mutant peptide, in which the buried Asp34 is replaced by asparagine still folds co-operatively, but is much less thermostable than the wild-type. NMR spectroscopy and ANS titrations showed that Asp34 is vital for the stability and specificity of this structure, which folds in the absence of disulphide bonds or metal or ligand-binding sites.[262] The folding and unfolding rates of psbd41 measured using dynamic NMR lineshape analysis indicated a very fast folding rate for this domain.[263] The study of shorter domains, psbd36 and psbd33, indicated that more than 33 residues are required for the protein to adopt a fully stable native structure, although the entire sequence is not required for folding.[264] Several studies have also been devoted to the investigation of the three-dimensional structure of the larger lipolyl domain of *B. stearothermophilus* pyruvate dehydrogenase multienzyme complex, combining multi-dimensional NMR spectroscopy, T_2 relaxation experiments and site-directed mutagenesis.[265–268]

5.5. Prion

With the background of the 'mad cow crisis' in Europe, questions relating to the prion diseases have attracted intensive interest. It is now widely accepted that prion diseases, such as Creutzfeldt-Jakob disease (CJd) in humans and bovine spongiform encephalopathy (BSE) are caused by a conformational change of the prion protein (PrP) from a normally folded cellular form, PrP^{C}, to an alternate, aggregation-prone, pathogenic scrapie form, PrP^{Sc}.[269]

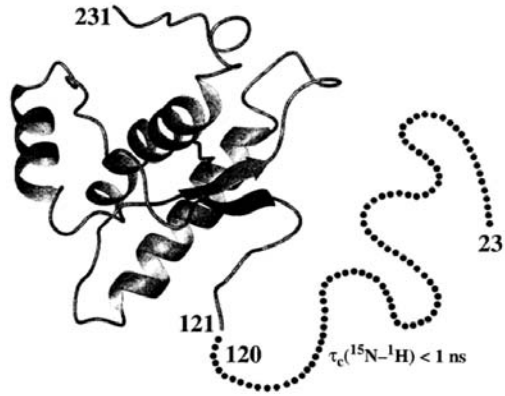

Fig. 6. Global structural characterization of *m*PrP(23–231). Dots represent the 98 residues of the N-terminal segment 23–120, which shows features of a flexible, random coil-like polypeptide with rotational correlation times for the ^{15}N–^1H groups of $\tau_c < 1$ ns. Reprinted from *FEBS Lett*., Vol. 413, R. Riek, S. Hornemann, G. Wider, R. Glockshuber and K. Wüthrich, 'NMR characterization of full-length recombinant murine prion protein, mPrP(23–231)', pp. 282–288, Copyright 1997, with permission from Elsevier Science.

Although PrP^C and PrP^{Sc} have identical amino acid sequences, they have profoundly different secondary, tertiary and quaternary structures. PrP^C is mainly α-helix and monomeric, whereas PrP^{Sc} is much richer in β-sheets and oligomeric.[269] Prion is highly resistant to inactivation by heat. The denaturation midpoint temperature of human PrP has been found to be around 70 °C,[270] whereas strains derived from sheep showed inactivation temperatures of up to 97 °C.[271] For inactivation of *scrapie* and BSE agents in meat and bone meals, EU recommendations consider effective processing conditions including treatment at temperatures higher than 133 °C for 20 min and 3 bars of pressure.[272,273] Since no suitable crystals for X-ray structure determination of prion proteins have so far been obtained, NMR has been the main technique used for structural studies of these proteins.

NMR characterization of the recombinant mouse,[274–276] hamster,[277–280] bovine[281] and human[282] prion proteins showed that all these molecules share a common architecture, consisting of a flexible unstructured N-terminal 'tail' of about 100 residues from position 23 to position 124 attached to a globular domain within residues 125–228. The globular domain contains a double-stranded anti-parallel β-sheet and three α-helices (Fig. 6).

Several NMR studies were carried out to gain insight into the molecular basis for the conversion of the PrP^C into the pathogenic conformer, PrP^{Sc}. They mainly involve the study of prion-derived peptides believed to be essential for prion propagation,[283–288] although other studies also include the investigation of the whole prion protein[289,290] and prion mutants.[291–294]

Recently, high-pressure NMR measurements have enabled us to identify an intermediate conformer of the hamster prion protein, which has been suggested to be the PrP* factor responsible for the PrP^{C}/PrP^{Sc} conversion or a closely related precursor.[295]

5.6. Villin and villin domains

The f-actin bundling protein villin is implicated in the formation of microvilli in the absorbtive epithelium of the gut and the proximal tube of the kidney. Villin comprises two domains: a 'core' domain of 84 kDa and a small 8 kDa C-terminal domain called 'headpiece'. Each of these domains contains an f-actin binding site, enabling villin to crosslink actin filaments into the structural bundle that supports the microvillar membrane. The headpiece comprises 76 amino acid residues and binds f-actin in the absence of the core domain. The thermal unfolding of headpiece is reversible and has a transition midpoint of 74 °C. McKnight and co-workers have studied the C-terminal 35-residue subdomain of villin headpiece which maintains similar ($T_m = 70$ °C) thermostability and retains full activity as the intact headpiece.[296,297] The structure of this villin subdomain was revealed by homonuclear and heteronuclear methods with a uniformly ^{15}N-enriched sample. It was found that the subdomain folds autonomously in a stable structure comprising three short helices surrounding a tightly packed hydrophobic core, thus defining a new protein fold. The role of aromatic residues in the hydrophobic core of the villin headpiece subdomain was studied by NMR spectroscopy and circular dichroism[298] whereas the temperature-dependent dynamics of the subdomain was studied by ^{15}N spin relaxation experiments.[299] NMR studies of a longer villin headpiece subdomain, comprising 67 residues, revealed two subdomains that share a tightly packed hydrophobic core. Two residues implicated in f-actin-binding form a buried salt-bridge between the two subdomains.[300] Other NMR works have been carried out on the villin structure although they did not directly study protein thermostability. They include investigations of the solution structure of villin C-terminal-domain[301] and N-terminal domain (14T),[302–306] in which two hydrophobic cores stabilize the interactions between a central β-sheet and the adjacent secondary structures (Fig. 7).

5.7. Sweet proteins

The design of safe sweeteners is very important for people who are affected by diabetes, hyperlipemia, caries and other diseases that are linked to sugar consumption. Sweet proteins, which are found in several tropical plants, are many times (100–100,000) sweeter than sucrose on a molar basis. Only a few sweet proteins are known: miraculin, monellin, thaumatin, curculin, mabinlin,

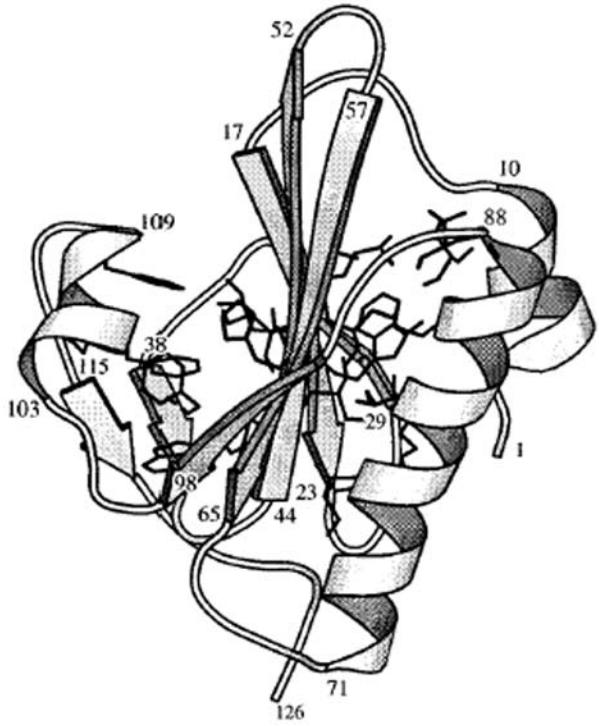

Fig. 7. Cartoon of villin 14T, based on the solution structure appearing in Refs. 302 and 305. Side chains constituting the two hydrophobic cores on either side of the central β-sheet are shown. Reprinted with permission from *Biochemistry*, Vol. 37, S. E. Choe, P. T. Matsudaira, J. Osterhout, G. Wagner and E. I. Shakhnovich, 1998, p. 14,508. Copyright (1998) American Chemical Society.

pentadin and brazzein, but only two have been studied from a structural point of view by NMR, monellin and brazzein. These proteins are thermostable, however they have been mainly studied in order to find a relation between structural conformations and sweetness.

Native monellin consists of two polypeptide chains, a 45-residue A-chain and a 50-residue B-chain, linked by non-covalent interactions.[307,308] At neutral pH, it is fairly resistant to heat denaturation with a T_m higher than 80 °C.[309] The crystal structure of native monellin shows a tertiary structure comprising an anti-parallel β-sheet with five strands and an α-helix.[310] ^{1}H NMR spectroscopy and hydrogen exchange methods have been used to characterize the alcohol-denaturated state of monellin in order to understand how its secondary structure depends on environmental conditions.[311] Structural and dynamic studies by NMR have been carried out in order to compare native monellin and a non-sweet analogue in which Asp^{B7} was replaced by Abu^{B7}. The three-dimensional structures of the two proteins are found to be very

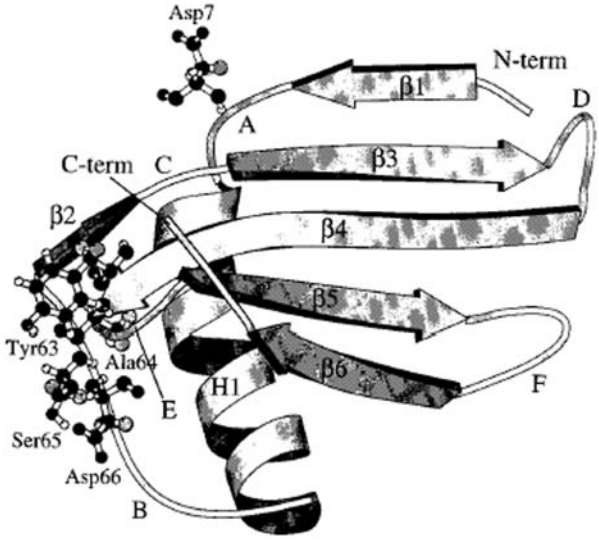

Fig. 8. Ribbon diagram of the restraint energy-minimized average structure of single-chain monellin displaying ordered secondary structure elements and relative orientation of secondary structures. The side chain atoms for residues thought to be responsible for sweetness and receptor binding are also displayed. Reprinted with permission from *Biochemistry*, Vol. 38, S. Y. Lee, J. H. Lee, H. J. Chang, J. M. Cho, J. W. Jung and W. Lee, 1999, p. 2340. Copyright (1999) American Chemical Society.

similar, but the flexibility was higher for native monellin, suggesting that the flexibility of Asp^{B7} may be important for receptor binding.[312]

An engineered single-chain monellin (SCM) constructed by fusing the two chains, A and B, covalently has been proved to retain all of the sweetening power and has a greater thermal stability.[309] SCM was studied by NMR both in solution (Fig. 8)[313,314] and in the solid-state.[315] Several SCM mutants were studied in order to investigate the origin of the taste of sweetness and it was found that residues Asp7 and Arg39 were closely correlated with changes in stability of secondary and tertiary structure.[316] The protein stability, activity and folding mechanisms of SCM and some mutants have also been investigated by heteronuclear NMR in the presence of guanidine hydrochloride.[317]

A second single-chain monellin (MNEI) was obtained linking the A and B chains via a Gly-Phe dipeptide and has been the object of solution NMR studies.[318,319] It is interesting that MNEI retains its activity at extreme pH and temperature conditions, i.e., it can be boiled for a short time without loosing sweetness. The secondary structure of MNEI is quite similar to those of native monellin and SCM: an α-helix cradled into the concave side of a five-strand anti-parallel β-sheet. The protein surface was investigated using an NMR paramagnetic probe and applying the enhanced Protein Hydration Observed through Gradient SpectroscopY (ePHOGSY) NMR experiment.[320] Since it

Table 3. NMR studies of several thermostable proteins

Protein	Source	T_m (°C)	Reference
Aqualysin I (serine protease)	*T. aquaticus* YT-1	70–72	331,332
Bovine pancreatic trypsin inhibitor (BPTI)	Bos taurus	84	333–339
Bet v 1(birch pollen allergen)	Birch pollen	66	340,341
CheW	*T. maritima*	>90	342
Curcubita maxima trypsin inhibitors (CMTI) – V	*Curcubita maxima*	71	343–348
Dissimilatory sulphite reductase	*Pyrobaculum aerophilum*	95	349
Llama antibody fragment	Llama	60	350
Lysozyme in glycerol	Hen egg-white	76	351
Peptide deformylase(zinc metalloprotease)	*E. coli*	>78	352–355
Phosphocarrier protein, HPr	*B. subtilis*	74	356,357
Stefin or cystatin (cysteine protease inhibitor)	Homo sapiens	95 (dimer form)	358–363
Streptomyces metallo proteinase inhibitor (SMPI)	*S. nigrescens*	Stable at 100 °C for 5 min	364,365
Streptomyces subtilisin inhibitor (SSI)	*Streptomyces* sp.	73	366–369
Stresgenin B (inhibitor of heat shock proteins)	*Streptomyces* sp. AS-9	88	370
Thermolysin (metalloprotease)	*B. thermoproteolyticus*	~70	371–373

has been reported that the three-dimensional structures of native monellin and two thiol proteinase inhibitors, cystatin and stefin B, are very similar,[321] it was suggested that monellin may have some other biological role beside its sweetness.

Brazzein is another small sweet-tasting protein whose solution structure has been recently solved by NMR.[322–324] Brazzein tastes 2000 times sweeter than sucrose on a weight basis and is exceptionally thermostable. As indicated by NMR, the structure of this 54 residue, single-chain polypeptide does not change between 32 and 82 °C and retains its sweetness after incubation at 98 °C for two hours.[322] Brazzein contains one α-helix and three strands of antiparallel β-sheet stabilized by four intramolecular disulphide bonds. It has been proposed that the disulphide bonds could be responsible for the thermostability of brazzein by forming a compact structure at the tertiary level.[324] The structure of brazzein does not resemble that of the other two sweet proteins with known structures, monellin and thaumatin, whereas sequence alignment and structural prediction indicate that brazzein shares the fold of a newly identified family of serine proteinase inhibitors.

5.8. Other thermostable proteins

The influx of genomic sequence information has led to the concept of structural proteomics, the determination of protein structures on a genome-wide scale. A structural proteomic project used the sequenced genome of the thermophilic *Methanobacterium thermoautotrophicum* as a source of targets for structure determination.[325] As expected, proteins from *M. thermoautotrophicum* possess high thermostability with a transition midpoint temperature between 68 and 98 °C. Small proteins were ^{13}C- and ^{15}N-labelled and their solution structures were solved using multinuclear and multidimensional NMR spectroscopy.[160,325–329] The project was also extended to some proteins from *Thermotoga maritima*.[330]

Several proteins from different sources have been shown to maintain stability at high temperatures and NMR studies have been carried out in order to reveal their structures and/or to understand their activity. The most relevant references of a miscellany of thermostable proteins are reported in Table 3. Some of them such as bovine pancreatic trypsin inhibitor (BPTI), thermolysin and lysozyme have been widely studied as model systems in protein science.

REFERENCES

1. C. Vieille, D. S. Burdette and J. G. Zeikus, *Biotechnol. Annu. Rev.*, 1996, **2**, 1.
2. C. Vieille and J. C. Zeikus, *Trends Biotechnol.*, 1996, **14**, 183.
3. M. W. W. Adams and R. M. Kelly, *Trends Biotechnol.*, 1998, **16**, 329.

4. M. J. Danson and D. W. Hough, *Trends Microbiol*., 1998, **6**, 307.
5. S. Witzmann and H. Bisswanger, *Biochim. Biophys. Acta*, 1998, **1385**, 341.
6. D. W. Hough and M. J. Danson, *Curr. Opin. Chem. Biol*., 1999, **3**, 39.
7. C. Vieille and G. J. Zeikus, *Microbiol. Mol. Biol. R*., 2001, **65**, 1.
8. R. J. M. Russell and G. L. Taylor, *Curr. Opin. Biotech*., 1995, **6**, 370.
9. A. Shaw and R. Bott, *Curr. Opin. Chem. Biol*., 1996, **6**, 546.
10. S. M. Malakauskas and S. L. Mayo, *Nat. Struct. Biol*., 1998, **5**, 470.
11. S. B. Petersen, P. H. Jonson, P. Fojan, E. I. Petersen, M. T. N. Petersen, S. Hansen, R. I. Ishak and E. Hough, *J. Biotechnol*., 1998, **66**, 11.
12. V. V. Loladze, B. Ibarra-Molero, J. M. Sanchez-Ruiz and G. I. Makhatadze, *Biochemistry*, 1999, **38**, 16419.
13. B. S. Hartley, N. Hanlon, R. J. Jackson and M. Rangarajan, *Biochim. Biophys. Acta*, 2000, **1543**, 294.
14. M. Lehmann, L. Pasamontes, S. F. Lassen and M. Wyss, *Biochim. Biophys. Acta*, 2000, **1543**, 408.
15. J. M. Sanchez-Ruiz and G. I. Makhatadze, *Trends Biotechnol*., 2001, **19**, 132.
16. K. M. Noll, *Encyclopedia Microbiol*., 1992, **1**, 149.
17. E. Blöchl, R. Rachel, S. Burggraf, D. Hafenbradl, H. W. Jannasch and K. O. Stetter, *Extremophiles*, 1997, **1**, 14.
18. K. O. Stetter, *Ciba Found. Symp*., 1996, **202**, 1.
19. K. O. Stetter, *FEBS Lett*., 1999, **452**, 22.
20. P. M. Hicks and R. M. Kelly, *Encyclopedia of Bioprocess Technology: Fermentation, Biocatalysis and Bioseparation*, M. C. Flickinger and S. W. Drew, eds., Wiley, Chichester, UK, 1999, 2536.
21. R. M. Kelly, T. L. Peeples, S. B. Halio, K. D. Rinker and G. D. Duffaud, *Ann. N.Y. Acad. Sci*., 1994, **745**, 409.
22. R. Jaenicke and P. Závodszky, *FEBS Lett*., 1990, **268**, 344.
23. R. Jaenicke, *Eur. J. Biochem*., 1991, **202**, 715.
24. B. W. Matthews, L. H. Weaver and W. H. Kester, *J. Biol. Chem*., 1974, **249**, 8030.
25. M. Perutz and H. Raidt, *Nature*, 1975, **255**, 256.
26. K. S. P. Yip, T. J. Stillman, K. L. Britton, P. J. Artymiuk, P. J. Baker, S. E. Sedelnikova, P. C. Engel, A. Pasquo, R. Chiaraluce, V. Consalvi, *Structure*, 1995, **3**, 1147.
27. K. S. P. Yip, K. L. Britton, T. J. Stillman, J. Lebbink, W. M. de Vos, F. T. Robb, C. Vetriani, D. Maeder and D. W. Rice, *Eur. J. Biochem*., 1998, **255**, 336.
28. A. H. Elcock, *J. Mol. Biol*., 1998, **284**, 489.
29. C. Vetriani, D. L. Maeder, N. Tolliday, K. S. P. Yip, T. J. Stillman, K. L. Britton, D. W. Rice, H. H. Klump and F. T. Robb, *Proc. Natl. Acad. Sci. USA*, 1998, **95**, 12300.
30. R. J. M. Russell, U. Gerike, M. J. Danson, D. W. Hough and G. L. Taylor, *Structure*, 1998, **6**, 351.
31. S. Kumar and R. Nussinov, *J. Mol. Biol*., 1999, **293**, 1241.
32. S. Kumar, B. Ma, C.-J. Tsai and R. Nussinov, *Proteins*, 2000, **38**, 368.
33. S. Kumar, C.-J. Tsai and R. Nussinov, *Protein Eng*., 2000, **13**, 179.
34. S. Kumar, C.-J. Tsai, B. Ma and R. Nussinov, *J. Biomol. Struct. Dyn*., 2000, **1**, 79.
35. C. Cambillau and J.-M. Claverie, *J. Biol. Chem*., 2000, **42**, 32383.
36. A. Karshikoff and R. Ladenstein, *Trends Biochem. Sci*., 2001, **26**, 550.
37. L. Xiao and B. Honig, *J. Mol. Biol*., 1999, **289**, 1435.
38. D. Perl, U. Mueller, U. Heinemann and F. X. Schmid, *Nat. Struct. Biol*., 2000, **7**, 380.
39. C. N. Pace, *Nat. Struct. Biol*., 2000, **7**, 345.
40. G. Vogt and P. Argos, *Fold. Des*., 1997, **2**, S40.
41. G. Vogt, S. Woell and P. Argos, *J. Mol. Biol*., 1997, **269**, 631.
42. S. Kumar, C.-J. Tsai and R. Nussinov, *Protein Eng*., 2000, **13**, 179.
43. M. M. Gromiha, *Biophys. Chem*., 2001, **91**, 71.
44. K. L. Britton, P. J. Baker, K. M. Borges, P. C. Engel, A. Pasquo, D. W. Rice, F. T. Robb, R. Scandurra, T. J. Stillman, K. S. Yip, *Eur. J. Biochem*., 1995, **229**, 688.

45. P. Haney, J. Konisky, K. K. Koretke, Z. Luthey-Schulten and P. G. Wolynes, *Proteins*, 1997, **28**, 117.
46. J. Chen, Z. Lu, J. Sakon and W. E. Stites, *J. Mol. Biol.*, 2000, **303**, 125.
47. N. Kannan and S. Vishveshwara, *Protein Eng.*, 2000, **13**, 753.
48. K. Watanabe, Y. Hata, H. Kizaki, Y. Katsube and Y. Suzuki, *J. Mol. Biol.*, 1997, **269**, 142.
49. O. Bogin, M. Peretz, Y. Hacham, Y. Korkhin, F. Frolow, A. J. Kalb (Gilboa) and Y. Burstein, *Protein Sci.*, 1998, **7**, 1156.
50. S. Kumar, C.-J. Tsai and R. Nussinov, *Protein Eng.*, 2000, **13**, 179.
51. C. Vieille, K. L. Epting, R. M. Kelly and G. Zeikus, *Eur. J. Biochem.*, 2001, **268**, 6291.
52. E. Christodoulou and C. E. Vorgias, *Extremophiles*, 2002, **6**, 21.
53. J. J. Tanner, R. M. Hecht and K. L. Krause, *Biochemistry*, 1996, **35**, 2597.
54. T. Salminem, A. Teplyakov, J. Kankare, B. S. Cooperman, R. Lahti and A. Goldman, *Protein Sci.*, 1996, **5**, 1014.
55. R. J. M. Russell, J. M. C. Ferguson, D. W. Hough, M. J. Danson and G. L. Taylor, *Biochemistry*, 1997, **36**, 9983.
56. E. Querol, J. A. Perez-Pons and A. Mozo-Villarias, *Protein Eng.*, 1996, **9**, 265.
57. R. Jaenicke and G. Bohm, *Curr. Opin. Struct. Biol.*, 1998, **8**, 738.
58. R. Ladenstein and G. Antranikian, *Adv. Biochem. Eng. Biotechnol.*, 1998, **61**, 37.
59. N. P. Fomenkova, N. A. Nevskaya, A. D. Nikulin and S. V. Nikonov, *Mol. Biol.*, 1998, **32**, 265.
60. S. Chakravarty and R. Varadarajan, *FEBS Lett.*, 2000, **470**, 65.
61. S. Kumar and R. Nussinov, *Cell. Mol. Life Sci.*, 2001, **58**, 1216.
62. A. Szilágyi and P. Závodszky, *Structure*, 2000, **8**, 493.
63. R. Sterner and W. Liebl, *Crit. Rev. Biochem. Mol.*, 2001, **36**, 39.
64. G. A. Petsko, *Methods in Enzymology*, Vol. 334, M. W. W. Adams and R. M. Kelly, eds., Academic Press, San Diego, 2001, 469.
65. H. Sticht and P. Rösch, *Prog. Biophys. Mol. Biol.*, 1998, **70**, 95.
66. B. J. Goodfellow and A. L. Macedo, *Annu. Rep. NMR Spectrosc.*, 1999, **37**, 119.
67. L. Banci, I. Bertini, K. L. Bren, M. A. Cremonini, H. B. Gray, C. Luchinat and P. Turano, *J. Biol. Inorg. Chem.*, 1996, **1**, 117.
68. L. Banci, I. Bertini, G. F. Savellini, A. Romagnoli, P. Turano, M. A. Cremonini, C. Luchinat and H. B. Gray, *Proteins*, 1997, **29**, 68.
69. L. Banci, I. Bertini, L. D. Eltis, I. C. Felli, D. H. W. Kastrau, C. Luchinat, M. Piccioli, R. Pierattelli and M. Smith, *Eur. J. Biochem.*, 1994, **225**, 715.
70. P. Guntert, C. Thaler and K. Wüthrich, *J. Mol. Biol.*, 1997, **273**, 283.
71. M. D. Lowery, J. A. Guckert, M. S. Gebhard and E. I. Solomon, *J. Am. Chem. Soc.*, 1993, **115**, 3012.
72. D. E. Bennet and M. K. Johnson, *Biochim. Biophys. Acta*, 1987, **911**, 71.
73. S. J. Wilkens, B. Xia, F. Weinhold, J. L. Markley and W. M. Westler, *J. Am. Chem. Soc.*, 1998, **120**, 4806.
74. M. Ayhan, Z. Xiao, M. J. Lavery, A. M. Hamer, K. W. Nugent, S. D. B. Scrofani, M. Guss and A. G. Wedd, *Inorg. Chem.*, 1996, **35**, 5902.
75. R. Kummerle, H. Zhuang-Jackson, J. Gaillard and J.-M. Moulis, *Biochemistry*, 1997, **36**, 15983.
76. C. M. V. Stalhandske, J. Dong, P. Tavares, M.-Y. Liu, J. LeGall, J. J. G. Moura, I. zMoura, J.-B. Park, M. W. W. Adams, R. A. Scott, *Inorg. Chim. Acta*, 1998, **273**, 409.
77. P. R. Blake, J.-B. Park, F. O. Bryant, S. Aono, J. K. Magnuson, E. Eccleston, J. B. Howard, M. F. Summers and M. W. W. Adams, *Biochemistry*, 1991, **30**, 10885.
78. P. R. Blake, B. Lee, M. F. Summers, J.-B. Park, H. Z. Zhi and M. W. W. Adams, *New J. Chem.*, 1994, **18**, 387.
79. F. Bonomi, S. Iametti, D. M., Jr., Ragg, E. M. Kurtz, K. A. Richie and E. Ragg, *J. Biol. Inorg. Chem.*, 1998, **3**, 595.
80. F. Bonomi, D. Fessas, S. Iametti, D. M., Jr. and Mazzini, S. Kurtz, *Protein Sci.*, 2000, **9**, 2413.

81. F. Bonomi, A. E. Burden, M. K. Eidsness, D. Fessas, S. Iametti, D. M., Jr., Mazzini, S. Kurtz, R. A. Scott and Q. D. Zeng, *J. Biol. Inorg. Chem.*, 2002, **7**, 427.
82. M. W. Day, B. T. Hsu, L. Joshua-Tor, J.-B. Park, Z. H. Zhou, M. W. W. Adams and D. C. Rees, *Protein Sci.*, 1992, **1**, 1494.
83. P. R. Blake, J.-B. Park, Z. H. Zhou, D. R. Hare, M. W. W. Adams and M. F. Summers, *Protein Sci.*, 1992, **1**, 1508.
84. P. R. Blake, M. W. Day, B. T. Hsu, L. Joshua-Tor, J.-B. Park, D. R. Hare, M. W. W. Adams, D. C. Rees and M. F. Summers, *Protein Sci.*, 1992, **1**, 1522.
85. J. E. Wampler, E. A. Bradley, D. E. Stewart and M. W. W. Adams, *Protein Sci.*, 1993, **2**, 640.
86. G. Hernández and D. M. LeMaster, *Biochemistry*, 2001, **40**, 14384.
87. K. A. Richie, Q. Teng, C. J. Elkin and D. M. Kurtz, *Protein Sci.*, 1996, **5**, 883.
88. P. Strop and S. L. Mayo, *J. Am. Chem. Soc.*, 1999, **121**, 2341.
89. P. Strop and S. L. Mayo, *Biochemistry*, 2000, **39**, 1251.
90. E. R. Zartler, F. E. Jenney, M. Terrel, M. K. Eidsness, M. W. W. Adams and J. H. Prestegard, *Biochemistry*, 2001, **40**, 7279.
91. P. Lamosa, L. Brennam, H. Vis, D. L. Turner and H. Santos, *Extremophiles*, 2001, **5**, 303.
92. B. Baumann, H. Schärpf, M. Sutter, W. Haenhel and P. Rösch, *Biochemistry*, 1996, **35**, 12831.
93. H. Hatanaka, R. Tanimura, S. Katoh and F. Inagaki, *J. Mol. Biol.*, 1997, **268**, 922.
94. R. Cammack, *Adv. Inorg. Chem.*, 1992, **38**, 281.
95. J. B. Howard and D. C. Rees, *Adv. Protein Chem.*, 1991, **42**, 199.
96. A. L. Macedo, P. N. Palma, I. Moura, J. Legale, V. Wray and J. J. C. Moura, *Magn. Reson. Chem.*, 1993, **31**, S59.
97. H. Beinert, R. H. Holm and E. Münck, *Science*, 1997, **277**, 653.
98. M. Poe, W. D. Phillips, C. C. McDonald and W. Lovenberg, *Proc. Natl. Acad. Sci. USA*, 1970, **65**, 797.
99. I. Bertini, P. Turano and A. J. Vila, *Chem. Rev.*, 1993, **93**, 2833.
100. H. Cheng and J. L. Markley, *Ann. Rev. Biophys. Biol. Struct.*, 1995, **24**, 209.
101. I. Bertini, S. Ciurli and C. Luchinat, *Structure and Bonding*, M. J. Clarke, ed., Springer-Verlag, Berlin, 1995, 1.
102. I. Bertini, A. Donaire, B. A. Feinberg, C. Luchinat, M. Piccioli and H. Yuan, *Eur. J. Biochem.*, 1995, **232**, 192.
103. I. Bertini, C. Luchinat and A. Rosato, *Prog. Biophys. Mol. Biol.*, 1996, **66**, 43.
104. L. Calzolai, C. M. Gorst, K. L. Bren, Z.-H. Zhou, M. W. W. Adams and G. N. La Mar, *J. Am. Chem. Soc.*, 1997, **119**, 9341.
105. I. Bertini, A. Dikiy, C. Luchinat, R. Macinai, M. S. Viezzoli and M. Vincenzini, *Biochemistry*, 1997, **36**, 3570.
106. S. L. Davy, M. J. Osborn and G. R. Moore, *J. Mol. Biol.*, 1998, **277**, 683.
107. S. Aono, I. Bertini, J. A. Cowan, C. Luchinat, A. Rosato and M. S. Viezzoli, *J. Biol. Inorg. Chem.*, 1996, **1**, 523.
108. I. Bertini, C. Luchinat and A. Rosato, *Adv. Inorg. Chem.*, 1999, **47**, 251.
109. B. J. Goodfellow, A. L. Macedo, P. Rodrigues, I. Moura, V. Wray and J. J. G. Moura, *J. Biol. Inorg. Chem.*, 1999, **4**, 421.
110. G. N. La Mar, *Methods in Enzymology*, Vol. 334, M. W. W. Adams and R. M. Kelly, eds., Academic Press, San Diego, 2001, 351.
111. R. C. Conover, J.-B. Park, M. W. W. Adams and M. K. Johnson, *J. Am. Chem. Soc.*, 1990, **112**, 4562.
112. S. C. Busse, G. N. La Mar, L. P. Yu, J. B. Howard, E. T. Smith, Z. H. Zhou and M. W. W. Adams, *Biochemistry*, 1992, **47**, 11952.
113. P. R. Blake, J. B. Park, M. W. W. Adams and M. F. Summers, *J. Am. Chem. Soc.*, 1992, **114**, 4931.
114. C. M. Gorst, Y.-H. Yeh, L. Calzolai, Z. H. Zhou, M. W. W. Adams and G. N. La Mar, *Biochemistry*, 1995, **34**, 600.

115. C. M. Gorst, Z. H. Zhou, K. Ma, Q. Teng, J. B. Howard, M. W. W. Adams and G. N. La Mar, *Biochemistry*, 1995, **34**, 8788.
116. L. Calzolai, C. M. Gorst, Z. H. Zhou, Q. Teng, M. W. W. Adams and G. N. La Mar, *Biochemistry*, 1995, **34**, 11373.
117. L. Calzolai, Z. H. Zhou, M. W. W. Adams and G. N. La Mar, *J. Am. Chem. Soc*., 1996, **118**, 2513.
118. S. Macedo-Ribeiro, B. Martins, P. Pereira, G. Buse, R. Huber and T. Soulimane, *J. Biol. Inorg. Chem*., 2001, **6**, 663.
119. K. A. Johnson, P. S. Brereton, M.F.J.M. Verhagen, L. Calzolai, G. N. La Mar, M. W. W. Adams and I. J. Amster, *J. Am. Chem. Soc*., 2001, **123**, 7935.
120. M. Webba da Silva, S. Sham, C. M. Gorst, L. Calzolai, P. S. Brereton, M. W. W. Adams and G. N. La Mar, *Biochemistry*, 2001, **40**, 12575.
121. S. Sham, L. Calzolai, P.-L. Wang, K. Bren, H. Haarklau, P. S. Brereton, M. W. W. Adams and G. N. La Mar, *Biochemistry*, 2002, **41**, 12498.
122. L. Yu, S. Faham, R. Roy, M. W. W. Adams and D. C. Rees, *J. Mol. Biol*., 1999, **286**, 899.
123. K. A. Johnson, P. S. Brereton, M.F.J.M. Verhagen, L. Calzolai, G. N. La Mar, M. W. W. Adams and I. J. Amster, *J. Am. Chem. Soc*., 2001, **123**, 7935.
124. I. Bertini, F. Capozzi, C. Luchinat, M. Picciolo and A. J. Villa, *J. Am. Chem. Soc*., 1994, **116**, 651.
125. H. Sticht, G. Wildegger, B. Baumann, D. Bentrop, B. Darimont, R. Sterner, M. Sutter, W. Haehnel and P. Rösch, in *Proceedings of the International Conference on Molecular Structural Biology*, A. J. Kungl, P. J. Andrew and H. Schreiben, eds., 1995, 73.
126. Q. Teng, Z. H. Zhou, E. T. Smith, S. C. Busse, J. B. Howard, M. W. W. Adams and G. N. La Mar, *Biochemistry*, 1994, **33**, 6316.
127. P.-L. Wang, L. Calzolai, K. L. Bren, Q. Teng, F. E., Jr., Brereton, P. S. Jenney, J. B. Howard, M. W. W. Adams and G. N. La Mar, *Biochemistry*, 1999, **38**, 8167.
128. G. Wildegger, D. Bentrop, A. Ejchart, M. Alber, A. Hage, R. Sterner and P. Rösch, *Eur. J. Biochem*., 1995, **229**, 658.
129. S. Macedo-Ribeiro, B. Darimont, R. Sterner and R. Huber, *Structure*, 1996, **4**, 1291.
130. H. Sticht, G. Wildegger, D. Bentrop, B. Darimont, R. Sterner and P. Rösch, *Eur. J. Biochem*., 1996, **237**, 726.
131. P.-L. Wang, A. Donaire, Z. H. Zhou, M. W. W. Adams and G. N. La Mar, *Biochemistry*, 1996, **35**, 11319.
132. A. Donaire, Z. H. Zhou, M. W. W. Adams and G. N. La Mar, *J. Biomol. NMR*, 1996, **7**, 35.
133. I. Bertini, C. Luchinat, G. Mincione and A. Soriano, *Inorg. Chem*., 1998, **37**, 969.
134. S. Aono, D. Bentrop, I. Bertini, A. Donaire, C. Luchinat, Y. Niikura and A. Rosato, *Biochemistry*, 1998, **37**, 9812.
135. M. A. Kemper, C. D. Stout, S. E. J. Lloyd, G. S. Prasad, S. Fawcett, F. A. Armstrong, B. Shen and B. K. Burgess, *J. Biol. Chem*., 1997, **272**, 15620.
136. I. Bertini, C. Luchinat, Y. Niikura and C. Presenti, *Proteins*, 2000, **41**, 75.
137. S. Aono, D. Bentrop, I. Bertini, C. Luchinat and R. Macinai, *FEBS Lett*., 1997, **412**, 501.
138. S. Aono, D. Bentrop, I. Bertini, G. Cosenza and C. Luchinat, *Eur. J. Biochem*., 1998, **258**, 502.
139. T. Iwasaki, T. Suzuki, T. Kon, T. Imani, A. Urushiyama, D. Ohmori and T. Oshima, *J. Biol. Chem*., 1997, **272**, 3453.
140. T. Iwasaki, E. Watanabe, D. Ohmori, T. Imani, A. Urushiyama, M. Akiyama, Y. Hayashi-Iwasaki, N. J. Cosper and R. A. Scott, *J. Biol. Chem*., 2000, **275**, 25391.
141. Y. Matsuura, T. Takano and R. E. Dickerson, *J. Mol. Biol*., 1982, **156**, 389.
142. D. J. Detlefsen, V. Thanabal, V. L. Pecoraro and G. Wagner, *Biochemistry*, 1990, **29**, 9377.
143. K. Fukuyama, H. Marsubara, Y. Sanbongi and T. Kodama, *J. Biochem*., 1991, **110**, 854.
144. J. Hasegawa, T. Yoshida, T. Yamazaki, Y. Sambongi, Y. H. Yu, Y. Igarashi, T. Kodama, K. Yamazaki, Y. Kyogoku, Y. Kobayashi, *Biochemistry*, 1998, **37**, 9641.

145. J. Hasegawa, H. Shimahara, M. Mizutani, S. Uchiyama, H. Arai, M. Ishii, Y. Kobayashi, S. J. Ferguson, Y. Sambongi, Y. Igarashi, *J. Biol. Chem*., 1999, **274**, 37533.
146. J. Hasegawa, S. Uchiyama, Y. Tanimoto, M. Mizutani, Y. Kobayashi, Y. Sambongi and Y. Igarashi, *J. Biol. Chem*., 2000, **275**, 37824.
147. E. F. Karan, B. S. Russell and K. L. Bren, *J. Biol. Inorg. Chem*., 2002, **7**, 260.
148. B. Reincke, C. Perez, P. Pristovsek, C. Lucke, C. Ludwig, F. Lohr, V. V. Rogov, B. Ludwig and H. Ruterjans, *Biochemistry*, 2001, **40**, 12312.
149. M. Beißinger, H. Sticht, M. Sutter, A. Ejchart, W. Haehnel and P. Rösch, *EMBO J*., 1998, **17**, 27.
150. B. Dangi, A. V. Dobrodumov, J. M. Louis and A. M. Gronenborn, *Biochemistry*, 2002, **41**, 9376.
151. S. K. Katti, D. M. LeMaster and H. Eklund, *J. Mol. Biol*., 1990, **212**, 167.
152. J. Qin, G. M. Clore and A. M. Gronenborn, *Structure*, 1994, **2**, 503.
153. M. F. Jeng, A. P. Campbell, T. Begley, A. Holmgren, D. Case, P. E. Wright and H. J. Dyson, *Structure*, 1994, **2**, 853.
154. A. Weichsel, J. R. Gasdaska, G. Powis and W. R. Montfort, *Structure*, 1996, **4**, 735.
155. V. Mittard, M. J. Blackledge, M. Stein, J. P. Jacquot, D. Marion and J. M. Lancelin, *Eur. J. Biochem*., 1997, **243**, 374.
156. J. M. Louis, R. E. Georgescu, M. L. Tasayco, O. Tcherkasskaya and A. M. Gronenborn, *Biochemistry*, 2001, **40**, 11184.
157. G. Nicastro, C. de Chiara, E. Pedone, M. Tatò, M. Rossi and S. Bartolucci, *Eur. J. Biochem*., 2000, **267**, 403.
158. D. Y. Lee, B. Y. Ahn and K. S. Kim, *Biochemistry*, 2000, **39**, 6652.
159. J. W. Cave, H. S. Cho, A. M. Batchelder, H. Yokota, R. Kim and D. E. Wemmer, *Protein Sci*., 2001, **10**, 384.
160. S. Bhattacharyya, B. Habibi-Nazhad, G. Amegbey, C. M. Slupsky, A. Yee, C. Arrowsmith and D. S. Wishart, *Biochemistry*, 2002, **41**, 4760.
161. H. Vis, R. Boelens, M. Mariani, R. Stroop, C. E. Vorgias, K. S. Wilson and R. Kaptein, *Biochemistry*, 1994, **33**, 14858.
162. H. Vis, M. Mariani, C. E. Vorgias, K. S. Wilson, R. Kaptein and R. Boelens, *J. Mol. Biol*., 1995, **254**, 692.
163. H. Vis, O. Vageli, J. Nagel, C. E. Vorgias, K. S. Wilson, R. Kaptein and R. Boelens, *Magn. Reson. Chem*., 1996, **34**, S81.
164. R. Boelens, H. Vis, C. E. Vorgias, K. S. Wilson and R. Kaptein, *Biopolymers*, 1996, **40**, 553.
165. H. Vis, C. E. Vorgias, K. S. Wilson, R. Kaptein and R. Boelens, *J. Biomol. NMR*, 1998, **11**, 265.
166. S. Takashima and K. Yamaoka, *Biophys. Chem*., 1999, **80**, 153.
167. S. Kawamura, Y. Kakuta, I. Tanaka, K. Hikichi, S. Kuhara, N. Yamasaki and M. Kimura, *Biochemistry*, 1996, **35**, 1195.
168. S. Kawamura, I. Tanaka, N. Yamasaki and M. Kimura, *J. Biochem. (Tokyo)*, 1997, **121**, 448.
169. S. Kawamura, Y. Abe, T. Ueda, K. Masumoto, T. Imoto, N. Yamasaki and M. Kimura, *J. Biol. Chem*., 1998, **273**, 19982.
170. J. G. McAfee, S. P. Edmondson, P. K. Datta, J. W. Shriver and R. Gupta, *Biochemistry*, 1995, **34**, 10063.
171. S. P. Edmondson, L. Qiu and J. W. Shriver, *Biochemistry*, 1995, **34**, 13289.
172. P. I. de Bakker, P. H. Hunenberger and J. A. McCammon, *J. Mol. Biol*., 1999, **285**, 1811.
173. H. Baumann, S. Knapp, T. Lundbäck, R. Ladenstein and T. Härd, *Nat. Struct. Biol*., 1994, **1**, 808.
174. R. Consonni, L. Santomo, P. Fusi, P. Tortora and L. Zetta, *Biochemistry*, 1999, **38**, 12709.
175. H. Baumann, S. Knapp, A. Karshikoff, R. Ladenstein and T. Härd, *J. Mol. Biol*., 1995, **247**, 840.
176. P. Agback, H. Baumann, S. Knapp, R. Ladenstein and T. Härd, *Nat. Struct. Biol*., 1998, **5**, 579.
177. R. Consonni, I. Arosio, B. Belloni, F. Fogolari, P. Fusi, E. Shehi and L. Zetta, *Biochemistry*, 2003, **42**, 1421.

178. W. Zhu, Q. Zg, C. M. Colangelo, M. L. Lewis, M. F. Summers and R. A. Scott, *Nat. Struct. Biol.*, 1996, **3**, 122.
179. X. Qian, S. N. Gozani, H. Yoon, C. J. Jeon, K. Agarwal and M. A. Weiss, *Biochemistry*, 1993, **32**, 9944.
180. H.-T. Chen, P. Legault, J. Glushka, J. G. Omichinski and R. A. Scott, *Protein Sci.*, 2000, **9**, 1743.
181. O. N. Pakhomova, Y. Cui, C. Zwieb and A. P. Hinck, *J. Biomol. NMR*, 2001, **20**, 187.
182. O. N. Pakhomova, S. Deep, Q. Huang, C. Zwieb and A. P. Hinck, *J. Mol. Biol.*, 2002, **317**, 145.
183. P. Brick, T. N. Bhat and D. M. Blow, *J. Mol. Biol.*, 1989, **208**, 83.
184. A. Pintar, V. Guez, C. Castagné, H. Bedouelle and M. Delepierre, *FEBS Lett.*, 1999, **446**, 81.
185. J. I. Guijarro, A. Pintar, A. Prochnicka-Chalufour, V. Guez, B. Gilquin, H. Bedouelle and M. Delepierre, *Structure*, 2002, **10**, 311.
186. J. N. Reeve, K. Sandman and C. J. Daniels, *Cell*, 1997, **89**, 999.
187. M. R. Starich, K. Sandman, J. N. Reeve and M. F. Summers, *J. Mol. Biol.*, 1996, **255**, 187.
188. K. Decannier, A. M. Babu, K. Sandman, J. N. Reeve and U. Heinemann, *J. Mol. Biol.*, 2000, **303**, 35.
189. W. Zhu, K. Sandman, G. E. Lee, J. N. Reeve and M. F. Summers, *Biochemistry*, 1998, **37**, 10573.
190. D. W. Hoffman, C. S. Cameron, C. Davies, S. W. White and V. Ramakrishnan, *J. Mol. Biol.*, 1996, **264**, 1058.
191. B. Kuhlman, J. A. Boice, R. Fairman and D. P. Raleigh, *Biochemistry*, 1998, **37**, 1025.
192. D. L. Luisi, B. Kuhlman, K. Sideras, P. A. Evans and D. P. Raleigh, *J. Mol. Biol.*, 1999, **289**, 167.
193. M. A. Markus, A. P. Hinck, S. Huang, D. E. Draper and D. A. Torchia, *Nat. Struct. Biol.*, 1997, **4**, 70.
194. A. P. Hinck, M. A. Markus, S. Huang, S. Grzesiek, I. Kustonovich, D. E. Draper and D. A. Torchia, *J. Mol. Biol.*, 1997, **274**, 101.
195. Y. Xing, D. GuhaThakurta and D. E. Draper, *Nat. Struct. Biol.*, 1997, **4**, 24.
196. M. A. Markus, D. Triantafillidou, T. Choli-Papadopoulou and D. A. Torchia, *J. Biomol. NMR*, 2001, **20**, 293.
197. E. A. Woestenenk, P. Allard, G. M. Gongadze, S. E. Moskalenko, D. V. Shcherbakov, A. V. Rak, M. B. Garber, T. Härd and H. Berglund, *J. Biomol. NMR*, 2000, **17**, 273.
198. E. A. Woestenenk, G. M. Gongadze, D. V. Shcherbakov, A. V. Rak, M. B. Garber, T. Härd and H. Berglund, *Biochem. J.*, 2002, **363**, 553.
199. T. Härd, A. Rak, P. Allard, L. Kloo and M. Garber, *J. Mol. Biol.*, 2000, **296**, 169.
200. M. A. Markus, R. B. Gerstner, D. E. Draper and D. A. Torchia, *EMBO J.*, 1998, **17**, 4559.
201. M. A. Markus, R. B. Gerstner, D. E. Draper and D. A. Torchia, *J. Mol. Biol.*, 1999, **292**, 375.
202. E. W. Sayers, R. B. Gerstner, D. E. Draper and D. A. Torchia, *Biochemistry*, 2000, **39**, 13602.
203. H. Berglund, A. Rak, A. Serganov, M. Garber and T. Härd, *Nat. Struct. Biol.*, 1997, **4**, 20.
204. P. Allard, A. V. Rak, B. T. Wimberly, W. M. Clemons Jr., A. Kalinin, M. Helgstrand, M. B. Garber, V. Ramakrishnan and T. Härd, *Structure*, 2000, **8**, 875.
205. B. L. Golden, D. W. Hoffman, V. Ramakrishnan and S. W. White, *Biochemistry*, 1993, **32**, 12812.
206. N. L. Davydova, A. V. Rak, O. I. Gryaznova, A. Liljas, B. H. Jonsson, H. Berglund, T. Härd and M. B. Garber, *FEBS Lett.*, 1997, **415**, 155.
207. M. Helgstrand, A. V. Rak, P. Allard, N. Davydova, M. B. Garber and T. Härd, *J. Mol. Biol.*, 1999, **292**, 1071.
208. S. Sato and D. P. Raleigh, *J. Mol. Biol.*, 2002, **318**, 571.
209. T. Yoshida, S. Uchiyama, H. Nakano, H. Kashimori, H. Kijima, T. Ohshima, Y. Saihara, T. Ishino, H. Shimahara, T. Yoshida, K. Yokose, T. Ohkubo, A. Kaji, Y. Kobayashi, *Biochemistry*, 2001, **40**, 2387.

210. T. Yoshida, H. Kijima, S. Oka, S. Uchiyama, H. Nakano, T. Ohkubo and Y. Kobayashi, *J. Biomol. NMR*, 2002, **22**, 195.
211. B. K. Blake, K. Ito, Y. Nakamura and S. L. Alam, *J. Biomol. NMR*, 2002, **24**, 81.
212. G. Dong, J. Nowakowski and D. W. Hoffman, *EMBO J.*, 2002, **21**, 1845.
213. P. L. Graumann and M. A. Marahiel, *Trends Biochem. Sci.*, 1998, **23**, 286.
214. S. Phadtare, J. Alsina and M. Inouye, *Curr. Opin. Microbiol.*, 1999, **2**, 175.
215. H. Schindelin, W. Jiang, M. Inouye and U. Heinemann, *Proc. Natl. Acad. Sci. USA*, 1994, **91**, 5119.
216. K. Newkirk, W. G. Feng, W. N. Jiang, R. Tejero, S. D. Emerson, M. Inouye and G. T. Montelione, *Proc. Natl. Acad. Sci. USA*, 1994, **91**, 5114.
217. A. T. Alexandrescu and K. Rathgeb-Szabo, *J. Biomol. NMR*, 1998, **11**, 461.
218. W. Q. Feng, R. Tejero, D. E. Zimmerman, M. Inouye and G. T. Montelione, *Biochemistry*, 1998, **37**, 10881.
219. H. Schindelin, M. A. Mahariel and U. Heinemann, *Nature*, 1993, **364**, 164.
220. A. Schnuchel, R. Wiltscheck, M. Czisch, M. Herrler, G. Willimsky, P. Graumann, M. A. Marahiel and T. A. Holak, *Nature*, 1993, **364**, 169.
221. U. Mueller, D. Perl, F. X. Schmid and U. Heinemann, *J. Mol. Biol.*, 2000, **297**, 975.
222. W. Kremer, B. Schuler, S. Harrieder, M. Geyer, W. Gronwald, C. Welker, R. Jaenicke and H. R. Kalbitzer, *Eur. J. Biochem.*, 2001, **268**, 2527.
223. N. Frankenberg, C. Welker and R. Jaenicke, *FEBS Lett.*, 1999, **454**, 299.
224. B. Schuler, W. Kremer, H.R.: Kalbitzer and R. Jaenicke, *Biochemistry*, 2002, **41**, 11670.
225. J. Horwitz, *Proc. Natl. Acad. Sci. USA*, 1999, **89**, 10449.
226. J. A. Carter, *Prog. Retin. Eye Res.*, 1999, **18**, 431.
227. R.H.P.H. Smulders, J. A. Carter, R. A. Lindner, M. A. M. van Boekel, H. Bloemendal and W. W. de Jong, *J. Biol. Chem.*, 1996, **271**, 29060.
228. Q. Hua, I. S. Dementieva, M. A. Walsh, K. Hallenga, M. A. Weiss and A. Joachimiak, *J. Mol. Biol.*, 2001, **306**, 513.
229. J. A. Carter, G. Esposito, G. Schwedersky and M. Gaestel, *FEBS Lett.*, 1995, **369**, 305.
230. R. A. Lindner, J. A. Carter, M. Ehrnsperger, J. Buchner, G. Esposito, J. Behlke, G. Lutsch, A. Kotlyarov and M. Gaestel, *Eur. J. Biochem.*, 2000, **267**, 1923.
231. T. Szyperski, M. Pellecchia, D. Wall, C. Georgopoulos and K. Wüthrich, *Proc. Natl. Acad. Sci. USA*, 1994, **91**, 11343.
232. M. Pellecchia, T. Szyperski, D. Wall, C. Georgopoulos and K. Wüthrich, *J. Mol. Biol.*, 1996, **260**, 236.
233. Y. Q. Qian, D. Patel, F. U. Hartl and D. J. McColl, *J. Mol. Biol.*, 1996, **260**, 224.
234. K. Huang, J. M. Flanagan and J. H. Prestegard, *Biophys. J.*, 1996, **70**, SU390.
235. K. Huang, J. M. Flanagan and J. H. Prestegard, *Protein Sci.*, 1999, **8**, 203.
236. K. Huang, R. Ghose, J. M. Flanagan and J. H. Prestegard, *Biochemistry*, 1999, **38**, 10567.
237. M. Martinez-Yamout, G. B. Legge, O. Zhang, P. E. Wright and J. Dyson, *J. Mol. Biol.*, 2000, **300**, 805.
238. H. Wang, A. V. Kurochkin, Y. Pang, W. D. Hu, G. C. Flynn and E. R. P. Zuiderweg, *Biochemistry*, 1998, **37**, 7929.
239. R. C. Morshauser, H. Wang, G. C. Flynn and E. R. P. Zuiderweg, *Biochemistry*, 1995, **34**, 6261.
240. R. C. Morshauser, W. Hu, H. Wang, Y. Pang, G. C. Flynn and E. R. P. Zuiderweg, *J. Mol. Biol.*, 1999, **289**, 1387.
241. D. Kulms, G. Schäfer and U. Hahn, *Biol. Chem.*, 1997, **378**, 545.
242. E. Shei, S. Serina, G. Fumagalli, M. Vanoni, R. Consonni, L. Zetta, G. Dehò, P. Tortora and P. Fusi, *FEBS Lett.*, 2001, **497**, 131.
243. P. Fusi, K. Goessen, R. Consonni, M. Grisa, P. Puricelli, G. Vecchio, M. Vanoni, L. Zetta, K. Heremans, P. Tortora, *Proteins*, 1997, **29**, 381.
244. C. D. Kroenke, M. Rance and A. G. Palmer, *J. Am. Chem. Soc.*, 1999, **121**, 10119.

245. J. Hollien and S. Marqusee, *Proc. Natl. Acad. Sci. USA*, 1999, **96**, 13674.
246. B. Wang, D. N. M. Jones, B. P. Kaine and M. A. Weiss, *Structure*, 1998, **6**, 555.
247. B. Wang, A. S. Stern and M. A. Weiss, *J. Biomol. Struct. Dyn.*, 2000, **S1**, 95.
248. C. D. Mackereth, C. Arrosmith, A. E. Edwards and L. P. McIntosh, *Proc. Natl. Acad. Sci. USA*, 2000, **97**, 6316.
249. A. Thiru, M. Hodach, J. J. Eloranta, V. Kostourou, R. O. J. Weinzierl and S. Matthews, *J. Mol. Biol.*, 1999, **287**, 753.
250. A. Yee, V. Booth, A. Dharamsi, A. Engel, A. M. Edwards and C. H. Arrowsmith, *Proc. Natl. Acad. Sci. USA*, 2000, **97**, 6311.
251. T. Wada, T. Yamazaki and Y. Kyogoku, *J. Biol. Chem.*, 2000, **275**, 16057.
252. M. Czjzek, D. N. Bolam, A. Mosbah, J. Allouch, C.M.G.A. Fontes, L. M. A. Ferreira, O. Bornet, V. Zamboni, H. Darbon, N. L. Smith, G. W. Black, B. Henrissat, H. J. Gilbert, *J. Biol. Chem.*, 2001, **276**, 48580.
253. H. Xie, H. J. Gilbert, S. J. Charnock, G. J. Davies, M. P. Williamson, P. J. Simpson, S. Raghothama, C.M.G.A. Fontes, M. V. Dias, L. M. A. Ferreira, D. N. Bolam, *Biochemistry*, 2001, **40**, 9167.
254. M. Abou Hachem, E. Nordberg Karlsson, E. Bartonek-Roxå, S. Raghothama, P. J. Simpson, H. J. Gilbert, M. P. Williamson and O. Holst, *Biochem. J.*, 2000, **345**, 53.
255. S. J. Jamieson, M. P. Williamson, M. Abou-Hachem, E. Nordberg Karlsson and P. J. Simpson, *J. Biomol. NMR*, 2002, **22**, 187.
256. P. S. Simpson, S. J. Jamieson, M. Abou Hachem, E. Nordberg Karlsson, H. J. Gilbert, O. Holst and M. P. Williamson, *Biochemistry*, 2002, **41**, 5712.
257. M. Abou Hachem, E. Nordberg Karlsson, P. J. Simpson, S. Linse, P. Sellers, M. P. Williamson, S. J. Jamieson, H. J. Gilbert, D. N. Bolam, O. Holst, *Biochemistry*, 2002, **41**, 5720.
258. B. L. Lytle, B. F. Volkman, W. M. Westler and J. H. D. Wu, *Arch. Biochem. Biophys.*, 2000, **379**, 237.
259. B. L. Lytle, B. F. Volkman, W. M. Westler, M. P. Heckman and J. H. D. Wu, *J. Mol. Biol.*, 2001, **307**, 745.
260. S. P. Smith, P. Béguin, P. M. Alzari and K. Gehring, *J. Biomol. NMR*, 2002, **23**, 73.
261. Y. N. Kalia, S. M. Brocklehurst, D. S. Hipp, E. Appella, K. Sakaguchi and R. N. Perham, *J. Mol. Biol.*, 1993, **230**, 323.
262. S. Spector, B. Kuhlman, R. Fairman, E. Wong, J. A. Boice and D. P. Raleigh, *J. Mol. Biol.*, 1998, **276**, 479.
263. S. Spector and D. P. Raleigh, *J. Mol. Biol.*, 1999, **293**, 763.
264. S. Spector, P. Young and D. P. Raleigh, *Biochemistry*, 1999, **38**, 4128.
265. F. Dardel, E. D. Laue and R. N. Perham, *Eur J. Biochem.*, 1991, **201**, 203.
266. F. Dardel, A. L. Davis, E. D. Laue and R. N. Perham, *J. Mol. Biol.*, 1993, **229**, 1037.
267. N. G. Wallis, M. D. Allen, W. Broadhurst, I. A. D. Lessare and R. N. Perham, *J. Mol. Biol.*, 1996, **263**, 463.
268. M. J. Howard, H. J. Chauhan, G. J. Domingo, C. Fuller and R. N. Perham, *J. Mol. Biol.*, 2000, **295**, 1023.
269. S. B. Prusiner, *Proc. Natl. Acad. Sci. USA*, 1998, **95**, 13363.
270. W. Swietnicki, R. B. Petersen, P. Gambetti and W. K. Surewicz, *J. Biol. Chem.*, 1998, **273**, 31048.
271. R. A. Somerville, R. C. Oberthur, U. Havekost, F. MacDonald, D. M. Taylor and A. G. Dickinson, *J. Biol. Chem.*, 2002, **277**, 11084.
272. D. M. Taylor, S. L. Woodgate and M. J. Atkinson, *Vet. Rec.*, 1995, **137**, 605.
273. D. M. Taylor, K. Fernie and I. McConnel, *Vet. Microbiol.*, 1997, **58**, 87.
274. R. Riek, S. Hornemann, G. Wider, M. Billeter, R. Glockshuber and K. Wüthrich, *Nature*, 1996, **382**, 180.
275. R. Riek, S. Hornemann, G. Wider, R. Glockshuber and K. Wüthrich, *FEBS Lett.*, 1997, **413**, 282.

276. R. Riek, G. Wider, M. Billeter, S. Hornemann, R. Glockshuber and K. Wüthrich, *Proc. Natl. Acad. Sci. USA*, 1998, **95**, 11667.
277. T. L. James, H. Liu, N. B. Ulyanov, S. Farr-Jones, H. Zhang, D. G. Donne, K. Kaneko, D. Groth, I. Mehlhorn, S. B. Prusiner, F. E. Cohen, *Proc. Natl. Acad. Sci. USA*, 1997, **94**, 10086.
278. D. G. Donne, J. H. Viles, D. Groth, I. Mehlhorn, T. L. James, F. E. Cohen, S. B. Prusiner, P. E. Wright and H. J. Dyson, *Proc. Natl. Acad. Sci. USA*, 1997, **94**, 13457.
279. H. Liu, S. Farr-Jones, N. B. Ulyanov, M. Llinas, S. Marqusee, D. Groth, F. E. Cohen, S. B. Prusiner and T. L. James, *Biochemistry*, 1999, **38**, 5362.
280. J. H. Viles, D. Donne, G. Kroon, S. B. Prusiner, F. E. Cohen, H. J. Dyson and P. E. Wright, *Biochemistry*, 2001, **40**, 2743.
281. F. López García, R. Zahn, R. Riek and K. Wüthrich, *Proc. Natl. Acad. Sci. USA*, 2000, **97**, 8334.
282. R. Zahn, A. Liu, T. Lührs, R. Riek, C. von Schroetter, F. López García, M. Billeter, L. Calzolai, G. Wider, K. Wüthrich, *Proc. Natl. Acad. Sci. USA*, 2000, **97**, 145.
283. H. Zhang, K. Kaneko, J. T. Nguyen, T. L. Livshits, M. A. Baldwin, F. E. Cohen, T. L. James and S. B. Prusiner, *J. Mol. Biol.*, 1995, **250**, 514.
284. E. Ragg, F. Tagliavini, P. Malesani, L. Monticelli, O. Bugiani, G. Forloni and M. Salmona, *Eur. J. Bioch.*, 1999, **266**, 1192.
285. S. A. Kozin, G. Bertho, A. K. Mazur, H. Rabesona, J.-P. Girault, T. Haertlé, M. Takahashi, P. Debey and G. H. B. Hoa, *J. Biol. Chem.*, 2001, **276**, 46364.
286. D. D. Laws, H. M. L. Bitter, K. Liu, H. L. Ball, K. Kaneko, H. Wille, F. E. Cohen, S. B. Prusiner, A. Pines, D. E. Wemmer, *Proc. Natl. Acad. Sci. USA*, 2001, **98**, 11686.
287. G. Bertho, S. Kozin, P. Debey, G. H. B. Hoa and J.-P. Girault, *C.R. Acad. Sci. II C*, 2001, **4**, 739.
288. N. Jamin, Y.-M. Coïc, C. Landon, L. Ovtracht, F. Baleux, J.-M. Neumann and A. Sanson, *FEBS Lett.*, 2002, **529**, 256.
289. L. L. P. Hosszu, N. J. Baxter, G. S. Jackson, A. Power, A. R. Clarke, J. P. Waltho, C. J. Craven and J. Collinge, *Nat. Struct. Biol.*, 1999, **6**, 740.
290. E. El-Bastawissy, M. H. Knaggs and I. H. Gilbert, *J. Mol. Graph. Model.*, 2001, **20**, 145.
291. S. Liemann and R. Glockshuber, *Biochemistry*, 1999, **38**, 3258.
292. L. Calzolai, D. A. Lysek, P. Güntert, C. von Schroetter, R. Riek, R. Zahn and K. Wüthrich, *Proc. Natl. Acad. Sci. USA*, 2000, **97**, 8340.
293. Y. Zhang, W. Swietnicki, M. G. Zagorski, W. K. Surewicz and F. D. Sönnichsen, *J. Biol. Chem.*, 2000, **275**, 33650.
294. J. Gsponer, P. Ferrara and A. Caflisch, *J. Mol. Graph. Model.*, 2001, **20**, 169.
295. K. Kuwata, H. Li, H. Yamada, G. Legname, S. B. Prusiner, K. Akasaka and T. L. James, *Biochemistry*, 2002, **41**, 12277.
296. C. J. McKnight, D. S. Doering, P. T. Matsudaira and P. S. Kim, *J. Mol. Biol.*, 1996, **260**, 126.
297. C. J. McKnight, P. T. Matsudaira and P. S. Kim, *Nat. Struct. Biol.*, 1997, **4**, 180.
298. B. S. Frank, D. Vardar, D. A. Buckley and C. J. McKnight, *Protein Sci.*, 2002, **11**, 680.
299. L. Vugmeyster, O. Trott, C. J. McKnight, D. P. Raleigh and A. G. Palmer, *J. Mol. Biol.*, 2002, **320**, 841.
300. D. Vardar, D. A. Buckley, B. S. Frank and C. J. McKnight, *J. Mol. Biol.*, 1999, **294**, 1299.
301. C. Simenel, T. Rose, M. Goethals, J. Vandekerckhove, E. Friederich, D. Louvard and M. Delepierre, *Int. J. Pept. Prot. Res.*, 1995, **45**, 574.
302. M. A. Markus, T. Nakayama, P. Matsudaira and G. Wagner, *Protein Sci.*, 1994, **3**, 70.
303. M. A. Markus, T. Nakayama, P. Matsudaira and G. Wagner, *J. Biomol. NMR*, 1994, **4**, 553.
304. M. A. Markus, K. T. Dayie, P. Matsudaira and G. Wagner, *Biochemistry*, 1996, **35**, 1722.
305. M. A. Markus, P. Matsudaira and G. Wagner, *Protein Sci.*, 1997, **6**, 1197.
306. S. E. Choe, P. T. Matsudaira, J. Osterhout, G. Wagner and E. I. Shakhnovich, *Biochemistry*, 1998, **37**, 14508.

307. M. Kohmura, N. Nio and Y. Ariyoshi, *Agric. Biol. Chem.*, 1990, **54**, 2219.
308. Z. Bohak and S. L. Li, *Biochim. Biophys. Acta*, 1976, **427**, 153.
309. S. H. Kim, C. H. Kang, R. Kim, J. M. Cho, Y. B. Lee and T. K. Lee, *Protein Eng.*, 1989, **2**, 571.
310. C. Ogata, M. Hatada, G. Tomlinson, W. C. Shin and S. H. Kim, *Nature*, 1987, **328**, 739.
311. P. Fan, C. Bracken and J. Baum, *Biochemistry*, 1993, **32**, 1573.
312. T. Mizukoshi, M. Kohmura, E. Suzuki and Y. Ariyoshi, *FEBS Lett.*, 1997, **413**, 409.
313. M. T. Tomic, J. R. Somoza, D. E. Wemmer, Y. W. Park, J. M. Cho and S. H. Kim, *J. Biomol. NMR*, 1992, **2**, 557.
314. S. Y. Lee, J. H. Lee, H. J. Chang, J. M. Cho, J. W. Jung and W. Lee, *Biochemistry*, 1999, **38**, 2340.
315. J. R. Somoza, F. Jiang, L. Tong, C. H. Kang, J. M. Cho and S. H. Kim, *J. Mol. Biol.*, 1993, **234**, 390.
316. Y.-H. Sung, J. Shin, H.-J. Chang, J. M. Cho and W. Lee, *J. Biol. Chem.*, 2001, **276**, 19624.
317. Y.-H. Sung, H.-D. Hong, C. Cheong, J. H. Kim, J. M. Cho, Y.-R. Kim and W. Lee, *J. Biol. Chem.*, 2001, **276**, 44229.
318. T. Tancredi, H. Iijima, G. Saviano, P. Amodeo and P. A. Temussi, *FEBS Lett.*, 1992, **310**, 27.
319. R. Spadaccini, O. Crescenzi, T. Tancredi, N. De Casamassimi, G. Saviano, R. Scognamiglio, A. Di Donato and P. A. Temussi, *J. Mol. Biol.*, 2001, **305**, 505.
320. N. Niccolai, R. Spadaccini, M. Scarselli, A. Bernini, O. Crescenzi, O. Spiga, A. Ciutti, D. Di Maro, L. Bracci, C. Dalvit, P. A. Temussi, *Protein Sci.*, 2001, **10**, 1498.
321. A. Z. Murzin, *J. Mol. Biol.*, 1993, **230**, 689.
322. J. E. Caldwell, F. Abildgaard, D. Ming, G. Hellekant and J. L. Markley, *J. Biomol. NMR*, 1998, **11**, 231.
323. J. E. Caldwell, F. Abildgaard, Z. Dzakula, D. Ming, G. Hellekant and J. L. Markley, *Nat. Struct. Biol.*, 1998, **5**, 427.
324. G. H. Gao, J. X. Dai, M. Ding, G. Hellekant, J. F. Wang and D. C. Wang, *Int. J. Biol. Macromol.*, 1999, **24**, 351.
325. D. Christendat, A. Yee, A. Dharamsi, Y. Kluger, A. Savchenko, J. R. Cort, V. Booth, C. D. Mackereth, V. Saridakis, I. Ekiel, G. Kozlov, K. L. Maxwell, N. Wu, L. P. McIntosh, K. Gehring, M. A. Kennedy, A. R. Davidson, E. F. Pai, M. Gernstein, A. M. Edwards and C. H. Arrowsmith, *Nat. Struct. Biol.*, 2000, **7**, 903.
326. J. R. Cort, A. Yee, A. M. Edwards, C. H. Arrowsmith and M. A. Kennedy, *J. Struct. Funct. Genom.*, 2000, **1**, 15.
327. J. R. Cort, A. Yee, A. M. Edwards, C. H. Arrowsmith and M. A. Kennedy, *J. Mol. Biol.*, 2000, **302**, 189.
328. G. M. Lee, A. M. Edwards, C. H. Arrowsmith and L. P. McIntosh, *J. Biomol. NMR*, 2001, **21**, 63.
329. A. Pineda-Lucena, G.-S. Yi, X. Chang, J. R. Cort, M. A. Kennedy, A. M. Edwards and C. H. Arrowsmith, *J. Biomol. NMR*, 2002, **22**, 291.
330. A. Yee, X. Chang, A. Pineda-Lucena, B. Wu, A. Semesi, B. Le, T. Ramelot, G. M. Lee, S. Bhattacharyya, P. Gutierrez, A. Denisov, C.-H. Lee, J. R. Cort, G. Kozlov, J. Liao, G. Finak, L. Chen, D. Wishart, W. Lee, L. P. McIntosh, K. Kalle Gehring, M. A. Kennedy, A. M. Edwards and C. H. Arrowsmith, *Proc. Natl. Acad. Sci. USA*, 2002, **99**, 1825.
331. S.-H. Lin, T. Wakagi, H. Matsuzawa and E. Yoshimura, *J. Inorg. Biochem.*, 1999, **77**, 205.
332. K. Suefuji, S. J. Lin, T. Wakagi, H. Matsuzawa and E. Yoshimura, *Biosci. Biotech. Bioch.*, 2002, **66**, 1281.
333. C. P. M. VanMierlo, N. J. Darby, D. Neuhaus and T. E. Creighton, *J. Mol. Biol.*, 1991, **222**, 353.
334. C. P. M. VanMierlo, N. J. Darby, D. Neuhaus and T. E. Creighton, *J. Mol. Biol.*, 1991, **222**, 373.
335. C. P. M. VanMierlo, N. J. Darby, J. Keeler, D. Neuhaus and T. E. Creighton, *J. Mol. Biol.*, 1993, **229**, 1125.
336. K. D. Berndt, P. Guntert, L. P. M. Orbons and K. Wuthrich, *J. Mol. Biol.*, 1992, **227**, 757.

337. E. Barbar, V. J. LiCata, G. Barany and C. Woodward, *Biophys. Chem.*, 1997, **64**, 45.
338. Y. Kuroda and P. S. Kim, *J. Mol. Biol.*, 2000, **298**, 493.
339. T. Cierpicki and J. Otlewski, *J. Mol. Biol.*, 2002, **321**, 647.
340. C. Faber, A. Lindemann, H. Sticht, A. Ejchart, A. Kungl, M. Susani, R. W. Frank, D. Kraft, M. Breitenbach, P. Rösch, *J. Biol. Chem.*, 1996, **271**, 19243.
341. M. Boehm and P. Rösch, *Biol. Chem.*, 1997, **378**, 687.
342. I. J. Griswold, H. J. Zhou, M. Matison, R. V. Swanson, L. P. McIntosh, M. I. Simon and F. W. Dahlquist, *Nat. Struct. Biol.*, 2002, **9**, 121.
343. M. Cai, Y. Gong, J.L.-F. Kao and R. Krishnamoorthi, *Biochemistry*, 1995, **38**, 5201.
344. M. Cai, Y. Gong, O. Prakash and R. Krishnamoorthi, *Biochemistry*, 1995, **38**, 12087.
345. J. Liu, O. Prakash, M. Cai, Y. Gong, Y. Huang, L. Wen, J. J. Wen, J.-K. Huang and R. Krishnamoorthi, *Biochemistry*, 1996, **35**, 1516.
346. M. Cai, Y. Huang, O. Prakash, L. Wen, S. P. Dunkelbarger, J.-K. Huang, J. H. Liu and R. Krishnamoorthi, *Biochemistry*, 1996, **35**, 4784.
347. J. Liu, O. Prakash, Y. Huang, L. Wen, J. J. Wen, J.-K. Huang and R. Krishnamoorthi, *Biochemistry*, 1996, **35**, 12503.
348. M. Cai, Y. Gong, L. Wen and R. Krishnamoorthi, *Biochemistry*, 2002, **41**, 9572.
349. J. R. Cort, S. V. Mariappan, C. Y. Kim, M. S. Park, T. S. Peat, G. S. Waldo, T. C. Terwilliger and M. A. Kennedy, *Eur. J. Biochem.*, 2001, **268**, 5842.
350. J. M. J. Perez, J. G. Renisio, J. J. Prompers, C. J. van Platerink, C. Cambillau, H. Darbon and L. G. J. Frenken, *Biochemistry*, 2001, **40**, 74.
351. T. Knubovets, J. J. Osterhout, P. J. Connolly and A. M. Klibanov, *Proc. Natl. Acad. Sci. USA*, 1999, **96**, 1262.
352. T. Meinnel, S. Blanquet and F. Dardel, *J. Mol. Biol.*, 1996, **262**, 375.
353. T. Meinnel, C. Lazennec, F. Dardel, J.-M. Schmitter and S. Blanquet, *FEBS Lett.*, 1996, **385**, 91.
354. F. Dardel, S. Ragusa, C. Lazennec, S. Blanquet and T. Meinnel, *J. Mol. Biol.*, 1998, **280**, 501.
355. J. F. O'Connell, K. A. D. Pryor, S. K. Grant and B. Leiting, *J. Biomol. NMR*, 1999, **13**, 311.
356. M. Wittekind, P. Rajagopal, B. R. Branchini, J. Reizer, M. H. Saier and R. E. Klevitt, *Protein Sci.*, 1992, **1**, 1363.
357. J. M. Scholtz, *Protein Sci.*, 1995, **4**, 35.
358. J. R. Martin, R. Jerala, L. Kroonzitko, E. Zerovnik, V. Turk and J. P. Waltho, *Eur. J. Biochem.*, 1994, **225**, 1181.
359. J. R. Martin, C. J. Craven, R. Jerala, L. Kroonzitko, E. Zerovnik, V. Turk and J. P. Waltho, *J. Mol. Biol.*, 1995, **246**, 331.
360. S. Tate, T. Ushioda, N. Utsunomiyatate, K. Shibuya, Y. Ohyama, Y. Nakano, H. Kaji, F. Inagaki, T. Samejima, M. Kainosho, *Biochemistry*, 1995, **34**, 14637.
361. I. Ekiel, M. Abrahamson, D. B. Fulton, P. Lindhl, A. C. Storer, W. Levadoux, M. Lafrance, S. Labelle, Y. Pomerleau, D. Groleau, L. LeSauteur, K. Gehring, *J. Mol. Biol.*, 1997, **271**, 266.
362. R. Jerala and E. Zerovnik, *J. Mol. Biochem.*, 1999, **291**, 1079.
363. C. J. Craven, N. J. Baxter, E. H. Murray, N. J. Hill, J. R. Martin, K. Ylinenjarvi, I. Bjorg, J. P. Waltho and I. A. Murray, *Biochemistry*, 2000, **39**, 15783.
364. A. Ohno, S. Tate, S. S. Seeram, K. Hiraga, M. B. Swindells, K. Oda and M. Kainosho, *J. Mol. Biol.*, 1998, **282**, 421.
365. S. Tate, A. Ohno, S. S. Seeram, K. Hiraga, K. Oda and M. Kainosho, *J. Mol. Biol.*, 1998, **282**, 435.
366. A. Tamura, K. Kanaori, S. Kojima, I. Kumagai, K. Miura and K. Akasaka, *Biochemistry*, 1991, **30**, 5275.
367. A. Tamura, K. Kimura and K. Akasaka, *Biochemistry*, 1991, **30**, 11313.
368. A. Tamura, M. Matsushita, A. Naito, S. Kojima, K. I. Miura and K. Akasaka, *Protein Sci.*, 1996, **5**, 127.
369. H. Sasakawa, A. Tamura, S. Fujimaki, S. Taguchi and K. Akasaka, *J. Biochem.*, 1999, **126**, 859.

370. H. Akagawa, Y. Takano, A. Ishii, S. Mizuno, R. Izui, T. Sameshima, N. Kawamura, K. Dobashi and T. Yoshioka, *J. Antibiot*., 1999, **52**, 960.
371. M. A. Jimenez, M. Bruix, C. Gonzalez, F. J. Blanco, J. L. Nieto, J. Herranz and M. Rico, *Eur. J. Biochem*., 1993, **211**, 569.
372. M. Rico, M. A. Jimenez, C. Gonzalez, V. De Filippis and A. Fontana, *Biochemistry*, 1994, **33**, 14834.
373. F. Conejero-Lara, C. González, M. A. Jiménez, S. Padmanabhan, P. L. Mateo and M. Rico, *Biochemistry*, 1997, **36**, 11975.

High Pressure NMR Studies on Lyotropic Lipid Mesophases and Model Biomembranes

R. WINTER

Department of Chemistry, Physical Chemistry I, University of Dortmund, Otto-Hahn Str. 6, D-44227 Dortmund, Germany

For about 15 years now, high pressure NMR techniques have been used to study the structure, dynamics and phase behaviour of biomolecular systems. After a brief introduction discussing the important reasons for using high pressure as an experimental variable in studies of volume effects in biochemical systems, a section on instrumentation follows which deals with high resolution, high pressure NMR probes. In the main part, various high pressure NMR experiments on model biomembrane systems consisting of pure phospholipid bilayers and of lipid bilayers with additives, such as cholesterol, anaesthetics and polypeptides, are reviewed and discussed.

ANNUAL REPORTS ON NMR SPECTROSCOPY
VOLUME 50 ISSN 0066 4103
DOI 10.1016/S0066-4103(3)50004-7

1. INTRODUCTION

Phospholipid bilayers constitute the primary structural element of biological membranes and their physical properties are of considerable interest to biochemists and biophysicists.[1,2] Membrane physical properties are presumed to influence biological processes such as intercellular interactions, transmembrane transport and signalling, changes in cell surface morphology, and the functioning of membrane-associated proteins. Some insight into the nature and function of the complex biological membranes can already be gained by studying synthetic lipid bilayers consisting of a single type of phospholipid molecule or simple bilayer mixtures consisting of phospholipids and phospholipids with cholesterol and selected polypeptides. Such systems are sufficiently simple to permit a detailed analysis of their properties, yet complex enough to retain certain essential properties associated with their natural counterparts. In addition to their obvious biological importance, synthetic membranes consisting of amphiphilic lipid molecules are also of intrinsic physico-chemical interest as soft condensed material systems because of their self-assembling properties and the intriguing range of structural and dynamic phenomena exhibited. In addition, they can serve as matrices in a range of pharmaceutical applications.

The rationale for using pressure as an experimental variable in studies of proteins and model membranes has already been discussed by a number of authors;[3–5] therefore, we highlight only some important points. First, changing the temperature of a system at atmospheric pressure produces a simultaneous change in thermal energy and volume; therefore, in order to separate the thermal and volume effects, one has to perform pressure dependent experiments. Second, the environment (e.g., viscosity) of a biomolecule can be changed continuously with pressure without having to change the solvent composition. Because non-covalent interactions play a primary role in the stabilization of biochemical systems, the use of pressure allows one to change, in a controlled way and reversibly, the intermolecular interactions without the major perturbations produced by changes in temperature and/or chemical composition. Third, the current investigations of the structure and dynamics of model biomembranes by changing the temperature of the system could be greatly enhanced by high pressure experiments, since pressure is as important a thermodynamic variable as is temperature. Hence, the phase behaviour and dynamics of phospholipid membranes can be explored more completely by carrying out experiments at high pressure. Fourth, it has been quite often found that the volume effects determine the mechanism of a dynamic process, whereas temperature only changes the frequency of the motions without actually affecting the mechanism.[4,6] Therefore, one can expect to obtain new, fundamental information about various processes from high-pressure NMR experiments. Fifth, according to the high-pressure phase diagram of water, even at $-15\,^{\circ}C$ water is still a liquid. Therefore, biomolecular systems

(e.g., proteins in aqueous solution), can be studied at subzero temperatures to investigate their cold-denaturation behaviour.

Hydrostatic pressure has not only been used as a physical parameter for studying the stability and energetics of biomolecular systems, but also because high pressure is an important feature of certain natural membrane environments (e.g., of marine biotopes in the deep sea) and because the high pressure phase behaviour of biomolecules is of biotechnological interest (e.g., for high pressure food processing).[3–5]

The effect of pressure on chemical equilibria and reaction rates is described by the following standard equations which define the reaction volume ΔV and activation volume $\Delta V^{\#}$ of a reaction:

$$\Delta V = -\left(\frac{RT\partial \ln K}{\partial p}\right)_T \qquad \Delta V^{\#} = -\left(\frac{RT\partial \ln k}{\partial p}\right)_T \tag{1}$$

where the other symbols have their usual meaning. Another important relationship that can be obtained from high pressure experiments is $\mathrm{d}T_\mathrm{m}/\mathrm{d}p$ where T_m denotes the transition temperature between two phases, for example for the transition between the gel and liquid-crystalline (LC) phase of a phospholipid bilayer.

There are several recent reviews discussing the wide spectrum of biochemical problems that can be investigated by high pressure techniques.[3–6] The techniques that have been used most extensively in the investigation of biological systems at high pressure include fluorescence methods, vibrational spectroscopy, optical absorption spectroscopy, light scattering, X-ray and neutron diffraction. In spite of the fact that NMR is one of the most promising spectroscopic tools for the investigation of biochemical systems at ambient conditions, relatively few high-pressure NMR studies on biological molecules have been reported to date.

Compared to other biomolecular systems, lipid bilayer membranes and lyotropic lipid mesophases in general have been shown to respond most sensitively to hydrostatic pressure. The methods used in the high pressure studies have mainly included X-ray and neutron diffraction, fluorescence, IR and Raman spectroscopy, light transmission and volumetric measurements.[3–5,7–13] Only a small amount of work has been performed using NMR techniques combined with high-pressure, a field which was pioneered by Jonas and co-workers[3,6,14–20] although the method is very powerful, non-invasive and allows the study of a series of structural and dynamic properties of the systems in detail and with atomic resolution.

This review describes experimental techniques, then gives some selected results of ^{1}H, ^{31}P and ^{13}C NMR studies of pressure effects on the structure, dynamics and phase transitions of phospholipid bilayers. Other examples deal with 2D-NOESY experiments on lipid vesicles and pressure effects on the interaction of anaesthetics with phospholipid bilayers. Furthermore, we discuss

^{2}H NMR measurements on deuterated phospholipid bilayers and phospholipid/cholesterol mixtures, measurements of self-diffusion of phosphatidylcholines in lipid bilayers, and finally pressure effects on the structure and phase behaviour of model biomembranes consisting of phospholipid bilayers with incorporated peptides will be discussed.

2. HIGH-PRESSURE NMR MEASUREMENTS

Advances in superconducting magnet technology in the last decades have resulted in the development of superconducting magnets capable of attaining a high homogeneity of the magnetic field over the sample volume, so that even without sample spinning, high resolution can still be achieved. The ability to record high-resolution NMR spectra on dilute spin systems opened a new field of high-pressure NMR spectroscopy which deals with pressure effects also on biochemical systems. The literature on the techniques and the equipment available for experiments at high pressure has significantly increased in recent years. Comprehensive reviews can be found in Refs. 3, 6.

Generally, the pressure is generated outside the NMR probe. The components necessary for building a high-pressure setup, the pressure-generating system (such as piston hand pump, high-pressure tubings and valves, intensifiers) and the pressure-measuring system are available from commercial sources. Pressure is transferred from the pressure-generating equipment via a capillary tube to the sample inside the probe by a pressurizing medium. The main experimental obstacle for performing NMR experiments at high pressure is the construction of reliable high-pressure probes. Essentially, two approaches have emerged for the measurement of NMR spectra at high hydrostatic pressure.[6] One approach is a pressure sample tube (strengthened glass cells, made from borosilicate or quartz capillaries) which can be placed directly in a standard spectrometer probe. Such systems give good resolution but often suffer from the lack of a good temperature control and a limited pressure range of about 2–3 kbar. The alternative approach is the manufacture of a dedicated high-pressure probe head which replaces the ambient pressure commercial probe head. Both, radio frequency (rf) coil and sample are immersed in the high-pressure fluid and the coil is wound on a support placed closely around the sample tube. Generally, the sample cannot be made to spin, so in order to obtain good resolution from the static sample, the tube diameter has to be kept small. The system we have been using is of the latter type and described in the following. In addition, we give some details about measurements of 1D and 2D ^{1}H and ^{2}H NMR spectra at high pressure.

The material for any high-pressure NMR vessel must be non-magnetic and of high mechanical strength. The most commonly used materials for this purpose are beryllium copper (Berylco) and titanium alloys which allow building pressure vessels up to pressures of about 8–10 kbar. In such an

autoclave-style NMR vessel, rf-pulses enter the pressure vessel through electrical feedthroughs. Since the tuning–matching capacitor network is typically located outside the pressure vessel, the feedthroughs become part of the rf-circuit. The type, as well as the shape of the sample cell, i.e., a piston-based design or a bellow system, is related to the type of the experiment performed.[3,6] In the piston design, the part of the sample cell which is in the rf-cell region is made of a commercial NMR tube which is then connected via capillary tubing to precision-bore glass tubing that contains the piston. The piston, which is made of PTFE (Teflon), has a plunger equipped with a driver to provide tighter contact with the glass surface. Two O-rings made of rubber are used on the piston in order to ensure no sample contamination and a good seal.

Figure 1 shows a schematic drawing of one type of vessel we have been using in our laboratory for ^{1}H and ^{2}H NMR measurements. The high-pressure probe was constructed to fit into the room temperature bore of a wide-bore superconducting magnet, Ø 72 mm, operating at a magnetic field of 9.4 T. An aluminium support, carrying a brass cylinder, holds the pressure bomb in place. The pressure vessel is made of a titanium alloy, Ti–6Al–4V, and has an external diameter of 64 mm, an inner diameter of 18 mm and an inner length of 140 mm. A recess is cut in the outside of the vessel for the circulation of the thermostating liquid (an ethylene glycol–water mixture). It is jacketed with a

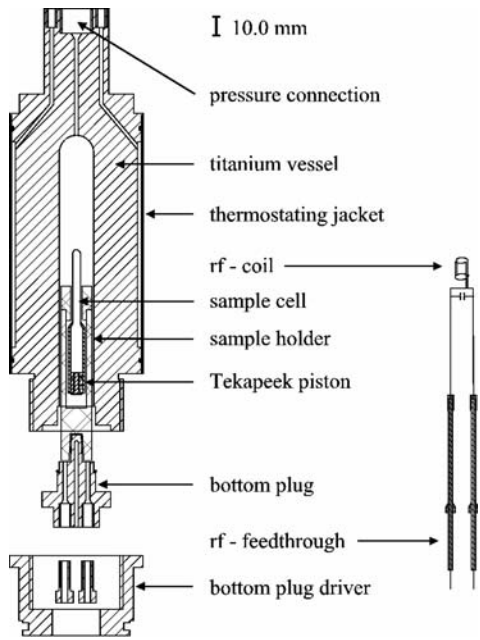

Fig. 1. Schematic drawing of the high pressure NMR autoclave.

brass cylinder with an outer diameter of 70 mm. On top of the pressure vessel are three threaded connections, one for pressurization, the others for inlet and outlet of the thermostating liquid. The high-pressure plug at the bottom of the vessel is sealed with an O-ring made of Viton. For pressures above ~ 3 kbar, Bridgman seals (e.g., Everdur-lead-Everdur) or c-seals (e.g., a lead-coated heat-threaded Inconel) may be used to contain the pressure. The plug has two threaded connections for the electrical feedthroughs and a drilling for a thermocouple which measures the temperature close to the sample. At the bottom plug driver, the rf-box is attached, containing the tuning and matching circuit, e.g., for a ^{1}H (400 MHz) observation frequency and a ^{2}H (61.4 MHz) field lock. Both resonance frequencies can be adjusted using screwdrivers from outside the magnet. The high-pressure electrical feed-throughs consist of a low capacitance signal transmission cable which is sealed with a steel cone soldered to the metal surface or of Berylco 25 (1.7–1.9% Be) which is electrically isolated by a polymer material (Vespel SP1). The internal sample holder contains a two turned saddle-shaped rf-coil, home-made from silver-coated copper wire, and the sample tube, made of a shortened commercial NMR glass tube of outer diameter 5 mm, which is fused to a precision glass tube (inner diameter 8.00 ± 0.01 mm, wall thickness 1.6 ± 0.2 mm) which separates the sample from the pressurizing liquid by a movable Tekapeek piston, sealed with two Viton O-rings. To increase the sensitivity and to reduce loss of rf-power an internal ceramic capacitor (1.0 pF) is placed close to the Helmholtz coil. This capacitor is resistant to the pressurizing liquid; fine-tuning is achieved with the external rf-circuit. The pressure is generated by a standard system consisting of a hand pump and valves (Nova Swiss Co., Effretikon, Suisse) and a Heise-Bourdon gauge (accuracy ± 10 bar) using liquid CS_2, tetrachloroethylene or methylcylcohexane as pressurizing medium for proton or deuteron studies, respectively. The current apparatus is capable of temperature control in a range from -20° up to $80\,^\circ$C with a maximum working pressure of 3000 bar (6000 bar can be reached after special treatment of the Ti–alloy).

One-dimensional (1D) ^{1}H NMR experiments were performed accumulating 64 FID's with 4 K data points and a spectral width of 4.5 kHz using a standard pulse sequence with water suppression by presaturation of the HDO resonance between pulses. A 90° excitation pulse was used with an relaxation delay of 2 s. Test spectra showed a linewidth better than 2.5 Hz (resolution 6.0×10^{-9}) for a 5 mm sample of 10% $CHCl_3$ in $CDCl_3$ in the high-pressure vessel with a signal-to-noise ratio of 220 : 1. Two-dimensional ^{1}H NOESY spectra were obtained using the pulse sequence $\pi/2{-}t_1{-}\pi/2{-}t_m{-}\pi/2{-}$acquire($t_2$) with phase-cycling, where t_1, t_m and t_2 are the evolution, mixing and detection time periods, respectively. The pulse sequence was employed with 512 t_1 values and the mixing times range from 50 to 500 ms. The spectral width was set to 4.5 kHz and like in the 1D experiments water suppression via presaturation was applied. Each spectrum consisted of

4 K × 512 real data points with zero-filling applied in the t_1 dimension to 2 K data points. For each increment 16 or 32 FID's were accumulated with a relaxation delay of 2 s.

The ^{2}H NMR experiments were performed using the quadrupolar echo pulse sequence $\pi/2_x-\tau_1-\pi/2_y-\tau_2-$acquisition with phase-cycling and quadrature detection. A Bruker MSL 400 spectrometer was used for the high pressure studies operating at a resonance frequency of 61.4 MHz. In the liquid–crystalline phase, perdeuterated lipids display ^{2}H NMR spectra, which are superpositions of axially symmetric quadrupolar powder patterns of all C–D bonds.[21–28] From the sharp edges, the quadrupolar splittings

$$\Delta\omega_Q = \frac{3}{4}\frac{e^2qQ}{h}S_{CD} \tag{2}$$

can be obtained, where e^2qQ/h (the static quadrupole coupling constant) for ^{2}H(D) in C–D bonds is about 167 kHz,[27] and the C–D bond order parameter S_{CD} for distinguishable deuterons can be calculated, which is defined by:

$$S_{CD} = \frac{1}{2}\langle 3\cos^2\theta - 1\rangle. \tag{3}$$

Here θ is the instantaneous angle between a given C–D bond vector and the axis of rotational symmetry of the molecules, i.e., the bilayer normal. The brackets denote an average over the time scale of the experiment ($\sim 10^{-5}$ s) so that S_{CD} is the time-averaged orientation of the particular C−D bond with respect to the bilayer normal.

Furthermore, in all phases studied the first spectral moment M_1 of the ^{2}H NMR spectra can be calculated and the weighted mean splitting of the ^{2}H NMR spectrum can be obtained, which is proportional to the average chain orientational order parameter of the lipid, using:

$$M_1 = \frac{\int_0^\infty \omega\cdot f(\omega)\mathrm{d}\omega}{\int_0^\infty f(\omega)\mathrm{d}\omega} = \frac{4\pi}{3\sqrt{3}}\langle\Delta\omega_Q\rangle \propto \langle S_{CD}\rangle \tag{4}$$

where $f(\omega)$ is the spectrum.

3. PRESSURE EFFECTS ON THE STRUCTURE, DYNAMICS AND PHASE TRANSITIONS OF PHOSPHOLIPID VESICLES

Phosphatidylcholines are the most prominent components of biological membranes and therefore often serve as model biomembrane systems in biophysical studies.[1,2] Due to their amphiphathic character, phospholipids have a strong tendency to spontaneously form bilayer structures when

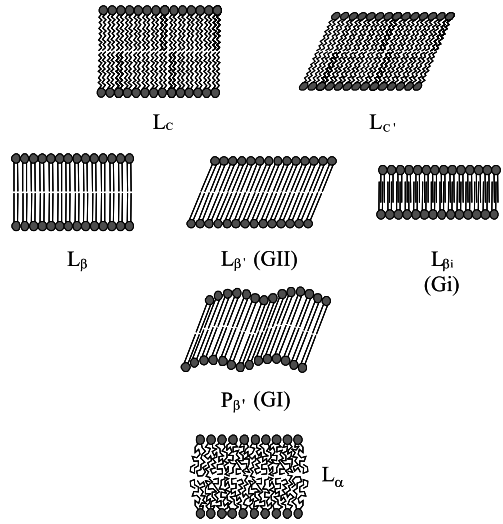

Fig. 2. Schematic representation of typical lamellar phospholipid phases.

dispersed in water and to aggregate to ordered, usually multilamellar structures (liposomes), consisting of concentric, stacked bilayers, each separated by a layer of water. According to the fluid mosaic model,[29] the lipid bilayer structure forms a fluid-like two-dimensional matrix, which provides cells with permeability barriers and allows the insertion of other membrane components, such as cholesterol and polypeptides. The structure and dynamic state of the lipid bilayer has often been found to have a significant influence on the function of the membrane proteins.

Even simple one-component phospholipid bilayers exhibit various phases, depending on the lipid configuration, level of hydration, ionic strength of the solvent, temperature and pressure.[1–4,30] At ambient pressure, four major types of thermotropic phases have been observed for saturated phosphatidylcholines. Their structure is shown in Fig. 2. For example, in DPPC (1,2-dipalmitoyl-*sn*-glycero-3-phosphatidylcholine (di-$C_{16:0}$)), after prolonged storage at low temperatures, a sub-gel phase L_c is formed. It is a highly ordered phase with an orthorhombic acyl chain packing, where the free rotation of the chains is hindered. Around 17 °C, the $L_{\beta'}$ (GII) gel phase is formed, in which the acyl chains are fully extended, packed in a distorted hexagonal lattice and tilted with respect to the lipid bilayer normal. At ~34 °C the so-called pretransition from the $L_{\beta'}$ to the $P_{\beta'}$ (GI)-phase occurs, which has a two-dimensional lattice structure in which the lipid bilayers are distorted by a periodic ripple in the plane of the lamellae. The chains are still ordered and packed in a regular hexagonal lattice. Further increase of temperature leads to the formation of a liquid-crystalline (LC) or L_α phase, at the main phase transition temperature $T_m = 42$ °C. In this fluid-like phase, the hydrocarbon chains are conformationally

disordered ('melted') and undergo extensive *trans*/*gauche* isomerizations reminiscent of fluid hydrocarbon chains, thus leading to the high lateral mobility of lipid molecules required for optimal physiological function.

Besides these thermotropic phase transitions, a variety of pressure-induced phase transformations can be observed,[4,11–13,30] and it has been demonstrated that temperature and pressure have non-congruent effects on the structural and phase behaviour of these systems.

3.1. ^{1}H and ^{13}C NMR experiments on phospholipid vesicles

^{1}H and ^{13}C NMR experiments were carried out that deal with the effects of pressure on the liquid-crystalline to gel phase transitions in phospholipid vesicles. Among those, DPPC dispersions were extensively investigated followed by the fact that it is a well-studied model phospholipid for natural membrane systems and specifically, it is found at high levels in lung surfactant.

The reason why one chose to follow the main liquid-crystalline to gel phase transition in DPPC by monitoring the linewidth of the various ^{1}H or natural abundance ^{13}C resonance is evident when we consider the expressions for the spin-lattice relaxation time (T_1) and the spin–spin relaxation time (T_2). The first one is given by $1/T_1 \propto A[J_1(\omega_0) + J_2(2\omega_0)]$ where $J_1(\omega_0)$ is the Fourier transform of the correlation function at the resonance frequency ω_0 and A is a constant related to internuclear separation. The relaxation rate $1/T_1$ thus reflects motions at ω_0 and $2\omega_0$. In contrast, the expression for T_2 shows that $1/T_2$ monitors slow motions: $1/T_2 \propto \mathrm{B}[J_0(0) + J_1(\omega_0) + J_2(2\omega_0)]$, where $J_0(0)$ is the Fourier component of the correlation function at zero frequency. Since the linewidth $\nu_{1/2}$ (full-width at half-maximum intensity) is proportional to $1/T_2$, the changes of linewidth will reflect changes in the mobility of various carbon atoms in the DPPC bilayer.

As an example, proton-decoupled natural-abundance^{13}C Fourier-transform NMR spectra of Jonas and co-workers on sonicated DPPC vesicles at $\sim 53\,^{\circ}$C as a function of pressure are shown in Fig. 3. The assignment of the main ^{13}C resonances[14,31–34] is given in Table 1. As the pressure increases, one moves from a bilayer in which the two palmitoyl chains are very flexible and mobile into the pressure-induced first gel state, in which the bilayer organization is retained but the acyl chains become rather rigid. The linewidth results shown in Fig. 4 indicate that, in the liquid-crystalline state, the carbonyl carbons in the glycerol backbone region have the most restricted motions, the acyl-chain methyl groups have intermediate mobility, and the methylene and methyl carbons of the head group are most mobile. By ~ 800 bar, when we enter the pressure-induced gel state of DPPC, the motions of most carbon atoms in the acyl-chains become so hindered that their resonance peaks broaden beyond detection; the choline methyl carbons in the head group region, however, remain sufficiently mobile in the gel state to give sharp resonance peaks.

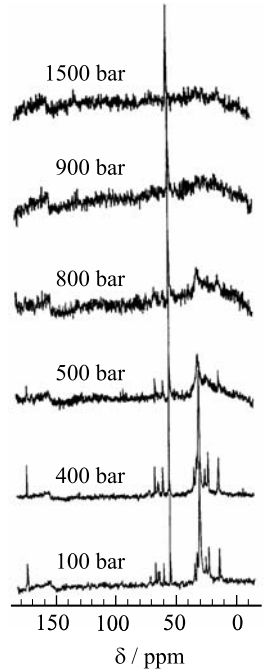

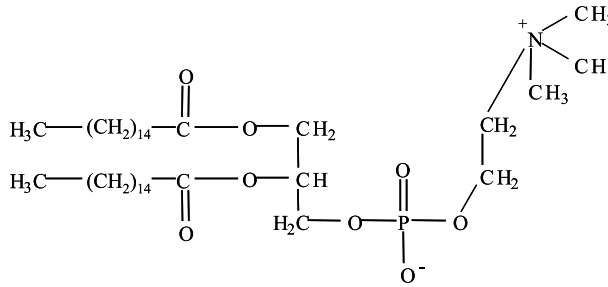

Fig. 3. Proton-decoupled natural abundance ^{13}C Fourier-transform NMR spectra of DPPC (chemical structure at the bottom) in excess H_2O as a function of pressure at 52.7 °C (after Ref. 14).

The choline head group maintains considerable mobility, even in the gel phase, because it is exposed to water, and its methyl groups can still rotate quite freely.

3.2. 2D-NOESY investigations of phospholipid vesicles

Two-dimensional (2D) Nuclear Overhauser Effect Spectroscopy (NOESY) has been proven to be a valuable technique which provides both structural and

Table 1. Assignment of ^{13}C NMR resonances in DPPC vesicles

Resonance	δ/ppm
Palmitoyl methyl	16
First methylene	25
Second methylene	28
Bulk methylene	31
Methylene	34, 36
Choline methyl	56
Choline methylene	61
Glycerol methylene	65, 65.5
Choline methylene	68
Glycerol methylene	73
Carbonyl	175

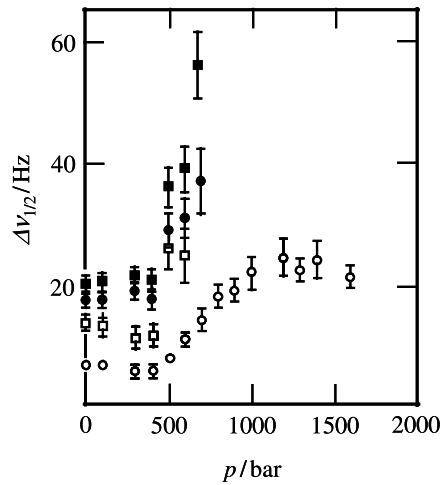

Fig. 4. Pressure dependence of the ^{13}C linewidths in DPPC vesicles for choline methyl groups (○); choline methylene groups (□); palmitoyl methyl groups (●); and carbonyl carbons (■) at 52.7 °C (after Ref. 14).

dynamical information. Dipolar cross-relaxation, responsible for the NOE, depends on both spatial proximity and relative motion of the interacting nuclei. NOESY has been successfully applied to study membrane systems and their interactions with probe molecules at ambient conditions.[35–38]

In order to provide quantitative information on the effects of pressure on cross-peak intensities, we carried out 2D-NOESY experiments on pure POPC (1-palmitoyl-2-oleoyl-*sn*-glycero-3-phosphatidylcholine ($C_{16:0}$, $C_{18,cis}$)) and DMPC (1,2-dimyristoyl-*sn*-glycero-3-phosphatidylcholine (di-$C_{14:0}$)) lipid bilayers.[19] As an example, we present data on POPC, a phospholipid which is also a very important component of animal cell membranes. It has an

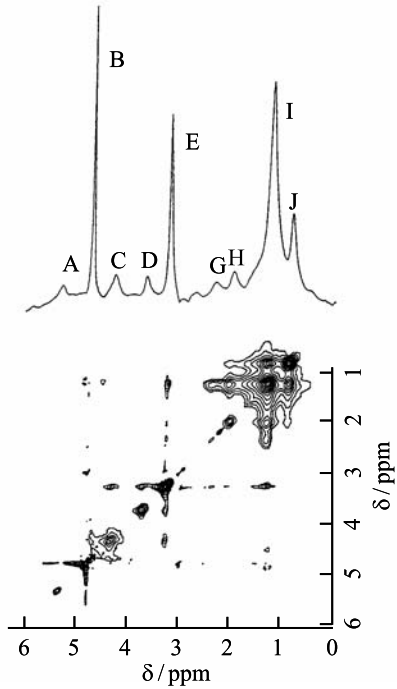

Fig. 5. ^{1}H, ^{1}H NOESY spectrum for sonicated POPC vesicles (0.09 M) in the high-pressure autoclave at 28 °C and 0.1 MPa. The 1D spectrum included was taken with 16 acquisitions, a data size of 4 K; the 2D phase sensitive NOESY spectrum for $\tau_M = 250$ ms, with 64 acquisitions, a data size of 1024×1024 (after Ref. 19).

unsaturated (C_{18}) and a saturated (C_{16}) acyl-chain, and the gel to fluid $L_{\beta'}$–L_α transition of POPC dispersions occurs at −5 °C. The double bond on the *sn*-2 chain of this lipid gives POPC the property of being highly fluid at physiological temperature and also makes it an ideal system for studies at increased pressure near ambient temperature. Figure 5 shows the 1D proton spectrum of sonicated POPC vesicles in D_2O at room temperature together with the 2D-NOESY spectrum of POPC under the same experimental conditions for the mixing time $\tau_M = 250$ ms. One can clearly see the presence of many intense cross peaks between the individual resonances (Table 2). Figure 6 shows the evolution of the cross-peak intensities for the $(CH_2)_n/NMe_3$ resonances for DMPC vesicles as a function of mixing time τ_M in the pressure range from 1 to 2000 bar at $T = 64$ °C; i.e., in its liquid–crystalline phase ($T_m = 23.5$ °C). The intensities of the cross-peaks are normalized to those of the corresponding diagonal peaks at the shortest mixing time used ($\tau_M = 50$ ms). The NOE build-up curves show a strong dependence upon pressure as the cross peak intensities grow stronger with increased pressure. Indeed, an evaluation of

Table 2. Assignment of ^{1}H NMR resonances in POPC vesicles[41,42]

Peak	δ/ppm	Group assignment
A	5.25	–CH=CH–
B	4.68	HDO
C	4.25	$-CH_2-CH_2-N^+(CH_3)_3$
D	3.65	$-CH_2-N^+(CH_3)_3$
E	3.18	$CH_2-N^+(CH_3)_3$
G	2.24	$C-CH_2-$
H	1.95	$-CH_2-CH=$
I	1.17	$-CH_2-$(bulk methylene)
J	0.80	$-CH_2-CH_3$

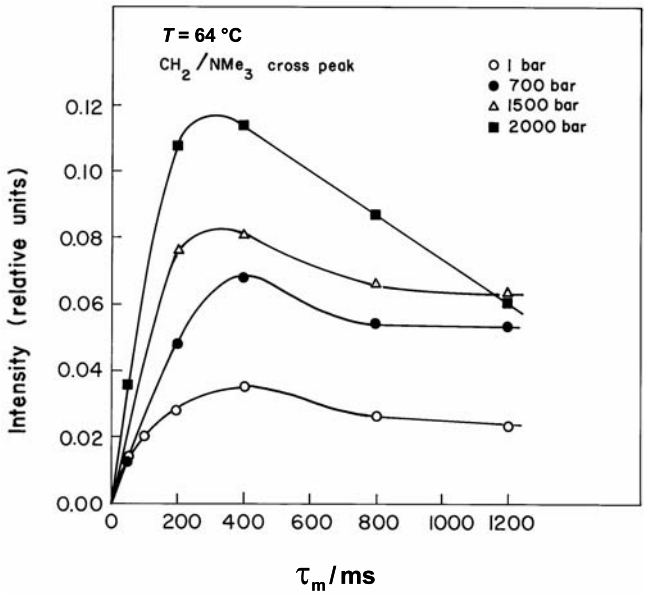

Fig. 6. The intensity of the $(CH_2)_n/CH_3$ cross-peaks in sonicated DMPC vesicles (0.09 M) at different pressures from 1 bar to 2000 bar as a function of the mixing time ($T = 64\,^\circ$C) (after Ref. 19).

the NOE build-up curves revealed the increase in cross-peak intensities with increasing pressure for all cross-peaks observed for the sonicated POPC and DMPC vesicle systems, even for a short mixing time of $\tau_M = 75$ ms (Fig. 7).

In view of the complexity of the cross-relaxation phenomena in membranes, a rigorous theoretical description of the results of these high pressure NOESY experiments was not possible. To demonstrate the complexity of the

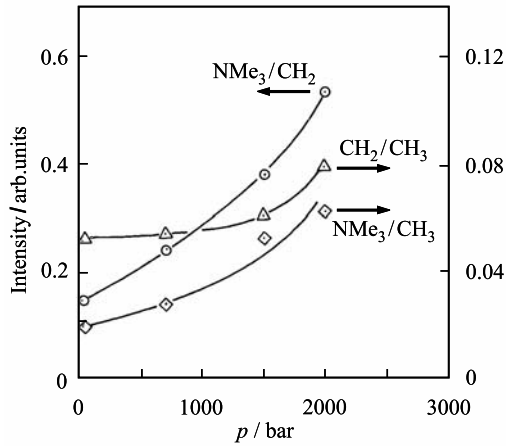

Fig. 7. The intensity of different ^{1}H, ^{1}H NOESY cross-peaks in sonicated DMPC vesicles (0.09 M) as a function of pressure at a mixing time τ_M of 200 ms ($T = 64\,^\circ$C) (after Ref. 19).

problem,[19] we can write the following simplified expression for the pressure dependence of the cross-relaxation rate σ_{ij} between spins i and j

$$\sigma_{ij} \propto \sigma_{ij}[r_{ij}, S_{HH}(p), \tau_\perp(p), \tau_\parallel(p), \tau_J(p), SD(p)] \tag{5}$$

where r_{ij} is the distance between spin i and j; $S_{HH}(p)$ is the pressure dependent order parameter; $\tau_\perp$, $\tau_\parallel$ and τ_J are the correlation times for anisotropic inter- and intramolecular motions, respectively, as for example discussed by Mayer *et al.*[39,40] in their NMR study of DMPC; SD denotes the spin diffusion contribution to cross-relaxation. It is well known that pressures up to ~ 2 kbar do not change bond angles or bond distances, but of course, they can change conformations. As discussed in Ref. 19, the cross-relaxation rates depend on the spectral density functions and hence correlation times of slow and fast motions as well as on the order parameter S_{HH}, the pressure dependencies of which are largely unknown, however. The pressure effects on the correlation times are estimated to give a small contribution only when going from 1 to 2000 bar. In order to reproduce the large pressure changes in σ_{ij}, one must allow the order parameter S_{HH} to increase significantly from 0.36 at 1 bar to 0.6 at 2000 bar. This would be in agreement with SANS and ^{2}H NMR studies on this system. It is clear that quantitative interpretation of the observed pressure effects on σ_{ij} cannot be carried out solely on the basis of these studies, and therefore systematic high pressure NMR studies of selectively deuterated phospholipids are needed to determine the pressure effects on the various correlation times and order parameters (see below).

Finally, we focus on the role of pressure on the hydration of lipid bilayer membranes. Figure 8 displays the ^{1}H, ^{1}H NOESY spectra of sonicated DMPC

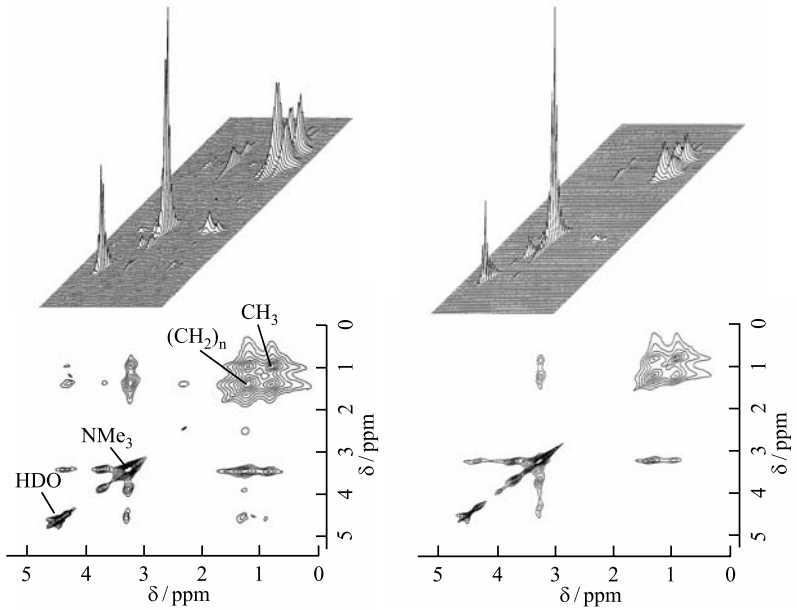

Fig. 8. ^{1}H, ^{1}H NOESY spectra (stagged and contour plot) of sonicated DMPC vesicles at 700 bar (left) and 2000 bar (right) for $T = 64\,^{\circ}$C ($\tau_M = 800$ ms).

vesicles at two pressures (700 and 2000 bar) for $T = 64\,^{\circ}$C. It can be clearly seen that the cross peak intensity of water (HDO) to the $(CH_2)_n$ groups of the acyl-chains of DMPC drastically decreases with increasing pressure. With increasing pressure, the number of *gauche* conformers and kinks in the lipid acyl-chains decreases and most of the water in the upper chain and lower headgroup region is expelled.

3.3. Pressure effects on the interaction of anaesthetics with phospholipid bilayers

As an example of a study demonstrating the use of 2D NOESY experiments in determining the interaction and location of biomolecules in membranes, such as drugs, anaesthetics or peptides, we present data on a lipid bilayer system containing a local anaesthetic, tetracaine (TTC). The mechanism of anaesthetic action is still uncertain,[43] but the site of this action is generally assumed to be the cellular membrane of the neuron and the anaesthetic potency is well known to be correlated with the anaesthetic partitioning into these membranes. The pressure reversal of anaesthesia both *in vivo* and *in vitro* has been known for a long time[44–46] and the investigation of the pressure-anaesthetic antagonism has thus been regarded as a possible key to elucidate

the mechanism of anaesthetic action. The anaesthetic TTC increases the partial molar lipid volume and leads to a disordering of the lipid acyl chains, and pressure is thus presumed to reverse both these effects.[7–10,20] As the location of TTC within the membrane may offer insight into its mechanism of action, this question has been addressed applying two-dimensional ^{1}H, ^{1}H NOESY as a function of pressure. This method can be used to estimate distances in space, or close approach, between pairs of protons that are separated by a distance of 2–5 Å, and the intermolecular cross-peaks yield valuable information about the location and conformation of TTC within the membrane and a possible expulsion at elevated pressures.

The NMR spectroscopic investigations were performed on POPC vesicles containing TTC at different pD values.[47,48] As an example, Fig. 9a shows the ^{1}H NMR spectrum of POPC–TTC vesicles at pD 5.5 and $T = 25\,^{\circ}$C. Figure 9b depicts the corresponding ^{1}H, ^{1}H NOESY spectrum for a mixing time of 100 ms. The NOESY spectrum at ambient pressure exhibits strong intramolecular cross-peaks between the phenyl-protons (e, f) and the $^{+}ND(CH_3)_2$-protons (i) of the tetracaine, suggesting a bent conformation of the anaesthetic molecule in the lipid bilayer. Also the formation of dimers may contribute to this observation at high anaesthetic concentration. Further, weak cross-peaks are observed between the phenyl-protons (e, f) of TTC and the lipid headgroup (I), as well as between the $^{+}ND(CH_3)_2$-protons (i) and the headgroup-protons (I), indicating that the TTC molecule is located in the polar/apolar interfacial region of the lipid bilayer.

Previous investigations raised concern because they reported intense cross-peaks between almost all lipid resonances (e.g., see also Fig. 5). The data suggested that even protons of lipid headgroups and the ends of the acyl-chains are in contact. Hence, it has been assumed that cross-relaxation rates in lipid membranes might reflect not only the close approach of lipid protons through space. A relay of spin polarization through the network of protons with strong dipolar couplings, i.e., spin diffusion, could lead to 'anomalous' NOESY cross-peaks.[35,36,38] Recently it has been shown by Gawrisch *et al.*,[37,49] however, that interactions between lipid protons, which are not nearest-neighbours by chemical bonding are exclusively intermolecular and that spin diffusion within lipid molecules does not contribute to the cross-relaxation rates. Their data further indicate that shifts in location of neighbouring lipid segments by several Å along the bilayer normal are very likely, which is also a reminder that membranes are highly dynamic structures with significant molecular disorder. Lipid molecules in biological and fluid model membranes are continually fluctuating via *trans-gauche* isomerization, axial rotation, lateral diffusion, and vertical (single particle and collective) motions (dynamic surface roughness), all occurring on a time scale of micro- to picoseconds. Hence, a distribution of cross-peaks between lipid molecules and between lipid and TTC and no unique location for the embedded molecule might be expected, and the intensity of a cross-peak might indicate the probability for

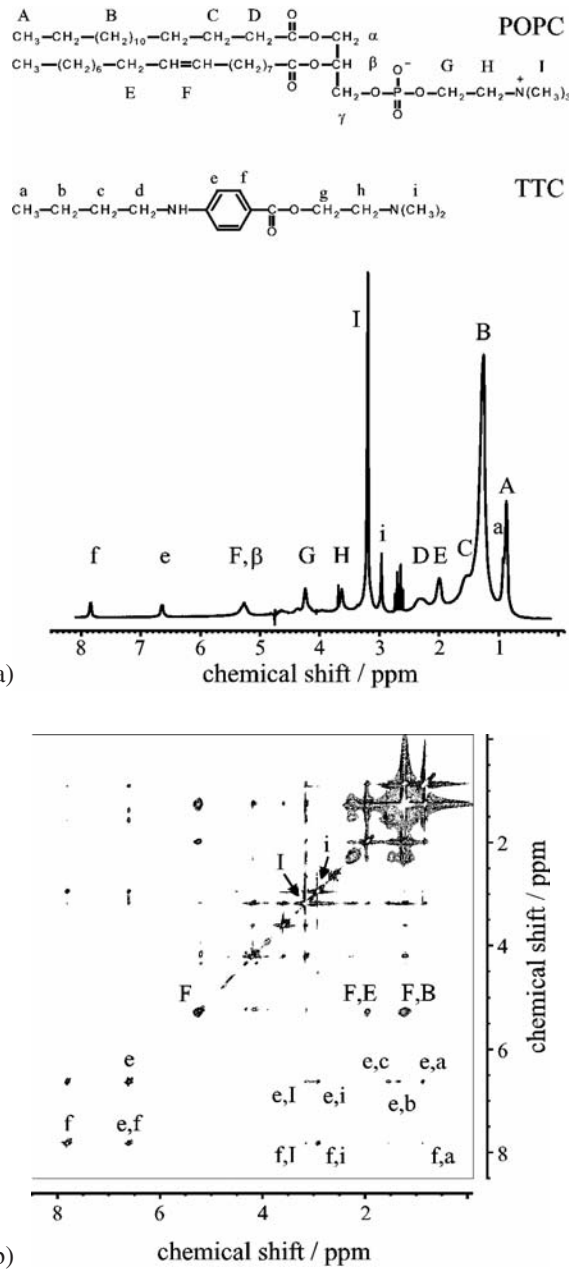

Fig. 9. (a) 1D ^{1}H-NMR spectrum and proton resonance assignments[41,42] of sonicated POPC−TTC vesicles (25 mol% TTC) at $T = 25\,^{\circ}$C and pD = 5.5; (b) ^{1}H, ^{1}H-NOESY spectrum of sonicated POPC−TTC vesicles (25 mol% TTC) at a mixing time of 100 ms at ambient pressure ($T = 25\,^{\circ}$C, pD = 5.5) (after Ref. 49).

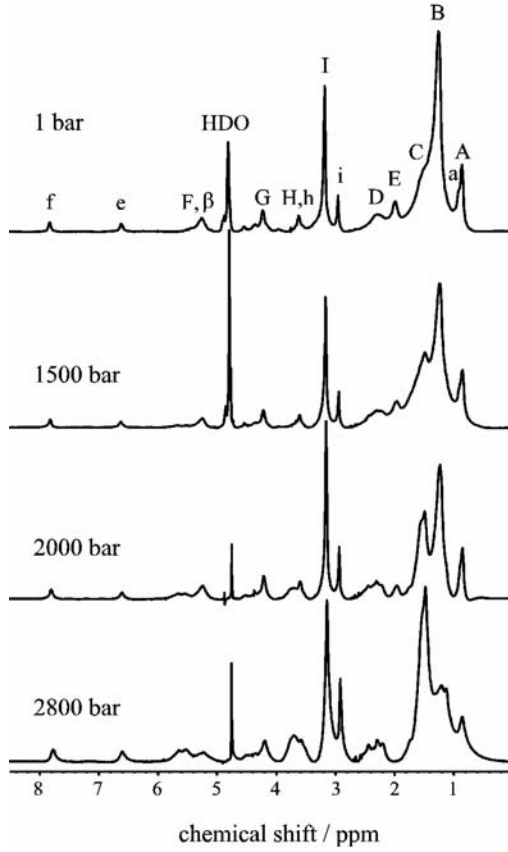

Fig. 10. High-pressure 1D ^{1}H-NMR spectra of sonicated POPC–TTC vesicles (25 mol% TTC) at room temperature ($T = 22\,^{\circ}$C) and pD = 5.5 (after Ref. 49).

a particular location only. The strongest lipid-TTC cross-peaks are observed with lipid protons from the choline headgroup and upper chain segments, which supports the hypothesis of an interfacial location for TTC in phospholipid bilayers.

Figure 10 shows the ^{1}H NMR spectrum of sonicated POPC–TTC vesicles at room temperature and selected pressures.[47,48] Already the one-dimensional ^{1}H NMR spectra exhibit some interesting features. With increasing pressure, the signal intensity of the acyl-chain protons at 0.85 and 1.24 ppm decrease due to the pressure-induced rigidization of the acyl-chains, as it is also observed for pure phospholipid samples. At pressures above the fluid-gel main transition, which is detected at a pressure of about 1200 bar at 20 °C in pure POPC dispersions, the acyl-chain signals of pure lipid samples disappear completely, whereas in the spectra of the POPC–TTC system considerable signal intensities remain even up to pressures of 2800 bar. Furthermore, we observe for the

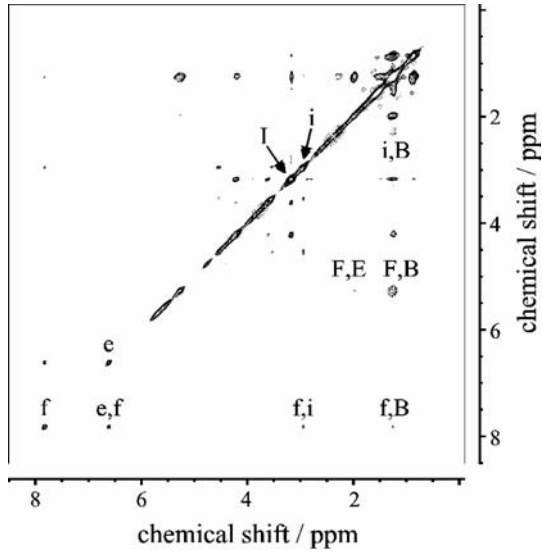

Fig. 11. ^{1}H, ^{1}H NOESY spectrum of sonicated POPC–TTC vesicles (25 mol% TTC) at 1000 bar ($\tau_M = 100$ ms, $T = 25\,^{\circ}$C, pD = 5.5) (after Ref. 49).

tetracaine containing sample an increasing signal at 1.60 ppm and the formation of three broad resonances at 2.3, 3.7 and 5.7 ppm. These data indicate that the incorporation of TTC has a fluidizing effect on the lipid membrane and a further structural phase transition seems to occur at the highest pressures.

Figure 11 shows the ^{1}H, ^{1}H NOESY spectrum of POPC–TTC at a pressure of 1000 bar at pD 5.5 and 22 °C. The intermolecular cross-peaks remain visible, although they become significantly weaker. In addition two new cross-peaks (i, B and f, B) build up at pressures above 500 bar, which leads us to the conclusion that the TTC molecule is located deeper in the lipophilic membrane region, giving rise to these cross-peaks between the methylene protons of the lipid and the amino-methyl and phenyl protons of the tetracaine. Up to the highest pressures measured here (~2 kbar), the local anaesthetic is not expelled from the bilayer, it seems to slightly change its location only. At much higher pressures, TTC might – at least partially – be expelled from the lipid bilayer, however.[8–10]

3.4. Deuterium NMR studies of chain and headgroup deuterated phospholipid bilayers and phospholipid–cholesterol mixtures

In several laboratories detailed high pressure ^{2}H NMR studies on phospholipid bilayer membranes have been performed.[15–17,50–56] Here, we first present data

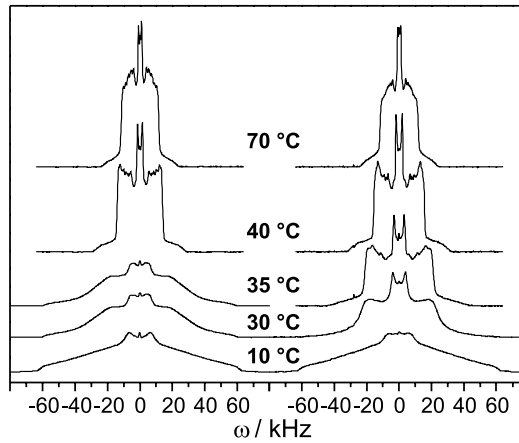

Fig. 12. ^{2}H NMR spectra of d_{62}-DPPC (left) and d_{62}-DPPC–GD (4.7 mol%) (right) at selected temperatures ($p = 1$ bar).

of perdeuterated 1,2-dipalmitoyl-*sn*-phosphatidylcholine (d_{62}-DPPC). At ambient pressure, a sharp transition from the LC to gel state occurs in DPPC vesicles at 42 °C (37 °C for the perdeuterated lipid) and is readily observable by ^{2}H NMR as a marked increase in width of the spectrum, in both, perdeuterated and selectively labelled samples (Fig. 12).[14–17,56] In the LC phase of the fully deuterated lipid bilayer, an averaged axially symmetric powder pattern composed of many overlapping peaks corresponding to the various C–D bonds is seen in the spectrum. Although, one cannot resolve every deuteron in the spectrum, one can follow several individual peaks and monitor different regions of the phospholipid molecule. In the more rigid gel state, these peaks are not resolved any more. The ^{2}H NMR spectra clearly show, however, that the gel state still does not consist of motionless acyl-chains in the *all-trans* state. At intermediate temperatures, below the LC state from 5 °C to 35 °C, the characteristic axially symmetric rigid lattice spectrum with sharp shoulders at ± 63 kHz is absent, and the spectra indicate the presence of motional averaging. The observed lineshapes can be modelled and interpreted in terms of various combinations of long axis rotation, chain fluctuations, and *trans–gauche* isomerizations. Only at very low temperatures (< 0 °C) a rigid lattice spectrum may be seen for DPPC indicating the absence of motion on the NMR timescale.

Fourier-transform infrared (FT-IR) spectroscopy and small-angle X-ray (SAXS) and neutron (SANS) scattering studies have shown the existence of a further pressure induced gel phase in DPPC bilayers.[4,11–13] Pressure dependent ^{2}H NMR studies yielded complementary information on the pressure-induced gel phases. The gel state of DPPC bilayers shows a variation in lineshapes which depend on the particular pressure and temperature. The types of lineshapes seen in a high pressure investigation of d_{62}-DPPC by Jonas *et al.* are

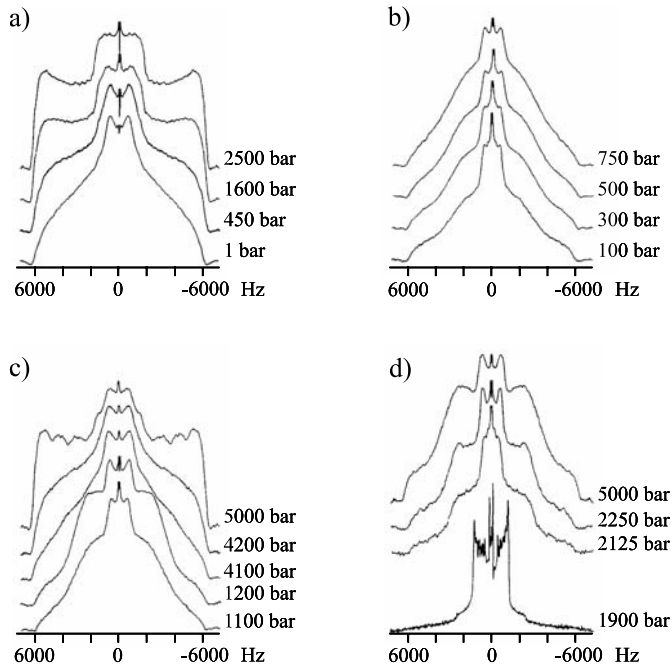

Fig. 13. Representative ^{2}H NMR lineshapes and lineshape changes as a function of pressure in gel states of d_{62}-DPPC at (a) 7 °C, (b) 34 °C, (c) 41 °C, and (d) 75 °C. Pressure conditions are noted for each spectrum.

depicted in Fig. 13.[14–17] The figure illustrates the lineshape changes which occur with pressure at four representative temperatures (7 °C, 34 °C, 41 °C, and 75 °C). Generally, a decrease of temperature or increase in pressure causes a change in lineshape from a fast motion axially asymmetric powder pattern of the LC state (Fig. 13d, 75 °C and 1900 bar) to the almost rigid methyl lattice spectrum at 7 °C and 1.6 kbar (Fig. 13a). Throughout most temperatures and pressures, a splitting from approximately ±10 to ±20 kHz is seen for the methyl group. It is also evident that no methylene resonances can be seen in the gel state, only an unresolved curved lineshape which is uniquely determined by the particular gel phase state.

Also spin-lattice relaxation times T_1 and spin–spin relaxation times T_2 were measured as a function of pressure on different selectively deuterated DPPC (at C_2, C_9 and C_{13}, respectively) by Jonas and co-workers (Fig. 14).[16] The spin-latticed relaxation time T_1 is sensitive to motions with correlation times τ_c near ω_0^{-1}, i.e., motions with correlation times in the range from 10^{-8} to 10^{-11} s. In comparison with T_1, the spin–spin relaxation time T_2 is more sensitive to motions with correlation times near $(e^2qQ/h)^{-1}$, i.e., in the intermediate to slow range (10^{-4} to 10^{-8} s). The T_1 and T_2 values obtained showed characteristic changes at various phase transition pressures, thus indicating abrupt changes

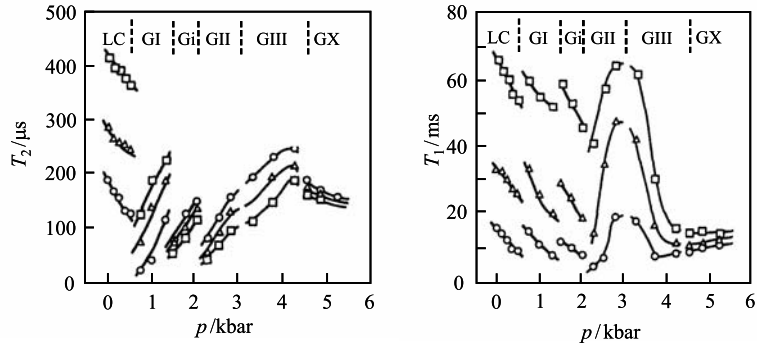

Fig. 14. The spin–spin (T_2) and spin-lattice (T_1) relaxation times as a function of pressure for 1,2(2′,2′-^{2}H)DPPC (○), 1,2(9′,9′-^{2}H)DPPC (△), and 1,2(13′13′-^{2}H)DPPC (□) samples at 50 °C (after Ref. 16).

in the rate for different modes of motion among these phases. In the LC phase, T_1 and T_2 values for all segments decreased with pressure, indicative of the fast correlation time regime. Similarly, T_1 decreased with pressure in the GI phase and the interdigitated Gi phase but changed to the slow correlation time regime at the Gi/GII transition. For all segments, a common T_1 value is observed in the GX phase only, suggesting a common motional mode that, most likely, is the *trans–gauche* isomerization. As expected, the order of magnitude of T_1 is $C_{13} > C_9 > C_2$ in all phases, indicating a greater motional freedom toward the end of the acyl chain. For T_2, which reflects slow motions, the transition to the slow correlation time regime occurs already at the LC–GI phase transition.

Methyl splitting and/or first moment analysis (Eqs. (2, 4)) as well as changes of the ratio of the central peak intensity to the shoulder intensities were used to determine phase changes. Figure 15 includes the phase transitions observed by these high pressure ^{2}H NMR studies.[17] The high pressure gel phases essentially differ in the tilt angle of the acyl-chains and the level of hydration around the head group.[11–13] Only in the interdigitated gel phase (Gi), the acyl-chains are partially interdigitated (see Fig. 2), in accordance with the high pressure SAXS and SANS results.[11–13] Further ^{2}H NMR experiments by Morrow *et al.* agreed with these findings of Driscoll *et al.*[17] with the exception of the position of the boundary between the GIII and GX phases and the presence of the L_c phase at low pressure and temperature.[55] It is thus clear from these data, that the gel state cannot be thought of as a single phase beyond the $P_{\beta'}$ or $L_{\beta'}$ transition, undergoing gradual lineshape changes in ^{2}H spectra with a gradual decrease in motion; rather there are abrupt changes in motion and structure at phase transitions occurring at specific temperatures and pressures.

Morrow *et al.* also examined the effects of pressure and temperature on DPPC and DMPC choline headgroup conformation using deuterium nuclear magnetic resonance.[50,53] The electric dipole resulting from charge separation in

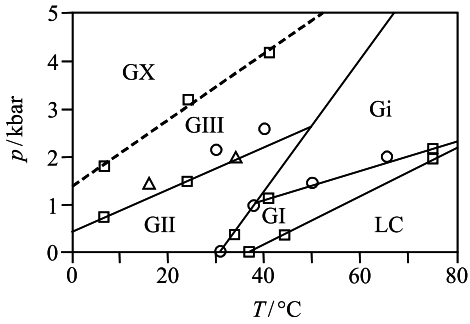

Fig. 15. Pressure–temperature phase diagam of d_{62}-DPPC in excess water as obtained from ^2H NMR experiments (after Ref. 17).

the phosphatidylcholine group is considered to lie roughly parallel to the bilayer surface under physiological conditions. Isothermal compression was found to produce a decrease in the choline α deuteron quadrupole splitting and an increase in the choline β and γ deuteron quadrupole splittings. A similar counterdirectional change, seen in the presence of positive surface charge, has been attributed to a tilting of the headgroup away from the bilayer surface in response to the torque exerted on the phosphatidylcholine dipole by positive surface charges.[22,28]

Fluid lipid bilayers are very anisotropic. They are generally more compressible in the plane of the bilayer than along the bilayer normal. The consequence of this, as confirmed by neutron scattering, is that the application of hydrostatic pressure increases the bilayer thickness while reducing the area per lipid. This effect can also be inferred from NMR results. Using a simple model, the observed changes in the first spectral moment M_1 are found to correspond to an increase in the mean extension by about 2.5% for DPPC over the 1 kbar pressure range examined and by about 3.5% for DMPC over a pressure range of 2 kbar. It is reasonable to assume that the pressure-induced change in fluid phase headgroup conformation and the increasing chain ordering are both responses to steric constraints arising from a reduced area per lipid. It is also interesting to note that the application of pressure changes the α and β deuteron splittings in directions opposite to those seen for decreasing hydration. Furthermore, it is significant that for M_1 and the headgroup deuteron splittings the sensitivity to pressure is larger in DPPC than in DMPC. This presumably reflects a difference between the lateral response to hydrostatic pressure of the two bilayers at a common temperature (at ambient pressure, the main transition of d_{54}-DMPC occurs at 19 °C).

Morrow *et al.* measured the spin-lattice relaxation time T_1 and quadrupole echo decay times (T_2^{qe}) of headgroup deuterated d_4-DMPC as a function of temperature and pressure to yield additional information about changes in the headgroup dynamics.[54] Generally, motions in a LC phospholipid bilayer can

span a range of characteristic times from shorter than 10^{-8} s for internal segment rotations and long-axis rotation or re-orientation, to times longer than 10^{-4} s for collective motions of the bilayer surface or reorientation due to diffusion of molecules through regions in which the direction of the bilayer normal changes significantly. At room temperature and above, these motions which are typically fast conformational changes and rotational diffusion, have correlation times that are shorter than the inverse of the Larmor frequency so that T_1 is expected to increase with increasing temperature. Increasing temperature shortens the correlation times for these motions and reduces the spectral density at the Larmor frequency. Quadrupole echo decay (Carr-Purcell-Meiboom-Gill) is sensitive to motions covering a wider range of time scales (down to 10^{-4} to 10^{-3} s). Within the LC phase, pressure has been found to reduce T_1 values and to increase T_2^{qe}. The first observation was taken to indicate a pressure induced increase of correlation times for fast motions contributing to spin-lattice relaxation. The quadrupole echo decay times are consistent with a distribution of slow motions in the bilayer (e.g., the diffusion of lipid molecules around curved vesicle surfaces or collective bilayer undulations) and the application of pressure appears to extend the range of this distribution to longer correlation times. In the gel phase, the spin-lattice relation times and quadrupole echo decays were found to be less sensitive to the application of pressure.

Natural biological membranes consist of lipid bilayers, which typically comprise a complex mixture of phospholipids and sterol, along with embedded or surface associated proteins. The sterol cholesterol is an important component of animal cell membranes, which may consist of up to 50 mol% cholesterol. As cholesterol can significantly modify the bilayer physical properties, such as acyl-chain orientational order, model membranes containing cholesterol have been studied extensively.[1,2] Spectroscopic and diffraction experiments reveal that cholesterol in a lipid-crystalline bilayer increases the orientational order of the lipid acyl-chains without substantially restricting the mobility of the lipid molecules. Cholesterol thickens a liquid-crystalline bilayer and increases the packing density of lipid acyl-chains in the plane of the bilayer in a way that has been referred to as a condensing effect.

Morrow *et al.* studied the effect of hydrostatic pressure on DPPC bilayers containing 28.5 mol% cholesterol,[55] where the membrane system is in a liquid-ordered state, up to $\sim$2100 bar. At 50 °C, the ambient pressure spectrum is a superposition of Pake doublets, characteristic of fast axially symmetric motion, but with significantly larger splittings than would be seen in the LC phase of the pure lipid bilayer. The larger splittings reflect the ordering effect of cholesterol on the lipid acyl-chains. Decreasing the temperature to 0 °C, the spectrum becomes broader and is no longer characteristic of a fast axially symmetric re-orientation. The evolution of the spectral shape is continuous, indicating that there is no change that can be identified as a phase transition in

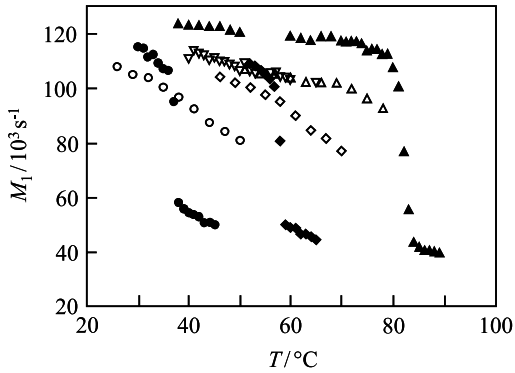

Fig. 16. Temperature dependence of first spectral moment M_1 for ^2H NMR spectra of d_{62}-DPPC (solid symbols) and d_{62}-DPPC with 28.5 mol% cholesterol (open symbols) at ambient pressure (○), 1000 bar (◇) and 2100 bar (△) (after Ref. 55).

the lipid mixture. For all pressures, the spectrum of the cholesterol-containing sample is characteristic of a fluid phase at the temperature corresponding to the pure lipid transition for that pressure. The spectrum shows a continuous change from fluid to more ordered over a wide temperature range for 210 MPa and below, without passing through a series of phases as observed with the pure lipid system. Figure 16 shows the temperature dependence of M_1 for d_{62}-DPPC and d_{62}-DPPC containing 28.5 mol% cholesterol at different pressures. Except for a pressure-induced shift in temperature, the behaviour of M_1 is similar for all cases. There is no evidence in these results of the formation of an interdigitated gel phase in the cholesterol-containing sample. The observation that the temperature dependence of M_1 does not change with increasing pressure, aside from an overall shift, is indirect evidence that pressure does not substantially alter the interaction of cholesterol within the bilayer and thus that the location of cholesterol within the bilayer is not changed by the application of pressure despite the anisotropic response of the bilayer to applied pressure. Indeed, the behaviour of the cholesterol-containing sample at high pressure appears to be analogous to that observed in the liquid-ordered phase at ambient pressure. In essence, cholesterol drastically modifies the response of the bilayer phase behaviour to applied pressure, which is in accordance with high pressure SAXS and FT-IR studies.[57,13] The presence of cholesterol also reduces the sensitivity of the bilayer thickness to pressure. These observations provide an example of how the response of lipid bilayer properties to pressure can be substantially altered by addition of a second amphiphilic component. This point may be particularly interesting in the light of the complexity of natural membranes that have evolved under the influence of various external stresses, such as low temperature or high hydrostatic pressure.

3.5. High-pressure ^{31}P NMR of the structure and dynamics of the headgroup of lipid bilayers

For pure phosphatidylcholine bilayers, the orientation of the headgroup has been well characterized showing that headgroups are aligned approximately parallel to the bilayer surface. Because only one phosphorus ^{31}P with 100% natural abundance is contained in the phospholipid molecule, ^{31}P NMR has become an important tool to study the phospholipid headgroup structure and dynamics.[58–62]

Jonas *et al.*[3,16,18,62] studied the ^{31}P NMR lineshapes and ^{31}P spin-lattice relaxation time of pure DPPC bilayers and DPPC bilayers containing charged tetracaine as a function of pressure from 1 bar to 5.1 kbar at 50 °C. The goals of the study were as follows: First, to determine the behaviour of the headgroup in the LC phase and the various gel phases accessible at high pressure. Second, to compare the pressure effects on pure DPPC bilayers with those observed for DPPC/tetracaine bilayers, and third, to determine whether the concept of molecular electrometer as introduced by Seelig *et al.*[23] is also applicable for gel phases induced at high pressures. Figure 17 shows representative ^{31}P NMR spectra for DPPC multilamellar bilayers at various pressures in the LC phase and the various gel phases induced by high pressure. By using ^{1}H decoupling, lineshape distortion caused by proton-phosphorous dipolar interactions can be avoided (see Fig. 17, spectra a and b). The ^{31}P spectra of DPPC in the LC state, the GI, interdigitated Gi and the GII gel phase show a typical axially symmetric powder lineshape. In contrast, the

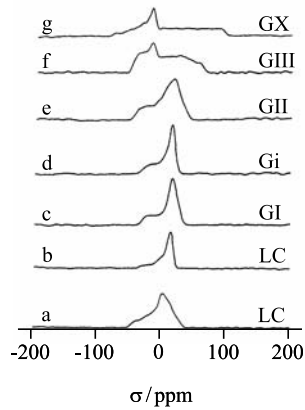

Fig. 17. ^{31}P NMR spectrum obtained using a single 90° pulse without ^{1}H decoupling in pure DPPC bilayers at 50 °C and 1 bar (a); and ^{31}P NMR spectra obtained using a fully phase-cycled Hahn echo sequence with inversely gated ^{1}H decoupling in pure DPPC bilayers at 50 °C and 1 bar in the LC phase (b), 1 kbar in the GI phase (c), 1.75 kbar in the interdigitated Gi gel phase (d), 2.5 kbar in the GII gel phase (e), 3.7 kbar in the GIII gel phase (f), and 5.1 kbar in the GX gel phase (g) (after Refs. 4, 18).

lineshape becomes axially asymmetric in the high pressure GIII gel phase. The asymmetry increases further in the last accessible gel phase GX for which a typical rigid lattice axially symmetric powder pattern is observed. The experimental chemical shielding anisotropy values, $\Delta\sigma$, were determined using standard procedures.[16] For the axially symmetric lineshapes the anisotropic part of the time averaged shielding tensor is defined as

$$\Delta\sigma = \sigma_{\parallel} - \sigma_{\perp} \tag{6}$$

where $\sigma_{11} = \sigma_{22} = \sigma_{\perp}$ and $\sigma_{33} = \sigma_{||}$.

For the axially asymmetric powder pattern, the shielding anisotropy was calculated using the following expression

$$(\Delta\sigma)^2 = \frac{3}{2}\left[(\sigma_{11} - \sigma)^2 + (\sigma_{22} - \sigma)^2 + (\sigma_{33} - \sigma)^2\right] \tag{7}$$

where σ_{11}, σ_{22}, σ_{33} have their usual meaning and σ denotes the isotropic part of the shielding tensor, which is

$$\sigma = \frac{1}{3}(\sigma_{11} + \sigma_{22} + \sigma_{33}). \tag{8}$$

The calculated $\Delta\sigma$ values of pure DPPC bilayers are plotted as a function of pressure in Fig. 18. Only the absolute value of $\Delta\sigma$ can be determined from Eq. (7), but in view of the fact that $\Delta\sigma$ is negative for the LC phase and the temperature-induced gel phases (GI, GII), it is expected that $\Delta\sigma$ will also be negative for the high pressure gel phases of DPPC. The absolute value of $|\Delta\sigma|$ increases slightly with pressure in the LC phase in the pressure range from 1 to 500 bar. The transition from the LC phase to the GI phase is accompanied by a

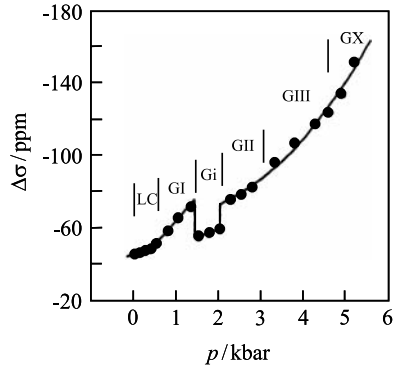

Fig. 18. Pressure dependence of ^{31}P chemical shift anisotropy values for DPPC bilayers at 50 °C. The pressure ranges for different phases of DPPC are indicated (after Refs. 4, 18).

reduction of gauche isomers in the acyl-chains affecting the available space for the headgroup motions and resulting in an increase of the absolute values of $|\Delta\sigma|$. An abrupt decrease of $|\Delta\sigma|$ accompanies the GI/Gi phase transition. In the interdigitated phase, Gi (see Fig. 2), the phospholipid headgroup has more available space and is thus less restricted. In this phase, the faster motion of the headgroup averages the chemical shielding anisotropy leading to lower $|\Delta\sigma|$ values. In contrast, in the GII phase, there is a further reduction of gauche conformers, and the two acyl-chains are almost extended. As a result, the available headgroup space decreases again, and the $|\Delta\sigma|$ value returns to higher values. In the GIII phase, the headgroup motion is further restricted, and the $|\Delta\sigma|$ value continues to increase with pressure. In agreement with the ^{2}H NMR results, the phase change from the GIII to the GX phase corresponds to a transformation to a rigid lattice spectrum which exhibits a typical lineshape and there is no discontinuity in $\Delta\sigma$ at the phase transition pressures corresponding to the GII/GIII and GIII/GX phase transitions. This may be due to the fact that the phase transitions are driven by co-operative interactions between the DPPC fatty acid chain segments.

The increase in pressure in all phases is accompanied by an increase in the ^{31}P chemical shielding anisotropy $|\Delta\sigma|$, as headgroup motions are slowed down, and the motional averaging is reduced. However, in view of the results obtained by SAXS and SANS, an alternative explanation should be considered for the $|\Delta\sigma|$ behaviour in the LC phase. Increasing pressure causes a decrease in overall volume available for the DPPC molecules by 'squeezing' them together, with an increase in the overall interactions. Since there is an increase in the thickness of the bilayer with pressure, a decrease in the overall cross-sectional area of the phospholipid molecule is needed to explain the volume decrease. The average surface area per headgroup thus decreases. With pressure, the headgroup which is normally oriented parallel to the bilayer surface, may change its orientation, thus contributing to the measured increase in bilayer thickness and leading to higher $|\Delta\sigma|$ values. In the gel phases, this explanation is probably not applicable. Knowledge of the ^{31}P $\Delta\sigma$ value alone is not sufficient to determine the average orientation of the headgroup; therefore, the increase in $|\Delta\sigma|$ due to pressure in the various gel phases of DPPC may be a consequence of slower motions.

3.6. Self-diffusion measurements of phosphatidylcholines in lipid bilayers

Lateral diffusion of phospholipids in model membranes at ambient pressure has been studied over the years by a variety of techniques including fluorescence recovery after photobleaching (FRAP), spin-label ESR, pulse field gradient NMR (PFG-NMR), quasielastic neutron scattering (QENS), excimer fluorescence and others.[1,2] In general, the values reported for the lateral diffusion coefficient (D) range from 10^{-9} to 10^{-6} cm^2/s in the

liquid-crystalline phase and from 10^{-10} to 10^{-7} cm^2/s in the gel phase at ambient pressure. Excimer formation and quasielastic neutron scattering methods give the highest D values and measure diffusion over short distances (~ 10 Å) and thus correspond to those techniques measuring local lateral diffusion, while the FRAP method gives lower D values and detects the lateral diffusion averaged over long distances greater than 10^4 Å. Over these long distances various boundaries or dislocations may be present which act as barriers to diffusion. The $T_{1\rho}$ NMR method introduced here is probably sensitive to diffusion distances that are intermediate between these methods.

Very little is known about the motions of lipid bilayers at elevated pressures. Of particular interest would be the knowledge of the effect of pressure on lateral diffusion, which is related to biological functions such as electron transport and some hormone–receptor interactions. However, pressure effects on lateral diffusion of pure lipid molecules and of other membrane components have yet to be studied carefully.

Jonas *et al*. measured the proton rotating frame spin-lattice relaxation time ($T_{1\rho}$) at pressures from 1 bar to 5000 bar and at temperatures of 50 to 70 °C for DPPC and at 5 to 35 °C for POPC.[62] If intermolecular dipolar interactions modulated by translational motion contribute significantly to the proton relaxation, the rotating frame spin-lattice relaxation rate ($1/T_{1\rho}$) is a function of the square root of the spin-locking field angular frequency ($\omega_1^{1/2}$):[62,63]

$$\frac{1}{T_{1\rho}} = C\omega_1^{1/2} + \frac{1}{T_2} \tag{9}$$

where C is a constant that contains the lateral diffusion coefficient and $1/T_2$ is the spin–spin relaxation rate. By taking the derivative of Eq. (9) with respect to $\omega_1^{1/2}$ and applying the resulting equation to motion in only two dimensions, an equation is obtained by which the lateral diffusion coefficient can be determined directly:

$$\frac{d(1/T_{1\rho})}{d(\omega_1^{1/2})} = -3\sqrt{3}\gamma^4\hbar^2 n/40D^{3/2} \tag{10}$$

where γ is the gyromagnetic ratio and n is the spin density (spins/mL). There are three experimental conditions that are necessary for the validity of Eq. (10): (i) the strength of the spin-locking field (H_1) must be larger than the strength of the local dipolar field (H_{loc}) in order to effectively lock all the spins; (ii) the value of the term $(\omega_1\sigma^2/D)^{1/2}$ must be < 2 in order to match an approximation used in the derivation of Eq. (10), where σ is the molecular diameter; and (iii) all other relaxation mechanisms besides the intermolecular relaxation modulated by the translational diffusion must be frequency independent or insignificant. Since $T_{1\rho}$ is most sensitive to molecular motions that have correlation times $\sim 1/\omega_1$ (i.e., 10^{-6} to 10^{-4} s), $T_{1\rho}$ measurements are suitable to

monitor the lateral diffusion of the phospholipids. However, for proton NMR, it is only when the lateral diffusion coefficient is less than 1×10^{-8} cm^2/s, that the locking-field dependence of $T_{1\rho}^{-1}$ becomes experimentally significant.

The $T_{1\rho}^{-1}$ values were plotted as a function of the square root of the spin-locking field angular frequency ($\omega_1^{1/2}$) and the lateral diffusion coefficient (D) calculated from the slope.[62] Pressure effects on lateral diffusion were observed in the LC phase, and the lateral diffusion coefficient exhibits sharp decreases in response to the various pressure-induced phase transitions encountered. The lateral diffusion coefficient for DPPC and POPC are $3–7 \times 10^{-9}$ cm^2/s in the LC phase, and the values of D of DPPC in the temperature-induced ripple-gel ($P_{\beta'}$) phase are 0.8 to 1.2×10^{-9} cm^2/s, that is, five times lower than in the LC phase. The values of D of DPPC in the temperature-induced $L_{\beta'}$ phase are 0.2 to 0.4×10^{-9} cm^2/s, 20 times lower than that in the LC phase.

Figure 19 shows the pressure effects on the lateral self diffusion coefficient of sonicated DPPC and POPC vesicles. The lateral diffusion coefficient of DPPC in the LC phase decreases with increasing pressure from 1 to 300 bar at 50 °C. A sharp decrease in the D-value occurs at the LC to GI phase transition pressure. From 500 bar to 800 bar in the GI phase, the values of the lateral diffusion coefficient ($\sim 1 \times 10^{-9}$ cm^2/s) are approximately constant. There is another sharp decrease in the value of the lateral diffusion coefficient at the

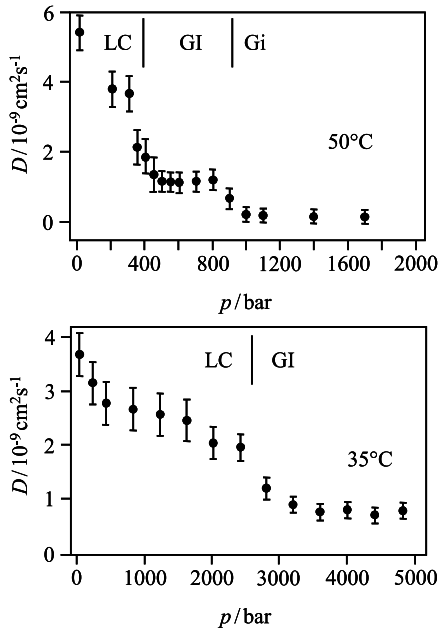

Fig. 19. Lateral self-diffusion constant D of DPPC (top) and POPC (bottom) in sonicated vesicles as a function of pressure at 50 °C and 35 °C, respectively (after Ref. 62).

GI–Gi phase transition pressure. In the Gi phase, the values of the lateral diffusion coefficient ($\sim 1 \times 10^{-10}$ cm^2/s) are again approximately constant. As shown in Fig. 19, the lateral diffusion coefficients of DPPC and POPC in the LC phase decrease almost exponentially with increasing pressure.

In the free volume theory, translational diffusion of a lipid molecule in the bilayer occurs only when a free volume larger than a certain critical size appears in the vicinity of the lipid molecule. The free volume theory implies that the smaller the overall volume, the lower the probability for a molecule to associate with a free volume of a critical size. The molecules diffuse slower if the probability for a molecule to associate with a free volume of critical size is small. With increasing pressure, the overall volume decreases and the lateral diffusion is thus reduced. The activation volume for diffusion in the LC phase was calculated using the expression[62]

$$\Delta V_D^{\neq} = -RT\left(\frac{\mathrm{d}\ln D}{\mathrm{d}p}\right)_T \tag{11}$$

where R is the gas constant and the other symbols have their usual meanings, for both DPPC and POPC in sonicated vesicles. The calculated values are 37 mL/mol at 50 °C, 34 mL/mol at 60 °C and 25 mL/mol at 70 °C for DPPC and 16 mL/mol at 5 °C, 9 mL/mol at 20 °C and 6 mL/mol at 35 °C for POPC.

There is an abrupt decrease in the lateral diffusion coefficient of DPPC upon the phase transition from the GI phase to the Gi phase. This is because the acyl-chain region is being packed even more efficiently in the Gi phase than in the GI phase, and the hydrocarbon volume in the Gi phase is smaller than in the GI phase. Also, in the Gi phase, the lipid acyl-chains from the opposing bilayer leaflets interdigitate. In order for a phospholipid molecule to diffuse it has to circumvent the nearby interdigitated molecules which hinder diffusion.

The increase of the lateral diffusion rate with increasing temperature was used to estimate the activation energy for diffusion in the LC and GI phases. The temperature dependence of the correlation-time for molecular diffusion, τ_D, can be formulated in terms of the activation energy (E_a) for the motion affecting τ_D in an Arrhenius expression ($\tau_D = \tau_D^0 \exp(E_a/RT)$). Since $D = \sigma^2/4\tau_D$ the activation energies for the diffusive process are calculated from $\ln D$ vs $1/T$ plots according to the Arrhenius equation. Generally, in liquids, experimental activation energies for diffusion range from ~ 8 to ~ 50 kJ/mol, with values for mobile liquids being less than ~ 29 kJ/mol. The activation energy for diffusion is identified as the energy required to form a void or hole into which the diffusing molecule can move. The energy needed to transfer the diffusing molecule from its surroundings into the hole, which is the activation energy for diffusion at constant volume, is only between 10 and 20% of the constant pressure activation energy. In this study,[62] the lateral diffusion coefficients of

DPPC in sonicated vesicles in the LC phase at ambient pressure were determined to be 5.4×10^{-9} cm^2/s at 50 °C, 6.5×10^{-9} cm^2/s at 60 °C and 7.4×10^{-9} cm^2/s at 70 °C. From these data the activation energy of diffusion (E_a) was calculated to be 14 kJ/mol in the LC phase at ambient pressure. The E_a value of POPC is ~16 kJ/mol in the LC phase at 1 bar and ~18 kJ/mol at 800 bar. The increase in E_a values at higher pressures is due to the decrease in the total volume at higher pressures which results in a larger energy barrier to the production of a void around a diffusing molecule. Generally, the activation energy is ~20 kJ/mol in the fluid phase and ~40 kJ/mol in the gel phase for phospholipids. It is interesting to note that the pressure-induced GI phase and $P_{\beta'}$ phases have different E_a values. Because temperature changes produce both volume and energy effects while pressure changes produce only volume effects, temperature- and pressure-induced gel phases are not necessarily the same.

3.7. Pressure effects on the structure and phase behaviour of phospholipid–polypeptide bilayers

Understanding the molecular basis of interactions between phospholipids and membrane proteins in cell membranes is an important aim of structural biology. As a simple model system, we investigated the effect of incorporation of 2–5 mol% gramicidin D (GD), a naturally occurring mixture of gramicidin from Bacillus brevis, on the structure and phase behaviour of aqueous dispersions of fully hydrated DPPC bilayers in the temperature range 0–80 °C at pressures up to 4 kbar. The primary sequence of gramicidin consists of only 15 amino acid residues which have alternate L and D chirality, and the peptide adopts conformations of β-helices, which can be right- or left-handed, and they can differ in the number of amino acid residues per turn and therefore in length and diameter.[64–66] As a consequence, gramicidin is highly polymorphic, being able to adopt a wide range of structures with different topologies. Common forms are the dimeric single-stranded right-handed $\beta^{6.5}$- and $\beta^{6.3}$-helices with a length of 24–25 Å, and the antiparallel double-stranded $\beta^{5.6}$-helix, being approximately 32 Å long. For comparison, the hydrophobic fluid bilayer thickness is about 30 Å for DPPC bilayers. The hydrophobic thicknesses of the lipid gel phases are 4–5 Å larger.

Pressure was applied in this study to fine tune the lipid chain-lengths and conformation and to select specific lamellar phases. For example, the phospholipid bilayer thickness increases by ~1 Å/kbar in the liquid-crystalline phase, and up to six gel phases have been found in fully hydrated DPPC dispersions in the pressure–temperature phase space up to 15 kbar and 80 °C, respectively.[12] ^{2}H NMR spectral parameters were used to detect structural and dynamic changes upon incorporation of the polypeptide into the lipid bilayers.

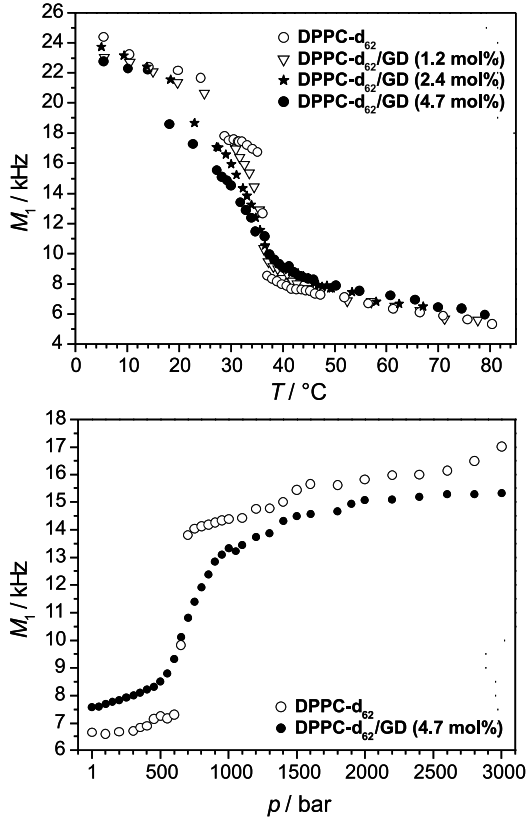

Fig. 20. (a) Temperature dependence (top) and (b) pressure dependence (bottom) of the first spectral moment M_1 of d_{62}-DPPC and d_{62}-DPPC–GD mixtures at 55 °C.

The influence of gramicidin insertion on the acyl-chain segmental order could be determined by the analysis of the ^{2}H NMR spectra of perdeuterated lipid samples. The data exhibit the well-known downward shift of ~4 °C in the main transition temperature of the perdeuterated lipid relative to the transition temperature of the normal lipid bilayer. The ^{2}H NMR spectra of the pure d_{62}-DPPC bilayers exhibit a drastic change in lineshape from a rigid lattice type to a motionally averaged spectrum at the main phase transition temperature (Fig. 12, left). Incorporation of GD broadens the phase transition, so that in the fluid-gel co-existence region the NMR lineshapes show the characteristics of both, motionally averaged and rigid lattice type spectra (Fig. 12, right). This is also obvious in the temperature dependence of the first moment M_1, shown in Fig. 20a, which decreases at the melting temperature of $T_m = 37$ °C by about 50% in pure d_{62}-DPPC.[56,67,68] The M_1-data show that incorporation of GD leads to a significant decrease of the molecular order of

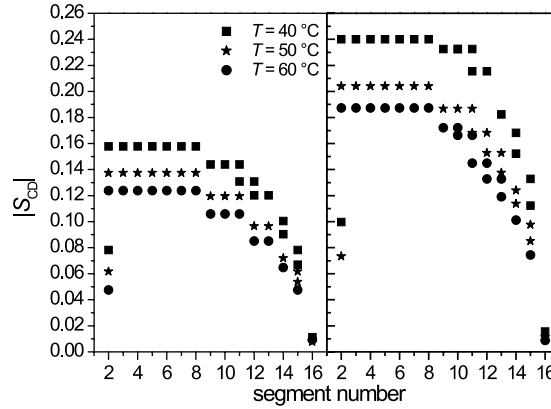

Fig. 21. Measured segmental order parameter profiles of d_{62}-DPPC (left) and the d_{62}-DPPC–GD (4.7 mol%) mixture (right) at selected temperatures (40, 50 and 60 °C).

the acyl-chains in the gel phase, whereas in the fluid phase the mean quadrupolar splitting, and therefore the mean order parameter increases slightly. To study these effects in greater detail, the segmental order parameters in the liquid-crystalline phase were calculated. The C–D bond order parameter profiles (Fig. 21) show that the methylene bond order parameter increases about 30% in the d_{62}-DPPC–GD (4.7 mol%) system compared to pure d_{62}-DPPC, almost independent of the position in the acyl-chain. The methyl group order parameter changes only slightly. As expected, all segmental order parameters decrease with increasing temperature owing to an increase in the population of gauche conformers and kinks in the acyl-chains. The data clearly show that GD in fluid-like DPPC has a significant effect on the methylene segmental order along the whole acyl chain. From these spectroscopic data, the hydrophobic thickness D_C and the average chain cross-sectional area $\langle A \rangle$ of the lipid molecule can be calculated. D_C is ~13.8 Å at 50 °C in pure fluid DPPC and increases by 0.4, 0.6 and 0.8 Å by adding 1.2, 2.4 and 4.7 mol% GD; $\langle A \rangle$ is ~65 Å^2 at 50 °C in pure DPPC and decreases concomitantly from 64 to 62 Å^2 in the DPPC–GD mixtures.[56]

The pressure dependent studies on d_{62}-DPPC and the d_{62}-DPPC–GD mixtures were performed at a temperature of $T = 55$ °C (Fig. 22). The pressure-induced main phase transition of pure d_{62}-DPPC is identified at a pressure of 650 bar as an increase of the first spectral moment M_1 which is shown in Fig. 20b. Also observed at this pressure is a drastic change in the lineshape from a motionally averaged spectrum in the liquid-crystalline phase to a rigid lattice type ^{2}H NMR spectrum. Further increase of pressure leads to a significant change in the lineshape above 1500 bar, whereas the first moment shows only a slight change. At this pressure the interdigitated gel phase is formed and the observed lineshapes are consistent with data from Driscoll *et al.*[17] Incorporation of GD into the lipid bilayer drastically broadens the

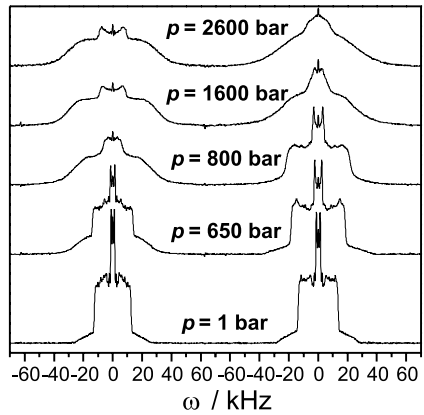

Fig. 22. ^{2}H NMR spectra of pure d_{62}-DPPC (left) and the d_{62}-DPPC–GD (4.7 mol%) mixture (right) at $T = 55\,^{\circ}C$ and selected pressures.

main phase transition, as can be clearly seen in the change of the first spectral moment. The ^{2}H NMR lineshapes of the d_{62}-DPPC–GD (4.7 mol%) mixture are markedly different, showing features of both, motionally averaged and rigid lattice type spectra over a wide pressure range. At high pressures, the lineshapes of the mixture are no longer comparable to the ones obtained by the pure lipid dispersion and show no indication of the Gi ($L_{\beta i}$) phase (see Fig. 2) any more. From the M_1 data we conclude that insertion of GD leads to an increase of the molecular order in the liquid-crystalline phase and to a decrease of average conformational order in all high pressure gel phases of DPPC. The pressure dependence of the segmental C–^{2}H order parameters is depicted in Fig. 23. As expected the chain order parameter values, S_{CD}, increase with increasing pressure, in particular at the terminal methylene segments and in the fluid to gel phase transition regions. For example, for d_{62}-DPPC–4.7 mol% GD, $T = 55\,^{\circ}C$ and $p = 600$ bar, the order parameter has increased by $\sim 20\%$ in the plateau region (in the upper part of the acyl-chains) and by 40–50% for the methylene groups at the end of the chains, i.e., in the inner part of the lipid bilayer.

The hydrophobic thickness D_C of the pure DPPC monolayer increases from 13.7 Å at 1 bar to 14.7 Å at 600 bar ($T = 55\,^{\circ}C$); for the d_{62}-DPPC−4.7 mol% GD mixture, D_C increases from 14.2 to 15.6 Å. The average chain cross-sectional area $\langle A \rangle$ decreases concomitantly from ~ 66 Å^2 in pure DPPC at 1 bar to 60 Å^2 at 600 bar. Adding 4.7 mol% GD to the DPPC bilayer at 55 °C yields values of 63.5 Å^2 at ambient pressure and 55.5 Å^2 at 600 bar, respectively.[56]

The data thus clearly shows that, depending on the gramicidin concentration, the structure of the temperature- and pressure-dependent lipid bilayer is significantly altered by the insertion of the polypeptide. It has also been shown

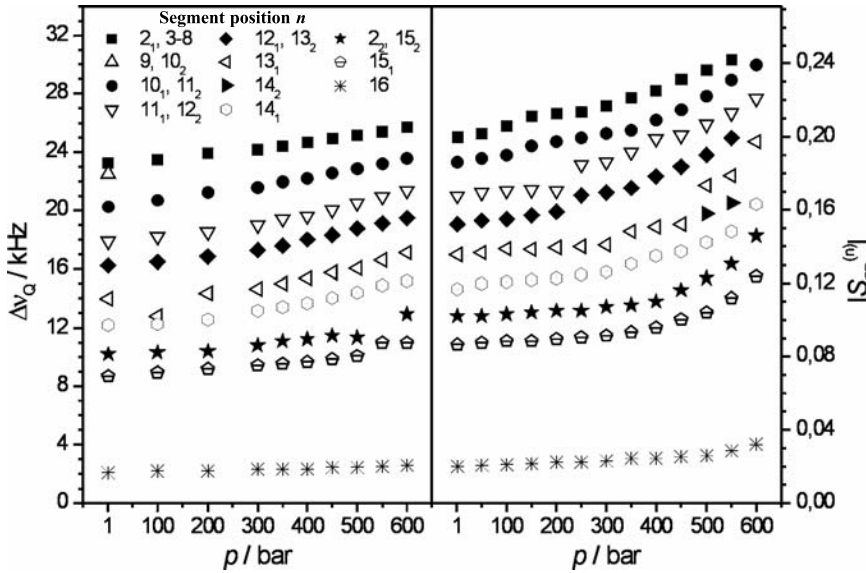

Fig. 23. Measured quadrupolar splittings and segmental order parameter profiles of fluid d_{62}-DPPC bilayers (left) and the d_{62}-DPPC–GD (4.7 mol%) bilayer mixture (right) as a function of pressure at $T = 55\,^{\circ}C$.

recently that the tendency to avoid hydrophobic mismatch can influence the gramicidin conformer population in lipid bilayer–GD systems, in a way that the equilibrium of gramicidin species is shifted to a conformation of comparable length to avoid large hydrophobic mismatch.[69] In DPPC lipid bilayers, the population of the longer double helical forms increases in the gel state, whereas the helical dimer is abundant at high temperature. For the intermediate temperature range a continuous change in the population ratio has been observed in FT-IR spectroscopy studies.[69]

4. CONCLUSIONS

We conclude that high pressure work on lipid and membrane systems using one- and two-dimensional ^{1}H, ^{13}C, ^{31}P and ^{2}H NMR experiments as well as relaxation time measurements can yield a wealth of enlightening new information on the structure, dynamics and phase behaviour of these systems. These variable pressure studies are very valuable not only from a physico-chemical point of view for studying the self-assembly and energetics of these systems over a large region of phase space, they are also important for the development of new technological and pharmaceutical applications, such as in the field of high pressure food processing and micellar baroenzymology.[3,4] It is clear that the application of the pressure variable in the biochemical and

biophysical research area has only just started and many interesting results are expected in the near future.

ACKNOWLEDGEMENTS

This work was supported by the Deutsche Forschungsgemeinschaft (DFG) and the Fonds der Chemischen Industrie.

REFERENCES

1. G. Cevc, ed., *Phospholipids Handbook*, New York, Marcel Dekker, 1993.
2. R. Lipowski and E. Sackmann, eds., *Structure and dynamics of membranes*, Vols. 1A and 1B, Elsevier, Netherlands, 1995.
3. C. Balny, P. Masson and K. Heremans, *Biochim. Biophys. Acta*, 2002, **1595**, 3.
4. R. Winter and J. Jonas, eds., *High Pressure Molecular Science*, NATO ASI E358, Kluwer Academic Publishers, Dordrecht, 1999.
5. C. Balny, R. Hayashi, K. Heremans and P. Masson, eds., *High Pressure and Biotechnology*, Colloque Inseram, Vol. 224, John Libbey Eurotext, Montrouge, 1992.
6. J. Jonas, ed., *High Pressure NMR*, Springer-Verlag, Berlin, 1991.
7. M. Böttner and R. Winter, *Biophys. J.*, 1993, **65**, 2041.
8. M. Auger, H. C. Jarrell, I. C. P. Smith, P. T. T. Wong, D. J. Siminovitch and H. H. Mantsch, *Biochemistry*, 1987, **26**, 8513.
9. M. Auger, I. C. P. Smith, H. H. Mantsch and P. T. T. Wong, *Biochemistry*, 1990, **29**, 2008.
10. O. Reis, A. Zenerino and R. Winter, in *Biological Macromolecular Dynamics*, S. Cusack, H. Büttner, M. Ferrand, P. Langan, P. Timmins, eds., Adenine Press, Schenectady, NY, 1997, 41.
11. R. Winter and W. C. Pilgrim, *Ber. Bunsenges. Phys. Chem.*, 1989, **93**, 708.
12. C. Czeslik, O. Reis, R. Winter and G. Rapp, *Chem. Phys. Lip.*, 1998, **91**, 135.
13. R. Winter and C. Czeslik, *Z. Kristallogr.*, 2000, **215**, 454.
14. J. Jonas, C.-L. Xie, A. Jonas, P. J. Grandinetti, D. Campbell and D. Driscoll, *Proc. Natl. Acad. Sci. USA*, 1988, **85**, 4115.
15. D. A. Driscoll, S. Samarasinghe, S. Adamy, J. Jonas and A. Jonas, *Biochemistry*, 1991, **30**, 3222.
16. X. Peng, A. Jonas and J. Jonas, *Biophys. J.*, 1995, **68**, 1137.
17. D. A. Driscoll, J. Jonas and A. Jonas, *Chem. Phys. Lip.*, 1991, **58**, 97.
18. X. Peng and J. Jonas, *Biochemistry*, 1992, **31**, 6383.
19. J. Jonas, R. Winter, P. J. Grandinetty and D. Driscoll, *J Magn. Res.*, 1990, **87**, 536.
20. X. Peng, A. Jonas and J. Jonas, *Chem. Phys. Lip.*, 1995, **75**, 59.
21. J. Seelig and A. Seelig, *Q. Rev. Biophys.*, 1980, **13**, 19.
22. J. Seelig and P. M. MacDonald, *Acc. Chem. Res.*, 1987, **20**, 221.
23. J. H. Davis, *Biophys. J.*, 1979, **27**, 339.
24. R. L. Smith and E. Oldfield, *Science*, 1984, **225**, 280.
25. H. H. Mantsch, H. Saito and I. C. Smith, *Prog. Nucl. Magn. Reson. Spectrosc.*, 1977, **11**, 211.
26. J. H. Davis, *Adv. Magn. Reson.*, 1989, **13**, 195.
27. J. H. Davis, *Biochim. Biophys. Acta*, 1983, **737**, 117.
28. P. M. MacDonald, *Acc. Chem. Res.*, 1997, **30**, 196.
29. S. J. Singer and G. L. Nicolson, *Science*, 1972, **175**, 720.

30. R. Winter, A. Landwehr, T. Brauns, J. Erbes, C. Czeslik and O. Reis, in *High Pressure Effects in Molecular Biophysics and Enzymology,* J. L. Markley, D. B. Northrop, and C. Royer, eds., Oxford University Press, 1996, 274.
31. J. R. Brainard and E. H. Cordes, *Biochemistry*, 1981, **20**, 4607.
32. E. Oldfield, J. L. Bowers and J. Forbes, *Biochemistry*, 1987, **26**, 6919.
33. R. J. Wittebort, A. Blume, T.-H. Huang, S. K. Gupta and R. G. Griffin, *Biochemistry*, 1982, **21**, 3487.
34. Y. K. Levine, N. J. Birdsall, A. G. Lee and J. C. Metcalfe, *Biochemistry*, 1972, **11**, 1416.
35. J. F. Ellena, W. C. Hutton and D. S. Cafiso, *J. Am. Chem. Soc*., 1985, **107**, 1530.
36. Y. Kuroda and K. Kitamura, *J. Am. Chem. Soc*., 1984, **106**, 1.
37. L. L. Holte and K. Gawrisch, *Biochemistry*, 1997, **36**, 4669.
38. Z.-C. Xu and D. S. Cafiso, *Biophys. J*., 1986, **49**, 779.
39. C. Mayer, K. Müller, K. Weisz and G. Kothe, *Liq. Cryst*., 1988, **3**, 797.
40. E. Rommel, F. Noack, P. Meier and G. Kothe, *J. Phys. Chem*., 1988, **92**, 2981.
41. J. M. Neumann, A. Zachowski, S. Tran-Dinh and P. F. Devaux, *Eur. Biophys. J*, 1985, **11**, 219.
42. J. R. Schuh, U. Banerjee, L. Müller and S. I. Chan, *Biochim. Biophys. Acta*, 1982, **687**, 219.
43. N. P. Franks and W. R. Lieb, *Nature*, 1982, **300**, 487.
44. F. H. Johnson and E. A. Flagler, *Science*, 1951, **112**, 91.
45. M. J. Lever, K. W. Miller, W. D. M. Paton and E. B. Smith, *Nature*, 1971, **23**, 368.
46. W. MacNaughtan and A. G. MacDonald, *Biochim. Biophys. Acta*, 1980, **597**, 193.
47. A. Zenerino, Ph.D. Thesis, University of Dortmund, 1997.
48. J. Eisenblätter, A. Zenerino and R. Winter, *Magn. Reson. Chem*., 2000, **38**, 662.
49. D. Huster, K. Arnold and K. Gawrisch, *J. Phys. Chem. B*, 1999, **103**, 243.
50. B. B. Bonev and M. R. Morrow, *Biophys. J*., 1995, **69**, 518.
51. B. B. Bonev and M. R. Morrow, *Biophys. J*., 1996, **70**, 2727.
52. B. B. Bonev and M. R. Morrow, *Rev. Sci. Instrum*., 1997, **68**, 1827.
53. B. B. Bonev and M. R. Morrow, *Phy. Rev. E*, 1997, **55**, 5825.
54. D. C. Fiech, B. B. Bonev and M. R. Morrow, *Phy. Rev. E*, 1998, **57**, 3334.
55. B. B. Bonev and M. R. Morrow, *Can. J. Chem*., 1998, **76**, 1512.
56. J. Eisenblätter, Ph.D. Thesis, University of Dortmund, 2002.
57. O. Reis, R. Winter and T. W. Zerda, *Biochim. Biophys. Acta*, 1996, **1279**, 5.
58. J. Seelig, *Biochim. Biophys. Acta*, 1978, **515**, 105.
59. P. L. Yeagle, in *Biological Magnetic Resonance*, L. J. Berliner, ed., Plenum Press, New York, 1990, **9**, 1.
60. I. C. P. Smith and I. H. Ekiel, in *Phosphorus 31 NMR: Principles and Applications*, D. G. Gorenstein, ed., Academic Press, Orlando, 1984, 447.
61. E. J. Dufourc, D. Mayer, J. Stohrer, G. Althoff and G. Kothe, *Biophys. J*., 1992, **61**, 42.
62. B.-S. Lee, S. A. Mabry, A. Jonas and J. Jonas, *Chem. Phys. Lip*., 1995, **78**, 103.
63. R. W. Fisher and T. I. James, *Biochemistry*, 1978, **17**, 117.
64. B. A. Wallace, *Annu. Rev. Biophys. Chem*., 1990, **19**, 127.
65. R. E. Koeppe, II and O. S. Andersen, *Annu. Rev. Biophys. Biomol. Struct*., 1996, **25**, 231.
66. B. A. Wallace, *J. Struct. Biol*., 1998, **121**, 123.
67. J. Eisenblätter, M. Zein and R. Winter, in *Trends in High Pressure Bioscience and Biotechnololgy*, R. Hayashi, ed., Elsevier Science B.V., Amsterdam, 2002, 131.
68. J. Eisenblätter and R. Winter, *Defect and Diffusion Forum*, Vols. 208–209, Scitec Publications Ltd, Switzerland, 2002, 35.
69. M. Zein and R. Winter, *Phys. Chem. Chem. Phys*., 2000, **2**, 4545.

Diffusion in a Closed Sphere

W. S. VEEMAN

Institute of Chemistry, Universität Duisburg-Essen, Duisburg, Germany

Three analytical expressions for the spin-echo intensity as a function of the gradient in a pulsed field gradient NMR experiment for spins diffusing in a sphere with reflecting walls are reinvestigated. It is found that none of the published formulas are completely correct. By numerical comparisons the correct formula is found.

1. INTRODUCTION

The phenomenon of diffusion of fluids or gases in a medium plays an important role in many processes in geology, chemistry, chemical technology, engineering, biology and the science of air and soil. NMR spectroscopy in combination with the application of magnetic field gradients (pulsed or continuous) has been very successful to quantitatively measure this diffusion in a non-invasive and non-destructive way. Especially pulsed field gradient echo (PFGE) NMR methods are widely applied.

In many cases the medium in which the molecules move is not homogeneous and the diffusion motion of the molecules is influenced by the structure of the medium. Examples are the diffusion of water and oil in porous rock or in water–oil emulsions. Many publications have shown that the NMR diffusion results can be used to quantitatively study the porous structure, like the determination of pore and droplet sizes, pore connectivity and pore hopping or of the surface to volume ratio of the pores.

ANNUAL REPORTS ON NMR SPECTROSCOPY
VOLUME 50 ISSN 0066 4103
DOI 10.1016/S0066-4103(03)50005-9

In most porous media the pore structure is so complicated (variations in pore size and shape) that one can only expect to determine average properties, like the average surface to volume ratio of the pores.[1] In some cases, however, the 'pores' have a well-defined shape but vary only in size. This is the case for emulsions if the concentration of one of the components is low.

The spherical shape of water droplets in an oil emulsion should allow an accurate determination of the average size of the droplet and of the distribution of droplet radii. Packer and Rees[2] have reported such a study in 1972. They fitted the experimental echo intensity $E(g, \Delta)$ as a function of the gradient strength g and the diffusion time Δ of the PFGE-experiment with an approximate theoretical model for diffusion in a closed sphere by Murday and Cotts.[3] The Murday-Cotts model is derived from a theory by Neumann[4] in which it is assumed that the phase of the magnetization vector of the diffusing spins always follows a Gaussian distribution.

Since the Murday-Cotts' paper in 1968 much progress has been made toward the theoretical description of the spin-echo intensity $E(g, \Delta)$ for spins diffusing in well-defined geometries. Tanner and Stejskal[5] derived already in 1968 the exact expression of $E(g, \Delta)$ for spins diffusing in a rectangular box. The derivation of an exact expression for $E(g, \Delta)$ for diffusion in a sphere with reflecting walls is not a trivial mathematical problem and it took between 1992 and 1994 when three expressions were published.[6–8] All three expressions are only valid in the short-gradient-pulse approximation (see below).

When we wanted to numerically fit experimental PFGE data of water diffusion in a water-in-oil emulsion,[9] we found that for a beginner in this field the literature is quite confusing. First, all three expressions for diffusion in a sphere with reflecting walls are somewhat different and lead to very different fitting results, especially when the formulas are combined with a radius distribution function. Since the derivation of the published expressions needs some tedious algebra (which has not been published), it is not trivial to check the derivation in order to establish which expression is the correct one. Here we use a numerical approach to decide which expression is correct.

As an introduction to the problem, we will first describe the general mathematical method for free diffusion and linear bounded diffusion, after a short outline of the standard PFGE NMR experiment.

2. THE PULSED FIELD GRADIENT ECHO (PFGE) NMR EXPERIMENT

For the basic PFGE experiment a spin-echo experiment (either the two-pulse Hahn echo sequence, Fig. 1a, or the three-pulse stimulated echo sequence, Fig. 1b) is combined with two magnetic field gradient pulses with duration δ and separated by the time duration Δ. The gradient pulses generate a magnetic

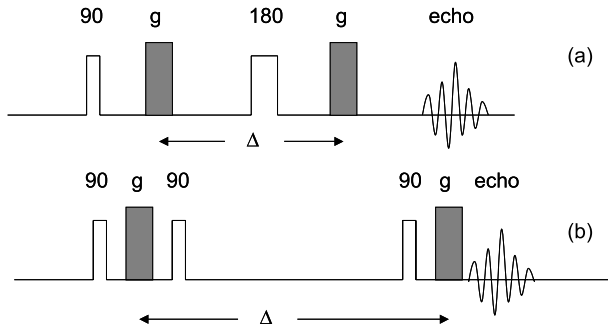

Fig. 1. The pulse sequences for the pulsed field gradient echo NMR experiment (a) Hahn echo, (b) stimulated or three-pulse sequence.

field gradient in a certain direction $\vec{u}$ of g Tesla/m, which cause a phase shift of the precessing transversal magnetization vector of the spins in the volume element $d\vec{r}$ at the position vector $\vec{r}$ equal to$\gamma\delta g\vec{u}\cdot\vec{r}$, where $\vec{u}\cdot\vec{r}$ is the component of $\vec{r}$ along the field gradient and γ the gyromagnetic ratio**.**

When we assume that the gradient pulses are so short that the spins do not move during the pulses (*short gradient pulse limit* $\delta\rightarrow 0$, $\delta g =$ constant), then the spins, which were at position $\vec{r}$ at the time of the first gradient pulse and at $\vec{r}'$ at the time of the second gradient pulse have at the time of the spin-echo acquired a relative phase of $\gamma g\delta\vec{u}\cdot\left(\vec{r}'-\vec{r}\right)$, where $\vec{u}\cdot\left(\vec{r}'-\vec{r}\right)$ is the distance the spins have moved along $\vec{u}$ during the diffusion time t.

Callaghan [10] points out the analogy between PFGE NMR experiments in the short-gradient-pulse limit and diffraction experiments. Under the short gradient pulse condition the echo intensity obtained from a PFG NMR experiment can be written as:

$$E\left(\vec{q},\Delta\right)=\int\rho(\vec{r})\int P\left(\vec{r}|\vec{r}\,',\Delta\right)\exp\left(i2\pi\vec{q}\cdot\left(\vec{r}'-\vec{r}\right)\mathrm{d}\vec{r}'\mathrm{d}\vec{r}\right) \tag{1}$$

where the wave vector $\vec{q}$ is defined as $\vec{q}=\gamma\delta g\vec{u}/2\pi$ and $\rho(\vec{r})P\left(\vec{r}|\vec{r}\,',\Delta\right)$ is the probability to find a molecule at position $\vec{r}$ at time t and the same molecule at position $\vec{r}'$ at time $t+\Delta$.

Equation (1) shows a Fourier relationship between the echo attenuation $E\left(\vec{q},\Delta\right)$ and the *propagator* $P\left(\vec{r}|\vec{r}',\Delta\right)$. This propagator plays an important role in the description of PFGE NMR, because in principle the spin-echo intensity as a function of the gradient strength can be determined when the propagator as a function of $\vec{r}$, $\vec{r}'$ and Δ is known. Callaghan[10] shows that the propagator is a solution of the diffusion equation and it is therefore appropriate to first consider the diffusion equation.

3. THE DIFFUSION EQUATION

The diffusion of particles can be described by the second-order differential equation (Fick's second law):

$$\frac{\partial C}{\partial t} = D\left(\frac{\partial^2 C}{\partial x^2} + \frac{\partial^2 C}{\partial y^2} + \frac{\partial^2 C}{\partial z^2}\right) \tag{2}$$

where C is the concentration, which in general is a function of the time t and the spatial co-ordinates x, y and z; D is the diffusion coefficient, which is assumed to be independent of the concentration and the co-ordinates x, y and z.

Equation (2) implies that the concentration $C(x, y, z)$ in a certain point (x, y, z) can change in time only when the second derivatives of C with respect to x, y or z are all not zero. Equation (2) cannot be used as such for the description of self-diffusion, since self-diffusion even occurs when the macroscopic concentration is the same everywhere in the system.

However, as mentioned above, the propagator $P(\vec{r}|\vec{r}', \Delta) \equiv P$ with $\vec{r} = (x, y, z)$ and $\vec{r}\,' = (x', y', z')$ fulfils the diffusion equation:

$$\frac{\partial P}{\partial t} = D\left(\frac{\partial^2 P}{\partial x'^2} + \frac{\partial^2 P}{\partial y'^2} + \frac{\partial^2 P}{\partial z'^2}\right). \tag{3}$$

Note that the differentiation in the right hand part of Eq. (3) is with respect to the $\vec{r}'$ co-ordinates. $P(\vec{r}|\vec{r}', t)$ is not only a solution of Eq. (3) but, since it is a probability function, it must also fulfil the normalization equation:

$$\int_{\vec{r}'} P(\vec{r}|\vec{r}', \Delta)\mathrm{d}\vec{r}' = 1 \tag{4}$$

the initial condition:

$$P(\vec{r}|\vec{r}', 0) = \delta(\vec{r} - \vec{r}') \tag{5}$$

and the appropriate boundary conditions.

The diffusion equation (3) can be written in a more concise form as:

$$\frac{\partial P}{\partial t} = D\nabla'^2 P \tag{6}$$

where the Laplace operator

$$\nabla'^2 = \left(\frac{\partial^2}{\partial x'^2} + \frac{\partial^2}{\partial y'^2} + \frac{\partial^2}{\partial z'^2}\right).$$

4. THE PROPAGATOR FOR ONE-DIMENSIONAL DIFFUSION

Before we show the general solution of the three-dimensional diffusion Eq. (3) or Eq. (6), we first solve the diffusion equation for diffusion along one axis, e.g., the z axis parallel to the pulsed field gradient. The diffusion equation is then:

$$\frac{\partial P}{\partial t} = D\frac{\partial^2 P}{\partial z'^2} \tag{7}$$

where $P \equiv P(z|z',\, t)$.

Equation (7) can be solved by separation of the variables. We write P as a product of two functions X and T:

$$P(z|z',\, t) = X(z')T(t),$$

where X is a function of z' only and T of t only, and substitute it for P in Eq. (7):

$$X\frac{\partial T}{\partial t} = DT\frac{\partial^2 X}{\partial z'^2}. \tag{8}$$

By writing Eq. (8) in the following form:

$$\frac{1}{DT}\frac{\partial T}{\partial t} = \frac{1}{X}\frac{\partial^2 X}{\partial z'^2} \tag{9}$$

we see that the left hand side only depends on t and the right hand side only on z, each side therefore must be equal to a constant $-\lambda^2$, independent of t and z':

$$\frac{1}{DT}\frac{\partial T}{\partial t} = -\lambda^2 \tag{10}$$

and

$$\frac{1}{X}\frac{\partial^2 X}{\partial z'^2} = -\lambda^2. \tag{11}$$

The solutions of Eqs. (10) and (11) are:

$$T = Ce^{-\lambda^2 Dt} \tag{12}$$

$$X = C_1 e^{i\lambda z'} + C_2 e^{-i\lambda z'} = (C_1 + C_2)\cos(\lambda z') + (C_1 - C_2)\sin\lambda z'. \tag{13}$$

Here the constants are arbitrary integration constants, which in general are different for different λ. The propagator is then (setting $t = \Delta$):

$$P(z|z',\,\Delta) = C\left\{(C_1 + C_2)\cos(\lambda z') + (C_1 - C_2)\sin(\lambda z')\right\} e^{-\lambda^2 D\Delta}. \tag{14}$$

In Eq. (14) we took care of the fact that the differentiation in the diffusion Eq. (3) was with respect to the primed co-ordinates. Because λ is an arbitrary constant, the general one-dimensional solution of the diffusion equation is:

$$P(z|z',\,\Delta) = \int \left\{c_1'(z,\,\lambda)\cos(\lambda z') + c_2'(z,\,\lambda)\sin(\lambda z')\right\} e^{-\lambda^2 D\Delta}\,\mathrm{d}\lambda. \tag{15}$$

Solution (15) is written in the form of a 'normal mode' expansion with eigenvalues $-\lambda^2 D$ and eigenfunctions represented by the spatial parts of Eq. (15). Of course, the above solution must fulfil the appropriate initial and boundary conditions.

The propagator $P(z|z',\,\Delta)$ is a function of the co-ordinates z and z', the z-dependence in Eq. (15) must be hidden in the coefficients c_1' and c_2'. From the fact that the propagator value does not change when we interchange the co-ordinates z and z' (time reversibility), we find immediately:

$$P(z|z',\,\Delta) = \int \left\{c_1(\lambda)\cos(\lambda z)\cos(\lambda z') + c_2(\lambda)\sin(\lambda z)\sin(\lambda z')\right\} e^{-\lambda^2 D\Delta}\,\mathrm{d}\lambda. \tag{16}$$

Then the propagator of Eq. (16) must fulfil the following conditions:

$$P(z|z,0) = 1 \tag{17}$$

$$P(z|z',\,0) = 0 \quad \text{for} \quad z \neq z' \tag{18}$$

$$\int_{-\infty}^{+\infty} P(z,\,\Delta)\,\mathrm{d}z' = 1. \tag{19}$$

The integration limits in Eq. (19) have to be adjusted when the diffusion is restricted to a certain domain of z'.

5. FREE DIFFUSION

In the absence of restrictions on the diffusion, i.e., for free diffusion, the Eqs. (17)–(19) must be true for every arbitrary value of z. Equation (17):

$$P(z|z,\,0) = \int \left\{c_1(\lambda)\cos^2(\lambda z) + c_2(\lambda)\sin^2(\lambda z)\right\} d\lambda = 1 \tag{20}$$

for every value of z implies that

$$c_1(\lambda) = c_2(\lambda) \text{ for every } \lambda \tag{21}$$

and

$$\int c_1^2(\lambda)\,\mathrm{d}\lambda = 1. \tag{22}$$

By substituting Eq. (21) in Eq. (16) one finds the propagator for free diffusion:

$$P(z|z',\,\Delta) = \int c_1(\lambda)\cos\lambda(z-z')\,e^{-\lambda^2 D\Delta}\,\mathrm{d}\lambda \tag{23}$$

showing that the propagator for free diffusion only depends on the distance $|z-z'|$ the spins have travelled, as it should be. The co-efficients $c_1(\lambda)$ can be calculated from Eqs. (17) and (18):

$$P(z|z+s,\,0) = \int_0^{+\infty} c_1(\lambda)\cos\lambda s\,\mathrm{d}\lambda = \frac{1}{2}\int_{-\infty}^{+\infty} c_1(\lambda)\cos\lambda s\,\mathrm{d}\lambda = \delta(s) \tag{24}$$

where $\delta(s)$ is the Dirac delta function. The last part of Eq. (24) represents a cosine Fourier integral, of which the inverse integral is:

$$c_1(\lambda) = \frac{1}{2\pi}\int_{-\infty}^{+\infty} 2\delta(s)\cos\,\lambda s\,\mathrm{d}s = \frac{1}{\pi}. \tag{25}$$

Substituting Eq. (25) into Eq. (23) we find the expression for the propagator of free diffusion in the normal mode representation:

$$P(z|z',\,\Delta) = \frac{1}{\pi}\int \cos\lambda(z-z')\,e^{-\lambda^2 D\Delta}\,\mathrm{d}\lambda. \tag{26}$$

The well-known Gaussian expression for free diffusion is found by evaluating the standard integral in Eq. (26):

$$P(z|z',\,\Delta) = \frac{1}{\pi}\int \cos\,\lambda(z-z')\,e^{-\lambda^2 D\Delta}\,\mathrm{d}\lambda = \frac{1}{\sqrt{4\pi D\Delta}}\,e^{-((z-z')^2/4D\Delta)}. \tag{27}$$

In many treatments of free diffusion the propagator is immediately written as a Gaussian function with the argument that it fulfils the diffusion equation. Equation (27) shows the relation with the normal mode solution of the diffusion equation. For diffusion in a bounded region the propagator is no

longer a Gaussian function. We will see in Section 6 that the normal mode representation is convenient for the case of restricted diffusion.

6. DIFFUSION IN A BOX

The normal mode expression for the propagator Eq. (16) is perfect for working out the propagator for diffusion in a rectangular box with reflecting walls between the xy-planes at $z=0$ and $z=a$. One of the boundary conditions here is (reflecting walls):

$$\left(\frac{\partial P}{\partial z'}\right)_{z'=0 \text{ or } z'=a} = 0. \tag{28}$$

With Eq. (16) we find:

$$\left(\frac{\partial P}{\partial z'}\right) = \frac{1}{\pi}\int_0^\infty (-c_1\lambda \sin\lambda z' \cos\lambda z + c_2\lambda \cos\lambda z' \sin\lambda z)\, e^{-\lambda^2 D\Delta}\, \mathrm{d}\lambda. \tag{29}$$

From

$$\left(\frac{\partial P}{\partial z'}\right)_{z'=0} = \int_0^\infty c_2\lambda \sin\lambda z\, e^{-\lambda^2 D\Delta}\, \mathrm{d}\lambda = 0 \tag{30}$$

for every value of z between 0 and a, we find $c_2 = 0$.

From

$$\left(\frac{\partial P}{\partial z'}\right)_{z'=a} = \int_0^\infty -c_1\lambda \sin\lambda a \cos\lambda z\, e^{-\lambda^2 Dt}\, \mathrm{d}\lambda = 0 \tag{31}$$

one finds $\lambda = n\pi/a$, where n is one of the integer values between $-\infty$ and $+\infty$.

With these values we can write Eq. (16) as:

$$\begin{aligned} P(z|z',\,\Delta) &= c_1(a) \sum_{n=-\infty}^{\infty} \left\{ \cos\left(\frac{n\pi}{a}z\right) \cos\left(\frac{n\pi}{a}z'\right) \exp\left(-\frac{n^2\pi^2}{a^2} D\Delta\right)\right\} \\ &= c_1(a) + 2c_1(a) \sum_{n=1}^{\infty} \left\{ \cos\left(\frac{n\pi}{a}z\right) \cos\left(\frac{n\pi}{a}z'\right) \exp\left(-\frac{n^2\pi^2}{a^2} D\Delta\right)\right\}. \end{aligned} \tag{32}$$

The only remaining constant in Eq. (32) can be found by applying Eq. (19):

$$\begin{aligned}&\int_{-\infty}^{+\infty} P(z|z',\,\Delta)\,\mathrm{d}z'\\&= \int_0^a \left[c_1(a) + 2c_1(a) \sum_{n=1}^{\infty} \left\{ \cos\left(\frac{n\pi}{a} z\right) \cos\left(\frac{n\pi}{a} z'\right) \exp\left(-\frac{n^2\pi^2}{a^2} D\Delta\right) \right\} \right] \mathrm{d}z'\\&= c_1(a)\, a = 1. \end{aligned} \tag{33}$$

The propagator for linear diffusion in a box is then:

$$P(z|z',\,\Delta) = \frac{1}{a} + \frac{2}{a} \sum_{n=1}^{\infty} \left\{ \cos\left(\frac{n\pi}{a} z\right) \cos\left(\frac{n\pi}{a} z'\right) \exp\left(-\frac{n^2\pi^2}{a^2} D\Delta\right) \right\}. \tag{34}$$

This equation agrees with the expression originally derived by Tanner and Stejskal[5] (the expression reproduced in the book by Callaghan[10] misses the normalization factor $1/a$).

The PFGE signal resulting from the propagator Eq. (34) is calculated by Eq. (1) with $\rho(\vec{r}) = 1/a$:

$$\begin{aligned} E(g,\Delta) &= \int\int \frac{1}{a} \left[\frac{1}{a} + \frac{2}{a} \sum_{n=1}^{\infty} \left\{ \cos\left(\frac{n\pi}{a} z\right) \cos\left(\frac{n\pi}{a} z'\right) \exp\left(-\frac{n^2\pi^2}{a^2} D\Delta\right) \right\} \right] e^{i\gamma\delta g(z'-z)}\,\mathrm{d}z\,\mathrm{d}z'\\ &= \frac{1}{a^2} \int_0^a e^{i\delta\gamma g z'}\,\mathrm{d}z' \int_0^a e^{-i\delta\gamma g z}\,\mathrm{d}z\\ &\quad + \frac{2}{a} \sum_{n=1}^{\infty} e^{((-n^2\pi^2 D\Delta)/a^2)} \int_0^a \cos\left(\frac{n\pi z'}{a}\right) e^{i\gamma\delta g z'}\,\mathrm{d}z' \int_0^a \cos\left(\frac{n\pi z}{a}\right) e^{-i\gamma\delta g z}\,\mathrm{d}z\\ &= \frac{2 - 2\cos(\gamma\delta g a)}{(\gamma\delta g a)^2} + 4(\gamma\delta g a)^2 \sum_{n=1}^{\infty} e^{((-n^2\pi^2 D\Delta)/a^2)} \left[\frac{1 - (-1)^n \cos(\gamma\delta g a)}{\{n^2\pi^2 - (\gamma\delta g a)^2\}} \right]. \end{aligned} \tag{35}$$

Equation (35) is identical with the corresponding expression of Tanner and Stejskal[5] and as reproduced in Callaghan's book.[10] Note that expression (35) only results when the normalization constant $1/a$ is taken into account in the propagator (34).

7. THREE-DIMENSIONAL DIFFUSION IN A SPHERICALLY SYMMETRIC SYSTEM

The three-dimensional diffusion equation

$$\frac{\partial P}{\partial t} = D\,\nabla'^2 P \tag{6}$$

can be solved again by separation of variables:

$$P = R\left(\vec{r}'\right) T(t) \tag{36}$$

where $\vec{r}' = (x, y, z)$ in Cartesian co-ordinates or $\vec{r}' = (r' \sin\theta' \cos\phi', r' \sin\theta' \sin\phi', r' \cos\theta')$ in polar co-ordinates.

Inserting Eq. (36) in Eq. (6) gives:

$$\frac{1}{R}\nabla^2 R = \frac{1}{DT}\frac{\partial T}{\partial t} = -\lambda^2. \tag{37}$$

By solving for the time dependent function T one finds:

$$T = Ce^{-\lambda^2 Dt}. \tag{38}$$

For diffusion in a sphere the propagator should be independent of the azimuth angle ϕ, then we can write for R:

$$R\left(\vec{r}'\right) = S(r')Q(\theta'). \tag{39}$$

The Laplace operator in polar co-ordinates is:

$$\nabla'^2 = \frac{\partial^2}{\partial r'^2} + \frac{2}{r'}\frac{\partial}{\partial r'} + \frac{1}{r'^2}\frac{\partial^2}{\partial \theta'^2} + \frac{1}{r'^2}\frac{\cos\theta'}{\sin\theta'}\frac{\partial}{\partial \theta'}. \tag{40}$$

Inserting Eq. (39) in the left part of Eq. (37):

$$Q\frac{\partial^2 S}{\partial r'^2} + \frac{2}{r'}Q\frac{\partial S}{\partial r'} + \frac{1}{r'^2}S\frac{\partial^2 Q}{\partial \theta'^2} + \frac{1}{r'^2}\frac{\cos\theta'}{\sin\theta'}S\frac{\partial Q}{\partial \theta'} = -\lambda^2 SQ \tag{41}$$

and multiplying both sides with r'^2/SQ we find:

$$\frac{r'^2}{S}\frac{\partial^2 S}{\partial r'^2} + \frac{2r'}{S}\frac{\partial S}{\partial r'} + \lambda^2 r'^2 = -\frac{1}{Q}\frac{\partial^2 Q}{\partial \theta'^2} - \frac{1}{Q}\frac{\cos\theta'}{\sin\theta'}\frac{\partial Q}{\partial \theta'} = \kappa^2 \tag{42}$$

or:

$$\frac{r'^2}{S}\frac{\partial^2 S}{\partial r'^2} + \frac{2r'}{S}\frac{\partial S}{\partial r'} + \lambda^2 r'^2 - \kappa^2 = 0 \quad \text{and} \quad \frac{1}{Q}\frac{\partial^2 Q}{\partial \theta'^2} + \frac{1}{Q}\frac{\cos\dot{\theta}}{\sin\theta'}\frac{\partial Q}{\partial \theta'} + \kappa^2 = 0. \tag{43}$$

By the substitution $\lambda r' = s$ the first equation of (43) becomes:

$$s^2\frac{\partial^2 S}{\partial r^2} + 2s\frac{\partial S}{\partial r} + \left(s^2 - \kappa^2\right)S = 0 \tag{44}$$

and with the substitution $\mu = \cos\theta'$ the second equation of (43) changes into:

$$\left(1-\mu^2\right)\frac{\partial^2 Q}{\partial \mu^2} - 2\mu\,\frac{\partial Q}{\partial \mu} + \kappa^2 Q = 0. \tag{45}$$

For $\kappa^2 = n(n+1)$ Eq. (44) is the differential equation of Bessel and Eq. (45) the Legendre differential equation with solutions:

$$\text{Spherical Bessel functions}: \; S = j_n(\lambda r') = \sqrt{\frac{\pi}{2r'}}\,J_{n+\frac{1}{2}}(\lambda r') \tag{46}$$

$$\text{Legendre functions}: \; Q = P_n(\cos\theta'). \tag{47}$$

The general solution of the diffusion equation for a system with spherical symmetry can therefore be written as:

$$P(r,\theta|r',\theta',\,\Delta) = \int C_{n,\lambda}\, j_n(\lambda r)\, j_n(\lambda r')\, P_n(\cos\theta)\, P_n(\cos\theta')\, e^{-\lambda^2 D\Delta}\,\mathrm{d}\lambda. \tag{48}$$

The variable constant λ can be determined by the boundary condition Eq. (28):

$$\left(\frac{\partial P}{\partial r'}\right)_{r'=a} = 0 \tag{49}$$

where a is the radius of the sphere. For every value of r, θ and θ':

$$\left(\frac{\partial P}{\partial r'}\right)_{r'=a} = \int C_{n,\lambda}\, j_n(\lambda r)\, j_n'(\lambda r')\, P_n(\cos\theta')\, P_n(\cos\theta)\, e^{-\lambda^2 D\Delta}\,\mathrm{d}\lambda = 0 \tag{50}$$

or

$$j_n'(\lambda a) = 0. \tag{51}$$

When we define the roots α_{nk} by $j_n'(\alpha_{nk}) = 0$ we have as a condition for λ:

$$\lambda_k = \frac{\alpha_{nk}}{a}. \tag{52}$$

The general solution for diffusion in a sphere is then:

$$P(r,\,\theta|r',\,\theta',\,\Delta) = \sum_{n=0}^{\infty}\sum_{k=0}^{\infty} C_{nk}\, j_n\!\left(\frac{\alpha_{nk}}{a}r\right) j_n\!\left(\frac{\alpha_{nk}}{a}r'\right) P_n(\cos\theta)\, P_n(\cos\theta')\, e^{-(\alpha_{nk}/a)^2 D\Delta} \tag{53}$$

Table 1. The roots of $j'_n(z) = 0$

	$k=0$	1	2	3	4	5	6	7
$n=0$	0	4.4934	7.7252	10.9041	14.0662	17.2207	20.3713	23.5194
1	0	2.0816	5.9404	9.2058	12.4044	15.5792	18.7426	21.8997
2	0	3.3421	7.2899	10.6139	13.8461	17.0429	20.2219	23.3905
3	0	4.5141	8.5837	11.9727	15.2445	18.4681	21.6666	24.8501
4	0	5.6467	9.8404	13.2956	16.6093	19.8624	23.0828	26.2833
5	0	6.7565	11.0702	14.5906	17.9472	21.2311	24.4748	27.6937
6	0	7.8511	12.2793	15.8632	19.2627	22.5781	25.8461	29.0843
7	0	8.9348	13.472	17.1175	20.5594	23.9064	27.1992	30.4575
8	0	10.0104	14.6513	18.3563	21.84	25.2187	28.5365	31.8151
9	0	11.0794	15.8192	19.5819	23.1066	26.5166	29.8595	33.1588
10	0	12.1432	16.9775	20.796	24.3608	27.8019	31.1698	34.4898

where α_{nk} are the non-negative roots of Eq. (51). These roots have not been published in the NMR literature and because we need them for the numeric simulation of the echo signal they are numerically determined by Mathematica® up to $n = 10$ and $k = 8$, see Table 1. Because so far it is not clear whether the value zero for α_{nk} has to be included in the double sum Eq. (53). Table 1 also shows the zero roots.

For a complete definition of Eq. (53) we need to determine the constants C_{nk} from the conditions (17)–(19) and then calculate the Fourier integral Eq. (1) for the echo signal. To avoid the tedious algebra we compare the three published solutions numerically, but first reproduce these solutions here using our notation. Two of these solutions[6,8] resulted from a calculation that included the effect of surface relaxation. To make a correct comparison we eliminate from the equations the terms due to relaxation. Then we have the following formulae for the echo intensity for diffusion in a sphere with radius a and reflecting walls:

Mitra and Sen[6]

$$E(g,\ \Delta) = 6\sum_{kn}^{\infty} \frac{(2n+1)\alpha_{nk}^2}{\alpha_{nk}^2 - n^2 - n} \exp\left(-\frac{\alpha_{nk}^2}{a^2} D\Delta\right) \frac{\gamma\delta g a j'_n(\gamma\delta g a)}{\left[\alpha_{nk}^2 - (\gamma\delta g a)^2\right]^2}. \tag{54}$$

Balinov *et al.*[7]

$$E(g,\ \Delta) = \frac{9[\gamma g\delta a\cos(\gamma g\delta a) - \sin(\gamma g\delta a)]^2}{(\gamma g\delta a)^6} + 6\sum_{n=0}^{\infty}\sum_{k} \frac{(2n+1)\alpha_{nk}^2}{\alpha_{nk}^2 - n^2 - n} \exp\left(-\frac{\alpha_{nk}^2 D\Delta}{a^2}\right)\left[\frac{\gamma g\delta a j'_n(\gamma g\delta a)}{\alpha_{nk}^2 - (\gamma g\delta a)^2}\right]^2. \tag{55}$$

Callaghan[8]

$$E(g,\ \Delta) = 6\sum_{n,\,k}\frac{(2n+1)\,\alpha_{nk}^2}{\alpha_{nk}^2 - n^2 - n}\exp\left(-\frac{\alpha_{nk}^2 D\Delta}{a^2}\right)\left[\frac{\gamma\delta g a\, j_n'(\gamma\delta g a)}{\alpha_{nk}^2 - (\gamma\delta g a)^2}\right]^2. \qquad (56)$$

By comparing Eqs. (54)–(56) a few differences are evident. Compared to Eqs. (55) and (56) the numerator of the last quotient in Eq. (54) is unsquared. In the publication of Balinov *et al.*[7] the sign of the second term in Eq. (54) was negative, but in a later publication[11] the sign has been changed into +, as we already have written. Further, the first term of the Balinov equation (55) seems to be missing in the other two equations.

Because it is not clear from the published equations what the first value of n and k in the sums has to be (0 or 1) and because Mathematica does not like the term with $\alpha_{nk} = 0$, we first separately calculate the contribution of the term with $\alpha_{nk} = 0$ in Eq. (56). All α_{nk} with $k = 0$ are zero (Table 1) but the only non-zero term of Eqs. (54)–(56) with $\alpha_{nk} = 0$ is for $n = k = 0$:

$$E(g,\ \Delta)_{n=k=0} = 6\left(\frac{j_0'(\gamma\delta g a)}{(\gamma\delta g a)^2}\right)^2 = 6\frac{(\gamma\delta g a\cos\ \gamma\delta g a - \sin\ \gamma\delta g a)^2}{(\gamma\delta g a)^6}. \qquad (57)$$

We can therefore write the Mitra and Sen formula and the Callaghan formula as:

$$E(g,\ \Delta) = 6\frac{(\gamma\delta g a\cos\ \gamma\delta g a - \sin\ \gamma\delta g a)}{(\gamma\delta g a)^3} + 6\sum_{k=1,\,n=1}^{\infty}\frac{(2n+1)\alpha_{nk}^2}{\alpha_{nk}^2 - n^2 - n}\exp\left(-\frac{\alpha_{nk}^2}{a^2}D\Delta\right)\frac{\gamma\delta g a\, j_n'(\gamma\delta g a)}{\left[\alpha_{nk}^2 - (\gamma\delta g a)^2\right]^2} \qquad (58)$$

$$E(g,\ \Delta) = 6\frac{(\gamma\delta g a\cos\gamma\delta g a - \sin\gamma\delta g a)^2}{(\gamma\delta g a)^6} + 6\sum_{n=1}^{\infty}\sum_{k=1}^{\infty}\frac{(2n+1)\alpha_{nk}^2}{\alpha_{nk}^2 - n^2 - n}\exp\left(-\frac{\alpha_{nk}^2 D\Delta}{a^2}\right)\left[\frac{\gamma\delta g a\, j_n'(\gamma\delta g a)}{\alpha_{nk}^2 - (\gamma\delta g a)^2}\right]^2. \qquad (59)$$

Now the Eqs. (55), (58) and (59) are practically identical, except for the square of the first term and of the last numerator in Eq. (58) and the factor 6 of the first term in Eqs. (58) and (59) compared to Eq. (55). Note that the summations in Eqs. (58) and (59) start with $n = k = 1$.

By numerical calculation of the three equations (55), (58) and (59) by Mathematica for different ratios $D\Delta/a^2$ and using the α_{nk} values of Table 1, we immediately find that the Mitra and Sen equation (58) cannot be correct. The result for Eq. (58) deviates so much from what is expected, that it is certain that

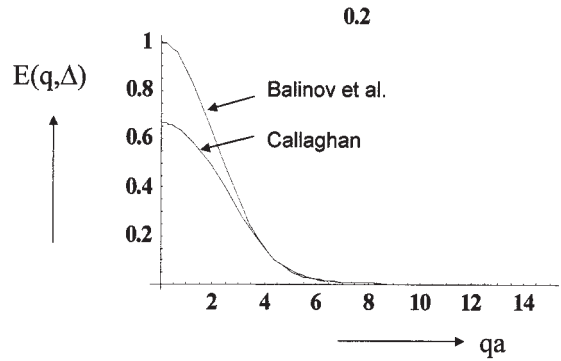

Fig. 2. Mathematica simulation of the Eqs. (55) and (58) for $D\Delta = 0.2\ a^2$.

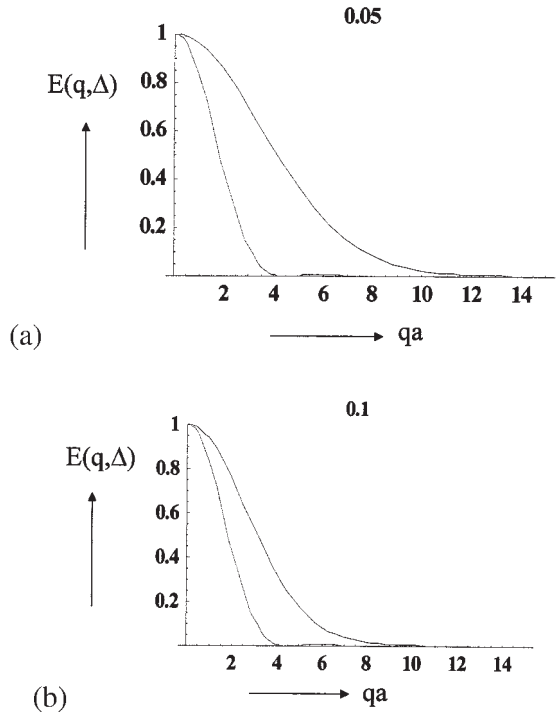

Fig. 3. Simulation of Eq. (58) for different $D\Delta/a^2$ ratios, (a) $D\Delta = 0.05a^2$, (b) $D\Delta = 0.1a^2$, (c) $D\Delta = 0.2a^2$, (d) $D\Delta = 0.5a^2$ and (e) $D\Delta = a^2$. In these figures also the curve for the long time limit $D\Delta \gg a^2$ is drawn.

the missing of the square is a print error. The curves for the two other equations are shown in Fig. 2 for the ratio $D\Delta/a^2 = 0.2$. From these curves we see that the Callaghan curve deviates from the Balinov curve for small $q = \gamma\delta g/2\pi$ values and does not reach the value 1 for $q = 0$. The conclusion

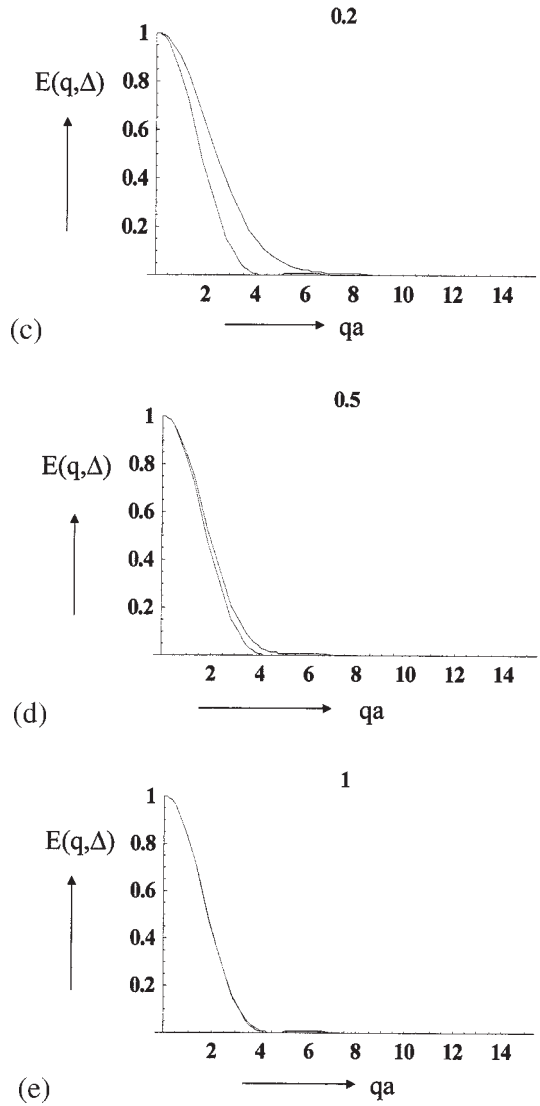

Fig. 3. Continued.

therefore is that the correct exact formula for diffusion in a sphere with radius a and reflecting walls is represented by Eq. (55) when the summations over n and k start with the value 1.

Figure 3 shows the curves calculated with Eq. (55) for different ratios $D\Delta/a^2$, for increasing $D\Delta/a^2$ the curves approach more and more the curve corresponding to the long time limit $D\Delta \gg a^2$, given by the first term of Eq. (55) and which was derived in 1968 by Tanner and Stejskal.[5]

8. CONCLUSION

We have shown numerically which of the three published exact expressions for the echo signal in a pulsed field gradient NMR experiment for diffusion in a closed sphere with reflecting walls is correct. When these formulae are to be used in a fitting procedure of experimental data the exact expression is necessary. Also it has been shown how these theoretical expressions are derived from a normal mode solution of the three-dimensional diffusion equation. Knowing the correct expression of the echo signal for diffusion in a sphere, it is straightforward to extend the formulae to the case of surface relaxation. For that purpose the terms in the original formula of Mitra and Sen or of Callaghan which describe surface relaxation can be simply added to the expression found here.

REFERENCES

1. L. L. Latour, P. P. Mitra, R. L. Kleinberg and C. H. Sotak, *J. Magn. Reson.*, 1993, **A101**, 342.
2. K. J. Packer and C. Rees, *J. Coll. Int. Sci.*, 1972, **40**, 206.
3. J. S. Murday and R. M. Cotts, *J. Chem. Phys.*, 1968, **48**, 4938.
4. C. H. Neumann, *J. Chem. Phys.*, 1974, **60**, 4508.
5. J. E. Tanner and E. O. Stejskal, *J. Chem. Phys.*, 1968, **49**, 1768.
6. P. P. Mitra and P. N. Sen, *Phys. Rev. B*, 1992, **45**, 143.
7. B. Balinov, B. Jönsson, P. Linse and O. Söderman, *J. Magn. Reson.*, 1993, **A104**, 17.
8. P. T. Callaghan, *J. Magn. Reson.*, 1995, **A113**, 53.
9. I. Broekmann, 2002, Thesis, University of Duisburg.
10. P. T. Callaghan, *Principles of Nuclear Magnetic Resonance Microscopy*, Clarendon Press, Oxford, 1991.
11. P. Linse and O. Söderman, *J. Magn. Reson.*, 1995, **A116**, 77.

Automatic Analysis of NMR Spectra

LEE GRIFFITHS

AstraZeneca, Mereside, Alderley Park, Macclesfield, Cheshire SK10 4TG, UK

Automatic spectral processing, spectral analysis, spectral prediction and structural confirmation/elucidation have been reviewed. ^{13}C and two-dimensional spectra have been included, but particular emphasis has been placed on one-dimensional ^{1}H spectra of small to medium-sized molecules. This is highly pertinent to the explosion in flow NMR currently taking place, which supports multiple parallel synthesis and combinatorial chemistry.

ANNUAL REPORTS ON NMR SPECTROSCOPY
VOLUME 50 ISSN 0066 4103
DOI 10.1016/S0066-4103(03)50006-0

1. INTRODUCTION

From the inception of NMR, there has been an interest in rendering the interpretation more facile. This has been tackled from both sides: on the one hand the prediction of key spectral parameters such as chemical shift and scalar coupling, and on the other, the extraction of the corresponding parameters from the experimental spectrum. When the switch from continuous wave (CW) to Fourier Transform (FT) spectrometers took place, in broad terms during the late 1970s, the spectra were digitized and the efficient extraction of key spectral parameters from the experimental spectrum became feasible. In 1982 Bruker[1] demonstrated their first 60 position sample changer at the Pittsburg Conference. This was subsequently shipped to the BASF group in Germany (who have remained a key part of the development of automated spectral analysis and interpretation), to complement the sample changer they had developed themselves in 1981. From that point, automation within data processing and subsequent analysis became much more a necessity rather than a desire.

Automatic post-processing soon appeared. Bruker's 'apk' automatic phasing routine first appeared in 1980 and was improved in 1988.[2] Similarly Bruker's 'abs' automatic baseline correction and automatic integral region selection routine appeared in 1980 and was also improved in 1988.[2] It was a small step to write peak-picking software that would yield a table of resonance positions expressed as real numbers for subsequent searching against a database. This is of course a trivial exercise in the case of ^{13}C where spectra are commonly proton decoupled and every peak represents a unique nucleus (or collection of equivalent nuclei). It is not a trivial exercise for ^{1}H where coupling complicates the situation.

While NMR spectra possess a high information content, this confers a level of complexity that can be obstructive if a quick and simple answer is required. The use of NMR flow probes has reduced the time taken to acquire a ^{1}H spectrum to 2–3 min[3] and flow NMR has consequently found considerable application in robot synthesis, multiple parallel synthesis (MPS) or combinatorial chemistry.[4–7] Since ^{1}H possesses 5600 times the receptivity of ^{13}C, it is inevitable that it will continue to be the nucleus of choice in this area, complicating the analysis. Unless automatic analysis is able to transcend the 'aid to interpretation' role and into the 'confirm or refute the structure' role, the higher information content of the NMR spectrum constitutes a threat rather than an opportunity.

Flow NMR is a burgeoning area in which automatic spectral analysis can make an enormous contribution. The applicability of various methods to flow NMR, is referred to on occasion throughout this review. Whilst the review is biased in this direction it is not wholly so: it is still highly relevant to the whole of NMR.

2. SPECTRAL PROCESSING

2.1. Introduction

A pre-requisite for the successful extraction of key NMR parameters from an experimental spectrum is the way it is processed after acquisition. The success criteria are low noise levels, good resolution and flat baseline. Clearly, there are also experimental expedients that can further these aims, but these are not the subject of this review *per se*. In choosing window functions prior to FT, the criteria of low noise levels and good resolution run counter to one another and the optimum is just that. Zero filling the free induction decay (FID) to the sum of the number acquired in both the 'u' and 'v' spectra (in quadrature detection) allow the most information to be extracted.

2.2. Baseline subtraction

Baseline subtraction of the frequency domain spectrum is a critical part of data processing. It affects the calculation of integrals, the selection of integral regions and it affects peak-picking. Automatic baseline correction is relatively undemanding where all the solute peaks are narrow and all baseline distortions possess a much larger width. If solute peak widths are large, e.g., where exchange or restricted rotation is present, automatic baseline correction poses a much more significant challenge.

In older spectrometers, it was common for the first few points of the FID to exhibit a linear ramp as the electronics switched in, rather than the sine * exponential shape one might expect. Baseline distortion was therefore an inverted quasi-sinc shape (the FT of a triangle). This was particularly acute for large spectral widths (large sampling frequencies). Left shifting the FID was a commonly available expedient, but this introduced significant phase errors. A more rigorous approach was back-construction of the FID to $t = 0$.[8,9] More modern spectrometers are less prone to this problem. Alternatively, the spectrum could be fitted in order to treat a variety of other baseline problems, using Fourier series,[10] various polynomials,[11–13] and a special function for baseline flattening two-dimensional spectra including large solvent residuals (IFLAT).[14] Williams and Golotvin published a method for one-dimensional NMR spectra[15] in which they split the process into two parts: baseline recognition and baseline modelling. Of course, all methods must do that, but, this work describes in some detail how they achieved both. In the case of baseline recognition, in order to determine whether the *i*th point is baseline or not, they take a section of the spectrum $\pm n$ points and then determine whether the difference between the maximum and the minimum is more than a constant times the standard deviation of the noise. If it's greater it's peak, if it is smaller, it's baseline. Of course, the smaller '*n*', the more likely wide peaks will be

recognized as such, but the more likely baseline features will be deemed peaks. Baseline modelling was simply a smoothed spectrum where each peak region was replaced by a straight sloping line joining the edges of the baseline region on either side.

2.3. Peak-picking

Peak-picking appears to be a domain largely occupied by instrument manufacturers. As a consequence, many of the algorithms remain unpublished.

The partial convolution of two peaks poses special problems and with high signal to noise, it is easy to see how the first derivative would help this process. Differentiation accentuates the noise, so this will not be a universally successful procedure.

The role of peak-picking is to return only one position per peak, and in the presence of noise, this again poses problems. It is likely that most algorithms will start from a position of intensity maximum, and then search either side for the first point significantly lower, i.e., a multiplier of the noise. This defines a new peak region and the process could then be repeated. Some software additionally offers the facility of a horizontal threshold, above which values are returned and below which they are not.

Zero filling the FID more than a factor of two does not contribute to information extraction and any features revealed by this are artefacts. In most instances, zero filling by a factor of two amounts to an interpolation procedure benefiting primarily peak-picking.[16,17] There are other procedures which can allow peak-picking interpolation between data points and the one used by the author is a simple equation to fit the maximum intensity and one point either side to a parabola and compute the position of its maximum. Bruker peak-pick table positions for instance are not separated by a multiple of the digital resolution and it would seem that they use the same or an analogous procedure.

Ernst[18] published a method for the identification of cross-peaks in two-dimensional spectra based on the recognition of their unique anti-phase portion in phase-resolved two-dimensional spectra. Glaser and Kalbitzer[19] presented a generalized and fully automated method for the recognition of cross-peaks in two-dimensional NMR spectra.

Bodenhausen[20,21] developed a pattern-recognition programme (MARCO POLO) in order to extract coupling pathways in COSY spectra. He subsequently[22] described a recursive deconvolution technique for the measurement of couplings, but this seems to offer more benefits to the measurement of scalar couplings in two-dimensional spectra than in one-dimensional spectra.

Wüthrich *et al.*[23] published a tour de force on the Automated Peak-Picking and Peak Integration in Macromolecular Spectra (AUTOPSY). This work deals primarily with two-dimensional spectra, but the algorithms are equally

applicable to one-dimensional spectra. Noise was determined locally (it can be larger at the periphery of spectra or localized in two-dimensional spectra as t_1-noise, solvent, etc.). Five percent regions whose standard deviations (in order to exclude peaks) were minimal, were chosen. A method of segmenting (specifying regions containing peaks as opposed to noise) was described. The position of isolated peaks (the general case being asymmetric peaks) was also determined using a symmetrized line shape (i.e., the minimum intensity on either side of a putative centre). Previous methods[24] had iterated this putative centre to yield the position yielding the minimum sum of squares between the symmetrized and the actual line shape. However, Wüthrich described a novel function, which while employing the same symmetrized line shape, favoured the position of the peak of maximum intensity where the asymmetric line shape was due to two convoluted peaks. He also described a deconvolution procedure, which employed the line shape of resolved peaks rather than theoretical line shapes. Wüthrich has also published a method for the automatic identification of NOEs in NOESY two-dimensional spectra.[25]

3. SPECTRAL ANALYSIS

Pattern recognition has been used and is being developed to correlate spectral and structural information in relatively complex systems.[26] It is however, a technique that is susceptible to the solvent, temperature and concentration induced shifts as well as magnetic field dependence. It is likely therefore, that the information yielded by this technique will be indicative rather than diagnostic: sufficient in complex matrices where expectations are low but insufficient in simple ones where the expectations are much higher. In simple matrices, it is unlikely that anything other than separating the spectrum into its constituent parts, i.e., the chemical shifts and couplings (probably) and comparing these against theoretical values will yield the required certainty.

Spectral databases can be used for exact matching ('finger printing') and if this is a practical proposition, the spectral analysis step can be avoided. In this situation, it is essential that the number of possibilities is finite. An obvious application of this in the pharmaceutical industry would be the validation of identity and purity of compound collection sub-sets prior to high throughput screening. ^{1}H NMR is not currently suitable, because coupling patterns (themselves dependent on external magnetic field) add to chemical shift differences induced by concentration and temperature. If chemical shifts could be extracted reliably from coupled spectra, tolerances could be applied to solvation effects in a consistent fashion. Indeed, if chemical shifts could be extracted in this fashion, the building of ^{1}H NMR databases would be facile and considerably faster than it is at present. The need for spectral analysis is

therefore extremely compelling, even when a more rigorous approach is not required by the presence of novel compounds.

3.1. Chemical shift

'J' spectra are able to yield chemical shifts experimentally[27] but this is a projection of a two-dimensional experiment. It is inevitable that one-dimensional 'pulse and collect' will be the most rapid experiment available. An efficient method of post-extracting chemical shifts from the experimental spectrum is therefore required.

It could be argued that at say 500 MHz, most multiplets will be less than 0.1 ppm in width. Even if the central proton were not extracted accurately, the error in chemical shift would be less than the error in the predicted shifts. The errors are additive however, and this will compromise the certainty ascribed to the yes/no decision. The inability to separate convoluted multiplets would seriously prejudice this approach.

Griffiths demonstrated the possibility of automatically and reliably identifying multiplets, couplings and chemical shifts in peak-pick tables derived from ^{1}H spectra.[28] The identification of separated multiplets was based on simple separation criteria while the subsequent identification of overlapping multiplets was based on the recognition of symmetry about identical points, i.e., the identification of doublets of doublets (of which triplets, quartets, etc. were special cases). This multiplet refinement was limited by the requirement that overlapping multiplets did not possess a common coupling, since by definition, apparent doublets of doublets would tie the two real multiplets together.

A key factor in this pattern processing, was the tolerance criterion employed in judging whether say two pairs of peaks shared a common position, whether two couplings were the same, etc. In this work, the peak position tolerance from which these criteria were derived, was simply a multiplier of the digital resolution. In later work,[29] a more sophisticated tolerance was developed which depended on both signal intensity to noise and peak width.

3.2. Scalar coupling measurement

3.2.1. *Introduction*

Scalar couplings encode geometry and electronegativity. However, whilst the causes of variation in scalar couplings are known, precise prediction is not possible. It is therefore true that in most situations, it is possible to extract scalar couplings more precisely than it is to predict them. This does not render them valueless, indeed information can be inferred in conformational analysis,

but more particularly, precise extraction is a pre-requisite for the extraction of the number of couplings. The number of couplings can be invaluable in reducing the degrees of freedom in assigning observed chemical shifts to atoms and hence in structural elucidation.

3.2.2. *First-order spectra*

It is fortunate that most applications devolve into one of two camps: small molecules or proteins. In the former case, the size of these molecules has stayed fairly constant and the inexorable rise in magnetic fields has meant that the number of incidences of second-order spectra has decreased (although complications will always exist with virtual couplings). It is therefore pertinent to examine methods, which are not only designed to extract couplings from first-order spectra, but are also amenable to automation.

In analysing coupling patterns (necessarily assumed to be first-order), Griffiths[28] used an algorithm similar to Hoye *et al.*[30] in which the separation of the outside two resonances on each side of the multiplet was deemed to be the smallest coupling. That coupling was found throughout the multiplet and the average positions where that coupling was found, carried through to the next loop. The process was repeated until only one or two averaged resonance(s) remain. The exception is the situation where one coupling is double another. If nothing extraordinary is done, three identical couplings will emerge from such an approach. The key criterion in identifying this situation is the relative intensity of the outside pair of resonances: the closer the intensity ratio is to unity, the higher the probability that the coupling is double.

Indeed, since Griffiths's initial work was published, the explicit identification of doublets within otherwise random multiplets has increased the correct identification of couplings from 80 to 85%.[29] However, it was also demonstrated that peak intensities employed in that work, were not a reliable method of determining stoichiometry nor in the identification of impurities. Instead, Griffiths[31] developed a method for the extraction of accurate multiplet integrals, even where the multiplets were overlapped, by assigning a portion of integral to each peak. The method, by which this was achieved, was to split the integral between peaks at a position based on the peak widths and apparent relative intensities. Furthermore, Griffiths published a method by which these multiplet integrals (in arbitrary units), may be converted into numbers of protons, without prior knowledge of the postulated structure. This method was based on a scoring system aimed at identifying methine protons, whereby 'good ratios', e.g., 1, 2, 3, etc. scored positive and 'bad ratios', e.g., $\frac{1}{3}$, $\frac{1}{2}$, $\frac{2}{3}$, etc. scored negative. Again, a key parameter was the ratio tolerance applied in determining similar integrals, and this was found to be 1.15.

The methodology was relatively simple and undemanding of computation which contrasts with the integral transform (IT) method[32–35] requiring a full

analysis of the spin system in order to yield chemical shifts and couplings. Whilst it could be argued that computation becomes forever faster, it can equally be argued that magnetic field also becomes forever larger, reducing the need for a full analysis of the spin system.

It was later asserted that in confirming proposed structures, the experimental stoichiometries as well as the chemical shifts, would be important and a methodology was proposed for their determination.[31]

Advanced Chemistry Development Inc. have recently published their 'J-Coupler' software for automatic analysis[36] of non-overlapped multiplets, partially implementing a batch capability in Version 5 and fully in Version 6. ACD's approach is essentially the same as in Refs. 28 and 30, except that their method of identification of a coupling double the size of another, was different. Their method involved the assumption that all averaged pairs were of the same intensity. If they were not, the excess intensity at a given position, was allowed to contribute to another pair in the same layer, as the multiplet was deconstructed. 'Roof effects', or the canting of nearby coupled multiplets,[30] was accommodated by a symmetrization procedure, cf. the line of best fit ratioing in Ref. 28. Thereafter, the total area of the multiplet was normalized to 2^{NJ}, where NJ is the number of couplings. Unit intensity was the required intensity for each coupling pair and in determining the existence of excess intensity at each position, the intensities were allowed a 15% tolerance, interestingly the same integral tolerance was used in Ref. 31. The problem with this approach is that it does require NJ *a priori*, which can only be obtained from the structure.

Stonehouse and Keeler[37] developed an intriguing method for the accurate determination of scalar couplings even in multiplets with partially convoluted peaks (one- or two-dimensional). They recognized that the time domain signal is completely resolved and that convolution of the frequency domain spectrum is a consequence of the Fourier transform of the signal decay. The method requires that the multiplet be centred about zero frequency and this was achieved by the following method:

- Excise the multiplet from the spectrum.
- Inverse Fourier transform.
- Adjust zero time until the sum of squares of the imaginary spectrum is zero (i.e., the FID is then centred about zero).

It is worth noting in passing that this could be developed into a generalized peak (and multiplet) picking algorithm. Because the multiplet (more easily visualized as a doublet) is centred about zero time, the time domain signal then has a zero crossing at $1/2J$. Keeler *et al.* developed a related time domain function, which could be minimized to find this zero crossing point in a reliable fashion, even where signal decay was rapid with respect to $1/2J$ and where noise was present. Indeed, they commented that this procedure was amenable to automation. Keeler published another method,[38] which utilized both COSY

and TOCSY cross-peaks. The experimental time domain signal was multiplied by a corresponding time domain function of an anti-phase stick doublet (COSY) and in-phase for TOCSY. By iterating J_{trial}, when $J_{\text{trial}} = J_{\text{active}}$, the two resultant spectra are identical.

Nuzillard *et al*. developed a related method[39] named 'log-abs' which utilized the same extraction and centring technique as Keeler, but output a '*J*-spectrum', i.e., a plot of probability as a function of *J*. As with Keeler's method, this method was subject to increasing unreliability with increased convolution and lower signal to noise. Unlike Keeler's method, it was not suited to anti-phase multiplets in two-dimensional spectra.

Other techniques designed to obtain scalar couplings in similar situations are '*J* Doubling'[40] and '*J* Deconvolution',[41] both of which operate on the time domain signal.

Lindon and co-workers[42] employed Maximum Entropy deconvolution in order to measure couplings in complex multiplets. Here, doublets etc. were incorporated into the Point Spread Function (PSF), which would normally only encode line shape. The maximum entropy procedure yielded the most likely couplings. Clearly, this is a procedure well suited to high convolution and high noise situations, but it is less clear how amenable it would be to automation.

3.2.3. *Second-order spectra*

In second-order spectra, pattern recognition in all its various forms, is of little help. Instead an iterative quantum mechanical simulation of the observed spectrum is required. The most celebrated programme in this respect is LAOCOON.[43,44] However, this approach suffers two main drawbacks in terms of automation: it is restricted to 7–8 spins, and trial values of δ and J are required to start the process. In most instances, spin systems are interrupted by sufficient non-proton bearing atoms before such a limit is reached, and one might reasonably attempt to recognize these distinct spin-systems using two-dimensional COSY or TOCSY experiments. Pattern recognition could be used to furnish trial values of δ and J, but unless these are close to the actual values, the result of the iteration may well be dependent on the exact starting values chosen. Laatikainen[45] investigated the errors produced by LAOCOON3, producing the Modified LAOCOON (MAOCON) programme. His approach accurately reproduced an arbitrary model containing normally distributed errors. In particular he found increased correlation where two δs converged, i.e., in terms of the solutions, either the sum or the difference in parameters were determined accurately, but not both. By 1986 MAOCON had acquired an automatic assignment procedure,[46] i.e., as the iteration evolved, the calculated position changes made it appropriate to reassign calculated and observed chemical shift pairs, this was performed automatically. Within the same work, Laatikainen also proposed a weighted (by intensity) average chemical shift for convoluted (assuming experimental line width)

calculated resonances, having previously shown that an unweighted average can lead to errors.[47] MAOCON was developed to an unprecedented degree, to include the fitting of residual dipolar interactions. In spectra with line widths as little as 0.025 Hz, Laatikainen was able to probe the stacking and solvent interactions of naphthalene and benzene.[48,49] In doing so, Laatikainen developed the 'peak top-fitting' method, which instead of comparing the total lineshape of the calculated and observed spectra as in DAVINS,[50] NMRCON[51] and Bruker's DAISY,[1] a method with a large dependence on the exact choice of line shape and the presence of impurities, it compared the frequency of the calculated peak maxima with those observed. Laatikainen later employed the 'integral transform' method,[34] to furnish trial parameters for the iteration. The integral transform is a procedure for convoluting both the calculated and observed spectra with simple broad functions, e.g., triangles. By judicious choice of IT width, in order of decreasing width, the fitting procedure can be made to be sensitive to δ, large J and small J in a sequential fashion. It is asserted that such a stepwise approach is less prone to the selection of local minima during the iteration. Laatikainen later presented[35] the IT method within what was then named 'PERCH' software.[52] This work also included an interesting 'coupling finder' algorithm which took combinations of spectral intensity at each point in the spectrum, and those $+/-$ a given separation. By incrementing this separation, perturbations occurred when this separation became equal to a coupling. The size of scalar couplings and which multiplets contained these couplings, could therefore be determined. The PERCH software was demonstrated with a complete analysis of the 400 MHz spectrum of β-pinene[53] and now includes a ^{1}H prediction module, which takes for input an optimized three-dimensional structure. However, this module has not been published in written form.[54]

3.2.4. *Two-dimensional spectra*

Whilst scalar couplings are readily identified in two-dimensional spectra, their measurement from cross-peak multiplets poses special problems.

Kessler *et al.*[55] developed the Difference and Sums of Traces within Cosy Spectra (DISCO) technique for the extraction of couplings from the cross-peaks of two-dimensional (COSY) spectra. This post-processing technique combined selected cross-sections of these peaks in order to extract the 'active coupling', i.e., J_{AB} from the cross-peak of A and B. After such combination, the active coupling was the separation of the in-phase and anti-phase DISCO peaks. DISCO requires accurate scaling of the constituent spectra and resolved cross-peaks. An alternative and simpler method for the accurate measurement of vicinal couplings from COSY spectra has been presented by Kim and Prestergard.[56]

4. SPECTRAL PREDICTION

Prediction of a spectrum corresponding to a postulated structure is a key element in structural confirmation or elucidation.

4.1. ^{13}C chemical shifts

4.1.1. Ab initio *calculations*

Ab initio calculations have been employed by Schindler and Kutzelnigg,[57] Gauss[58] and Cheesman *et al.*[59] This method suffers from the obvious disadvantage of requiring large amounts of computation (although this problem reduces with time) and that the quality of the results depend on the basis set chosen. Less obvious is the requirement of a reliable 3D structure, which could also come from *ab initio* calculations (an element of tautology may be involved here) or molecular mechanics calculations. Where mobility is possible, because the calculations are non-linear, the weighted average of the chemical shifts for each conformer would need to be calculated rather than the chemical shifts of the weighted average conformer: this certainly constitutes a lot of computation. Conformer energies will be for the gaseous state and less applicable for polar molecules in polar solvents, reducing the reliability of the calculation. The irony is that in ^{13}C, it is the through-bond interactions that dominate, most of which can be derived from a two-dimensional structure. The advantage of the *ab initio* approach however, is that it is not dependent on precedent and is applicable to areas of novel chemistry.

4.1.2. *Additivity rules*

At the opposite extreme of complexity, is the application of additivity rules or substituent chemical shifts (SCS). Here, the replacement of a hydrogen by another atom or group, results in a chemical shift difference at various positions relative to that substituent. When calculating the chemical shift of a given nucleus in a given molecule, all relevant SCS are added. This is a simple approach and can work quite well in molecules with low levels of substitution. However, steric interactions and large electronegativity differences coupled with finite polarizability ensure that SCS are non-additive in the case of multiple substitution. The earliest compilations of such ^{13}C chemical shifts were for paraffins[60] and *n*- and *iso*-alkanes[61] branched alkanes,[62] cyclohexanes,[63] other saturated rings,[64] alcohols,[65] amines[66] and halogen-substituted compounds.[67] The range of applicability increased significantly when the SCS approach was extended to benzene rings.[68] Further publications have rendered SCS more general.[69,70] Two comprehensive compilations of ^{13}C chemical shifts have been published in book form.[71,72]

In large molecules, manual addition of all the SCS can be tedious and a computer programme was soon developed in order to do this automatically[73] and others followed.[74,75]

4.1.3. *Database approaches*

A much more common and probably more successful approach to the prediction of ^{13}C shifts are those derived from databases. Here, a database manager searches a database of structures for those containing sub-structures within the postulated structure. The key elements necessary for this approach are:

- A validated database of compounds and associated chemical shifts. Experience shows significant levels of inaccuracy (both in structure and assignment) even in published data.
- A comprehensive database (either through diversity or through direct relevance to the intended chemistry areas). An exact match of sub-structure is much more likely to yield a satisfactory result.
- A good algorithm for the identification of similar sub-structures.
- Where sub-structure matches do not exist, a reasonable interpolation procedure.

Some builders of such databases (usually vendors) run periodic 'cleaning' procedures, i.e., use the database and manager to calculate each of the spectra in the database. Provided the sub-structures of each target molecule are well represented within the database and derive from different sources, this is a good check for self-consistency. If the sub-structures of each target molecule are not well represented, self-consistency may imply self-consistent and wrong. Accordingly, such cleaning procedures should be used with discretion. Indeed, it is relatively common to use the database to lead the assignment of the spectra of novel compounds, which are similar to existing compounds within the database. This is only satisfactory as long as the existing compounds were confirmed by orthogonal analytical techniques and assignments made unambiguous by a sufficiency of more sophisticated NMR techniques. If this is not the case, errors are simply perpetuated.

Bremser was the first person to assemble significant sized ^{13}C spectral and structure databases. In order to encode structures and sub-structures and search for similarity, Bremser developed the Hierarchically Ordered Spherical description of Environment (HOSE) codes.[76] HOSE codes give a description code for each molecular skeleton atom, out to three or four coordination spheres. Within each sphere, priority is given to atoms bearing more substituents. There are different codes for different atoms and types of atom, e.g., *C is a ring carbon, O is an oxygen, X is chlorine and Y is bromine. The code appears as a string and '/' is a coordination sphere separator. HOSE makes use of a derivative of Hierarchically Ordered Ring Description (HORD), which is a ring-centric descriptor for rings of less than ten members

(essentially a shorthand). HOSE was designed to make computer searching as efficient as possible, essential in the days it was crafted, but still ensures databases of increasing size can still be searched efficiently. It is worth noting that HOSE was designed with ^{13}C chemical shifts in mind: more substituents mean larger perturbation of the ^{13}C chemical shift, hence these atoms receive higher priority. HOSE has been used in other applications, e.g., physical properties[77] but its success in other such applications (or indeed in ^{1}H chemical shift prediction) should be regarded as fortunate.

Bremser *et al*. combined this sub-structure handling with BASF's database (65,000 spectra) to produce the Automatic Computer Correlation and Evaluation of Spectra based on Sub-structures (ACCESS) programme.[78] ACCESS later evolved into SpecInfo.[79] Both these programmes attempted to assemble a postulated structure from the constituent sub-structures. SpecInfo was later commercialized and most users (the author included) found the spectral prediction extremely useful in the assignment of spectra, but the generation of postulate structures from spectra of complete unknowns, less useful. At the point of commercialization, SpecInfo seems to have evolved along two paths, first with Chemical Concepts GmbH[80–82] and second, with the originating group at BASF. A similar approach was adopted by Advanced Chemistry Development Inc. with their programme CNMR,[77] Bio-Rad/Sadtler with CSEARCH,[83,84] PredictIt NMR from Cambridge Soft Co.[85] and SpecEdit.[86] A critical difference between these various programmes is the manner in which they handle sub-structures not wholly represented within the associated database. Unfortunately these interpolation procedures are both variable in reliability and remain unpublished.

4.1.4. *Neural networks*

The remaining approach to ^{13}C chemical shift prediction is neural networks (see Ref. 87 for a general introduction to neural networks). Neural networks offer a formal method of parameterizing a multi-dimensional problem. For example, in the case of ^{13}C chemical shift prediction, each substituent (class) has a contribution assigned to it. Each occurrence of this class within the training data set is a neuron and the 'training' of the neural network is essentially the establishment of the optimal value for each and every class. The main advantage of this approach over the simpler SCS one, is that contributions need not be combined linearly. The advantage over the database approach, is that the database is only employed during training and not for subsequent predictions, giving rise to a substantial increase in speed. The definition of classes and how they are combined, e.g., feed-back, feed-forward, are fairly arbitrary. In principle, provided sufficient neurons are present, issues such as multiple substitution are accommodated, but in practice, the number is usually truncated for computational reasons, or perhaps more importantly since computation advances inexorably, by insufficient experimental data. One problem using neural networks (although this need not be the case in principle)

is the separation of the training and use. If a dubious prediction is generated, it is more difficult to scrutinize the structures and assignments on which it was indirectly based. Neural networks have been used to predict ^{13}C chemical shifts in substituted benzenes,[88,89] saturated hydrocarbons,[90] alkanes,[91,92] substituted naphthalenes[93] and acyclic alkenes.[94] Meiler *et al*. published predictions for a more generic set of compounds,[95] this work containing a more detailed description of the derivation of classes/descriptors, and they have recently made a comparison of the neural network approach to the calculation of ^{13}C chemical shifts with other approaches described within this document.[96] The main conclusion was that the r.m.s. error for SCS approaches was in excess of 3 ppm whereas database and neural network approaches both achieved an r.m.s. of approximately 1.5 ppm. These results are a little trite: the database approach yields much better results if the test molecules are similar to compounds resident in the database and the neural network approach yields better results the narrower the diversity of compounds used for training and for subsequent test. Le Bret has also employed neural nets to predict ^{13}C chemical shifts amongst a wide range of compounds[97] and the programme has been commercialized as NMRPred. Le Bret claims ± 2.4 ppm error within the training set and ± 4.5 ppm amongst the test data set.

4.2. ^{1}H chemical shifts

^{13}C chemical shift prediction is much better established than ^{1}H prediction. This is in part a consequence of ^{13}C spectra typically being proton decoupled, whence they comprise a collection of single peaks corresponding to each ^{13}C nucleus. Data analysis is trivial: a competent peak-picking algorithm, which will either invoke an intensity threshold (itself a ratio of the most intense peak, preferably ignoring solvent) or require peaks to be more than a given ratio of the baseline noise. This will in turn yield a table of positions and intensities which can be readily submitted to a database, used in the development of SCS, or used to train a neural network.

However, the necessity of the analysis of multiplet structure is not the only complication in ^{1}H chemical shift prediction. All the factors giving rise to a ^{13}C chemical shift are operative for ^{1}H, but the through-space interactions which are difficult to predict, are no longer diluted by the readily predicted through-bond interactions typically 20 times their size (as in ^{13}C). Instead, the through-space interactions are of a similar size to the through-bond interactions. This poses a significant challenge.

4.2.1. *Additivity rules*

Again, collections of ^{1}H shifts exist which can be searched manually e.g., methine[98] and methylenes.[99] More usefully, proton chemical shifts have also been the subject of SCS or additivity rules. Prestsch and co-workers devised

a set of proton SCS[100,101] and a computer programme within which they were implemented. They subsequently extended their generality.[102] This methodology was subsequently commercialized as ChemDraw Ultra[103] and SpecTool[104,105] claiming an r.m.s. within the test data set of ± 0.18 ppm and anticipating ± 0.3 ppm more generally. Consistent with assertions in previous paragraphs, planar molecules, e.g., benzenes, with low levels of substitution are well treated.

4.2.2. *Database approaches*

Advanced Chemistry Development Inc.[77] has built a sizeable proton chemical shift database derived from published spectra (most commonly in $CDCl_3$ solution). Their H NMR predictor programme accesses this database and allows the prediction of ^1H chemical shifts. Whilst this software takes account of geometry in calculating scalar couplings, in predicting chemical shifts it essentially treats the structure as planar. It would therefore seem doomed to failure. However, if closely related compounds, run at infinite dilution and in the same solvent, are present in the database, the conformation is implied and the results can be quite accurate. Of course, the results will not be reliable if sub-structures are not well represented within the database and the wide dispersion of errors (dependent on whether a compound is represented or not) can cause serious problems in structure confirmation (later). ACD are currently revising their strict adherence to HOSE codes for sub-structure identification[106] and this will hopefully remove infrequent odd sub-structure selections made currently.

Using databases or tables of SCS to predict proton chemical shifts, only 'through-bond' effects are effectively considered, and a typical r.m.s. difference between calculated and experimental shifts is 0.3 ppm.[107] This is a lower value than for ^{13}C shifts, but this is a much higher proportion of the chemical shift range (3 vs. 0.75%).

4.2.3. *Molecular mechanics approaches*

Ideally, a successful approach is one which (a) additionally consider 'through-space' interactions, necessitating reliable three-dimensional structures; (b) produces a reasonably tight normal error distribution (with no significant outliers); (c) makes a reasonable attempt at novel compounds not represented within the database. The last point is important: it is the business of most chemical research organizations to produce novel compounds! Abraham *et al.* have developed a scheme based on 'nuclear' partial charges. The partial charges calculated by other approaches are designed to reproduce dipole moments and bonding-related effects and will thus be heavily weighted towards peripheral electron density. The effect of the circulation of electrons in generating magnetic fields, which perturb chemical shift, will most likely be related to r^{-3} and hence be heavily weighted towards electron density close to the nucleus. This charge is calculated by redistributing charge between

neighbouring atoms based on their electronegativity (times a constant) and between the second and third atoms from a given atom, based on the electronegativity of the considered atom and the polarizability of the second and third atoms. In principle the polarizability could in turn depend on the partial charge on the atom, necessitating that the partial charges within the molecule be calculated in an iterative fashion, but thus far this level of sophistication has proved to be unnecessary. Abraham *et al.* have added steric or van der Waals interactions, electric field effects and bond anisotropy and achieved an r.m.s. difference of 0.1 ppm for the classes of compounds they have considered and parameterized: hydrocarbons,[108,109] haloalkanes,[110] ethers,[111] ketones[112] and aromatic compounds.[113,114] Abraham has also reviewed this work.[115] Whilst this molecular mechanics approach can achieve high levels of accuracy, it is not wholly general and requires an accurate three-dimensional structure. Where the molecule is rigid, this does not pose insuperable problems, but where mobility is present, a reliable calculation of conformer energies in solution is required, along with chemical shift calculations for all the major conformers. The predicted shifts are then the weight averaged shifts from each conformation, not the chemical shifts calculated for the average conformer. At present, the various effects have been parameterized for $CDCl_3$ solvent, but work is currently underway to produce corresponding chemical shifts in d_6-DMSO.

5. CONFIRMATION OF STRUCTURE

The confirmation or refuting of a structure require that there is a chemical structure postulate. Any such decision is subject to errors, in particular those imposed by chemical shift prediction errors. A more robust decision can be made if the spectrum is not only compared against the postulate (where it exists) but also a series of closely related compounds. Such a list is most likely to originate from chemical diversity software or prior chemical knowledge.

Statistical analysis[116] has demonstrated that the demands placed upon the reliability of the chemical shift predictions intrinsic in this automated confirmation of structure, are greater if predicted and experimental stoichiometries cannot be compared. Furthermore, it is inevitable that high throughput environments will not yield pure compounds and the reliable identification of impurities (identified as fractional stoichiometry) will be key.

NMR has been used extensively to quantify the main component of a mixture relative to an internal standard, or the level of individual impurities after their explicit identification. The main application area is that of impurities in drugs, and this has been reviewed by Szántay and Demeter.[117] The reliability

and sources of error in the use of an internal standard have also been investigated.[118,119]

Experienced spectroscopists do not require accurate and fully quantitative integrals in establishing identity. Instead, prior knowledge of the chemistry, the appearance of multiplets, the chemical shifts, etc. mean that integrals often do little more than confirm the assignment of *t*-butyl, *i*-propyl, methyl, methylene and methine. This process of diminishing the importance of accurate integrals is of course that of interpretation. However, the objective in a high throughput environment is to provide as much information as possible from ^{1}H NMR spectra, in order to allow the automatic confirmation (or otherwise) of postulated structures, not the automation of interpretation, *per se*. Since interpretation cannot take place, increased demands are placed on the accuracy of the information that is extracted.

Whilst the two main inputs to a decision on confirming a chemical structure postulate have already been discussed, i.e., the extraction of key NMR parameters from the experimental spectrum and the prediction of a spectrum of the postulate, the mechanism by which the decision could be made, remains. The most desirable output from such a decision would be a percentage confidence that the postulated structure is in fact correct. The decision is a narrower one than complete structural elucidation, i.e., 'given a spectrum, what is the structure?' and a wider one than the MPS (later) one addressed by AutoDROP, viz 'given a spectrum and a structure, how certain can we be that they correspond'. A key question from the high throughput stand point, is whether this decision is approachable by ^{1}H alone.

In general, the criterion employed in judging whether the experimental and predicted shifts match, is either a constant tolerance, or unpublished. Lebedev however, has published his 'groups' concept in his work on comparisons against a spectral database.[120]

Before examining how this has been achieved automatically, it is worth examining how the spectroscopist might confirm a postulated structure manually. The following strategy is commonly employed:

- Do the number of observed protons correspond to the postulated structure? Provided this question can be answered unambiguously within the uncertainties imposed by labile protons and spectral quality, it can on its own refute an incorrect structure. In practice, this is not the spectroscopist's usual first step, most preferring to grapple with making chemical shifts and couplings fit.
- Do the chemical shifts fit? The reliability of these judgements should be no better than within an automated approach (since they both operate by precedent) although in practice the spectroscopist may be better at resolving conflicting precedents.
- Do the scalar couplings fit? The absolute size of the couplings is not the definitive information, rather the number of couplings and the

identification of coupling pairs. In rare cases, a coupling path can be found through the whole spectrum, and if the multiplicity at each position of the path corresponds to that predicted from the structure, the only ambiguity possible is symmetry of the coupling path about its centre. The probability of another structure having an identical coupling path is extremely rare, but because the coupling path can only fit the structure one way (two with symmetry) the observed chemical shifts can be assigned directly to atoms within the structure and in turn compared with their predicted chemical shifts. This considerably reduces the number of possibilities and if a molecule clears all these hurdles, it must surely be correct. In practice, non-proton bearing moieties can intervene and the spectrum will comprise more than one coupling group: a mechanism for the introduction of some ambiguity, which may require more sophisticated NMR experiments or other spectroscopic techniques to resolve.

A simple automated approach to structure confirmation should necessarily make use of the total number of protons, the chemical shifts and perhaps some coupling information. True assignment would require an order of magnitude increase in complexity in the methodology and the question is: what level of certainty can be achieved without assignment? In particular, how different do structures have to be in order to be differentiated?

Griffiths and Bright[121] proposed a method in which the experimental and predicted shifts were placed in chemical shift order and 'enumerated', i.e., a methyl shift occurred three times. The number of resulting chemical shift pairs closer than a prescribed window width was then determined: one side of a pair could be ignored enabling the remainder to shuffle up, but once a chemical shift was paired, it could not be used again. The window width was increased incrementally and the area above a curve of number of matching pairs against window width taken as the 'mismatch'.

The inclusion of the number of protons at each chemical shift proved to be key: the number of false positives increased 5–7 fold (depending on how diverse the set of test compounds were) if this parameter was excluded. Various refinements were tested, but the most successful was the 'J Filter' which disallowed a combination in which the number of couplings measured at a given chemical shift in the experimental spectrum was greater than in the predicted. This proved to be particularly valuable in the differentiation of isomers, where changes in the overall table of chemical shifts alone, could be quite subtle. The inconsistent appearance of labile protons in the experimental spectrum reduced the accuracy and it was asserted that where possible, they should be removed from both the experimental spectrum and the predicted spectrum. The mismatch level not only encoded the divergence of the experimental spectrum and the postulated structure, but also encoded

inaccuracies in spectral analysis (shown to be quite small) but also errors in prediction (shown to be quite large).

In the absence of an accurate determination of prediction errors, it was not possible to calculate a mismatch level specific to each compound, although a method was proposed by which it could if this situation were to change. Instead, a generic mismatch level needed to be adopted above which postulates were rejected and below which postulates were accepted. The problem in this situation is the large variation in prediction accuracy, e.g., two similar postulates of which only one is truly correct, but whose common parts are well predicted, will both yield a mismatch below a generic threshold. A mismatch criterion specific to each postulate, would be a pre-requisite for a calculation of the probability that the postulate was indeed correct.

6. REQUIREMENTS OF MULTIPLE PARALLEL SYNTHESIS OR COMBINATORIAL CHEMISTRY

Multiple Parallel Synthesis (MPS) is typically carried out in a plate containing a matrix of 8×12 wells. It is typical for each well to contain a different combination of reactants (say an acid and an amine). Since the number of outcomes is then restricted (to say 96 amides) it could reasonably be argued that a full analysis of individual spectra need not take place in order to validate the plate for further work. Indeed, it may well be that the plate is destined for high throughput (biological activity) screening, and only hits from that process would then warrant a more rigorous approach.

Within the sample-limited, fast-throughput MPS environment, the acquisition of two-dimensional NMR and/or ^{13}C will inevitably compromise throughput. For example, HSQC[122] offers a 32-fold increase in sensitivity[123] over pulse and collect ^{13}C acquisition, but this still constitutes 0.6% of ^{1}H receptivity. Whilst it can be argued that HSQC additionally offers signal to noise benefits in not having its intensity reduced by coupling and an additional set of ^{13}C shifts on which to base a decision, it can also be argued that this additional set of shifts are reasonably well correlated within the errors in prediction. Furthermore, the loss of coupling information and quantitation are significant shortcomings.

The confirmation of structure is essentially the same as that described in the previous section, but because of the systematic way in which the well contents are derived, other less demanding analysis tools may be appropriate. One approach is to utilize the spectra of the individual sub-structures. In Bruker's AutoDROP[124,125] (Automated Definition and Recognition Of spectral Patterns, contained within the AMIX suite of software[126]) these can derive from spectra (most commonly HSQC two-dimensional spectra) of the reactants or from a basis set of product spectra containing sufficient combinations. The process by which the spectra of the sub-structures are

identified appears to be a manual one. By using these sub-spectra, the presence of all sub-structures in each product can then be confirmed automatically. Bruker's AURELIA software[126] supplies the pattern recognition and position tolerance that are required to accommodate the small variations in position that occur as a result of changes in neighbouring sub-structures. However, the extent to which this variation can be accommodated is bounded and protons immediately adjacent to the point of reaction have to be excluded. The problem with this that these protons are the most informative and if anything untoward occurred in the chemistry, this would go undetected. However, within the context of the precision currently achievable in ^{1}H prediction, this shortcoming cannot be regarded as serious.

Another alternative approach was proposed by Kalelkar *et al.*[127] These authors acknowledged the reality that no current automated approach was 100% reliable and that some level of human intervention was going to be required. The purpose of the automation was therefore to confirm the majority of wells within an MPS plate, but more particularly, to identify the minority that required the scrutiny of an experienced spectroscopist. Their approach was not to attempt to analyse the individual spectra but using a Self Organising Map (SOM), to:

- Cluster the 96 NMR spectra according to similarities across rows and columns of the plate.
- Position these clusters on a two-dimensional graphical representation where nearness codes similarity.
- Identify outlier spectra within the rows or columns that do not conform to a 'parent pattern'.

7. STRUCTURAL ELUCIDATION

7.1. Introduction

The generation of a structure from spectroscopic data alone (a true 'unknown' where there is no proposed synthetic route nor an *a priori* postulated structure) is a much more significant problem. The amount of computation required is clearly much higher, but even in 2003 unless *ab initio* calculations are required, this does not constitute a significant constraint on how rapidly this can be achieved. However, the acquisition of the pre-requisite manifold spectroscopic data does constitute a significant constraint and it is less clear where the applications of such an approach lie. Whereas the automated confirmation of postulated structure can be done rapidly and frees experienced spectroscopists from a repetitive and tedious task, the generation of an unknown structure from various spectroscopic data is a challenge in which most experienced spectroscopists revel. More particularly, because the interactive manner in

which they would tackle the problem, a lot of the spectroscopic data acquired as a matter of routine for a fully automated approach, would prove redundant, and this significantly reduces the time taken to obtain a solution in the manual approach. Nonetheless, in laboratories where instruments are much easier to acquire than experienced spectroscopists (typical of an industrial environment), automatic identification of unknowns remains an attractive proposition. In any case, the automatic identification of unknowns is a fascinating intellectual challenge and is justifiable on those grounds alone. Automation of structural elucidation has been reviewed previously.[128–132]

The simplest approach to this problem is to search a database for an 'identical', i.e., similar within certain tolerances, spectrum. This was developed for Infrared spectra[133] (a technique ideally suited to such a 'fingerprinting' method). The method was enhanced to include a more sophisticated statistical approach when applied to ^{13}C NMR spectra.[134] In ^{13}C NMR spectra, variation in peak position due to concentration and temperature effects is larger than the peak width, and a more sophisticated approach is mandatory. In either case, the method is clearly one which yields limited or even confusing information for novel compounds.

7.2. DENDRAL

Automated structure elucidation *per se*, was first introduced by the DENDritic Algorithm for acyclic isomer generation (DENDRAL) – CONGEN. This programme filtered chemical groups into required 'goodlist' components and excluded 'badlist' components based on various spectroscopic techniques, but initially considerable emphasis was based on EI mass spectrometry. The more limited the experimental data, the more postulates that will satisfactorily explain the experimental data. There is a tendency in a manual approach, to run with the first postulate that is consistent with the experimental data. The key attribute of the DENDRAL approach was in the exhaustive nature of the chemical postulates. A correct interpretation can only be arrived at, when all reasonable postulates are generated and the experimental data refined (both in diversity and quality) until only one postulate from the original exhaustive list remains consistent with the experimental data. Indeed, for this postulate to be deemed correct rather than just unique, it should in principle, survive an infinite amount of experimental data scrutiny. In practice, DENDRAL achieved this by: (1) a 'planning' phase in which all possible sub-structures were inferred from the available spectral and chemical data; (2) a 'generation' phase in which these sub-structures were assembled in all combinations; and (3) a 'test' phase in which these structures were subject to closer scrutiny with respect to the spectroscopic data. For example, an NMR spectrum is not just a superposition of the spectra of sub-structures, it also depends on the order in which the sub-structures are

assembled, i.e., the chemical shifts of nuclei at the interface of the sub-structures are perturbed. By predicting an NMR spectrum for each complete structure and comparing with the observed spectrum, a great many combinations can be ruled-out. Similarly, the EI spectra of the day contained fragmentation information not shown by the more commonly used ESI mass spectrometry of today, further reducing the degrees of freedom.

Even for simple acyclic structures the number of postulates was extremely large.[135] The problem with this approach is that spectral prediction is a time consuming process and if the only filtration of postulates is within the 'test' phase where full spectral prediction takes place for every postulate, the process is extremely time consuming. The concept of inferred sub-structural constraints was therefore developed.[136] These were implemented through a simple analysis of mass spectra and a limited range of ^{1}H NMR spectra for aliphatic ketones[137,138] and aliphatic ethers.[139] In the case of ^{1}H NMR, a score is accumulated for each multiplet >0.3 ppm from a predicted chemical shift. The score is incremented by the integral size for that multiplet and added to the score derived for the mass spectrum. The lowest scoring postulated structure is deemed to be the correct one. In determining priorities for spectral acquisition, it should be borne in mind that the certainty of the result in this approach (or indeed all the other approaches to structure generation) is greater the more independent the experimental data, e.g., NMR vs. MS as opposed to one type of NMR experiment vs. another. However, if the data already exists, there is no harm in employing all available data no matter how much overlap there may be.

The DENDRAL project has been reviewed by Gray[140] and responded to by Feigenbaum and co-workers.[141]

7.3. CONGEN/GENOA

Subsequent work on the DENDRAL project sought to broaden its range of application, especially polycyclic sytems. A key part of this was an algorithm for the systematic generation of all isomers for a given molecular formula.[142] This algorithm was combined with a manual sub-structural constraint input in order to limit the postulate generation: the CONstrained GENerator (CONGEN) programme.[143] CONGEN was subsequently employed on various problems and in several laboratories.[144–147] Further enhancements to CONGEN allowing more flexibility in the handling of sub-structural constraints and sterioisomers, together with the enhancement of the 'test' phase of DENDRAL to incorporate ^{13}C NMR spectra,[148,149] were rolled together into the programme GENOA.[150,151] It should be noted however, that the sophistication added by CONGEN and GENOA in order to enhance generality, have increased the amount of manual intervention required. The

^{13}C prediction component of these programmes was subsequently developed into a spectral assignment aid.[152]

DENDRAL–CONGEN–GENOA refines postulated structures by generating all possibles and filtering qualitatively. An alternative approach to reducing the number of postulates is to allow the postulates to evolve. The 'genetic algorithm' is a stochastic (random) process, which assembles diatomic molecular fragments.[153] At each stage, the course which is subsequently followed is a statistical one based on arbitrary rules of acceptability and a weighting 'fitness' function.

7.4. CHEMICS

Sasaki and co-workers developed the Combined Handling of Elucidation Methods for Interpretable Chemical Structures (CHEMICS) programme.[154–156] They hypothesized that (within certain bounds of molecular size) one could postulate all possible structures (e.g., $C_{23}H_{48}$ can have 5,731,580) and then filter these spectroscopically. They recognized that this not a reasonable thing to do in practice, but concentrated instead on developing a set of non-overlapping sub-structural units from which all molecules could be built, but each of which could also be differentiated spectroscopically. 189 such fragments were required to build all C, H and O containing compounds and a further 572 were added to build N, halogen and S containing molecules (whether the latter was exhaustive was not stated). By rejecting the fragments for which no spectroscopic evidence could be found, the number of possible complete molecules was considerably reduced, i.e., through comparison of IR, ^{1}H NMR and ^{13}C spectra against tables of frequency or chemical shift range for each fragment. Significant further reductions were available if the molecular formula was known. This could in principle derive from high-resolution mass spectrometry, but CHEMICS was designed to yield this from an EI mass spectrum and a ^{13}C spectrum. First, the molecular ion was recognized by examining each ion to high mass and rejecting those with common fragment losses (i.e., 4–14, 21–25, 33, 37 and 38). Second, in order to differentiate any remaining ambiguity, all combinations of C, H, O, N, halogens and S reproducing these masses were examined (with due consideration to the nitrogen rule) and the ones with the minimum number of Cs required to explain the number of peaks in the ^{13}C spectrum retained. Last, the mass spectrometry isotope pattern of the putative molecular ion was compared with that predicted for each molecular formula. The final set of postulated structures was filtered by manual input of chemical probability, correspondence with the number of peaks in the ^{13}C NMR spectrum (chemical equivalence was derived from the structure rather than from peak intensity) and calculations of strain energy. The development of

CHEMICS up to that point (1983) was reviewed.[157] Of course, the problem with such a mass spectrometry-centric approach is that not all molecules are amenable to mass spectrometry.

Sasaki and co-workers subsequently added INADEQUATE data handling into the CHEMICS programme.[158] INADEQUATE[159–162] is a two-dimensional NMR method which yields cross-peaks corresponding to ^{13}C–^{13}C coupling. As such, it allows the full carbon skeleton (except where heteroatoms intervene) to be assembled. Because INADEQUATE relies on ^{13}C detection and because ^{13}C–^{13}C interactions are so dilute, it suffers from incredibly low sensitivity and cannot be regarded as a routine technique and certainly not applicable to high throughput situations. Fortunately it has been superseded by inverse detection techniques which indirectly yield similar information in a fraction of the time. However, Sasaki's inclusion of INADEQUATE information at the various stages of execution, including the early stages of sub-structure selection, illustrates an important point – the dramatic decrease in the number of possible solutions as a result of the inclusion of carbon connectivity information, e.g., in an isomer of thujopsene, a reduction from 4450 to 1. At first sight this may not be surprising, but it should be borne in mind that CHEMICS does not involve an assignment phase. The consequence of this is that ^{13}C–^{13}C correlations can only be ascribed to specific carbons where their chemical shift is unambiguous. Even with current levels of reliability in chemical shift prediction (before) this will be some way short of all carbons in the molecule. It is worth noting in passing, that unambiguous assignment can only come from more precise spectral prediction and it may well be that such precision would also allow all other postulates to be discounted without recourse to connectivity information. In either event, more precise spectral prediction is pivotal to reliable structural elucidation. Another change in CHEMICS at that stage, was the separation of sub-structures into primary, secondary and tertiary categories, each of which were handled differently.

CHEMICS was then changed to incorporate a ^{1}H spectrum filter.[163] An algorithm for the simplification of the experimental spectrum is described (solvent and low intensity signal removal, integral normalization and 4 Hz convolution). The chemical shifts were predicted via a procedure published previously[164,165] and the spectrum simulated using the LAOCOON3 quantum mechanical procedure.[166] The latter required that the molecule be split into segments, each of which contained no more than seven protons and the coupling constants came from lookup tables containing couplings for each standardized fragment. The simulated spectrum was then subject to the same simplification procedure as the experimental spectrum, before comparison by an algorithm described in some detail. The ^{1}H handling was also developed into stand-alone ^{1}H spectral assignment tool. CHEMICS was also augmented to incorporate NOE data[167] and COSY data.[168]

7.5. ASSEMBLE/CASE/SESAMI/COCOA

In 1981 Munk first described the ASSEMBLE constitution generator,[169,170] i.e., a builder of structures from sub-structures, as part of the Computer Assisted Structure Elucidation (CASE) structure elucidator. However, where such sub-structures can overlap, the number of complete structures is extremely large. He therefore instituted a method for the removal of forbidden bonds at an early stage in the building process.[171] A two-dimensional NMR interpretor was subsequently added.[172] By 1991 CASE had evolved into Systematic Elucidation of Structure Applying Machine Intelligence (SESAMI)[173] and ASSEMBLE had evolved into COCOA. The structure generator relied on a database of Atom Centred Fragments (ACFs) and the final filtering of a limited number of possibles was left to the experienced spectroscopist. It was later asserted that the concerted use of neural networks for ^{13}C NMR and infrared spectroscopy was more reliable than ^{13}C NMR alone.[174] Yuan and co-workers developed an analogous approach (CISOC-SES)[175,176] in which there was more emphasis on automation and the efficiency by which two-dimensional NMR spectra were utilized. They also put a considerable amount of effort into the most effective way of handling ambiguities in distance (number of bonds, rather than through-space) constraints.[177]

7.6. SpecInt

Pretsch published a strategy for combining ASSEMBLE with further filtration, i.e., the generation of 'good-list' containing fragments that are definitely in, and a 'bad-list' for those definitely out.[178] This work described the development of 82 rules for the extraction of good and bad lists. In an environment where all postulates are possible (true for most structure elucidators) it is only the 'bad-list' that provides effective filtration. In the following paper[179] Pretsch gives a detailed description of fragments for which 'good-list' and 'bad-list' rules were developed and details of a thorough test of these rules against 99,000 ^{13}C spectra, 8000 ^{1}H spectra and 32,000 IR spectra (although the rules themselves were implied). Particular emphasis was placed on the simultaneous (as opposed to sequential) use of the various spectroscopic techniques in the filtering process. The programme was named SpecInt and for compounds of mass <250, it was able to reduce the number of isomers to 3% of those defined by the molecular formula alone. ASSEMBLE 2.0 was recently described in some detail,[180] but it was left to the reader to work out what the changes from the original version were. SpecInt 2 was then published[181], the main change being the automatic interface between itself and the (now) ASSEMBLE 2.1 structure generator. The methods for incorporating spectral information are described in some detail, particularly the data reduction method for ^{1}H spectra.

It is clear that the multiplicities derived from DEPT90 and DEPT135 spectra play a key part in sub-structure filtering, particularly where they allow general constraints to become local constraints (i.e., assigned to a particular carbon).

SpecInt is designed to be conservative, i.e., to avoid ruling out an incorrect structure at all costs. Like CHEMICS and unlike a spectroscopist, its main power is in postulating *all* possibles. How it deviates from CHEMICS is in the complete separation of the generation and the test phases (although there are plans to make them more interactive). The consequence is that the spectroscopist is presented with a limited number of possibles. In a low throughput situation where an absolute solution is required, this is playing to each participant's strengths: the computer for postulating all possibles and filtering them, the spectroscopist for invoking any other relevant information, introducing assumptions and developing further incisive and discriminating experiments. In a high throughput situation, a unique solution, even if probabilistic, is what is required.

7.7. SpecSolv/MOLGEN

The BASF group who developed SpecInfo (above) also developed a structure elucidator SpecSolv.[182] SpecSolv differs from other structure elucidators in not requiring a molecular formula. SpecSolv utilizes ^{13}C spectral information including multiplicities from DEPT spectra. It works in a similar way to the other structure elucidators, but starts with a much larger database of sub-structures (100,000 for two-sphere HOSE codes and 400,000 for three-sphere HOSE codes). SpecSolv prevents the explosion of possibles by stringent verification at every stage of the process. Of course, the BASF group are well set up for this having a very reliable predictor in SpecInfo and a very large database (200,000 ^{13}C spectra). This again illustrates a very important point: if spectral prediction was sufficiently precise, only one possible would pass verification and only one spectrum would be needed. The number of approaches and the number of spectral data brought to bear on the problem of structure elucidation are in part, a reflection of the lack of precision in spectral prediction. More precision in prediction would bring more reliability in structure verification with less experimental effort and less complex computation. It is in spectral prediction that we desperately need more progress. Meiler and Will[183,184] used the Specinfo database as a training set for a neural network prediction of ^{13}C chemical shifts and combined this with the 'Genius' genetic algorithm for the generation of postulates. The r.m.s. difference between the experimental and predicted ^{13}C chemical shifts (each in chemical shift order) and molecular formula were necessary for reducing the postulates to a manageable quantity (one if a sufficiently stringent r.m.s. was specified). Interestingly, a Multiplicity Deviation Factor (MDF) was also

defined and employed. SpecInfo has also been combined with the structure generated MOLGEN,[185,186] but the result is an interactive rather than fully automated structure elucidator. Meiler[187] assessed the efficiency of MOLGEN and concluded that, provided the molecule contained a maximum of 12 non-hydrogen atoms, and that a neural network prediction of ^{13}C chemical shift was utilized, a unique solution could be found on every occasion with calculation times varying between under 1 min to just over 2 h.

7.8. Logic for structure determination/CASA

Nuzillard *et al*. proposed the Logic for Structure Determination (LSD)/CASA[188,189] approach in which HMQC[190–192] and HMBC[193,194] spectra were used to generate virtual C–C–C and HMQC and COSY[195–197] were used to generate C–C correlations. However, they also required the molecular formula from a combination of a ^{13}C spectrum and high resolution mass spectrometry and the carbon 'status' or co-ordination number from DEPT[198] spectra. Clearly, less correlations meant more postulates and the great challenge was assigning. The approach was extended by restricting postulates to exclude trans double bonds in rings of less than or equal to seven members[199] and this was successfully applied to Azadirchtin,[200] Clerodane Diterpenoids and an Ursane Triterpenoid,[201] Gibberellic acid[202] alkaloids with a novel diaza-adamantane skeleton,[203] Limonoid derivatives[204,205] and a tetranortriterpenoid.[206] The Constraint Satisfaction Problem: the manner in which molecular fragments were assembled and how the number of possible outcomes was restricted, was subsequently described in some detail.[207]

7.9. COCON

Köck and co-workers developed the COnstitutions from CONnectivities (COCON) programme,[208,209] and subsequently applied it to proton-poor heterocycles.[210] This programme employs COSY, HSQC, HMBC and 1,1-ADEQUATE[211,212] data as input. COCON employs the two-dimensional NMR information (which has to be extracted manually) in order to generate the fragments and filter their subsequent building. The use of COCON in the structural elucidation of marine natural products has also been reviewed.[213] COCON was subsequently enhanced[214] to incorporate ^{13}C filtering of sub-structures and neural network calculations (as opposed to database calculations) of postulate ^{13}C chemical shifts in order to considerably increase the rate of calculation. This paper is a particularly good leading reference for the use of neural networks in the analysis and prediction of NMR spectra.

7.10. ACD's Structure Elucidator

ACD's Structure Elucidator[215,216] requires ^{13}C or two-dimensional NMR input. ^{1}H, DEPT multiplicities, MS and IR data can also be utilized. It appears to work in a similar way to preceding structure elucidators. ACD also offers a facility to do database matching and hence 'Auto-Assignment' and 'Match Factor' tools in their Version 6 software. These, amongst other things, require the arbitrary weighting of chemical shift (r.m.s. difference between observed and predicted), multiplicity and numbers of nuclei. They also require an arbitrary definition of 'Shift Looseness' or error in prediction. Comparison of relative values of the Match Factor will undoubtedly prove useful, but the absolute value of the Match Factor cannot be regarded as reliable. The algorithms have not yet been published. ACD's Structure Elucidator has subsequently been applied to a complex alkaloid[217] and other natural products.[218]

7.11. CISOC-SES

Peng *et al*. developed the Computerized Information System for Organic Chemistry-Structure Elucidation Subsystem (CISOC-SES) programme.[219–223] This programme turns DQF-COSY and HMBC spectra into bond constraints. Then it turns ^{13}C DEPT spectra and the molecular formula into building blocks such as $–CH_3$ and $–CH_2–$. These are then assembled into as many complete structures as are compatible with the bond constraints. CISOC-SES is designed to be as compatible with 'real-world' spectra with their attendant ambiguities as possible. CISOC-SES is a result of collaborative work with Bodenhausen *et al*. who had previously tackled the problem independently.[224,225] CISOC-SES has since been commercialized as NMR-SAMS[226] by Spectrum Research, LLC.

7.12. DARC-EPIOS

Dubois *et al*. developed the Description, Acquisition, Retrieval, Computer-aided design-Elucidation by Progressive Intersection of Ordered Structures (DARC-EPIOS) system for structural elucidation.[227] Their approach was based on ^{13}C spectra. These were predicted using an additive method, but based on their DARC descriptor of environment, as opposed to the more common HOSE code. The EPIOS system was designed to take account of the diagnostic (or not) nature of the ^{13}C spectrum with respect to environment, i.e., depending on the specific sub-structures.

8. CONCLUSIONS

Much progress has been made in the automation of NMR spectral analysis and interpretation. This has resulted in a multitude of tools which aid spectroscopists in their endeavours. However, a theme present throughout is that in the initial stages simple and elegant algorithms can handle large portions of chemistry. Thereafter, what follows are the diminishing returns of more and more sophisticated algorithms handling less and less frequently occurring exceptions in the pursuit of complete generality. It is a matter of judgement as to how the work in developing these algorithms is justified when balanced against manual intervention in subsequent use. The only thing that is certain is that advances in computation, increases in magnetic field strength and spectroscopic techniques will move the balance point over time.

In developing spectral analysis (in the strictest sense) algorithms and software, it has become obvious that the analysis and interpretation stages are very interactive and that to separate them imposes enormous demands on the quality of data and its subsequent analysis. It may well be that further progress in this area may require a level of unification. Herein lies a challenge: these stages are usually developed by different people and in different organizations. This is no more so, than in the handling of prior chemical knowledge, synthetic route and postulating chemical diversity. The impact this could make in reducing the degrees of freedom in structural elucidation is enormous.

Structural elucidation, being the most complex problem, remains the most elusive. However, in 1997, Pretsch and co-workers stated in their informal but excellent review,[228] 'There is no system in sight, let alone presently available, that is able to surpass the experienced chemist in the interpretation task'. In that sense, not much has changed since.

REFERENCES

1. Bruker Biospin GmbH, Silberstreifen, D-76287, Rheinstetten/Karlsruhe, Germany.
2. *XWIN-NMR Software Manual, Part 1*, Bruker Analytik GmbH, 1997.
3. M. Spraul, M. Hofmann, M. Ackermann, A. W. Nicholls, S. J. P. Damment, J. N. Haselden, J. P. Shockcor, J. K. Nicholson and J. C. Lindon, *Anal. Comm. 11*, 1997, **34**, 339.
4. W. J. Haap, J. W. Metzger, C. Kempter and G. Jung, *Mol. Divers.*, 1997, **3**, 29.
5. R. A. Houghten, C. Pinilla, S. E. Blondelle, J. R. Appell, C. T. Dooley and J. H. Cuervo, *Nature*, 1991, **84**, 354.
6. R. A. Houghten and C. T. Dooley, *Bioorg. Med. Chem. Lett.*, 1993, **3**, 405.
7. J. M. Kerr, S. C. Banville and R. N. Zuckerman, *J. Am. Chem. Soc.*, 1993, **115**, 2529.
8. A. Heuer and U. Haeberlen, *J. Magn. Reson.*, 1989, **85**, 79.
9. D. Marion and A. Bax, *J. Magn. Reson.*, 1988, **83**, 205.
10. D. S. Stephenson and G. Binsch, *J. Magn. Reson.*, 1980, **37**, 409.
11. G. A. Pearson, *J. Magn. Reson.*, 1977, **27**, 265.

12. W. Dietrich, C. H. Rudel and M. Neumann, *J. Magn. Reson*., 1991, **91**, 1.
13. D. E. Brown, *J. Magn. Reson*., 1995, **A114**, 268.
14. C. Bartels, P. Güntert and K. Wüthrich, *J. Magn. Reson*., 1995, **A117**, 330.
15. S. Golotvin and A. Williams, *J. Magn. Reson*., 2000, **146**, 122.
16. J. C. Lindon and A. G. Ferrige, *Prog. NMR Spectrosc*., 1980, **14**, 27.
17. L. Griffiths and A. M. Irving, *Analyst*, 1998, **123**, 1061.
18. B. U. Meier, G. Bodenhausen and R. R. Ernst, *J. Magn. Reson*., 1984, **60**, 161.
19. S. Glaser and H. R. Kalbitzer, *J. Magn. Reson*., 1987, **74**, 450.
20. P. Pfändler, G. Bodenhausen, B. U. Meier and R. R. Ernst, *Anal. Chem*., 1985, **57**, 2510.
21. P. Pfändler and G. Bodenhausen, *Magn. Reson. Chem*., 1988, **26**, 888.
22. D. Jeannerat and G. Bodenhausen, *J. Magn. Reson*., 1999, **141**, 133.
23. R. Koradi, M. Billeter, M. Engeli, P. Güntert and K. Wüthrich, *J. Magn. Reson*., 1998, **135**, 288.
24. W. H. Press, B. P. Flannery, S. A. Teukolsky and W. T. Vetterling, *Numerical Recipes in C*, Cambridge University Press, Cambridge, UK, 1988.
25. T. Herrmann, P. Güntert and K. Wüthrich, *J. Biomol. NMR*, 2002, **24**, 171.
26. E. Holmes, P. J. D. Foxall, G. H. Neild, C. Bedell, B. C. Sweatman, E. Rahr, J. C. Lindon, M. Spraul and J. K. Nicholson, *Anal. Biochem*., 1994, **220**, 284.
27. W. P. Aue, E. Bartholdi and R. R. Ernst, *J. Chem. Phys*., 1976, **64**, 2229.
28. L. Griffiths, *Magn. Reson. Chem*., 2000, **38**, 444.
29. L. Griffiths, unpublished results.
30. T. R. Hoye, P. R. Hanson and J. R. Vyvyan, *J. Org. Chem*., 1994, **59**, 4096.
31. L. Griffiths, *Magn. Reson. Chem*., 2001, **39**, 194.
32. P. Diehl, S. Sykora and J. Vogt, *J. Magn. Reson*., 1975, **19**, 67.
33. P. Diehl and J. Vogt, *Org. Magn. Reson*., 1976, **8**, 638.
34. R. Laatikainen, *J. Magn. Reson*., 1991, **92**, 1.
35. R. Laatikainen, M. Niemitz, U. Weber, J. Sundelin, T. Hassinen and J. Vepsäläinen, *J. Magn. Reson*., 1996, **A120**, 1.
36. S. Golotvin, E. Vodopianov and A. Williams, *Magn. Reson. Chem*., 2002, **40**, 331.
37. J. Stonehouse and J. Keeler, *J. Magn. Reson*., 1995, **A112**, 43.
38. J. J. Titman and J. Keeler, *J. Magn. Reson*., 1990, **89**, 640.
39. S. Bourg and J.-M. Nuzillard, *J. Chim. Phys*., 1998, **95**, 187.
40. L. McIntyre and R. Freeman, *J. Magn. Reson*., 1992, **96**, 425.
41. J.-M. Le Parco, L. McIntyre and R. Freeman, *J. Magn. Reson*., 1992, **97**, 553.
42. M. J. Seddon, A. G. Ferrige, P. N. Sanderson and J. C. Lindon, *J. Magn. Reson*., 1996, **A119**, 191.
43. A. A. Bothner-By and S. M. Castellano, *Computer Programs for Chemistry*, Vol. 1, D. F. DeTar, ed., W.A. Benjamin, New York, 1968.
44. Quantum Chemistry Program Exchange Catalog, Indiana University Chemistry Department.
45. R. Laatikainen, *J. Magn. Reson*., 1977, **27**, 169.
46. R. Laatikainen, *Magn. Reson. Chem*., 1986, **24**, 588.
47. T. Schaefer and R. Laatikainen, *Can. J. Chem*., 1983, **61**, 224.
48. R. Laatikainen, *J. Magn. Reson*., 1988, **78**, 127.
49. R. Laatikainen, J. Ratilainen, R. Sebastian and H. Santa, *J. Am. Chem. Soc*., 1995, **117**, 11006.
50. D. S. Stephenson and G. Binsch, *J. Magn. Reson*., 1980, **37**, 395.
51. J. Heinzer, *J. Magn. Reson*., 1977, **26**, 301.
52. R. Laatikainen, M. Niemitz, J.-P. Sundelin and T. Hassinen, PERCH Software, distributed by PERCH Project, Department of Chemistry, University of Kuopio, Kuopio, Finland, 1996.
53. E. Kolehmainen, K. Laihia, R. Laatikainen, J. Vepsäläinen, M. Niemitz and R. Suontamo, *Magn. Reson. Chem*., 1997, **35**, 463.
54. M. Niemitz, J. Vepsalainen, T. Hassinen, P. Samuli and R. Laatikainen, Abstract: 41st Experimental NMR Conference, Asilomar, 2000.
55. H. Kessler, A. Muller and H. Oschkinat, *Magn. Reson. Chem*., 1985, **23**(10), 844.

56. Y. Kim and J. H. Prestergard, *J. Magn. Reson.*, 1989, **84**, 9.
57. M. Schindler and W. Kutzelnigg, *J. Chem. Phys.*, 1982, **76**, 1919.
58. J. Gauss, *Beri. Busenges. Phys. Chem.*, 1995, **99**, 1001.
59. J. R. Cheesman, G. W. Trucks, T. A. Keith and M. J. Frisch, *J. Chem. Phys.*, 1996, **104**, 5497.
60. D. M. Grant and E. G. Paul, *J. Am. Chem. Soc.*, 1964, **86**, 2984.
61. L. P. Lindeman and J. Q. Adams, *Anal. Chem.*, 1971, **43**, 1245.
62. C. J. Carman, A. R. Tarpley and J. H. Goldstein, *Macromolecules*, 1973, **6**, 719.
63. D. K. Dalling and D. M. Grant, *J. Am. Chem. Soc.*, 1972, **94**, 6612.
64. F. G. Morin and D. M. Grant, *Conformational Analysis of Cyclohexanes, Cyclohexadienes and Related Hydroaromatic Compounds*, P. W. Rabideau, ed., VCH, Weinheim, 1989.
65. J. D. Roberts, F. J. Weigert, J. I. Kroschwitz and H. J. Reich, *J. Am. Chem. Soc.*, 1970, **92**, 1338.
66. H. Eggert and C. Djerassi, *J. Am. Chem. Soc.*, 1973, **95**, 3710.
67. G. R. Somayajulu, R. Kennedy, T. M. Vickrey and B. J. Zwolinski, *J. Magn. Reson.*, 1979, **33**, 559.
68. D. F. Ewing, *Org. Magn. Reson.*, 1979, **12**, 499.
69. A. Fürst, W. Robien and E. Pretsch, *Anal. Chim. Acta*, 1990, **233**, 213.
70. E. Pretsch, A. Fuerst and W. Robien, *Anal. Chim. Acta*, 1991, **248**(2), 415.
71. J. B. Stothers, *Carbon-13 NMR Spectroscopy*, Organic Chemistry Monograph Vol. 24, Academic Press, New York, 1972.
72. H.-O. Kalinowski, S. Berger and S. Braun, *Carbon-13 NMR Spectroscopy*, John Wiley & Sons, Chichester, 1988.
73. J.-T. Clerc and H. Sommerauer, *Anal. Chim. Acta*, 1977, **95**, 33.
74. A. Fürst and E. Pretsch, *Anal. Chim. Acta*, 1990, **229**(1), 17.
75. E. Pretsch, A. Fürst, M. Badertscher, R. Buergin and M. E. Munk, *J. Chem. Inf. Comput. Sci.*, 1992, **32**(4), 291.
76. W. Bremser, *Anal. Chim. Acta*, 1978, **103**, 355.
77. Advanced Chemistry Development Inc., 90 Adelaide Street W., Suite 702, Toronto, Ontario, Canada, M5H 3V9.
78. W. Bremser and W. Fachinger, *Magn. Reson. Chem.*, 1985, **23**, 1056.
79. W. Bremser, *Angew. Chem. Int. Ed. Engl.*, 1988, **27**, 247.
80. Chemical Concepts, Boschstrasse 12, D-69469 Weinheim, Germany.
81. Creon Lab Control, Europa-Allée, 27-29, D-50226, Frechen, Germany.
82. R. Neudert and M. Penk, *J. Chem. Inf. Comput. Sci.*, 1996, **36**, 244.
83. CSEARCH/HaveItAll™ NMR, Bio-Rad Laboratories, Informatics/Sadtler Group, 3316 Spring Garden Street, Philadelphia, PA 19104-2596, USA.
84. H. Kalchhauser and W. Robien, *J. Chem. Inf. Comput. Sci.*, 1985, **25**, 102.
85. Cambridge Soft Corporation, CS Chemdraw PRO 4.5, 1985–1997.
86. W. Maier, *Computer-Enhanced Analytical Spectroscopy*, C. L. Wilkens, ed., Plenum Press, London, 1993, 37–55.
87. J. Zupan and J. Gasteiger, *Neural Networks in Chemistry and Drug Design*, Wiley-VCH, Weinheim, 1993.
88. V. Kvasnicka, S. Sklenak and J. Pospichal, *J. Chem. Inf. Comput. Sci.*, 1992, **32**, 742.
89. J. Meiler, R. Meusinger and M. Will, *Monatsch. Chem.*, 1999, **130**(9), 1089.
90. O. Ivanciuc, *Rev. Roum. Chim.*, 1995, **40**, 1093.
91. D. Svozil, J. Pospichal and V. Kvasnicka, *J. Chem. Inf. Comput. Sci.*, 1995, **35**, 924.
92. Z. Li, Y. Hunag, F. Hu, Q. Sheng and S. Peng, *Bopuxue Zazhi*, 1997, **14**, 507.
93. S. Thomas and E. Kleinpeter, *J. Prakt. Chem. Chem.-Ztg.*, 1995, **337**, 504.
94. O. Ivanciuc, J. P. Rabine, D. Cabrol-Bass, A. Panaye and J.-P. Doucet, *J. Chem. Inf. Comput. Sci.*, 1996, **36**, 644.
95. J. Meiler, R. Meusinger and M. Will, *J. Chem. Inf. Comput. Sci.*, 2000, **40**(5), 1169.
96. J. Meiler, W. Maier, M. Will and R. Meusinger, *J. Magn. Reson.*, 2002, **157**, 242.

97. C. Le Bret, *SAR QSAR Environ. Res.*, 2000, **11**, 211.
98. H. M. Bell, D. B. Bowles and F. Senese, *Org. Magn. Reson.*, 1981, **16**, 285.
99. H. M. Bell, L. K. Berry and E. A. Madigan, *Org. Magn. Reson.*, 1984, **22**, 693.
100. R. Bürgin-Schaller, C. Arnold and E. Pretsch, *Anal. Chim. Acta*, 1994, **290**(3), 295.
101. R. Bürgin-Schaller, M. Junghans, H. Schriber, T. Kocsis, M. Badertscher, E. Pretsch and M. E. Munk, *Software Development in Chemistry 9; Proceedings of the 9th Workshop 'Computer in Chemistry'*, Bitterfield, 1994.
102. R. Bürgin-Schaller, C. Arnold and E. Pretsch, *Anal. Chim. Acta*, 1995, **312**(1), 95.
103. Cambridge-Soft Corporation, Cambridge, MA, USA.
104. R. Bürgin-Schaller, M. E. Munk and E. Pretsch, *J. Chem. Inf. Comput. Sci.*, 1996, **36**, 239.
105. SpecTool, Chemical Concepts GmbH, Weinheim, Germany.
106. A. Williams, private communication.
107. R. B. Schaller, C. Arnold and E. Pretsch, *Anal. Chim. Acta*, 1995, **312**, 95.
108. R. J. Abraham, L. Griffiths and M. A. Warne, *J. Chem. Soc., Perkins Trans.*, 1997, **2**, 31.
109. R. J. Abraham, M. A. Warne and L. Griffiths, *Magn. Reson. Chem.*, 1998, **36**, S179.
110. R. J. Abraham, L. Griffiths and M. A. Warne, *J. Chem. Soc., Perkins Trans. 2*, 1997, 881.
111. R. J. Abraham, L. Griffiths and M. A. Warne, *J. Chem. Soc., Perkins Trans. 2*, 1998, 1751.
112. R. J. Abraham and N. Ainger, *J. Chem. Soc., Perkins Trans. 2*, 1999, 441.
113. R. J. Abraham, M. Canton, M. Reid and L. Griffiths, *J. Chem. Soc., Perkins Trans. 2*, 2000, 803.
114. R. J. Abraham and P. E. Smith, *J. Comput. Chem.*, 1987, **9**, 288.
115. R. J. Abraham, *Prog. Nucl. Magn. Reson. Spectrosc.*, 1999, **35**, 85.
116. L. Griffiths and P. R. Ceuppens, unpublished results.
117. C. Szántay and Á. Demeter, *Identification and Determination of Impurities in Drugs*, S. Görög, ed., Elsevier, Oxford, 2000, 109–145.
118. L. Griffiths and A. M. Irving, *Analyst*, 1998, **123**, 1061.
119. J. K. Kwakye, *Talanta*, 1985, **32**, 1069.
120. I. I. Strokov and K. S. Lebedev, *J. Chem. Inf. Comput. Sci.*, 1999, **39**, 659.
121. L. Griffiths and J. D. Bright, *Magn. Reson. Chem.*, 2002, **40**, 623.
122. A. Bax, M. Ikura, L. E. Kay, D. E. Torchia and R. Tschudin, *J. Magn. Reson.*, 1990, **86**, 304.
123. R. Freeman, *A Handbook of Nuclear Magnetic Resonance*, Addison Wesley Longman, Harlow, 1987, 183.
124. K.-P. Neidig and H. Schröder, *Bruker Rep.*, 1999, **147**, 18.
125. H. Schröder, P. Neidig and G. Rossé, *Angewandte Chemie Int. Edition*, 2000, **39**, 3816.
126. AMIX; AURELIA; AutoDROP; Bruker Biospin Gmbh, Silberstreifen, D-76287 Rheinstetten, Germany.
127. S. Kalelkar, E. R. Dow, J. Grimes, M. Clapham and H. Hu, *J. Comb. Chem.*, 2002, **4**, 622.
128. N. A. B. Gray, *Computer-Assisted Structure Elucidation*, Wiley, New York, 1986.
129. D. H. Smith, ed., *Computer-Assisted Structure Elucidation, ACS Symposium Series*, American Chemical Society, Washington DC, 1977.
130. C. Peng, S. Yuan, C. Zheng and L. Chen, *Computers and Applied Chemistry. Computer Chemistry Monograph Series 4*, Science Press, Beijing, 1995, 26.
131. M. Jaspars, *Nat. Prod. Rep.*, 1999, **16**, 241.
132. A. Williams, *Curr. Opin. Drug Dis. Dev.*, 2000, **3**, 298.
133. J. Zupan and M. E. Munk, *Anal. Chem.*, 1985, **57**, 1609.
134. H. B. Woodruff, C. R. Snelling, C. A. Shelley and M. E. Munk, *Anal. Chem.*, 1977, **49**, 2075.
135. J. Lederberg, G. L. Sutherland, B. G. Buchanan, E. A. Feigenbaum, A. V. Robertson, A. M. Duffield and C. Djerassi, *J. Am. Chem. Soc.*, 1969, **91**, 2973.
136. B. G. Buchanan, G. L. Sutherland and E. A. Feigenbaum, *Machine Intelligence*, Vol. 4, B. Meltzer and D. Michie, eds., Edinburgh University Press, Edinburgh, 1969, 209.
137. A. M. Duffield, A. V. Robertson, C. Djerassi, B. G. Buchanan, G. L. Sutherland, E. A. Feigenbaum and J. Lederberg, *J. Am. Chem. Soc.*, 1969, **91**, 2977.

138. J. Lederberg, G. L. Sutherland, B. G. Buchanan, E. A. Feigenbaum, A. V. Robertson, A. M. Duffield and C. Djerassi, *J. Am. Chem. Soc.*, 1969, **91**, 2973.
139. G. Schroll, A. M. Duffield, C. Djerassi, B. G. Buchanan, G. L. Sutherland, E. A. Feigenbaum and J. Lederberg, *J. Am. Chem. Soc.*, 1969, **91**, 7440.
140. N. A. B. Gray, *Chemometrics and Intelligent Laboratory Systems*, 1988, **5**, 11.
141. B. G. Buchanan, E. A. Feigenbaum and J. Lederberg, *Chemometrics and Intelligent Laboratory Systems*, 1998, **5**, 33.
142. L. M. Masinter, N. S. Sridharan, J. Lederberg and D. H. Smith, *J. Am. Chem. Soc.*, 1974, **96**, 7702.
143. R. E. Carhart, D. H. Smith, H. Brown and C. Djerassi, *J. Am. Chem. Soc.*, 1975, **97**, 5755.
144. C. J. Cheer, D. H. Smith, C. Djerassi, B. Tursch, J. C. Beckman and D. Daloze, *Tetrahedron*, 1976, **32**, 1807.
145. M. J. Goldstein, Y. Nomura, Y. Takeuchi and S. Tomoda, *J. Am. Chem. Soc.*, 1978, **100**, 4899.
146. D. J. Vanderah, N. Rutledge, F. J. Schmitz and L. S. Ciereszko, *J. Org. Chem.*, 1978, **43**, 1614.
147. D. E. Dorman, *Abstracts of the 178th National Meeting of the American Chemical Society*, Washington, DC, September 9–14, 1979, Computers in Chemistry Division, papers 52 and 58.
148. N. A. B. Gray, C. W. Crandell, J. G. Nourse, D. H. Smith, M. L. Dageforde and C. Djerassi, *J. Org. Chem.*, 1981, **46**, 703.
149. N. A. B. Gray, J. G. Nourse, C. W. Crandell, D. H. Smith and C. Djerassi, *Org. Magn. Reson.*, 1981, **15**, 375.
150. R. E. Carhart, D. H. Smith, N. A. B. Gray, J. G. Nourse and C. Djerassi, *J. Org. Chem.*, 1981, **46**, 1708.
151. D. H. Smith, N. A. B. Gray, J. G. Nourse and C. W. Crandell, *Anal. Chim. Acta*, 1981, **133**, 471.
152. M. R. Lindley, N. A. B. Gray, D. H. Smith and C. Djerassi, *J. Org. Chem.*, 1982, **47**, 1027.
153. C. Le Bret, *J. Chem. Inf. Comput. Sci.*, 1996, **36**, 678.
154. S. Sasaki, Y. Kudo, S. Ochiai and H. Abe, *Mikrochimica Acta*, 1971, 726.
155. T. Yamasaki, H. Abe, Y. Kudo and S. Sasaki, ACS Symposium Series 54, *Computer Assisted Structure Elucidation*, D. H. Smith, ed., 1977, 108.
156. H. Abe, I. Fujiwara, T. Nishimura, Y. Okuyama, T. Kida and S. Sasaki, *Computer Enhanced Spectroscopy*, 1983, **1**, 55.
157. S. Sasaki and Y. Kudo, *J. Chem. Inf. Comput. Sci.*, 1985, **25**, 252.
158. K. Funatsu, Y. Susuta and S. Sasaki, *J. Chem. Inf. Comput. Sci.*, 1989, **29**, 6.
159. A. Bax, R. Freeman and S. P. Kempsell, *J. Am. Chem. Soc.*, 1980, **102**, 4849.
160. A. Bax, R. Freeman, T. A. Frenkiel and M. H. Levitt, *J. Magn. Reson.*, 1981, **43**, 478.
161. A. Bax, R. Freeman and T. A. Frenkiel, *J. Am. Chem. Soc.*, 1981, **103**, 2102.
162. A. J. Shaka and R. Freeman, *J. Magn. Reson.*, 1982, **50**, 502.
163. K. Funatsu, B. P. Acharya and S. Sasaki, *J. Chem. Inf. Comput. Sci.*, 1994, **34**, 735.
164. K. Funatsu, K. Eguchi and S. Sasaki, *Proceedings of the 16th Symposium of Chemical Information and Computer Sciences/21st Symposium on Structure–Activity Relationships*, T. Tsukihara, ed., Tokushima University, Tokushima, Japan, 1993, 81.
165. K. Funatsu, C. A. Del Carpio and S. Sasaki, *Fr. Z. Anal. Chem.*, 1986, **324**, 750.
166. S. Castellano and A. A. Bothner-By, *J. Chem. Phys.*, 1964, **41**, 3863.
167. K. Funatsu, M. Nishizaki and S. Sasaki, *J. Chem. Inf. Comput. Sci.*, 1994, **34**, 745.
168. K. Funatsu and S. Sasaki, *J. Chem. Inf. Comput. Sci.*, 1996, **36**, 190.
169. C. A. Shelley and M. E. Munk, *Anal. Chim. Acta*, 1981, **133**, 507.
170. M. Munk, C. Shelley, H. Woodruff and M. Trulson, *Fresnius Z. Anal. Chem.*, 1982, **313**, 473.
171. B. D. Christie and M. E. Munk, *J. Chem. Inf. Comput. Sci.*, 1988, **28**, 87.
172. B. Christie and M. Munk, *Anal. Chim. Acta*, 1987, **200**, 347.
173. B. D. Christie and M. E. Munk, *J. Am. Chem. Soc.*, 1991, **113**, 3750.
174. M. E. Munk, M. S. Madison and E. W. Robb, Abstracts of 216th ACS National Meeting, Boston, August 1998, 397.

175. C. Peng, S.-G. Yuan, C.-Z. Zheng and Y.-Z. Hui, *J. Chem. Inf. Comput. Sci.*, 1994, **34**, 805.
176. C. Peng, S.-G. Yuan, C.-Z. Zheng, Y.-Z. Hui, H.-M. Wu, K. Ma and X.-W. Han, *J. Chem. Inf. Comput. Sci.*, 1994, **34**, 814.
177. C. Peng, S.-G. Yuan, C.-Z. Zheng, Z.-S. Shi and H.-M. Wu, *J. Chem. Inf. Comput. Sci.*, 1995, **35**, 539.
178. H. Schriber and E. Pretsch, *J. Chem. Inf. Comput. Sci.*, 1997, **37**, 879.
179. H. Schriber and E. Pretsch, *J. Chem. Inf. Comput. Sci.*, 1997, **37**, 884.
180. M. Badertscher, A. Korytko, K.-P. Schulz, M. Madison, M. E. Munk, P. Portmann, M. Junghans, P. Fontana and E. Pretsch, *Chemometrics and Intelligent Systems*, 2000, **51**, 73.
181. P. Fontana and E. Pretsch, *J. Chem. Inf. Comput. Sci.*, 2002, **42**, 614.
182. M. Will, W. Fachinger and J. R. Richert, *J. Chem. Inf. Comput. Sci.*, 1996, **36**, 221.
183. J. Meiler and M. Will, *J. Chem. Inf. Comput. Sci.*, 2001, **41**, 1535.
184. J. Meiler and M. Will, *J. Am. Chem. Soc.*, 2002, **124**(9), 1868.
185. R. Grund, A. Kerber and R. Laue, *MATCH C.*, 1992, **27**, 87.
186. C. Benecke, R. Grund, R. Hohberger, A. Kerber, R. Laue and T. Wieland, *Anal. Chim. Acta*, 1995, **314**, 141.
187. J. Meiler and M. Meringer, *Match*, 2002, **45**, 85.
188. J.-M. Nuzillard and G. Massiot, *Tetrahedron*, 1991, **47**, 3655.
189. G. Massiot and J. M. Nuzillard, *Phytochem. Anal.*, 1992, **3**, 153.
190. L. Müller, *J. Am. Chem. Soc.*, 1979, **101**, 481.
191. A. Bax, R. H. Griffey and B. L. Hawkins, *J. Magn. Reson.*, 1983, **55**, 301.
192. G. E. Martin and A. S. Zektzer, *Two-Dimensional NMR Methods for Establishing Connectivity*, VCH, Weinheim, 1988, 213.
193. A. Bax and M. F. Summers, *J. Am. Chem. Soc.*, 1986, **108**, 2093.
194. G. E. Martin and A. S. Zektzer, *Two-Dimensional NMR Methods for Establishing Connectivity*, VCH, Weinheim, 1988, 267.
195. J. Jeener, *Ampère International Summer School*, Basko, Polje, 1971.
196. W. P. Aue, E. Bartholdi and R. R. Ernst, *J. Chem. Phys.*, 1975, **64**, 2229.
197. A. E. Derome, *Modern NMR Techniques for NMR Chemistry Research*, Pergamon, Oxford, 1987, 183.
198. D. M. Doddrell, D. T. Pegg and M. R. Bendall, *J. Magn. Reson.*, 1982, **48**, 323.
199. J.-M. Nuzillard, *J. Chem. Inf. Comput. Sci.*, 1994, **34**, 723.
200. S. V. Ley, K. Doherty, G. Massiot and J.-M. Nuzillard, *Tetrahedron*, 1994, **50**, 12267.
201. G. Almanza, L. Balderrama, C. Labbé, C. Lavaud, G. Massiot, J.-M. Nuzillard, J. D. Connolly, L. J. Farrugia and D. S. Rycroft, *Tetrahedron*, 1997, **53**, 14719.
202. J.-M. Nuzillard, *J. Chim. Phys.*, 1998, **95**, 169.
203. J.-M. Nuzillard, J. D. Connolly, C. Delaude, B. Richard, M. Zèches-Hanrot and L. Le Men-Olivier, *Tetrahedron*, 1999, **55**, 11511.
204. D. Mulholland, H. Mahomed, M. Kotsos, M. Randrianarivelojosia, C. Lavaud, G. Massiot and J.-M. Nuzillard, *Tetrahedron*, 1999, **55**, 11547.
205. D. A. Mulholland, M. Randrianarivelojosia, C. Lavaud, J.-M. Nuzillard and S. L. Schwikkard, *Phytochemistry*, 2000, **53**, 115.
206. D. A. Mulholland, S. L. Schwikkard, P. Sandor and J.-M. Nuzillard, *Phytochemistry*, 2000, **53**, 465.
207. J.-M. Nuzillard, W. Naanaa and S. Pimont, *J. Chem. Inf. Comput. Sci.*, 1995, **35**, 1068.
208. T. Lindel, J. Junker and M. Köck, *J. Mol. Model*, 1997, **3**, 364.
209. T. Lindel, J. Junker and M. Köck, *J. Org. Chem.*, 1999, 573.
210. M. Köck, J. Junker, W. Maier, M. Will and T. Lindel, *Eur. J. Org. Chem.*, 1999, 579.
211. B. Reif, M. Köck, R. Kerssebaum, H. Wang, W. Fenical and C. Griesinger, *J. Magn. Reson.*, 1996, **A118**, 282.
212. M. Köck, B. Rief, W. Fenical and C. Griesinger, *Tetrahedron Lett.*, 1996, **37**, 363.

213. M. Köck and J. Junker, D. Ulf, ed., *Bioorganic Chemistry*, Wiley-VCH, Weinheim, 1999, 365–378.
214. J. Meiler, E. Sanli, J. Junker, R. Meusinger, T. Lindel, M. Will, W. Maier and M. Köck, *J. Chem. Inf. Comput. Sci.*, 2002, **42**, 241.
215. M. E. Elyashberg, K. A. Blinov and E. R. Martirosian, *Autom. Inf. Manage.*, 1999, **34**(1), 15.
216. K. A. Blinof, M. E. Elyashberg, S. G. Molodtsov, A. J. Williams and E. R. Martirosian, *Fresnius J. Anal. Chem.*, 2001, **369**, 709.
217. G. E. Martin, C. E. Hadden, D. J. Russell, B. D. Kaluzny, J. E. Guido, W. K. Duholke, B. A. Stiemsma, T. J. Thamann, R. C. Crouch, K. Blinov, M. Elyashberg, E. R. Martirosian, S. G. Molodtsov, A. J. Williams, P. L. Schiff, *J. Heterocyclic Chem.*, 2002, **39**, 1241.
218. K. A. Blinov, D. Carlson, M. E . Elyashberg, G. E. Martin, E. R. Martirosian, S. Molodtsov and A. J. Williams*, Magn. Reson. Chem.*, 2003, **41** 359.
219. C. Peng, S. Yuan, C. Zheng and Y. Hui, *J. Chem. Inf. Comput. Sci.*, 1994, **34**, 805.
220. C. Peng, S. Yuan and C. Zheng, *J. Chem. Inf. Comput. Sci.*, 1995, **35**, 539.
221. C. Peng, S. Yuan, C. Zheng, Y. Hui, H. Wu, K. Ma and X. Han, *J. Chem. Inf. Comput. Sci.*, 1994, **34**, 814.
222. C. Peng, G. Bodenhausen, S. Qiu, H. H. S. Fong, N. R. Farnsworth, S. Yuan and C. Zheng, *Magn. Reson. Chem.*, 1998, **36**, 267.
223. C. Peng and S. Szalma, *Abstract paper Am. Chem. Soc., 221st*, 2001, COMP-181.
224. U. Eggenberger and G. Bodenhausen, *Anal. Chem.*, 1989, **61**, 2298.
225. P. Pfändler and G. Bodenhausen, *Magn. Reson. Chem.*, 1988, **26**, 888.
226. NMR-SAMS, Spectrum Research LLC., University Research Park, 505 South Rosa Road, Madison, WI 53719, USA.
227. J.-E. Dubois, M. Carabedian and I. Dagne, *Anal. Chim. Acta*, 1984, **158**, 217.
228. M. Badertscher, K. Bishofberger and E. Pretsch, *Trends Anal. Chem.*, 1997, **5**, 234.

Index

Note – Page numbers in *italic* type refer to figures and tables.